DISS. ETH No. 19936

A flexible software framework and post hoc cell type discrimination for *in vivo* two-photon calcium imaging of neuronal population activity

DISSERTATION

submitted to

ETH ZURICH

for the degree of

DOCTOR OF SCIENCES

presented by

DOMINIK LANGER

Dipl. natw. ETH

born 12th of December 1978

citizen of Zurich (ZH), Switzerland

accepted on the recommendation of

Prof. Dr. Kevan A.C. Martin, examiner, ETH Zurich

Prof. Dr. Fritjof Helmchen, co-examiner, University of Zurich

Prof. Dr. Jean-Marc Fritschy, co-examiner, University of Zurich

2011

After all, can the human soul be glimpsed through a microscope? Maybe, but you'd definitely need one of those very good ones with two eyepieces.

Woody Allen

Contents

List of Figures

Zusammenfassung

Der Neocortex, insbesondere der des Menschen, wird als die komplexeste Struktur im bekannten Universum betrachtet. Funktionell gesehen ist er massgeblich beteiligt an höheren Gehirnfunktionen wie der Verarbeitung von sensorischer Information, der motorischen Kontrolle des Körpers, sowie kognitiven Prozessen. Strukturell gesehen umschliesst er die beiden Gehirnhemisphären als eine 1-4 mm dicke Schicht und besteht aus einem hochkomplexen Netzwerk miteinander verbundener Zellen. Obwohl während der letzten Jahrzehnte eine riesige Menge anatomischer und physiologischer Daten über den Neocortex gesammelt worden sind, ist die funktionelle Organisation des neocorticalen neuronalen Netzwerkes nach wie vor nur ansatzweise verstanden. Sicher ist jedoch, dass Information im Neocortex als Fluktuationen der Zellmembranpotentiale, welche sich durch das neuronale Netzwerk fortpflanzen, repräsentiert und verarbeitet wird. Wir fassen diese elektrischen Potentialfluktuationen unter dem Begriff *neuronale Aktivität* zusammen.

Wegen seiner Eindringtiefe von bis zu einem Millimeter und seiner hohen dreidimensionalen räumlichen Auflösung hat sich die Zweiphotonenmikroskopie (2PM) zur Methode der Wahl entwickelt, wenn es darum geht, Populationen von Neuronen innerhalb des Neocortex lebender Tiere zu beobachten. In Kombination mit Techniken, welche es ermöglichen, mehrere hundert Zellen mit fluoreszenten Indikatoren neuronaler Aktivität (insbesondere Calciumindikatoren) zu beschicken, wurde es möglich, die Aktivität neuronaler Zellpopulationen im Gehirn *in vivo* (d.h. im lebenden Tier) zu beobachten.

Forscher, welche 2PM für Messungen am intakten, lebenden Gehirn einsetzen, haben in der Regel hohe Ansprüche an Flexibilität und verwenden daher oft selbstgebaute oder kundenspezifisch angefertigte Mikroskopaufbauten, welche von eigens entwickelter Software angesteuert werden. Wegen der kontinuierlichen technologischen Weiterentwicklung in diesem Forschungsfeld hat sich ein Bedürfnis nach einer Software-Lösung herauskristallisiert, welche sowohl dem Forscher Zugriff auf die neuesten Bildaufnahmetechniken gewährt, als auch dem Entwickler eine solide Ausgangsplattform zur Verfügung stellt, mit welcher Erweiterungen einfach implementiert und neue Ideen rasch realisiert werden können. Im ersten Teil dieser Doktorarbeit stelle ich HelioScan, ein mit LabVIEW entwickeltes Software-Paket vor. Es dient a) als eine Sammlung von Komponenten, aus welchen eine Ansteuerungs- und Bilderfassungs-Anwendung flexibel entsprechend den eigenen Bedürfnissen zusammengesetzt werden kann, und b) als ein Gerüst (Framework), innerhalb dem neue Funktionalität schnell und strukturiert implementiert werden kann.

Definiert durch vom Benutzer erstellte Konfigurationsdateien setzt sich eine HelioScan-Anwendung zu Laufzeit aus einzelnen Software-Komponenten zusammen. Dieser Ansatz

erlaubt eine hohe Flexibilität in Bezug auf vorhandene Hardware und funktionelle Anforderungen. Gegenwärtig verfügbare Komponenten erlauben a) kamera-basierte Aufnahmemodi wie z.B. zur Messung des intrinsischen optischen Signals von neuronalem Gewebe, sowie diverse laser-scanning-basierte Aufnahmemodi, basierend auf b) galvanometrischen Spiegeln und c) akusto-optischen Deflektoren (AODs). Die HelioScan-Komponenten sind in einem objektorientierten Ansatz implementiert. Generische abstrakte Klassen definieren sowohl die verschiedenen Arten von Komponenten, als auch deren mögliche Interaktionen. Neue Komponenten können erstellt werden, indem sie von existierenden Basisklassen abgeleitet werden. Diverse Gerüstklassen, welche sich ihrerseits von den generischen abstrakten Klassen ableiten, erlauben es, von bereits implementierter Funktionalität Gebrauch zu machen. Dank dieser komponentenbasierten Systemarchitektur unterstützt HelioScan auch kollaborative Ansätze, in welchen mehrere Entwickler gleichzeitig an neuer Funktionalität arbeiten.

Die zellulären Komponenten des neocorticalen neuronalen Netzwerkes zeigen eine hohe Diversität in Bezug auf ihre morphologischen, physiologischen und molekularen Eigenschaften. Diese Diversität ist jedoch nicht kontinuierlich, so dass Gehirnzellen durchaus verschiedenen Klassen mit gemeinsamen oder zumindest ähnlichen Eigenschaften zugeordnet werden können. Diesen Klassen (Zelltypen) wiederum können zunehmend unterschiedliche Funktionen im neuronalen Netzwerk zugeordnet werden. Daher ist es wichtig, dass auch bei der 2PM unterschiedliche Zelltypen unterschieden werden können. In einem zweiten Teil dieser Doktorarbeit stelle ich daher drei Methoden zur Zelltypunterscheidung bei funktionellen Calcium-Bildgebungsexperimenten im intakten Neocortex vor.

Der erste Ansatz erlaubt es, inhibitorische Interneuronen (GABAerge Neuronen), Astrocyten und exzitatorische Neuronen zu unterscheiden und basiert auf drei fluoreszenten Farbstoffen, welche gleichzeitig beobachtet und spektral unterschieden werden können. Verwendet wird dabei eine Kombination der transgenen GAD67-GFP-Mauslinie, in welcher GABAerge Neuronen grün fluoreszierendes Protein (GFP) exprimieren, sowie dem roten, astrocyten-spezifischen Farbstoff Sulforhodamin 101 und dem grünen, unspezifischen Calcium-Indikator Oregon Green 488 BAPTA-1 (OGB-1).

Die zweite Methode benützt eine Immunfärbung im Anschluss (d.h. post-hoc) an ein *in vivo* durchgeführtes two-photon laser-scanning microscopy (2PM)-Experiment, um Zellen anhand ihrer Expression molekularer Marker zu unterscheiden. Nach dem funktionellen Calcium-Bildgebungsexperiment und der Aufnahme eines dreidimensionalen Referenzbildstapels wird das Gehirn fixiert und anschliessend in coronale Scheiben geschnitten. Diejenigen Scheiben, welche das zu untersuchende Volumen enthalten, werden anhand des Blutgefässmusters auf ihrem dünnen Streifen Gehirnoberfläche identifiziert. Nach der Immunfärbung werden dreidimensionale Bildstapel von den entsprechenden Bereichen dieser Scheiben aufgenommen und im Computer so rotiert, dass ihre Orientierung der des ursprünglichen Referenzbildstapels entspricht. Zellen im Referenzbildstapel werden dann in den Bildstapeln der gefärbten Schnitte identifiziert und ihre Markerkombination festgestellt. Ich habe die Anwendbarkeit dieser Methode demonstriert, indem ich GABAerge

Zellen anhand ihres Expressionsmusters von calciumbindenden Proteinen unterschieden habe.

Die dritte Methode ist ähnlich der zweiten, verwendet aber ein Schneideverfahren, welches in bereits optimal ausgerichteten tangentialen Schnitten resultiert. Dieser Ansatz muss noch weiter optimiert und charakterisiert werden, erste Resultate zeigen aber, dass Zellen, welche zuerst *in vivo* beobachtet wurden, sehr einfach in den Schnitten wiedergefunden werden können.

Zusammengefasst habe ich in dieser Doktorarbeit zwei neue, flexible und erweiterbare Werkzeuge eingeführt. HelioScan hat meiner Meinung nach das Potential, zur Software der Wahl in 2PM-Laboratorien zu werden, welche einen hohen Grad an Diversität bei Hardware oder Funktionalität aufweisen oder häufige Änderungen derselben bewältigen müssen. Das Aufkommen chronischer Präparationen erlauben es – dank virus-induzierter Expression genetisch kodierter Calciumindikatoren – über Wochen oder gar Monate vom selben Tier Daten zu erheben. Damit sinkt der relative Aufwand, welcher für eine anschliessende Zelltypdiskriminierung mittels Immunhistochemie aufgewendet werden muss. Ich erwarte daher, dass post-hoc-Zelltypdiskriminierung in Zukunft routinemässig angewendet werden wird.

Summary

The neocortex, especially that of humans, is considered to be the most complex structure in the known universe. Functionally, it is involved in higher order brain functions such as sensory processing, generation of motor commands, and cognitive processes. Structurally, it encloses the cerebral hemispheres as a sheet that is one to four millimetres thick and consists of a highly complex network of interconnected cells. Even though a wealth of anatomical and physiological data has been collected over the past decades, the functional organization of the neocortical microcircuitry is still a mystery. What is known for sure is that information is represented and processed in the neocortex as membrane potential fluctuations travelling through the neuronal network. We refer to such fluctuations as neuronal activity.

Due to its tissue penetration capabilities of up to one millimetre and its high spatial resolution with spatial resolution in three dimensions, *2PM* has become the method of choice to image populations of neurons inside the neocortex of living animals. In combination with techniques that allow to load populations of several hundred cells with fluorescent indicators of neural activity (in particular: calcium indicators), it is possible to observe neuronal population activity inside the brain *in vivo*.

Researchers performing *in vivo* 2PM often use custom-built microscopy setups controlled by custom-written software due to the high flexibility they require. The continuous technical advancement of the field created a need for new control software that is flexible enough to supply both the biological researcher with the newest image acquisition techniques and the developer with a solid platform from which various new extensions can be implemented and ideas quickly realised. In the first part of this thesis, I introduce HelioScan, a software package written in LabVIEW. It serves i) as a component collection allowing to flexibly assemble a microscopy control software according to the individual needs of a researcher, and ii) as a framework within which new functionality can be implemented in a quick and structured manner.

A specific HelioScan application assembles at run-time from individual software components, based on user-defined configuration files. This concept allows high flexibility with regard to different hardware or functional requirements. Currently implemented components enable i) camera-based imaging such as intrinsic optical signal (IOS) imaging, as well as different laser-scanning modes employing ii) galvanometric mirrors and iii) acousto-optic deflectors (AODs). Components are implemented in an object-oriented fashion, with generic interface classes defining the component types as well as their possible interactions. New components can be implemented by inheriting from existing base classes. Various scaffold classes derived from the generic interface classes provide functionality that can be quickly

extended. Due to its component-based architecture, HelioScan promotes collaborative efforts in which several developers work in parallel on implementing new functionality.

The cellular components of the neocortical neural network are diverse with respect to their precise morphology, physiology and molecular composition. Their diversity does not form a continuum, however. As a consequence, they can be grouped into different classes based on common, or, at least, similar features. Different functional roles can be attributed to these classes (cell types). Thus, it is important to be able to distinguish between different cell types in two-photon calcium imaging. In the second part of this thesis, I present three methods for cell type discrimination in two-photon calcium imaging of the neocortex.

The first of these methods allows one to distinguish between GABAergic cells, astrocytes and excitatory neurons. It is based on a preparation with three fluorescent labels that can be simultaneously imaged and spectrally resolved. In particular, it involves the GAD67-GFP transgenic mouse line (in which GABAergic neurons express green fluorescent protein (GFP)), the red dye sulforhodamine 101 (SR101) for astrocyte-specific labelling and unspecific loading with the green calcium indicator OGB-1.

The second method uses post hoc immunostaining to discriminate cells according to their expression of molecular markers. Specifically, after *in vivo* two-photon calcium imaging and the acquisition of a three-dimensional reference image stack, the brain is fixed and then cut into coronal sections. Slices containing parts of the volume-of-interest are selected based on the blood vessel pattern on their thin stripe of pial surface. After immunostaining, the slices are imaged and rotation-fitted to the reference image stack. Cell-to-cell assignment between reference image stack and slice image stacks allows cell type discrimination according to different combinations of molecular markers. In this thesis, I demonstrate the applicability of this approach by discriminating different GABAergic cells based on their expression of calcium-binding proteins both in GAD67-GFP mice and in wild type mice expressing a genetically encoded calcium indicator (GECI).

The third method is similar to the second one, but it uses a cutting procedure that results in tangential sections and provides intrinsic rotation-fitting. Although further exploration of this approach is still pending, the first results indicate that cells previously imaged *in vivo* can be easily re-identified in the sectioned brain.

In summary, I introduced two flexible and extensible tools. I expect HelioScan to become the software of choice in two-photon imaging laboratories that have to deal with diverse and frequently changing hardware and functionality requirements. The rise of chronic preparations based on viral-induced GECI expression allows activity read-outs to be recorded over weeks or months. Due to the associated decrease in the relative overhead, I expect post hoc cell type discrimination to become a technique that is routinely applied in future 2PM calcium imaging experiments.

1 Introduction

[...] for the limits to which our thoughts are confind, are small in respect of the vast extent of Nature itself; some parts of it are too large to be comprehended and some too little to be percieved. And from thence it must follow, that not having a full sensation of the Object, we must be very lame and imperfect in our conceptions about it, and in all the propositions which we build upon it; hence we often take the shadow of things for the substance, small appearances for good similitudes, similitudes for definitions; and even many of those which we think to be the most solid definitions, are rather expressions of our own misguided apprehensions then of the true nature of the things themelves.

Robert Hooke [140]

1.1 Microanatomy of the neocortex

1.1.1 The beginning

Cellular neurobiology has a rather young history. The cell was proposed as the basic building unit of all animals[1] at the end of the 1830s, but the nervous system was still considered to be an exception to that rule during the second half of the nineteenth century. The nervous system was thought of as a continuous network rather than an aggregate of individual cellular units. This so-called *reticular theory* was challenged by the *hypothesis of free endings*, which initially had only a few followers (Figure 1.1a on page 8).

Using a newly developed staining method, the Spanish neuroscientist Santiago Ramón y Cajal finally helped the hypothesis of free endings to get accepted [235, 64]. With his staining technique, Cajal managed to reliably visualise the morphology and connectivity of different types of neurons (Figure 1.1b and Figure 1.1c on page 8). Based on his observations, he proposed some of the most fundamental corner stones of neuroscience, including the neuron doctrine[2] (1888), the existence of the dendritic spine (1888), the existence and function of the axonal growth cone (1890), the law of dynamic polarisation[3] (1891), the neurotropic hypothesis[4] (1892), and the concept of learning as selective strengthening of

---

[1]The so-called *cell theory.*

[2]The *neuron doctrine* is the basic principle of neuroscience declaring individual neurons to be the elementary signalling units of the nervous system [155].

[3]The *law of dynamic polarisation* states that electrical signals within a nerve cell flow only in one direction: from their reception sites towards the soma and from there through the axon towards target cells [155].

[4]In his *neurotropic hypothesis*, Cajal proposed that chemoattractive substances might guide the growth cones towards their final targets during the development of the nervous system [234, 65].

synapses [8, 65, 64].
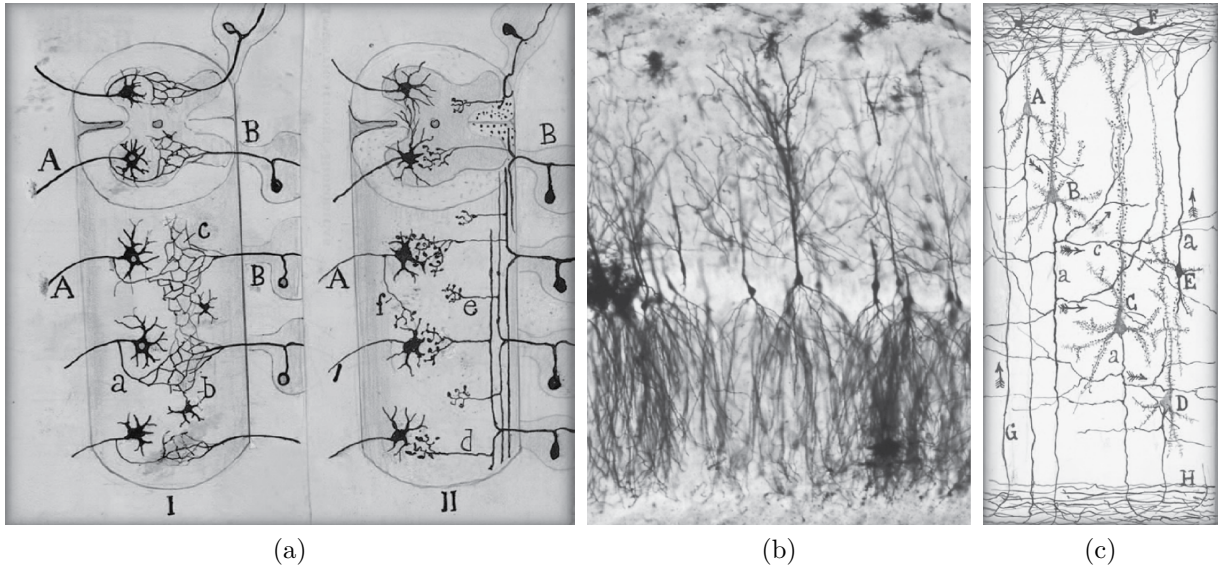
Figure 1.1: Cajal's microanatomical studies of nervous tissue. **(a)** Drawing explaining the differences between the reticular (left) and the neuron (right) theory. (from [68]). **(b)** Photomicrograph of one of Cajal's original preparations (here: rabbit pyramidal cells) obtained using the double impregnation method (from [65]). **(c)** Drawing showing synaptic connections and the suggested flow of information in cerebral circuits (from [65]).

1.1.2   Main cell types

In the brain—as in any other organ—cells are specialised for different functions. In biology, form and function always go hand in hand. It is therefore not surprising that already Cajal in his extensive histological studies found a plethora of different neuron shapes [8]. Today, with many more tools at hand, researchers categorise neural cells not only according to morphology as did Cajal, but also according to electrophysiology, connectivity, and molecular phenotypes (see Section 1.2.1) [20]. In fact, one of the two main achievements of this thesis is a technique that can be employed for cell type discriminiation (see Section 1.6.2 and Chapter 3).

Below, I briefly describe the major cell types in order to introduce the key players in the following sketches of cortical microcircuits. Additionally, in the section about GABAergic cells, I will present in more detail the ongoing dispute on cell classification (Section 1.2).

Pyramidal neurons

Pyramidal neurons received their name due to the shape of their cell bodies, which possess a triangular cross-section (Figure 1.1 on page 8). The upper tip of their cone-shaped somata continues into the *apical dendrite*, which ascends vertically to the border of cortical

layer I (L1) and cortical layer II (L2), where it branches into a terminal dendritic tuft. Nearly horizontal side branches can divert from the vertically oriented apical dendrite. *Basal dendrites* emanate directly from the cell body and radiate into all directions. Most dendrites are strewn with small membrane protuberances called *dendritic spines* (a few ten thousands per cell), serving as input compartments for synapses with other neurons' axon terminals. The base of the cell body gives rise to the axon that descends vertically downwards, in most cases leaving the cortex and diving into the white matter. Collaterals branch off the main axon and ramify in well-defined patches to contact nearby cells [9].

Pyramidal neurons exert excitatory action onto their postsynaptic target neurons using the neurotransmitter *glutamate* [155].

Interneurons

Although different types of pyramidal neurons have been shown to exist [301, 300], the diversity among non-pyramidal neurons is even more staggering. To bring order into this diversity, classifications can be made according to different criteria.

One major distinction can be made between *projection neurons* sending efferents to other brain regions through the white matter and *interneurons* forming local connections. Based on this criterion, most non-pyramidal cells can be classified as interneurons ("short-axon" neurons in the terminology of the first pioneers who studied them [183]).

Another distinction can be made based on the effect neurons exert on their postsynaptic targets by classifying them into *excitatory* or *inhibitory*. The most prominent excitatory interneuron type is the spiny stellate cell in cortical layer IV (L4), which serves as the major input relay station for sensory afferents. They are equipped with spine-studded dendrites radiating from the soma in a star-like appearance, and the main axon branches either ascend or descend vertically to reach their supra- and infragranular target layers. In contrast, the population of inhibitory interneurons accounts for most of the diversity among non-pyramidal neurons. The latter can also be categorised according to their neurotransmitter content. Here, it is most important to distinguish according to the presence or absence, respectively, of the neurotransmitter γ-amino butyric acid (GABA)[5].

These three classification schemes largely overlap; GABAergic cells are almost exclusively of inhibitory nature and can mainly be categorised as interneurons. For the moment, we will leave the topic of GABAergic interneurons. It will be more extensively examined in Section 1.2.

Glial cells

The non-neuronal neocortical cell population mainly consists of glial cells. These cells serve a multitude of functions; for example, providing support for the neural tissue or maintaining homeostasis [290]. In the adult neocortex, astrocytes and microglia are two key players in the glial population.

---

[5]IUPAC name: 4-hydroxy butanoic acid

Astrocytes, named after their star-like appearance, closely contact microscopic blood vessels with their end feet. This morphological feature is related to their involvement in the blood-brain barrier and the provision of nutrients to the neural cells. For *in vivo* two-photon microscopy as used in this thesis, astrocytes can be selectively labelled by applying the red fluorescent dye SR101 to the brain surface [219]. Rapidly taken up by transporter proteins, the dye is transported through a syncytium of gap-junction-coupled astrocytes by passive diffusion [219, 143].

Related to cells of the monocyte/macrophage lineage, *microglia* are a key component of the brain's immune system. Being able to perform amoebal movements, they scavenge the surrounding tisse for cell debris, infectious agents and plaques [107, 218].

1.1.3   Laminar structure

Already in 1782, Francesco Gennari observed a layered structure of the part of human cortex that later became known as the striate cortex. Roughly one hundred years later, cell-staining techniques revealed that the neocortex indeed consists of several distinct tangential layers. A six-layered structure of the neocortex became generally accepted at the beginning of the twentieth century and is reflected in cytoarchitectonics[6], myeloarchitectonics[7] and chemoarchitectonics[8] (Figure 1.2 on page 11) [9]. The faint band originally observed by Gennari, termed *lamina granularis* due to its densely packed cell bodies as revealed by a Nissl stain, is now mostly referred to as L4 and still dominates nomenclature by dividing the cortex into *supragranular* and *subgranular* layers [252].

Differences in the characteristics of the separate layers (cell density, thickness and constituent cell types) among different parts of the cortex have been used to define different cortical regions [293, 28].

1.1.4   Vertical structure

Rafael Lorente de Nó, a former student of Cajal [8], observed in 1938 that chains of synaptically connected neurons in the neocortex are preferentially oriented vertically [9] (Figure 1.3a on page 11). Based on this finding, he later proposed that an *elementary unit* of the cortex, a vertical cylinder, could contain all the elements necessary to accomplish the process of transmitting impulses from the afferent fibre to the efferent axon [142]. Different aspects of verticality, in terms of anatomy and physiology, have subsequently been discovered in the cortex, coining the term of the *cortical column* [210, 142]. However, the terminology in the field is not well-defined and can be confusing.

---

[6] *Cytoarchitectonics* refers to the arrangement of cell bodies, as well as their size, shape and densities. It can for example be visualised by a Nissl or nuclear stain (e.g. a 4',6-diamidino-2-phenylindole (DAPI) stain).

[7] *Myeloarchitectonics* refers to the arrangement, density and thickness of neurites.

[8] *Chemoarchitectonics* refers to the distribution of specific chemical substances.
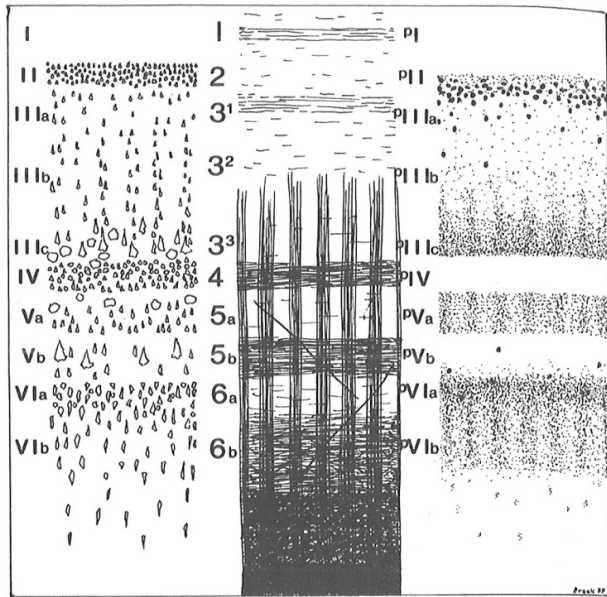
Figure 1.2: Layered structure of the neocortex (from [9]). Left: cytoarchitectonics; middle: myeloarchitectonics; right: lipofuscin pigment architectonics. Numbering of layers is from outside (pial surface) to inside of the brain [155]:

- *Layer I (L1)*: mostly tangentially oriented axons and dendrites of neurons located in deeper layers, also some sparsely distributed cells (most of them GABAergic).
- *Layer II (L2)*: densely packed, mainly small and spherical cells.
- *Layer III (L3)*: largely pyramidal-shaped cells, which seem to form vertical columns; on average, soma size increases with depth.
- *Layer IV (L4)*: small cell bodies of polyhedral shape.
- *Layer V (L5)*: mainly pyramidal cell bodies.
- *Layer VI (L6)*: rather heterogeneous in terms of cell body shapes; blends into the subjacent white matter.

(a)   (b)   (c)   (d)
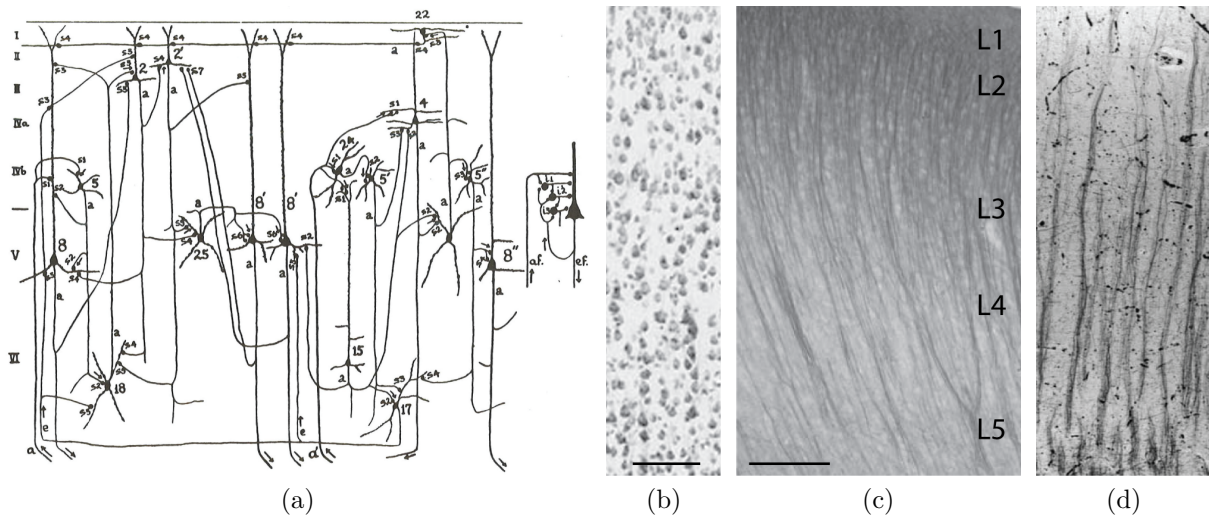
Figure 1.3: Different vertical structures in the neocortex. **(a)** Diagram of cortical structure by Lorente de Nó (1938) depicting the preferentially vertical orientation of neuron chains in the neocortex (from [9]). **(b)** Nissl stain revealing vertical cell rows in L2/3 (adapted from [240]). Scale bar: 100 µm. **(c)** Bundles of apical dendrites revealed by immunostaining of microtubule-associated protein 2 (adapted from [240]). Scale bar 200 µm. **(d)** Bundles of myelinated fibers in human cortex (adapted from [38]; scale bar not provided in source).

The minicolumn

Minicolumns (sometimes called microcolumns) refer to vertical anatomical structures with a diameter of 20–60µm that are horizontally repeated with a mean distance of 80 µm (reviewed in [208, 210, 38, 240]). Differently defined structures (Figure 1.3 on page 11)

have been shown to largerly overlap. The minicolumn has therefore been suggested as a basic neocortical unit containing the majority of neocortical constituents.

During development, neocortical cells are provided by a series of asymmetric divisions of progenitor cells. They then migrate into the cortex in a radial fashion along so-called radial glial cells, thereby forming *ontogenetic cell columns*. It is assumed that these columnar structures eventually develop into the above-mentioned minicolumns [210].

Structures of minicolumnar dimensions have also been identified in various functional studies (reviewed in [38]), which in some cases have been shown to be correlated to underlying anatomical structures. For example in sensory cortex, cells belonging to the same minicolumn have similar overlapping receptive field location and submodality [240].

None of the different vertical structures shown in Figure 1.3 spans the whole six neocortical layers [240]. Furthermore, the degree of verticality strongly depends on the cortical region [240] and also varies among species and even individuals [142]. Even within an area, minicolumns are thought to be variable [208, 240]. Taking into consideration this variability (reviewed in [142, 38]), it is not surprising that it is still a matter of debate how far an anatomical minicolumn is identical with a module or building brick of the neocortec in terms of function or microcircuitry [62, 142, 77, 210, 39].

The macrocolumn

In the sensory cortex, functionally defined cortical columns have been found to be an organising principle [155]. Seminal experiments by Vermont Mountcastle (1957) in the somatosensory cortex [209] and shortly thereafter by Torsten Wiesel and David Hubel (1963) in the visual cortex [145] showed that neurons close to each other in the horizontal dimension do not only have spatially overlapping receptive fields, but may also share the selectivity for a certain stimulus modality or a specific extent of a stimulus feature.

The diameters of such functionally defined columns have been reported to be in the range of 300–600µm. The hypothetical construct of the *macrocolumn* was introduced as a bundle of neighbouring minicolumns bound together by many short-range horizontal connections, which share certain static or dynamical physiological properties [210]. However, except for the columns representing individual whiskers in the rodent barrel cortex, clear anatomical substrates of macrocolumn-sized functionally defined columns have not been found. The concept is further challenged by the fact that columns defined by different stimulus features are arranged in non-congruent patterns. It has thus been suggested that it is the pre-structured afferent input that organises cortical neurons into columns in a dynamic fashion [142].

1.2   GABAergic interneurons of the neocortex

As briefly mentioned in Section 1.1.2, GABAergic cells are the main inhibitory neurons of the cortex. *Inhibitory* means that their own activity decreases the firing probability of their target neurons. Briefly, the inhibitory action of their neurotransmitter GABA is

mediated by the inflow of chloride ions through ionotropic $GABA_A$ receptors or by indirectly inhibiting action through metabotropic $GABA_B$ receptors [155].

Only recently has it become possible to distinguish GABAergic from non-GABAergic neurons or even discriminate subtypes in the GABAergic population using *in vivo* two-photon calcium imaging (see Section 1.3 and Section 1.4 for more details on this technique). This achievement is one of the two main topics of this thesis. For this reason, I will use this section to shine light on the known facts about neocortical GABAergic neurons.

1.2.1 Diversity

In addition to their mostly inhibitory action on target neurons, the most prominent feature of GABAergic neurons is their diversity [199]. Various classification attempts have been suggested (see below), but the individual outcomes have rarely been completely congruent or without exceptions [13, 192, 79, 124]. As a result, a continuum of GABAergic cells has been suggested as an alternative to distinct subtypes [192, 224]. Even more drastically, the question has been raised whether GABAergic neurons might endanger the concept of cell types [264] in the brain. Certainly, reality is more complex than the abstractions we build on top of it. However, in that respect, GABAergic cells are not much different from any other topic in biology [30]—maybe, their diversity is just more salient to the human observer than that of excitatory neurons [301, 205].

Classification approaches

The following classical classification approaches are frequently used, either alone or in combination (reviewed in [192, 13, 35]). They are based on properties of GABAergic neurons that are more thoroughly discussed in Section 1.2.2

- *Morphological properties*, including cell body shape and size, as well as arrangement and structure of dendrites, axon and boutons relative to the own soma and that of target cells can be used for classification [183]. Limited information about such features can already be obtained *in vivo* or *in vitro* using appropriate fluorescent labelling and microscopy techniques. More detailed information about the three-dimensional (3D) structure of a neuron is usually obtained by targeted filling of particular neurons with biocytin[9].

- Various *molecular markers* have been identified that occur only in some GABAergic neurons. Markers at the protein- or peptide-level can be detected using immunohistochemistry (IHC) [67]. At the messenger RNA (mRNA)-level, techniques such as fluor-

---

[9]The cell is usually patched in whole-cell mode and filled with biocytin solution. Tissue sections are then incubated with a solution of the biocytin-binding protein Avidin conjugated either to a fluorescent label or the enzyme horse-radish peroxidase. The latter can then catalyse a reaction leading to local accumulation of a dark stain.

escence *in situ* hybridisation (FISH)[10] [176] or reverse transcription PCR (RT-PCR)[11] [269, 282] can be employed. Although the presence of a certain mRNA can be interpreted as a strong hint that also the encoded protein or peptide is present in the cell, th translation products cannot always be detected with IHC [44, 35]. Such discrepancies can be explained by the lower sensitivity of IHC compared to RT-PCR or by regulatory mechanisms acting at posttranscriptional levels [4].

- Different *spiking patterns*—recorded with electrophysiological techniques such as whole-cell patch-clamp or intracellular recordings—can be observed upon injection of a current pulse and used to classify GABAergic neurons.

While such approaches have been used for a few decades, the future will probably lie in unsupervised classification approaches. In the latter, morphological, molecular and electrophysiological properties are quantitatively described and fed into mathematical algorithms searching for clusters in a multidimensional feature space or for correlations between individual features [281, 45]. For such attempts, the Petilla convention provides a strong foundation by listing the parameters that can be used to describe individual interneurons. Maybe, in the future, neuroscientists will no longer try to strictly attribute individual cells to single cell types according to different non-congruent classification schemes; rather, fuzzy classification approaches might express the percentage of how much a particular cell belongs to each of a small number of archetypes [124].

GABAergic neurons in the neocortex differ from their non-GABAergic counterparts in that they migrate to their residential area from distant sites of the telencephalon. Many, if not all, GABAergic neurons originate from the subcortical *ganglionic eminences* and migrate tangentially into the cortex [305]. Thereby, it seems to be their precise location and time of origin that determines their later properties [36, 311] (reviewed in [305, 108]). As a consequence, it has been suggested that GABAergic cells should be classified based on their origin. In turn, the spatiotemporal characteristics of their origin is probably reflected in the set of transcription factors active during their time of "birth". Thus, this combination of transcription factors might be another way to classify them in the future [316].

1.2.2   Important characterising properties

Connectivity

As already mentioned (Section 1.1.2), most GABAergic neurons are interneurons, i.e. their axons do not leave grey matter, but rather contact postsynaptic targets in close vicinity of

---

[10]In FISH, fluorescently labelled oligonucleotide probes cooperatively bind to specific mRNA molecules present in cells in thin tissue slices.

[11]In RT-PCR, one or several mRNAs contained in a mixture are first reverse-transcribed to deoxyribonucleic acid (DNA) by reverse transcriptase and subsequently amplified in a regular PCR reaction. In single-cell RT-PCR, the cytoplasm of a specific cell is sucked into a micropipette and then processed accordingly, such that the transcriptional state of the cell is revealed.

their cell bodies[12].
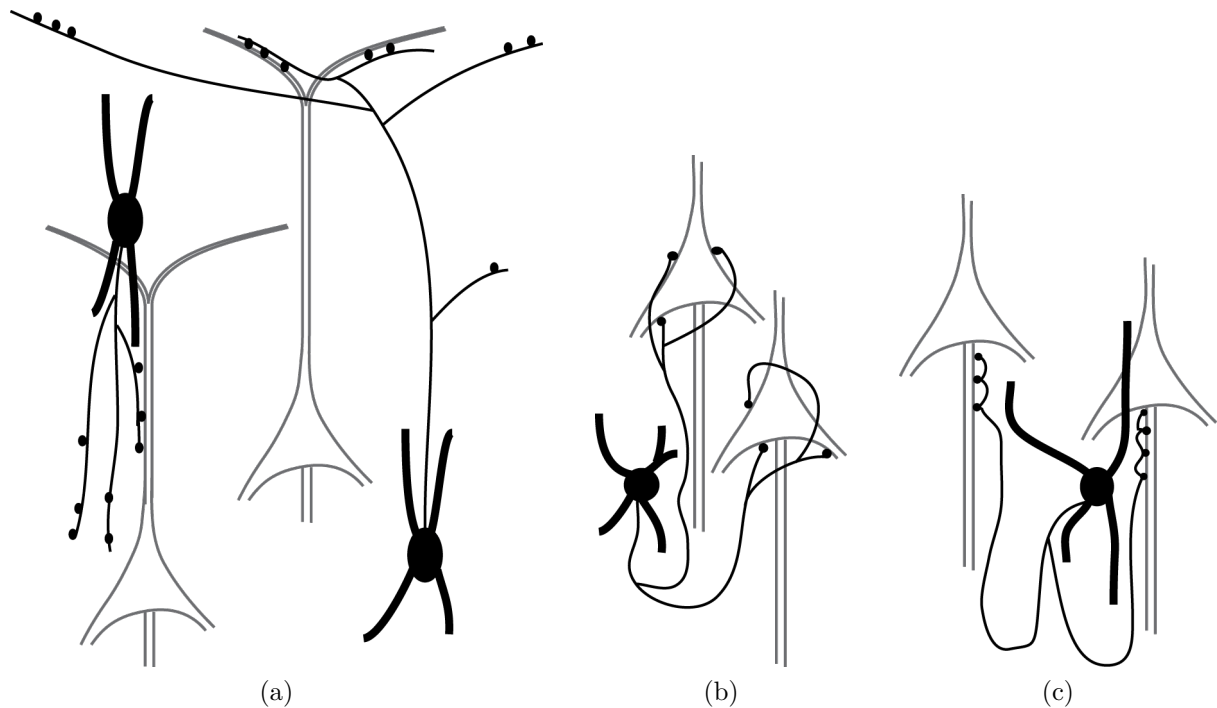
Figure 1.4: Axonal targeting patterns of GABAergic neurons in the neocortex (adapted from [35, 192]). **(a)** Dendrite targeting cells (shown in black). Left: double-bouquet cells have an axon that is oriented away from the pia; right: Martinotti cells have an axon that is oriented towards the pia. **(b)** Soma-targeting cell (shown in black). **(c)** Axon-targeting cell (shown in black).

A characteristic feature of GABAergic neurons is the axonal targeting pattern. They can contact different membrane domains of the postsynaptic neurons. An individual GABAergic interneuron forms synapses mainly on the same domain. Based on this target domain, we can distinguish between the three groups of GABAergic neurons listed below. Probably, these structural differences are also reflected in the impact the respective GABAergic neurons have on their postsynaptic targets.

- The inhibitory postsynaptic potentials (IPSPs) induced by *dendrite-targeting cells* (Figure 1.4a on page 15) arrive only in attenuated form at the axon hillock of postsynaptic targets, where action potential (AP) generation is initiated [155]. It is assumed that their effect is mainly of a fine-tuning kind by contributing to spatiotemporal integration in the dendritic tree, influencing plasticity or affecting the generation of dendritic calcium spikes [192]. Examples include *double bouquet cells*, *bipolar cells*, *bitufted cells* and *Martinotti cells* [157, 35, 192].

- The impact of *soma-targeting cells* (Figure 1.4b on page 15) on the firing probability of the target neuron is thought to be of greater extent than that of dendrite-targeting

---

[12]As exceptions to this rule, GABAergic neurons forming long-range connections through the white matter of the brain have been identified [274, 136] (reviewed in [283]).

cells, due to the proximity to the axon hillock (see [96] for a review of perisomatic inhibition). Examples include different types of *basket cells* (*large*, *small* and *nest basket cells* [157, 299]).

- *Axon-targeting cells* (Figure 1.4c on page 15) are hypothesised to be in a pole position to impact the firing probability by directly targeting the axon initial segment (AIS) of pyramidal cells (reviewed in [144]). They could thus exert a veto right on AP firing. The only type known, the *chandelier cell* [262], was also shown to be able to exert a depolarising effect on its targets due to the higher chloride reversal potential in the AIS than in the soma [273, 307] (reviewed in [308]).

Neurochemistry

Especially substances from the following three groups have so far been found to be differentially expressed in different GABAergic neurons, and have been used as markers for subtype classification (reviewed in [79, 35, 192]).

- Three *calcium-binding proteins (CaBPs)* are differentially expressed among GABAergic neurons: Parvalbumin (PV) [46], Calretinin (CR) and Calbindin (CB) (reviewed in [16]). Although they tend to be present in three separate subpopulations of GABAergic cells, some co-expression is nevertheless observed, especially between PV and CB. No clear one-to-one relationship between the presence of a CaBP and morphologically defined subtypes has been found, although certain tendencies can be recognised [67].

- The four *neuropeptides*[13] Somatostatin (SOM), Vasointestinal Peptide (VIP), Cholecystokinin (CCK) and Neuropeptide Y (NPY) have been used as markers [35]. For individual neuropeptides, co-expression among each other and together with CaBP is not uncommon. Certain neuropeptides have been found to be always expressed in certain morphologically defined subtypes, while others are of exclusive nature [192].

- The combination of *ion channels and receptor proteins* expressed by a neuron can directly influence its electrophysiological properties [155]. It is thus not astonishing that the high diversity in electrophysiological properties (see next paragraph for details) is reflected in the diversity of the underlying membrane proteins [280].

A vast number of studies based on IHC and RT-PCR have tried to relate the presence of such molecular markers to morphology, electrophysiology, and the origin or function of GABAergic neurons. They have revealed an abundance of tendencies and exceptions [281, 79, 192]). The situation is further complicated by the fact that exact marker expression profiles depend on species [312, 138], cortical localisation [67, 175, 113], age [31, 66, 222], neural activity [150] and pathophysiological conditions [236, 88].

---

[13]Neuropeptides can be released as signalling molecules acting in a modulatory fashion on other neurons [155].

Electrophysiology

The diversity of GABAergic neurons is also reflected in their electrophysiological properties, both in their passive electrical membrane properties (e.g. resting membrane potential, membrane time constant, input resistance) and their AP firing characteristics (reviewed in [13, 35, 192]). For a long time, especially the AP firing characteristics have been used to identify and classify inhibitory interneurons [196, 123, 13], mainly by looking at the following two features of responses upon standardised current injection protocols:

- *Firing onset:* Upon a somatic current step that drives a neuron's membrane potential above firing threshold, different response types relative to the step onset can be observed. Cells can respond with an initial *burst* of APs, in which the interspike interval is much shorter than during the later steady-state firing pattern, they can respond with a delay (i.e. *delayed*), or immediately engage in steady-state-like firing without a burst or delay (an onset-type called *continuous*) [13, 123].

- *Steady-state response:* After extended current injection, cells can differ in their firing pattern. Important features include the presence or absence of spike frequency adaption, the maximum steady-state AP frequency, the variance of the interspike interval and the occurrence of bursts. Based on these criteria, different classification schemes have been suggested over time [13, 35, 192], using terms such as *fast-spiking, irregular spiking* or *bursting.*

Certain correlations between spiking properties and molecular or morphological properties have been found. However, in most cases no strict rules could be established [171, 186].

1.2.3 Their role in microcircuits

Although GABA is also known for excitatory action [307, 120, 42], the main effect of GABAergic neurons in the mature neocortex is the provision of inhibition. As part of a local neuronal network they can exert different types of inhibition, depending on the underlying wiring scheme. In turn, these different types of inhibition can serve different functional roles. In combination with the high diversity discussed above, a huge range of computational possibilities results [192]. In the following paragraphs, I will briefly present three different wiring-dependent types of inhibition.

Feed-forward inhibition

In *feed-forward* inhibition, excitatory input from a common input drives both an inhibitory interneuron and a target neuron (Figure 1.5a on page 18). The increased firing rate of the inhibitory neuron in turns dampens the firing of the target cell. The effect of such inhibition is an *increased temporal precision* of the target cell response: excitatory input to the two neurons causes firing of the target cell, which is quickly suppressed by the inhibitory input of the inhibitory cell [271, 40].
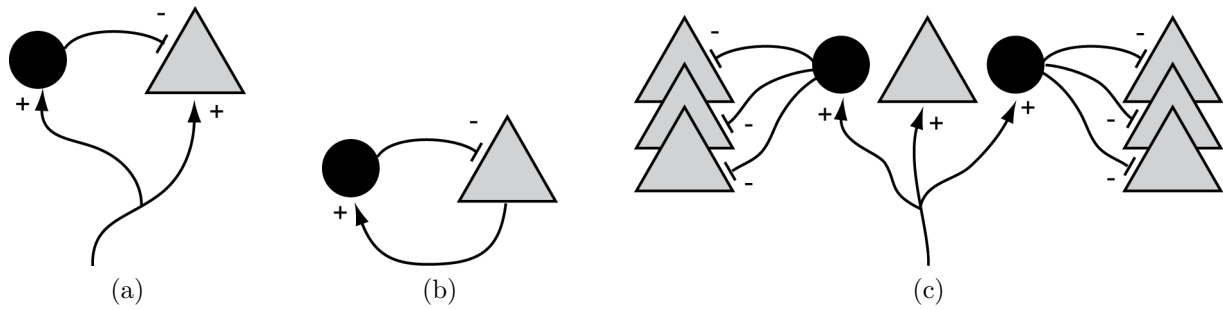
Figure 1.5: Three basic types of neuronal inhibition (adapted from [35, 152]). Principal neurons are shown in grey, inhibitory interneurons in black. **(a)** Feed-forward inhibition. **(b)** Feedback inhibition. **(c)** Lateral inhibition.

Feedback inhibition

In the case of *feedback* inhibition, an excitatory neuron targets an inhibitory interneuron which in turn connects back to the same excitatory cell (Figure 1.5b on page 18). Firing of the excitatory neuron causes firing of the inhibitory interneuron, which in turn may decrease the firing rate of the excitatory neuron, thus representing a regulatory feedback cycle. The effect of such wiring is to *provide stability* by suppressing the build-up of excessive neuronal activity [35, 152].

Lateral inhibition

Lateral inhibition is an extended case of feed-forward inhibition. Excitatory input to a certain subpopulation of principal cells at the same time inhibits principal cells in another subpopulation by means of intermediary inhibitory interneurons (Figure 1.5c on page 18). If both subpopulations of principal cells receive common input, differences in synaptic strengths can result in segregation of the resulting principal cell activity: one subpopulation becomes more active than the other. Lateral inhibition can thus *spatially sharpen* a population response by confining it to a certain subpopulation [35, 152, 9].

These three pure forms of inhibition can be easily grasped. In networks involving multiple interconnected excitatory and inhibitory neurons, each of which equipped with a more or less different set of properties, possible spiking behaviours are fairly more complex [152]. This richness explains why GABAergic cells play crucial roles in many important cortical processes [261].

1.3   Two-photon laser-scanning microscopy

Two-photon laser-scanning microscopy (2PM) was the main technique used in this thesis. Introduced in 1990 by Winfried Denk and colleagues [69], this type of three-dimensional light microscopy has become very popular during the last years for observing neural cell

populations in the brain of living animals due to its high penetration depth in scattering tissue.

In this section, the underlying physical principles are introduced and the architecture and mode of operation of two-photon microscopes are explained.

1.3.1 Fundamentals

Different modes of interaction between light and matter

When a photon hits an atom or molecule, there can be different types of interactions [279]. The most important processes in the context of this thesis are the following:

- *Scattering:* If the energy of the photon is not high enough to bring the atom or molecule to an excited state, the photon is elastically scattered (i.e. its energy and thus its frequency stays the same). The exact laws governing scattering are dependent on the size of the particles (atoms, molecules or larger aggregates) relative to the wavelength of the light with which they interact. Under our conditions, we can generally state that light of shorter wavelength is more strongly scattered than light of longer wavelength.

- *Fluorescence:* When the energy of the photon is high enough to excite the atom or molecule to enter an excited state of higher energy than the lowest excited state, the absorbed energy can be subsequently released by spontaneous emission of a photon to reach states of lower energy.

- *Photoeffect:* The atom absorbs the photon and emits an electron with a kinetic energy corresponding to the difference between the energy of the incoming photon and the ionisation energy of the atom.

- *Stimulated emission:* In this case, the atom is already in an excited state and the incoming photon has exactly the energy corresponding to the energy difference to a lower state. The photon stimulates the emission of a second photon with the same frequency, direction and phase, while the atom relaxes to the lower state.

- *Photochemical reaction:* After absorption, the electronically excited state promotes changes in the chemical bonds of the molecule.

Fluorescence

The process of fluorescence consists of the following sequence of steps. First, the molecule is lifted to an excited electronic state by absorption of an incoming photon. Excited states of different energy levels can be reached with different probability, as is reflected in the *absorption spectrum*[14] characteristic for a given compound (Figure 1.6a on page 20).

---

[14]Also referred to as *excitation spectrum.*

The excited molecule subsequently looses energy by colliding with surrounding molecules and thereby steps down the ladder of vibrational energy states (Figure 1.6b on page 20). After this process of *radiationless decay*, the still excited molecule emits the remaining energy as a photon. The lifetime of the excited state is in the range of 10^{-8}s, such that emission occurs nearly immediately. With this *spontaneous emission*, the molecule can reach different vibrational levels of the ground state, which results in the *emission spectrum* [15, 267]. Because the photons emitted are of a lower energy than the stimulating photon, the emission spectrum is shifted to longer wavelengths compared to the excitation spectrum (Figure 1.6a on page 20).

Lasers

Nowadays, excitation of fluorophores is often—and also in 2PM—achieved using lasers. For this reason, I will introduce some basic principles of laser physics in the following paragraphs.

In the process of stimulated emission, an excited state of an atom or molecule is stimulated to emit a photon of the same frequency as that of an incoming photon. The fact that the probability of emission is dependent on the intensity of stimulating radiation can lead to positive feedback and thus self-stimulating light amplification in a so-called laser[15]. For a single molecule, this probability of stimulated emission is equal to the probability of stimulated absorption. Thus, whether in total more photons are absorbed or emitted depends on the relative population of the two energy states. Under conditions of thermal equilibrium—according to the Boltzman distribution—a lower energy state is more densely populated than a higher energy state (Figure 1.7a on page 21). Under these conditions, absorption prevails over stimulated emission. As a consequence, there are the following two key requirements for a laser [15]:

- An excited state that lives long enough to take part in stimulated emission (a so-called

---

[15]*Laser* is the acronym for *l*igth *a*mplification by *s*timulated *e*mission of *r*adition.

Figure 1.6: Fluorescence. **(a)** Normalised absorption (grey) and emission (black) spectrum of fluorescein acquired in ethanol solution. In the structure of the fluorescein molecule, note the highly conjugated π electron system characteristic for organic compounds fluoresceing in the visible range of the spectrum. **(b)** Steps involved in fluorescence (adapted from [15]). The ground state is shown in black, the excited state in grey.

(a)

(b)
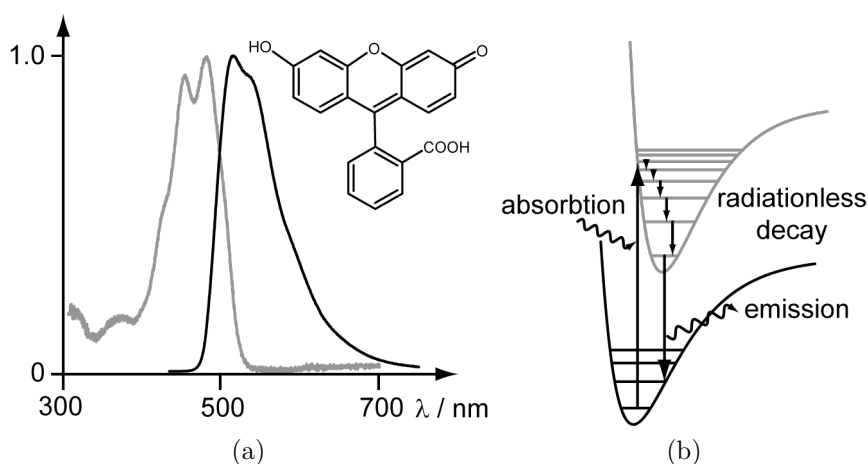
metastable excited state).

- *Population inversion*, i.e. a situation where the higher state is more strongly populated than the lower state (Figure 1.7b on page 21).
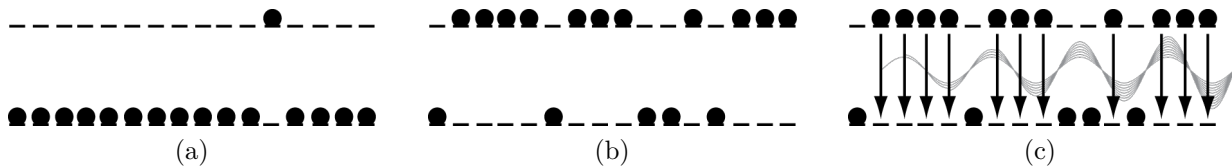
Figure 1.7: Laser action (adapted from [15]). **(a)** Thermal equilibrium: the ground state is more populated than the excited state. **(b)** Population inversion: the excited state is more populated than the ground state. **(c)** Laser action: light amplification by stimulated emission.

The first condition is met by a suitable *laser medium*. In the case of the Ti:sapphire laser, which is typically used in 2PM, the laser medium is a sapphire (Al_2O_3 crystal) containing a small proportion of Ti^{3+} ions [207]. The Ti^{3+} ions in the crystal structure lead to more vibrational energy levels [279], enabling transitions by stimulated emission from the lowest vibrational level of the excited state to many different vibrational levels of the ground state. This is the basis for the tunability of the Ti:sapphire laser: the output wavelength can be chosen by the user from a spectral range between 670 nm and 1070 nm [98].

Population inversion is achieved in a process called *pumping*: an external light source populates the excited state via an intermediate state[16] [15].

The laser medium is confined to a region between two mirrors, the so-called *cavity*. These two mirrors enable a photon to take part in many rounds of light-amplification before it is released from the cavity (one mirror reflects hundred percent, whereas the other transmits a small fraction of the light, resulting in the *laser beam*). Furthermore, the characteristics of the cavity also select the type of photons that are amplified, i.e. their frequency, polarisation and direction:

- *Frequency:* Only wavelengths λ that can build standing waves in a cavity of length L are supported, i.e. those fitting the following condition:

$$n\frac{1}{2}\lambda_n = L, \qquad \text{where } n \in \mathbb{N}. \tag{1.1}$$

  Of these wavelengths, in turn, only a subset (the *resonant modes*) are amplified by the laser medium, resulting in a limited number of laser lines.

---

[16]In *Three-level lasers*, different intermediate states I quickly populate the excited state E via radiationless decay. From E, stimulated emission to the ground state G can take place if spontaneous decay to G is relatively slow. However, due to the initially highly populated ground state G and unpopulated excited state E, population inversion is rather difficult to obtain. It is easier to achieve in *four-level lasers*, where stimulated emission takes part from E to lower excited state E'. Because E' is initially unpopulated, any population of state E immediately creates a situation of population inversion.

- *Polarisation* can be achieved by integrating polarising filters into the cavity. In this case, only photons of suitable polarisation will be amplified.

- The *direction* of photons is given by the spatial extension of the cavity, because photons not travelling strictly parallel to the axis of the cavity are lost during amplification rounds by exiting through the side walls of the cavity. As a result, a laser beam is strongly *collimated.*

A further characteristic of the light of a specific laser line is that it is strongly coherent[17] when exiting the laser, both spatially (across the diameter of the beam) and temporally (i.e. along the beam)[18]. This results from the fact that a photon generated by stimulated emission has the same phase as the stimulating photon.

A laser can generate light as long as population inversion in the laser medium is maintained. In continuous-wave lasers, this is achieved by continuous pumping. Either to prevent overheating or due to the intrinsic properties of the underlying architecture, some lasers can only operate in a pulsed mode. Pulsing can be achieve in several ways. The one relevant in the case of the Ti:Sapphire laser is *mode-locking.* In mode-locking, the phases ϕ_n of N individual resonant modes are locked together (i.e. $\phi_n = const.$ in the below equation), resulting in interference (A_n and ω_n: amplitude and angular frequency, respectively, of a mode; I: intensity):

$$I(t) = \sum_{n=0}^{N} A_n \sin(\omega_n t + \phi_n) \tag{1.2}$$

In spatial terms, sharp peaks of high intensity due to constructive interference are separated by regions of destructive interference. In temporal terms, a short pulse of light is travelling back and forth in the cavity and further amplified with every round-trip; thus, it results in a pulsing frequency of $c/2L$. Mode-locking can either be achieved actively by driving a switch that impairs the cavity at the pulsing frequency, or passively. In the latter case, the laser light itself affects optical properties of the cavity, such that spontaneous fluctuations in intensity can build up to stable pulsing [15]. The Ti:sapphire laser used for 2PM uses passive mode-locking. In this case, the sapphire acts as a lens at high light intensities. As a result, pulses are focused more strongly than a continuous-wave beam due to their higher intensity. This eventually leads to self-stabilisation of pulses at repetition rates of 80-100 MHz [98]. Pulse durations in the range of 10-100 fs can be reached. Thus, we also speak of a *femtosecond laser.* Due to their short duration, pulses have a significant spectral bandwidth $\Delta\lambda$:

$$\Delta\omega\Delta t \approx 2\pi, \qquad \text{therefore} \qquad \Delta\omega \approx \frac{2\pi}{\Delta t} \qquad \text{and} \qquad \Delta\lambda \approx \frac{\lambda^2}{c\Delta t} \tag{1.3}$$

For example, pulses with the duration of $\Delta t = 100$ fs have a spectral bandwidth of $\Delta\lambda = 21$ nm.

---

[17]Coherence indicates that the electromagnetic waves have the same phase.

[18]Temporal coherence is not indefinitely maintained because no laser beam is perfectly monochromatic.

Two-photon absorption (TPA)

The excited state required for fluorescence emission is usually obtained by the absorption of a single photon (Section 1.3.1). Under conditions of extremely high light intensity (photon density), a molecule or atom can also reach an excited state by simultaneous absorption of two photons in a process called *two-photon absorption (TPA)*[19] [111, 154]. This statistical process is proportional to the square of light intensity I. This is in contrast to one-photon absorption, which is proportional to light intensity (x: path along which the absorbing substance is present; c: concentration of the absorbing substance; σ: absorption cross-section; β: TPA cross-section):

$$\frac{\mathrm{d}}{\mathrm{d}x}I = -\sigma cI \qquad \text{for one-photon absorption, and} \tag{1.4}$$

$$\frac{\mathrm{d}}{\mathrm{d}x}I = -\beta cI^2 \qquad \text{for TPA} \tag{1.5}$$

TPA spectra are usually broader than the single-photon absorption spectra of the same compound; however, they are not just simply scaled versions thereof [21, 310].

1.3.2 A generic two-photon microscope setup

Principle

Two-photon microscopy (2PM) is a type of laser-scanning microscopy (LSM). In LSM, a focused laser beam scans the specimen and the fluorescence excited at the scanning focal point is detected and sequentially assembled to an image (Figure 1.8a on page 24). It is important to note that the fluorescence detected can be assigned to the focal point alone rather than to the whole laser light cone in the sample. This feature essentially allows one to probe the fluorescence of the specimen in *three dimensions* by moving the focal point around accordingly. The two main types of laser-scanning microscopy differ in the way this *focal constraint* is achieved [131]:

- In *confocal laser scanning microscopy* [201, 6], fluorescence excitation is based on single-photon absorption and thus occurs within the whole light cone of the focused laser beam [225] (Figure 1.8b on page 24). Focal assignment is achieved on the detection side; light from outside the focal plane cannot pass through a so-called *pinhole* and does not reach the detector.

- In *two-photon laser laser scanning microscopy*, focal assignment is achieved on the side of excitation. Due to the fact that TPA depends on very high light intensities, it is essentially restricted to the laser focal point (Figure 1.8b on page 24) [70]. At any

---

[19]Under conditions of bright sunlight, a rhodamine B molecule, which possesses a high absorption and TPA cross-section, undergoes a single-photon absorption on average about once per second, and a TPA about every 10^7 years [70].

point of time, all light reaching the detector can be attributed to the focal point—provided that any reflected or scattered laser light is excluded (Figure 1.8c on page 24).
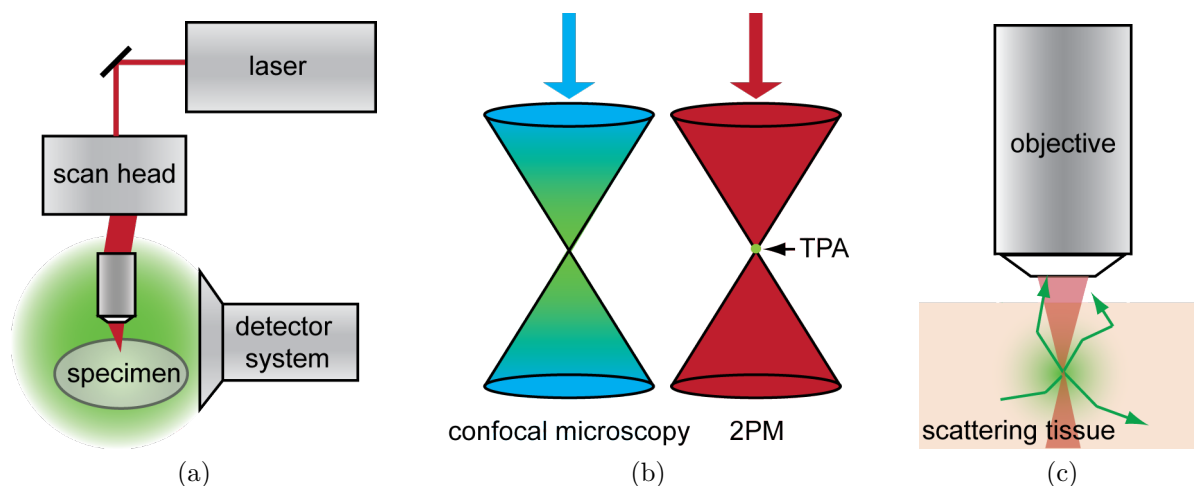
Figure 1.8: Two-photon laser-scanning microscopy. **(a)** General architecture of a laser-scanning microscope: the focal point of a laser scans a sample, thereby exciting fluorescence. Part of the emitted light is detected and assigned to the current scan position. **(b)** Different types of excitation in laser-scanning microscopy (adapted from [276]). Left: single-photon excitation is linearly proportional to light intensity, such that fluorescence does occur in the whole light cone (although more strongly towards the focal point). Right: two-photon absorption (TPA) depends on the square of light intensity. Fluorescence is thus essentially limited to the region around the focal point. **(c)** In scattering tissue, photons emitted in directions outside the aperture angle can still be detected if they are scattered accordingly (adapted from [276]).

Features

While confocal laser-scanning microscopy uses laser light in the ultraviolett (UV) and visible range of the spectrum, 2PM employs a femtosecond laser emitting in the near infrared (IR) range. The following three advantages result for 2PM and make it particularly suitable for long-term imaging in highly scattering tissue, such as the neocortex of living animals [131]:

- *Reduced bleaching and phototoxicity:* Most tissues do not contain single-photon-absorbing molecules for the excitation wavelengths used in 2PM [131], while two-photon absorption is limited to the perifocal volume. As a consequence, light above and below the focal plane induces less photochemical reactions than is the case for confocal laser-scanning microscopy.

- *Intrinsic optical sectioning:* Due to excitation-based focal assignment of the emitted light, all photons in the relevant emission bandwidth can be collected for detection

while still achieving three-dimensional resolution[20]. A pinhole as in confocal laser-scanning microscopy is not required, resulting in comparably higher light collection efficiency.

- *Better compatibility with highly scattering tissue:* The IR beam of the femtosecond laser is less susceptible to scattering than the shorter-wavelength laser light used in confocal laser-scanning microscopes. As a result, deeper imaging depths (up to 1 mm) can be achieved [276].

Instrumentation

Here, I briefly introduce the main components of a two-photon microscope (Figure 1.8a on page 24).

Excitation laser   In order to allow TPA of fluorophores emitting in the visible range of the spectrum, 2PM relies on pulsed IR laser light. Ti:Sapphire lasers are typically used as they are freely tunable in a range between 700 and 1000 nm and provide pulses of approximately 100 fs at repetition rates of around 100 MHz [70].

It is important to have a very stable beam intensity due to the non-linear dependence of fluorescence emission from excitation intensity.

Also, *group velocity dispersion*[21], caused by the significant amount of glass in the beam path of the microscope (due to the various lenses), should be minimised in order to keep short pulses at the specimen for optimal excitation. For this purpose, so-called *pre-chirping* arrangements can be introduced into the beam path. They consist of one or several prisms or gratings splitting up the pulse spectrum into the constituent wavelengths, and a delay path on which shorter wavelength components receive a negative pre-chirp that is precomponensating the dispersion in the glass, thus restoring short pulses at the specimen [131]. Some modern commercial laser systems already have inbuilt dispersion compensation units automatically adjusting their arrangement to the selected output wavelength of the laser[22].

In order to adjust the laser intensity to the imaging depth and absorption efficiency of the fluorophores used, a device with controllable transmission efficiency is introduced into the beam path. One possibility is to have a neutral density filter wheel with gradually variable transmission. Another is a polarisation filter that allows a variable fraction of the polarised laser light to transmit. In both cases, the rotation angle and thus transmission efficiency can either be adjusted manually or controlled in a motorised fashion. A faster

---

[20]Resolution in 2PM is *non-isotropic*, with lower resolution in depth (z direction) than in x/y direction. A small sphere is typically imaged as a vertically oriented, rugby-ball-shaped structure (representing the so-called *point-spread function* of the microscope.

[21]Laser pulses are not perfectly monochromatic but posses a wavelength spectrum that is directly related to their pulse duration (equation 1.3 on page 22). When travelling through matter, the speed of light is wavelength-dependent: components of longer wavelength travel faster than those with shorter wavelength, resulting in an effective pulse broadening.

[22]MaiTai DeepSee: `http://www.newport.com/InsightDeepSee`
Chameleon Vision: `http://www.coherent.com/products/?1841/Chameleon-Vision-Family`

method, that even allows the modification of light intensity on a pixel-by-pixel basis, is to use a *Pockels cell*. This electro-optical device contains a crystal of ammonium dihydrogenphosphate ($NH_4H_2PO_4$) that modifies the polarisation direction of the laser light in relation to the applied voltage, followed by a polarisation filter that acts as analyser and lets only a fraction of the light to pass through [15].

Laser scanners   Different types of physical devices can be used to deflect the laser beam at high speeds in a more or less controllable fashion and thus achieve scanning of the laser focal point in a horizontal plane through the specimen. Below is an overview of the most prominent of these devices (Figure 1.9 on page 27):

- *Galvanometric scan mirrors* reflect the laser beam (Figure 1.9c on page 27). The deflection angle can be electrically controlled [106, 105] (Figure 1.9a on page 27). An advantage is their easy controllability. The deflection angle is proportional to an analogue input voltage applied to their controller electronics (or for other types, can be digitally controlled). Their disadvantage is their mechanical inertia. At higher scan speeds or accelerations, the deflection angle starts to deviate from the control value.

- *Acousto-optic deflectors (AOD)* diffract the laser beam in a controllable fashion (Figure 1.9b on page 27): the angle of diffraction is dependent on the frequency (in the MHz range) of acoustic waves travelling through them [245]. Because no mechanical parts are involved, much faster beam deflection changes are possible than with galvanometric mirrors: the focal point can essentially hop from one position to another. Control and adjustment of AODs is more complicated than that of galvanometric scanners, however. In addition, because the beam has to transmit through significant amounts of glass, significant intensity losses and pulse broadening have to be compensated for [116].

- *Resonant scanners* contain a mirror that resonates harmonically around an axis at a fixed frequency (several kHz) (Figure 1.9c on page 27). Higher scan speeds than with galvanometric scan mirrors cans be achieved, which enables image acquisition at video rates [247, 215]. However, since the only modifiable parameter is the oscillation amplitude, control over the scan pattern is limited.

- *Piezo-electric elements* can be used to move the ends of an optical fibre at high speeds (in resonant or non-resonant modes), thereby changing the exit angle of laser light travelling through the fibre [86, 249] (Figure 1.9d on page 27). This approach has been used for miniature two-photon microscopes implanted on the head of freely moving rodents [250].

Detector system   Stimulated fluorescence emission light has to be transformed into a stream of electrical signals that can eventually be assembled into an image. Thereby, it is
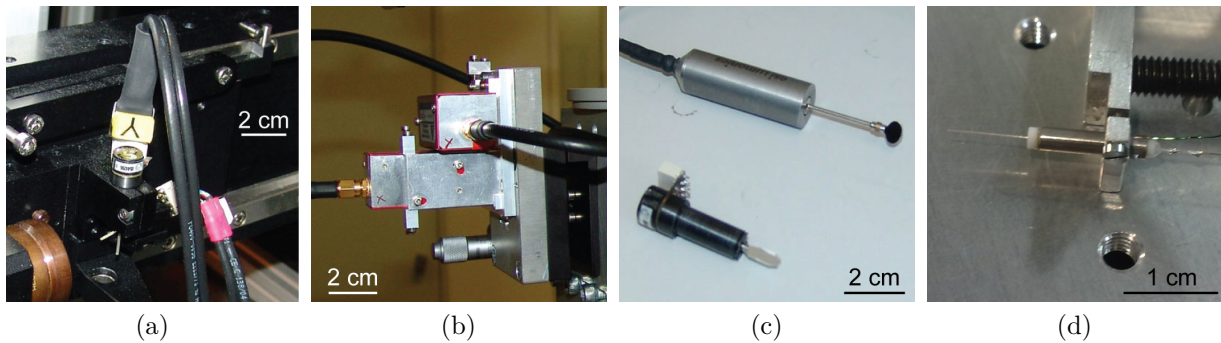
Figure 1.9: Different scanner types for custom-built two-photon micrsoscopes: different types of laser-scanners. **(a)** Galvanometric scan mirrors. **(b)** AODs. **(c)** Resonance scanner (upper half) compared to galvonometric scanner (lower half). **(d)** Piezo-electric fiber scanner.

important that back-reflected laser light does not reach the photon detectors responsible for transforming incoming photons into electrical impulses. This is usually achieved by guiding the fluorescence emission light into the detector system by a dichroic mirror that reflects mainly in the visible range, but much less in the IR range. Before reaching the photon detectors, the light further passes through filters that block any remaining IR light.

In many cases, different fluorescent dyes are present in the specimen. Due to the broad two-photon excitation spectrum of many dyes, often several fluorophores can be excited at the same time. With tunable femtosecond lasers, it may even be possible to compensate for differences in the individual excitation spectra. As much as possible, the detector system should separate the contributions of individual flurophores to the emission light. For this purpose, the incoming fluorescence emission light has to be split up into different spectral components that are guided to separate photon detectors (Figure A.4 on page 176). This is usually achieved by additional dichroic mirrors of suitable cut-off wavelengths and appropriate band-pass filters mounted in front of the individual detectors.

When imaging deep in biological tissue, as is the case for *in vivo* 2PM of the neocortex, fluorescent light arriving at the brain surface mainly contains diffuse light consisting of scattered photons. After passing through the objective, scattered photons do *not*—in contrast to ballistic photons—travel in parallel, which imposes some constraints on an optimal architecture of the detector system:

- *Short paths* should be maintained in order to minimise the loss of photons on the way; especially the most sensitive channel should be arranged as close as possible to the light source.

- *Large apertures* of lenses, filters, mirrors and detectors are important in order to let most of the photons pass through. For this reason, photo-multiplier tubes (PMTs)[23]

---

[23]PMTs are based on the photoeffect (Section 1.3.1): photons hitting a photocathode provoke the emission of electrons, which are subsequently amplified in a cascade of high-voltage electrodes (so-called dynodes), ultimately resulting in a detectable electric current at the anode.

are usually employed as photon detectors due to their comparably large opening windows [131].

Control software   Laser-scanning microscopy relies on specialised software that is able to control the scanners guiding the laser focal point in suitable trajectories through the specimen and to assign the acquired fluorescence signals to the corresponding pixels of an image. Both processes should optimally be performed in real-time so that the user can modify parameters of the scan trajectory while immediately receiving feed-back via the image that is being assembled. Design and application of such software is one of the two main topics of this thesis and will be extensively discussed in Chapter 2, such that I do not go into more detail here.

1.4   *In vivo* two-photon calcium imaging

Different modalities of functional imaging allow one to probe developmental, physiological and pathophysiological processes in nervous tissue at multiple spatial and temporal scales [133, 242]. In particular, two-photon calcium imaging enables access to such processes in the brain of living animals at a spatial scale ranging between cell populations and subcellular structures while providing subsecond temporal resolution.

Here, I introduce the basic principles underlying calcium indicators and present different existing possibilities to place such indicators into the tissue of interest. I will end this section with a brief overview of approaches to analyse data acquired in calcium imaging experiments.

1.4.1   Fundamentals

Action potentials and calcium

Cells in general, and neurons in particular, maintain concentration gradients for certain ions across their cell membranes by means of ion-specific pumps. In combination, these ion gradients build up an electrical membrane potential. In electrically excitable cells such as neurons, gateable transmembrane channels can temporarily change the permeability for certain ions types, which in turn affects the ion concentrations and thus membrane voltage. In neurons, membrane depolarisations—as associated with action potentials (APs)—are accompanied by an influx of calcium ions along their concentration gradient through voltage-gated calcium channels, leading to an increase of intracellular calcium concentration [155, 4]. Part of the inflowing calcium ions binds to intracellular buffers (mainly calcium-binding proteins (CaBPs)) so only a fraction is available as free calcium ions [132]. The increase in intracellular calcium concentration is only temporary because active mechanisms immediately engage in removing calcium ions from the cytoplasm—either to intracellular calcium stores or to the extracellular space [155, 4].

Calcium indicators

As early as the 1960s, success in optical probing of neural activity was already achieved [182, 257]. First measurements focusing on changes in intrinsic optical properties (birefringence, polarisation and scattering) of axons [55, 56, 294] were soon followed by the development of techniques involving the application of exogenous fluorescent probes of membrane voltage changes [294, 241, 43]. Such probes, now known as *voltage-sensitive dyes*, are still in use today. However, the relative changes of the optical read-out that need to be measured with all of these approaches are very small, and extensive signal averaging is usually required to isolate them from noise.

As outlined above, APs are accompanied by changes in intracellular calcium concentration[24]. Chemical compounds changing their optical properties upon the fluctuation in calcium concentration have been explored as intracellular indicators since the late sixties [14, 17, 29]. This culminated in the development of the first fluorescent calcium indicators [239] and a non-disruptive loading technique [288] by Roger Tsien around 1980.

A calcium indicator, Ind, binds to free calcium ions, resulting in the complex Ca−Ind. For a good indicator, this reaction, as well as its reverse reaction, are much faster than the inflow of calcium such that equilibrium conditions apply to the binding process:

$$Ca^{2+} + Ind \rightleftharpoons Ind-Ca^{2+} \tag{1.6}$$

The *affinity* of the indicator is quantitatively expressed by the *dissociation constant* K_D:

$$K_D = \frac{c(Ca^{2+})c(Ind)}{c(Ind-Ca^{2+})} \tag{1.7}$$

where

$$c_{total}(Ca^{2+}) = c(Ca^{2+}) + c(Ind-Ca^{2+}) \tag{1.8}$$
$$c_{total}(Ind) = c(Ind) + c(Ind-Ca^{2+}) \tag{1.9}$$

At a specific emission wavelength λ, the fluorescence intensity F is the sum of the contributions by Ind and Ind−Ca^{2+}:

$$F_\lambda = \beta_\lambda c(Ind) + \gamma_\lambda c(Ind-Ca^{2+}) \tag{1.10}$$

For a fluorescent calcium indicator, $\beta_\lambda \neq \gamma_\lambda$ due to different absorption and/or emission characteristics of Ind and Ind−Ca^{2+}. As a result, the fluorescence intensity depends on the total calcium concentration in a non-trivial way:

$$F_\lambda = f(c_{total}(Ca^{2+}), c_{total}(Ind), \lambda) \tag{1.11}$$

---

[24]More precisely, the concentration of Ca^{2+} ions, to which I will simply refer to as *calcium concentration* from now on.

Calcium imaging

For a neuron filled with an Indicator Ind at a concentration $c_{\text{total}}(\text{Ind})$, the baseline fluorescence F_0 is dependent on the intracellular calcium concentration $c_{\text{total}}(\text{Ca}^{2+})$ under resting conditions (5–10 nM). A calcium influx during an AP leads to an increase of the total intracellular calcium concentration by $\Delta c(\text{Ca}^{2+})$ (several µM can be reached), and the fluorescence intensity changes accordingly. Observed intensity changes are usually reported relative to the baseline fluorescence as $\Delta F/F$:

$$\Delta F/F = \frac{F - F_0}{F_0} = f(c_{\text{total}}(\text{Ca}^{2+}) + \Delta c(\text{Ca}^{2+}), c_{\text{total}}(\text{Ind})) - f(c_{\text{total}}(\text{Ca}^{2+}), c_{\text{total}}(\text{Ind}))$$
(1.12)

These fluorescence changes can be observed using epifluorescence microscopes with a camera, with confocal microscopes, or—using appropriate indicators—also with two-photon microscopes. The latter enable calcium imaging of cellular compartments of various sizes deep in scattering tissue. Studies in both brain slices and *in vivo* have been published during the last decade with a focus on cell bodies [163, 248, 139], dendrites [105, 270, 134], spines [48, 110] and axons [19].

1.4.2   Classical calcium indicators

Modern synthetic fluorescent calcium indicators are based on the aforementioned seminal work by Tsien. Consisting of organic dye molecules with low molecular weight, the general principle inherent to their molecular structure is a fluorescent part covalently bound to a calcium-binding part (Figure 1.10a on page 31).

When choosing an indicator for two-photon calcium imaging, important criteria are the following:

- The *calcium affinity* as expressed by the dissociation constant K_{D}: high-affinity indicators (i.e. with low K_{D}) are required for detection of small changes in the calcium concentrations such as those associated with single APs. However, higher affinity also implies that the indicator is more easily saturated during bursts of action-potentials [104].

- The *TPA cross-section:* the indicator has to be a good two-photon absorber at those excitation wavelengths compatible with other possible restrictions. Not all wavelengths available from the laser source and well-suited for excitation might be favourable. At shorter wavelengths, photodamage is usually stronger. In case of multi-label imaging, cell-specifically localised fluorophores may or may not want to be excited at the same time [175, 260, 219, 304].

- The *emission spectrum:* it should match the wavelength range in which the PMT is most sensitive. In addition, in the case of multi-label imaging, overlaps of the emission spectrum of the indicator with that of other labels in the specimen should be avoided as far as possible in order to maintain a good signal-to-noise ratio (SNR) [175,
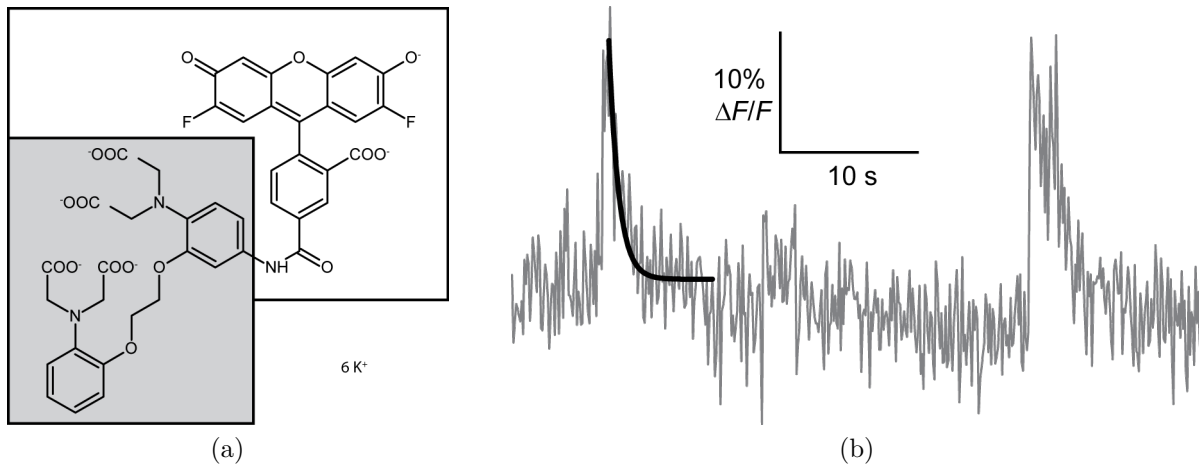
Figure 1.10: Classical calcium indicators. **(a)** Molecular structure of the classical calcium indicator used for the experiments presented in Chapter 3 of this thesis: Oregon Green 488 BAPTA-1 (OGB-1) (here displayed as the hexapotassium salt). The calcium-binding part (1,2-bis(*o*-aminophenoxy)ethane-N,N,N',N'-tetraacetic acid (BAPTA)) of the molecule is marked with a grey box, the fluorescent part (Oregon Green 488) with a white box. **(b)** Spontaneous calcium transients recorded *in vivo* (sampling rate: 10 Hz). For the first transient, an exponential function is fitted for the decay phase ($\tau = 0.71$ s).

304] (unless selective excitation is possible in case of sufficiently distinct absorption spectra, see previous point).

Loading techniques

Various techniques to fill neurons with synthetic fluorescent calcium indicators have been developed during the last thirty years (reviewed in [104]).

The approach that was initially used for the first calcium imaging experiments in the 1960s[25] was simply to gain access to a cell's cytoplasm via a micropipette and fill it with an indicator solution by a diffusion-based process. Especially for experiments that involve electrophysiological recordings via whole-cell patch clamp recordings, this is still the most convenient method today (Figure 1.11a on page 32). Another method based on micro-electrodes is *targeted single-cell electroporation*. Similar to patch clamp recordings, the electrode can be guided to distinct cells using two-photon microscopy [168]. However, a gigaseal is not necessarily established. Rather, an electrical pulse is applied to the electrode once it has contact with the target cell (Figure 1.11a on page 32). This pulse temporarily breaks down the cell membrane integrity and transports the electrically charged indicator molecules into the cell by means of electrophoresis [214, 165]. With a modified protocol, electroporation can be used to load a small number of cells in a small volume surrounding the pipette tip (*local electroporation*; Figure 1.11b on page 32) [213].

Calcium indicator molecules conjugated to dextrans can be locally injected into the

---

[25]These experiments involved the protein *Aequorin*, which changes its luminescence properties upon calcium binding.
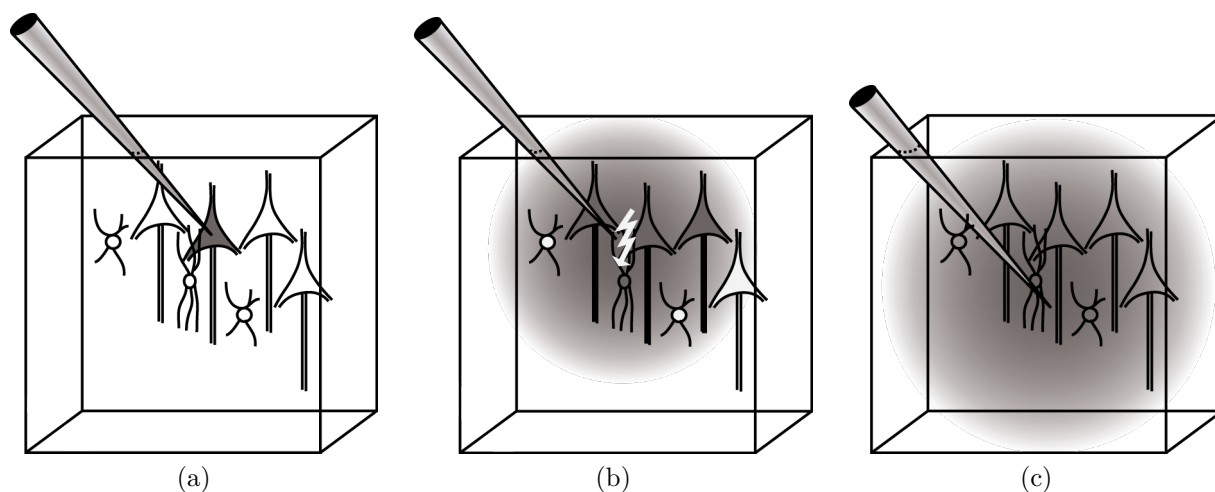
Figure 1.11: Loading techniques for classical calcium indicators (adapted from [104]). **(a)** Single cells can be filled under guidance of the two-photon microscope either by whole-cell patch clamping or by single-cell electroporation. **(b)** Cells in the vicinity of a pipette filled with indicator solution can be loaded by local electroporation. **(c)** Multi-cell bolus loading (MCBL) fills cells non-selectively in a larger volume.

brain and are spontaneously endocytosed by surrounding neurons. By means of retrograde axonal transport, the indicator-dextran conjugate can reach other areas in the brain. This is an excellent method to label cells projecting to a specific target area.

The method of choice to label larger volumes in brain slices or *in vivo* is called multi-cell bolus loading (MCBL), which is based on a method originally developed for bath application of calcium indicators to dissociated cells *in vitro* [288]. This latter method, which is still used for cultured cells today, employs a modified version of the indicator molecules, in which originally polar carboxy groups are rendered apolar by esterification (typicallly as methyl esters). Due to their apolar nature, the esterified indicator molecules can diffuse into cells[26], where non-specific intracellular esterases cleave the ester bonds of the molecules, resulting in free carboxy groups that are partly ionised under physiological conditions. The indicator molecules thus become trapped inside the cells due to their now polar or even ionic character. Also, the de-esterification restores the calcium-binding character of the molecules, which is based on a chelate effect of the free carboxy groups. In MCBL, a small volume of the acethoxymethyl ester (AM) indicator solution is injected locally to the site of interest (Figure 1.11c on page 32), where the apolar indicator molecules are taken up by cells within the "bolus" of indicator solution (typically around 300 μm in diameter) and subsequently entrapped after intracellular hydrolysis [102, 266].

---

[26]Usually, this process is facilitated by adding a detergent such as Pluronic F-100 to the indicator solution. Detergents increase the permeability of biological membranes.

1.4.3 Genetically-encoded calcium indicators

Structure and mechanism

Genetically encoded calcium indicators are engineered proteins that are artificially expressed in target cells after introducing the encoding DNA sequences (reviewed in [188, 166, 232]). Similar to classical indicator molecules, GECI molecules consist of fluorescent and calcium-binding parts. Upon binding of calcium ions to the calcium-binding domain, a conformational change is induced in the protein molecule, which changes the fluorescence properties of the fluorescent domain(s) (see [188] for a detailed review of different mechanisms).

For example, in the GECI Yellow Cameleon 3.60 (YC3.60), which was used for the experiments presented in Chapter 3 of this thesis, a cyan fluorescent protein (CFP)- and a yellow fluorescent protein (YFP)-derived domain are fused together via a domain derived from the CaBP Calmodulin and the Calmodulin-binding site M13 [212]. The two fluorescent domains can take part in fluorescence resonance energy tranfer (FRET), with the CFP domain acting as FRET donor and the GFP as acceptor. FRET efficiency is strongly dependent on the distance between the donor and the acceptor[27]. In YC3.60, this distance is strongly affected by a conformational change provoked by calcium binding to the calmodulin domain; the latter exposes a hydrophobic site that binds to the neighbouring M13 site, thereby moving the two fluorescent domains relative to each other.

FRET-based GECIs, such as the described YC3.60, are excited at wavelengths well absorbed by the domain acting as FRET donor, while fluorescence is monitored independently at suitable emission spectral ranges for both the donor and the acceptor domain. Upon an increase in calcium concentration, the fluorescence intensity of the donor decreases (due to increased FRET), while the fluorescence intensity for the acceptor increases. The actual read-out is the ratio of the two acquisition channels. Such *ratiometric* indicators have the advantage of being less susceptible to motion artefacts.

Expression approaches

In order to induce the production of a GECI in neuronal cells, the latter have to be provided with the DNA encoding the constituent polypeptide chain. Furthermore, the DNA section has to contain at least a promoter region in order to stimulate transcription [72]. Using appropriate promoter sequences, a limited cell type specificity can be achieved (e.g. the human synapsin promotoer stimulates expression only in neurons, but not in glial cells [164]). Further cell type specificity at the transcriptional level would require additional upstream or downstream regulatory sequences [289, 198], or even site-specific integration into the genome [275]. However, the latter strategies are not equally compatible with all of the techniques used to transfer DNA into target cells. These techniques are briefly presented in the following list:

---

[27]The FRET efficiency is given by the Förster equation: $E_{\text{FRET}}(r) = \frac{R_{\text{Förster}}^6}{R_{\text{Förster}}^6 + r^6}$, where $R_{\text{Förster}}$ corresponds to the distance where $E_{\text{FRET}} = 1/2$ [99].

- *Virus-mediated expression* is a method that has been frequently employed in various studies in recent years [184, 130, 7, 189]. Briefly, the DNA is packaged into virus particles that are able to infect the cells of interest. A small amount of liquid containing virus particles is then stereotactically injected at the site of interest. In principle, two-photon targeted injection would be possible and it would allow more precise targeting. Viral tropism can provide certain cell type specificity [164], which can be enhanced or modified by pseudotyping [57].

- *Single-cell electroporation* allows the transfer of DNA into specific cells under two-photon guidance [153].

- *Transgenic animal lines* stably expressing a GECI have been produced in the past [71, 212]. Their drawback is the high initial effort required to produce them; their advantage that individual animals are easily available once a line has been established. Therefore, and given the currently fast evolution of GECIs, viral expression strategies allow researchers to experiment more flexibly with the newest GECI constructs available.

- *In utero electroporation* is frequently used to express transgenes in the developing animal. New strategies based on *in utero* electroporation allow the integration of the transgene into the host cells' genome [315] and may be employed to express GECIs in adult animals in the future.

1.4.4   Data analysis

The analysis of *in vivo* two-photon calcium imaging data presents two main problems. First, the raw time series of the fluorescence intensity have to be extracted from the individual structures of interest. Second, from the extracted fluorescence intensity time series, the occurrences of underlying spiking events (optimally, single AP events) need to be inferred.

Time series extraction for individual units

When one is interested in whole populations of cells across many individual measurements, this process can be rather tedious when carried out manually. Reproducibility in this case is also limited, which may further increase the variability in data quality across different region-of-interests (ROIs). In particular, there is a trade-off between SNR and purity of the signal with respect to so-called *neuropil contamination*. In order to achieve a maximum SNR, as many pixels as possible should be averaged for a particular ROI (e.g. a cell soma). However, due to the three-dimensional structure of the point-spread function (PSF) of the two-photon microscope, each pixel contains contributions from surrounding pixels as well as volumes above and below the actual imaging plane[28]. The closer a particular pixel is to the

---

[28]Due to the non-isotropic resolution of two-photon microscopes that is reflected in the elongated PSF in z direction, these vertical contributions from above and below the imaging plane can be even stronger than

cell boundaries, the higher the contribution from the surrounding neuropil is. Especially for cells in which the imaging plane deviates from the equatorial plane, even a pixel in the middle of the soma can be significantly "contaminated" by contributions from the neuropil above or below the cell. This trade-off may be more reproducible if automated segmentation algorithms are used to define the ROIs. For experiments involving many ROIs, such algorithms also provide a significant gain in productivity. These algorithms have to deal with relatively low contrasts that might also be varying over a field of view[29]. Approaches based on independent component analysis (ICA) have been successfully demonstrated, making use of correlations in the activity-induced changes in the fluorescence among different pixels, to find associated regions that correspond to individual cells [211, 86]. Other methods are based on tracking contrast-gradients associated with cell borders [178] after pre-processing involving non-homogeneous contrast enhancement. This latter approach has also been successfully applied to segmentation of 3D reference stacks that are part of 3D two-photon calcium imaging (unpublished results achieved at our laboratory) [106, 179].

Inference of neural activity

Different algorithms to infer the underlying AP events from calcium imaging data have been published [291, 292]. For example, a recent paper presented a "peeling" algorithm, in which the time series is matched against an elementary transient as expected for a single AP. If found, the elementary transient is subtracted from the time series. This procedure is repeated until no more elementary transients are found. Especially in conjunction with high-speed recordings at sampling rates of several hundred Hertz, this approach proved to be very efficient and it was able to identify single APs in bursts of up to 30 Hz [116].

1.5 Recent technology developments

This thesis is primarily concerned with the application of 2PM for calcium imaging in the brain of living animals. In this field, laboratories developing new techniques have mainly focused on three aspects during the last few years (reviewed in [115]): (i) sampling more cells at once, (ii) sampling at higher speeds, and (iii) applying techniques to awake or even freely behaving animals. In this section, I will briefly discuss recent achievements.

---

the contribution from surrounding pixels in the imaging plane. The relative contributions depend on the physical resolution in the x and y direction (expressed in μm per pixel) as well as the three-dimensional extents of the PSF. The latter is dependent on characteristics of the objective (in particular, the numerical aperture (NA)) and their relation to the laser beam size (see [104] for a detailed description).

[29]Varying contrast over a field of view might have different causes, including non-homogeneous dye distribution (especially at the border of a bolus injection) and non-homogeneous illumination due to a suboptimally adjusted microscope or light-absorbing surface blood vessels. It has recently been demonstrated that the problem of light-absorbing blood vessels can be minimised by replacing the animal's blood by a non-absorbing perfluorocarbon emulsion suitable for oxygen transport [127].

1.5.1   Extending the population size

Many of the studies published during the last decade that employed *in vivo* two-photon calcium imaging recorded only around a dozen cells at once [163, 184, 248, 266]. This restriction is rooted in the two following points:

- the two-dimensional imaging plane (usually not all visible cells are optimally hit or they are not in focus);

- the relationship between noise and time sampled from a given neuron;

Various approaches have been explored in recent years to overcome these limitations and enable recordings from a higher number of cells. A number of pioneering achievements were dedicated to extending the two-dimensional sampling area to three-dimensional volumes. They all relied on techniques that allow the fast movement of the focal point along the z axis. Some of them are based on piezo-electrical focusing devices moving the objective quickly up and down [106, 105, 7]. Others employ electrically [117] or hydrostatically [286] controllable lenses in conjunction with traditional microscope objectives, still others use a mirror that can vary the length of the optical path for excitation light before entering the objective [27] or a wily arrangement of AODs that not only allows x/y scanning, but additionally fast z focusing [81]. Other approaches are based on sampling the specimen with more than one laser beam focus simultaneously. Examples include novel laser designs generating multiple beams [256], multiplexing with a single beam [49], or the use of a rotating disk with micro-lenses that splits up a beam into an array of beams [22].

1.5.2   Increasing the sampling rate

According to contemporary assumptions in neuroscience, APs in neurons are the key events in neural computation. Signal processing is thought to be fundamentally related to temporal sequences of APs in individual neurons[30] [125, 33]. Given this paradigm and the importance of precise timing of APs [1, 128], it is highly desirable to obtain as high sampling rates as possible for *in vivo* two-photon calcium imaging. In traditional frame-scan-based approaches, a lot of time is wasted on neuropil or out-of-focus cells during sampling. Although approaches have been explored that drive galvanometric mirrors at their maximum acceleration and velocity to minimise the time spent on non-important regions [180], there are limits due to mechanical inertia that cannot be overcome. Resonant scanners move at faster speeds and allow video-rate frame-scan imaging [215, 177, 247]. However, limited control over their motion does not allow to skip non-important regions. Recent achievements with AODs can overcome these limitations and allow sampling rates in the range of several hundred Hertz even for dozens of cells using random-access scan patterns in two or three dimensions [247, 81, 148].

---

[30]On an abstract level, we can think of a state space in which the state of each neuron as firing or non-firing is represented as an own dimension. Each possible brain state is represented as a specific point in this multidimensional state. Brain activity can then be thought of as a trajectory through this state space [90].

1.5.3 Imaging awake and behaving animals

In vivo two-photon calcium imaging allows the investigation of populations of neurons in their natural environment, i.e. the intact brain of a living animal [104]. However, until recently, most studies have been performed on anaesthetised animals in order to minimise animal suffering and ensure a stable preparation with minimal motion artefacts [163, 248, 317, 162]. During the last two years, a trend from acute preparations based on classical calcium indicators to long-living preparations based on the expression of GECIs could be observed. Such preparations involve the implantation of permanent windows into the skull, through which calcium imaging in repeated sessions is possible [7]. Significantly more data can be acquired from a single animal, which not only strongly reduces animal consumption, but also allows animals to be trained in an economic fashion such that imaging animals that are awake became possible. Most current studies involving awake animals are based on head-restrained preparations, for example using treadmills or floating balls. Such systems can even include virtual visual environments presented to the animal as part of a closed-loop system (i.e. motion of the animal on a floating ball is tracked and allows the animal to navigate in the virtual environment) [76, 75]. Studies involving freely moving animals are still in a pilot phase, while miniaturised, head-mountable two-photon microscopes are being improved [250].

1.6 Motivation and goals of this thesis

1.6.1 A software framework for two-photon microscopy

As outlined in Section 1.5, the field of *in vivo* two-photon microscopy is in constant development, with new technical advancements being published by some research group nearly on a monthly basis. Many of these developments consist not only of progress on the optomechanical or electronic side, but also require suitable support by the software used for controlling the microscope components, as well as for acquiring and processing the generated data streams accordingly.

For two reasons it is highly desirable to have a software system accessible that is compatible with the various possibilities available on the hardware side, as well as flexible enough to follow the evolution of new methods and techniques:

- For the purely *application-oriented researcher* who wants to make use of the best technologies within reach to answer his scientific questions, it is preferable to have a single multi-purpose microscopy software at hand, rather than having to switch between different software packages. First, a certain package might support a new functionality or piece of hardware, but not be compatible with other requirements imposed by the researcher. Second, a significant entry barrier is usually associated with familiarising oneself with new software.

- For the *developer of new methods*, productivity would be highly increased if he does not have to start from scratch when realising a new technical concept, but rather is

able to build on an already existing software system. In addition, the dissemination of his achievements is much easier if his new method is not based on a proprietary and exotic control software, but can rather be plugged into a well-established software as an add-on module.

At the beginning of my thesis work, I wanted to use existing two-photon imaging technology to approach a biological topic (see below). As I soon realised, the microscopy control software already in use at the laboratory was not able to cope with several requirements imposed by the biological problem. Unfortunately, this software had not been programmed for a newcomer to understand or extend the code. Following an initial phase of anger and frustration, I decided to design and implement a software framework complying with the above-mentioned primary requirements in order to make my future work, and that of any successors, more satisfying.

It is this microscopy control software framework, named HelioScan, that I will present as the first major part of this thesis (Chapter 2).

1.6.2 A flexible method for cell type discrimination applicable to *in vivo* two-photon calcium imaging

When I started with my thesis work, *in vivo* two-photon calcium imaging did not yet allow the distinction between different neurons. The only established technique for cell type discrimination was the application of sulforhodamine 101 (SR101), which results in a selective counter stain of astrocytes [219].

As outlined in the first two sections of this introductory chapter, the neural population is highly diverse and different subtypes are known to engage in different specialised functions. Thus, it is highly desirable to have methods at hand that allow the researcher to dissect a neural population—from which calcium imaging data has been acquired—into cellular subtypes. Therefore, as a first goal, I decided to establish a method that allows discriminating GABAergic from non-GABAergic neurons in two-photon calcium imaging. As a subsequent goal, subtype discrimination of GABAergic neurons based on molecular markers should be achieved.

As for the second major part of my thesis, I will present a method that allows cell type discrimination for *in vivo* calcium imaging by post hoc immunostaining (Chapter 3).

These two parts constitute significant methodological contributions to the developing field of *in vivo* 2PM.

2 HelioScan

And now, O Muse Calliope, daughter of Zeus, begin to sing of glowing Helios whom mild-eyed Euryphaessa, the far- shining one, bare to the Son of Earth and starry Heaven. For Hyperion wedded glorious Euryphaessa, his own sister, who bare him lovely children, rosy-armed Eos and rich-tressed Selene and tireless Helios who is like the deathless gods. As he rides in his chariot, he shines upon men and deathless gods, and piercingly he gazes with his eyes from his golden helmet. Bright rays beam dazzlingly from him, and his bright locks streaming form the temples of his head gracefully enclose his far-seen face: a rich, fine-spun garment glows upon his body and flutters in the wind: and stallions carry him. Then, when he has stayed his golden-yoked chariot and horses, he rests there upon the highest point of heaven, until he marvellously drives them down again through heaven to Ocean.

Hesiod - Homeric Hymn to Helios [135]

2.1 Introduction

2.1.1 Situation analysis

From the perspective of the software developer, custom-built microscopy systems, which are common for example in the field of *in vivo* 2PM, provide a couple of problems.

Problems

Hardware diversity   Each custom-made imaging setup is usually a unique combination of hardware components. Even within a single laboratory, several not completely identical set-ups can exist. Across laboratories, differences between set-ups are usually even more extensive. Among the reasons for structural diversity are i) different functional requirements, ii) historical reasons (i.e. when individual set-ups are built sequentially, the state of the art for individual parts usually changes over time), iii) personal preferences of the involved engineers or scientists and iv) the fact that labs developing new image acquisition technologies are constantly experimenting with various new hardware equipment. Examples of such hardware diversity include different microscopy stages, different signal acquisition and signal generation devices, and different types of scanners in the case of laser-scanning microscopes (Figure 1.9 on page 27) [50].

Functional diversity   Researchers generally desire an imaging system with functionality tailored to their experimental objectives. Since these objectives differ between researchers, and also change over time, a general consensus of what an imaging system should be capable of can hardly be reached [50]. Prominent examples for different kind of functionalities are different scanning trajectories in the case of 2PM set-ups (Figure 2.1 on page 40) and different kind of output patterns for sensory stimulation of animals in neuroimaging experiments.
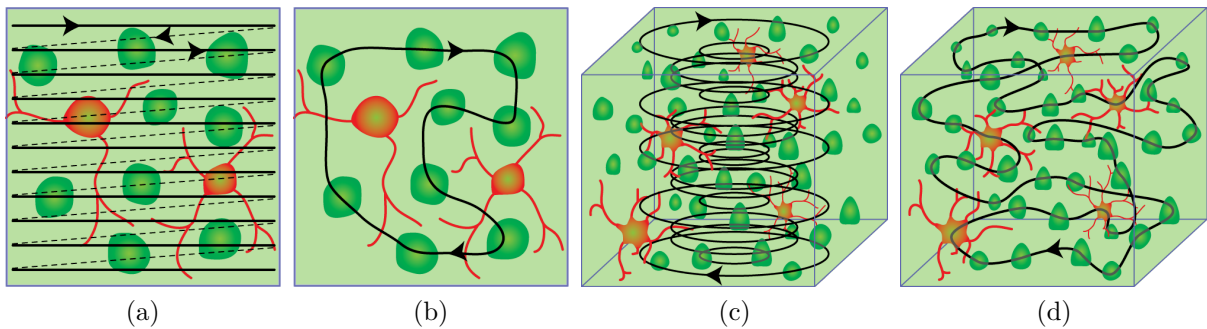
Figure 2.1: Example of functional diversity of custom-built two-photon microscopes: different types of laser-scanning trajectories. **(a)** Horizontal frame scan. **(b)** Custom horizontal line scan. **(c)** Three-dimensional spiral scan. **(d)** Custom three-dimensional line scan.

Understandability of code   The third problem is understandability of code. Larger pieces of software written by the typical scientist without experience in structured programming can quickly become difficult to understand (so-called spaghetti code, see Figure 2.2 on page 41 for an example). The main reason is a lack of structure and the fact that unstructured code cannot be documented. Unstructured, uncommented and undocumented code, in turn, requires a lot of time to be understood by outsiders. Even with well-structured program code, there are still differences between particular programming languages to be considered. Depending on the elements these programming languages provide and the way they are represented, they intrinsically differ in terms of how much time a newcomer to the project needs to understand the code.

Multiple developers   When huge monolithic software is modified independently by different researchers that want to adapt it to their individual needs, different versions quickly arise (so-called *forking*, Figure 2.3 on page 41). New functionality introduced in one version cannot be used by a researcher using another version. Also, the programmer is often not even aware that a certain problem has already been solved by a colleague and thus has to reinvent the wheel.

Usability   In an academic environment, software developed to control an experimental set-up is often not only used by the original programmer, but also by his colleagues or
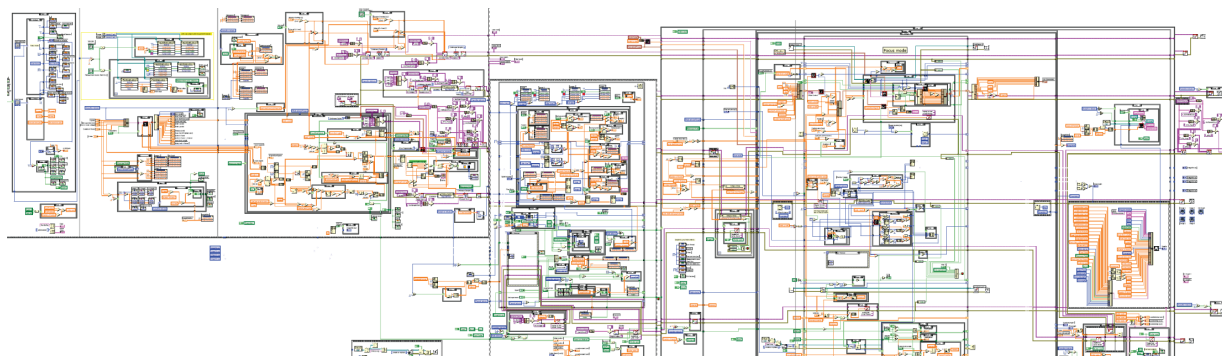
Figure 2.2: Example of badly structured, undocumented LabVIEW code that is difficult to understand for outsiders (real application encountered in an academic environment).
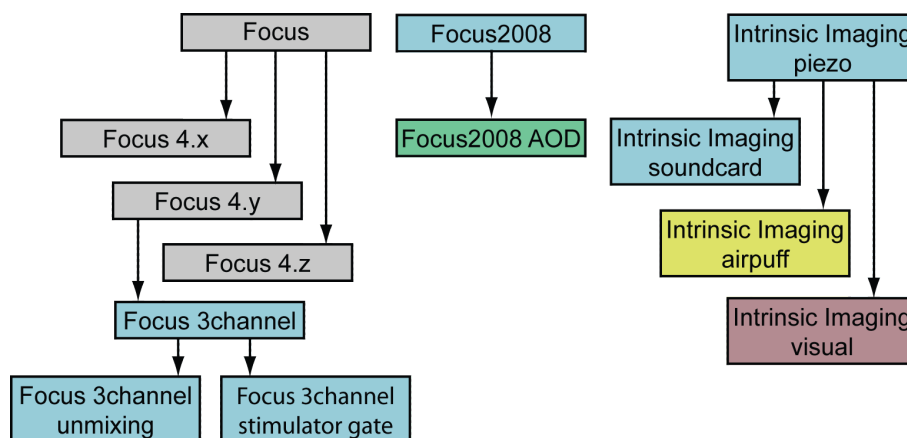
Figure 2.3: Example of version branching of imaging software written by individual scientists (authors are colour-coded).

successors. Unfortunately, attention is often not paid to usability, thus leading to accumulating cost over time. Specific problems revealed by follow-up users may include unlabelled graphical user interface (GUI) elements, run-time errors occurring when the GUI is accessed in a different sequence or timing than by the original developer, as well as poor or non-existing documentation. The following key features characterise software of high usability [147]:

- *Effectiveness*: the software does what the user wants.

- *Efficiency*: it requires minimum time to understand and learn how to use the software and later to perform a task. This aspect is centred around well-designed GUIs, which should be as self-explanatory as possible and allow fast work-flows, as well as documentation that can be consulted when in doubt.

- *Satisfaction of the user:* this is highly dependent on the above-mentioned two aspects.

Existing systems

A number of different software packages for microscopy applications already exist. Commercially available packages provide the advantage that a lot of man hours have been invested into their development and that many of the needs of a standard user have been taken into account. All big microscope manufacturers develop imaging software customised to control their hardware products (examples are *ZEN* from Zeiss[1], *LAS* from Leica[2], *cellsens* from Olympus[3], *NIS-Elements* from Nikon[4], *Metamorph* from Molecular Devices[5] and *iQ Software* from Andor[6]). The drawbacks of these commercial packages are their high prices and the fact that their source code is usually not available for modification. In addition, the standard user targeted by these packages is usually working with fixed tissue or cell cultures, such that it is not optimised for the needs of a neuroscientist performing *in vivo* microscopy. On the non-commercial side of the spectrum, a few software packages already exist:

- *ScanImage* is a two-photon microscopy software package written in Matlab[7] [231][8].

- *MPScope* is a two-photon microscopy software package written in Delphi[9] [217, 216][10].

- *Colibri* is a two-photon microscope control program written in LabVIEW[11][12].

- *µManager* is a powerful microscopy software framework that interfaces to ImageJ [268, 84, 50][13].

2.1.2   Rationale and goals

I concluded that in the expanding field of *in vivo* two-photon imaging systems the need for a *software framework*[14] exists. Commercially available packages did not fit the requirements and neither did the existing non-commercial packages because both do not provide frameworks but rather ready-made packages. An exception is the µManager mentioned above, which I was unaware of at the time the HelioScan project was started.

---

[1]http://www.zeiss.com/ZEN

[2]http://www.leica-microsystems.com/products/microscope-software

[3]http://www.microscopy.olympus.eu/microscopes/

[4]http://www.nis-elements.com

[5]http://www.moleculardevices.com/Products/Software/Meta-Imaging-Series/MetaMorph.html

[6]http://www.andor.com/software/iq/

[7]http://www.mathworks.com

[8]http://www.neuroptikon.org/projects/display/ephus/ScanImage

[9]http://en.wikipedia.org/wiki/Embarcadero_Delphi

[10]http://www-physics.ucsd.edu/neurophysics/links.html

[11]http://www.focusonmicroscopy.org/2011/PDF/373_Seebacher.pdf

[12]http://www.lrz.de/~chr

[13]http://valelab.ucsf.edu/~MM/MMwiki

[14]A software framework models a specific domain or aspect thereof, while providing a reusable design and reusable implementations [238].

The goals for this project were to design and implement a microscopy software framework promoting applications with the following properties:

- *flexibility* to meet many different hardware and functional combinations;

- *extensibility*, which requires understandable and well-documented code that can be edited by multiple developers in parallel without interference;

- *usability* according to the definition given above.

Trade-offs between these requirements might have to be made in certain cases, especially between flexibility and extensibility on the one side and usability on the other. A software can be exactly tailored to a certain purpose or workflow and the specific needs of a single user. However, this increases the probability that the underlying program code will become monolithic (i.e. tightly coupled) and thus neither flexible nor extensible. Or, from another perspective, for an application framework, which by definition has to allow for the implementation of different actual applications, the underlying architecture has to be designed in a very abstract and modular way. Due to the loose coupling required for this purpose, certain very specific interactions between modules might not be possible without impairing flexibility.

2.1.3   Solution approach

Definition of HelioScan

HelioScan has been developed to approach the problems listed above (Section 2.1.1). In this context, the term HelioScan[15] has two distinct meanings:

- a software framework facilitating the development of microscopy control applications according to a structured approach;

- a collection of components, built inside the above framework, that can be used to assemble a microscopy control application with high flexibility

These two aspects complement each other. First, from the developer's perspective, one does not have to start implementing an application from scratch but can make use of the many components already existing. Second, from the user's perspective, many needs can already be met by assembling and configuring existing components in an appropriate way. If a piece is missing, it is only this very piece that has to be newly implemented, according constraints provided by the framework.

---

[15]A catchy name is important for software package to become known in the community [85]. Helios, the Greek god of the sun who travels in his chariot over the sky, is a perfect metaphor for the laser focal point scanning the specimen in 2PM.

The basic concept

The basic concept of HelioScan is that a running application assembles at *run-time* from individual components. All components are derived from some abstract *component types* that define their basic behaviour and interaction (Figure 2.4 on page 44). Components of the same type can be exchanged for each other. This allows HelioScan to reach the goals presented above (Section 2.1.2) as follows:
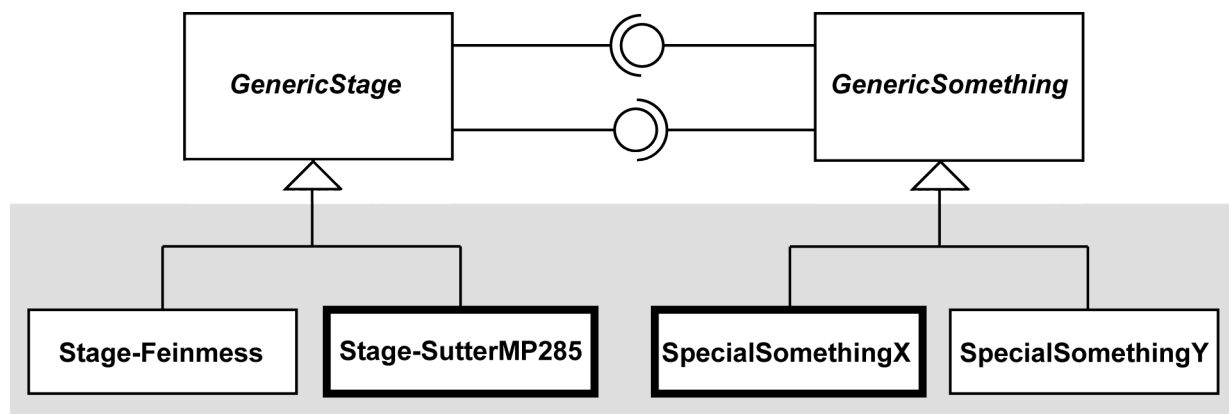
Figure 2.4: Basic concept of component-based architecture in HelioScan. Both hardware and functionality are encapsulated in software components (labelled boxes). HelioScan assembles at run-time from actual components (boxes on grey background) that are derived from abstract (generic) component types (boxes on white background). Each of the generic components provides an interface (shown as lollipop) that is inherited by and, thus, common to all derived components. In this example, a running HelioScan application instances the two components displayed as bold boxes, which—although of specialised nature— are still able to communicate with each other due to the generic interfaces inherited from their superordinate component types.

Flexibility   All distinct hardware components are encapsulated as software components. Different hardware combinations can be addressed by the corresponding combination of software components. As an example, different microscopy stages are encapsulated by different Stage components. The user chooses which Stage component he wants to use according to the actual stage device present at his setup. Likewise, different units of functionality are abstracted as distinct component types. Thus, as with hardware-abstraction components, a given functionality of a certain abstract type can be swapped for another functionality of the same type. For example, different laser-scanning trajectories can be swapped for each other (see Figure 2.1 on page 40).

Extensibility   If a software component supporting a specific hardware device or functionality does not yet exist, it can be created by deriving it from the corresponding abstract component type. The required time and effort is minimal because the framework already provides a lot of structure and established procedures for solving the problem. The existing components, especially the generic ones defining the actual framework, should be

well-documented, well-structured and programmed according to established style-rules [24]. This enhances both understandability of existing code and also promotes understandability of the code that underlies a new component. In order to develop a new component, the developer also does not have to understand the whole HelioScan framework or all of the already existing components in detail. Rather, due to the hierarchical architecture of the framework, he will only have to understand in a top-down fashion the vertical slice to which his new component will belong to. The fact that a HelioScan application assembles from individual components at run-time further implies that multiple developers can work simultaneously on different components Section 2.2.4. As long as they do not modify the interfaces defined at the level of generic component types, they will not interfere with each other. If such modifications at the abstract level are to be carried out, this has to be well-orchestrated because the implications will affect many components and their responsible developers and users.

Usability   Usability is mainly determined by the usability of the individual components and is thus the responsibility of the individual developer. For a component to be part of the official HelioScan distribution, it should comply to basic quality standards such as listed in [24]. Components with low understandability and usability can still be implemented, but their poor quality remains restricted and does not affect the remaining part of HelioScan.

The LabVIEW development environment

It was decided to implement HelioScan using LabVIEW due to a number of reasons (see Section 2.3 for a discussion of the problems encountered with LabVIEW during the project).

Visual programming   LabVIEW[16] is a graphic programming environment introduced in 1986 by National Instruments (NI)[17] to facilitate the development of data acquisition and automation applications based on their proprietary hardware [18]. The actual programming language featured by LabVIEW is called G. However, the latter term is rather uncommon and the word LabVIEW is often used for both the programming language as such as well as the surrounding integrated development environment (IDE). G (to which I will refer to simply as LabVIEW in the following) differs in two aspects from well-known programming languages such as C, C++, C#, Java, Python, Perl or Ruby.

First, it is a so-called data-flow programming language, which employs a programming paradigm that is fundamentally different from that of the conventional *imperative programming languages* listed above. The key advantage is that more than one operation can be executed in parallel [151] (see Figure 2.5 on page 46). Data-flow approaches had originally been developed to exploit massively parallel hardware architectures [151]. Although specific data-flow hardware architectures existed, LabVIEW was introduced for conventional computers and operating systems [303]. However, with the recent advent of multi-core

---

[16]originally an acronym for **Lab**oratory **V**irtual **I**nstrument **E**ngineering **W**orkbench
[17]http://www.ni.com

architectures in PCs, the intrinsic support of LabVIEW for parallelism has experienced a revival. Another key feature of pure data-flow languages is the absence of side-effects[18] because the output tokens are newly created upon completion of a node [151]. LabVIEW provides various constructs that can provoke side effects. These include local and global variables, references, input/output (I/O) from and to peripheral hardware or communication with other programs running on the same or another computer. Thus, a LabVIEW program is usually far from side-effect free. However, although easily circumvented, the data-flow principle should be followed as far as possible in LabVIEW in order to at least minimise the number of side effects [24].
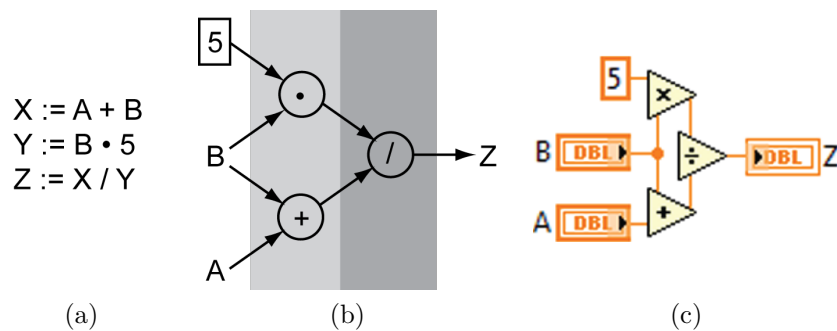
Figure 2.5: Imperative versus dataflow paradigm (adapted from [151]). **(a)** Simple program in an imperative pseudo-language. Each command is executed sequentially. **(b)** The corresponding data-flow equivalent, represented by a directed graph. Here, data flows along the edges of the graph as tokens. As soon as all input tokens have arrived at a node, the node is executed and the resulting value(s) flow as token(s) into the output edge(s). With these preconditions, the two parts underlaid in light grey can be executed in parallel. In addition, when the part underlaid in dark grey is being executed, the parts underlaid in light grey can already operate on a new set of data tokens (so-called *pipelining*). **(c)** How the program is implemented in LabVIEW. The edges of the graph in (b) are represented as wires. Pipelining as mentioned in (b) is not activated by default, but can be enabled by inserting a so-called feed-back node into a wire.

Second, while the above prominent languages are verbal programming languages[19], LabVIEW is a visual programming language (VPL) [251]. Productivity improvements up to ten times have been demonstrated with VPLs compared to verbal programming languages [18]. This can be attributed mainly to the native support of off-the-shelf interface cards in the case of industry-promoted languages such as LabVIEW [18]. Another efficiency boost stems from changes enabled in the software development life-cycle, namely the communication between customer, developer and computer [18].

Basic features   The basic building bricks of a LabVIEW program are termed Virtual Instruments (VIs). A VI consists of a *front panel*, which is identical to the GUI when the

---

[18]In computer science, a *side effect* denotes the change of a variable's value without this modification being explicitly recognisable in the program code [121]. Side effects render program execution dependent on history (i.e. stateful) and render the program code difficult to understand.

[19]Also referred to as *textual* or *text-based* programming languages, although strictly speaking a text is also a kind of visual information, thus *textual* is not actually complementary to *visual*.

VI is executed by the user directly, and a *block diagram*, which contains the VPL program code (Figure 2.6 on page 47). The front panel can contain various types of *controls* and *indicators*, by means of which data can be entered or displayed, respectively. Each front panel element is represented on the block diagram as a *terminal*, which represents either a data source (in the case of controls) or data sink (in the case of indicators). Controls and indicators of a VI can be connected to a so-called *connector pane*. A VI can be used as a building brick on the block diagram of another VI, acting as a *subVI* to which input and output wires can be connected as defined by the connector pane. This means that in addition to the many VIs already provided by LabVIEW itself or by third parties, the developer can also create his own building bricks.

(a)   (b)
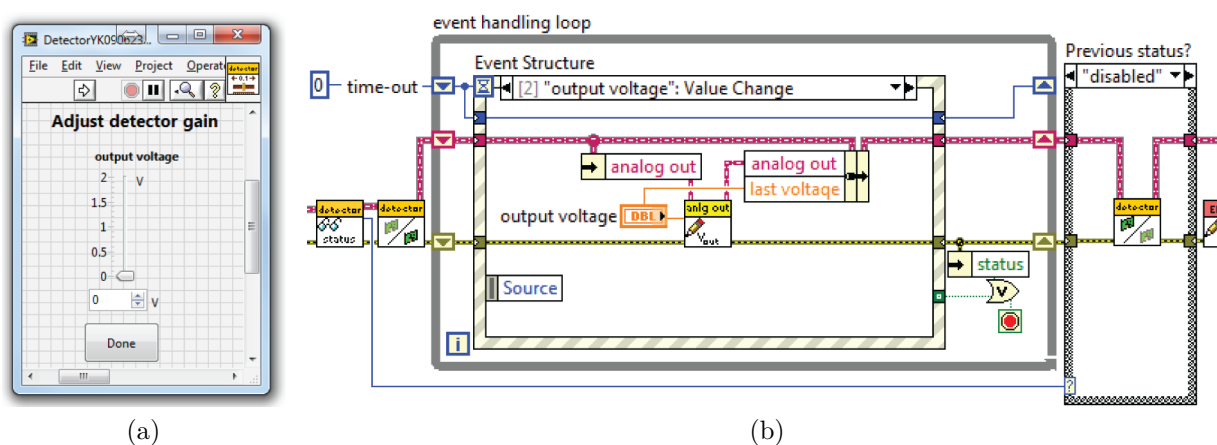
Figure 2.6: Front panel and block diagram of a LabVIEW VI. **(a)** Front panel of a LabVIEW VI. **(b)** Part of a VI's block diagram. The orange box labelled *output voltage* is the terminal correponding to the slider control element with the same name in (a). The square boxes are subVIs called by this VI.

Hardware access A central aspect of LabVIEW is that it provides immediate access to a huge catalogue of signal acquisition and generation hardware of NI. While NI also provides drivers to access their hardware from languages such as C++, it is clearly an advantage when both hardware and interfacing software is developed and tested by the same manufacturer. Additionally, due to the broad acceptance of LabVIEW in the automation and signal acquisition community, a growing number of hardware-producing companies also provide LabVIEW code to control their own products.

Understandability The data-flow paradigm, especially when displayed visually as in LabVIEW, is intrinsically familiar to researchers and engineers in academia because it is similar to many other concepts used in this environment (e.g. flowcharts, signal transmission between technical components). Thus, LabVIEW has a steep learning curve at the beginning and well-structured LabVIEW code can even be explained to somebody who has little or no understanding of computer programming.

Acceptance   LabVIEW is frequently used in the academic world for controlling custom laboratory equipment and data acquisition. In addition, LabVIEW is well-established for signal acquisition and automation applications in the industry.

Speed   LabVIEW provides speed in several aspects.

- *During development:* Instantaneous type-checking ensures wires are only connected to possible target nodes. Wrongly connected wires are immediately visualised. A VI is executable only when all required wires are connected in a correct fashion. In addition, unlike for other compiled languages, LabVIEW code is instantly compiled in the background, which means that a syntactically correct VI can be executed at any time. This makes feed-back and testing cycles much faster than in languages where source code modifications have to be followed by a phase of compiling and linking before testing is possible. Also, the development or modification of GUIs is easy and fast due to the front-panel/block-diagram approach described above.

- *Execution:* LabVIEW code gets compiled and thus finally translated to machine code. As a result, its is execution fast. Due to the intrinsic support of data-flow programming languages for parallelism, programming multi-threaded code is very easy. In principle, LabVIEW can assign any two paths of data-flow that can be executed in parallel to different cores of a multi-core processor or to different processors on a multi-processor computer. In combination with the LabVIEW FPGA module[20], appropriate VIs can even be compiled to a bit file that is executed on a field-programmable gate array (FPGA) on NI reconfigurable I/O hardware, allowing highly parallel real-time execution of code at iteration speeds of up to more than 100 MHz. FPGA hardware from NI is especially well-suited to enable high-speed pre-processing of acquired data or on-the-fly generation of analytically defined signals.

Structured programming   As with probably any programming language, certain ways of solving a problem have been accepted as standard solutions and are propagated as so-called patterns [24]. In addition, NI and third parties are constantly integrating new technology into the LabVIEW environment, either as integrated features or add-on modules. Some of these features specifically facilitate structured programming. These are:

- *LabVIEW object-oriented programming (LVOOP):* object-oriented programming (OOP) (Section B.2) was originally only accessible via the commercially available GOOP add-on[21]. However, since LabVIEW 8.2, NI provides OOP as an integrated part of LabVIEW (LVOOP), which can now be used independently of, or in conjunction with, GOOP. The basic differences between the two technologies is that GOOP works with reference-based class instances, while LVOOP strictly follows the original data-flow approach. A third approach, called G#[22], is available as a free add-on. Similar to

---

[20]http://www.ni.com/fpga/
[21]http://www.symbio.com/products
[22]http://www.addq.se/gsharp

GOOP, it allows reference-based objects. Furthermore, it provides additional features, such as interfaces and abstract classes.

- *Statechart module:* Available since LabVIEW 8.6, the statechart module allows programmers to graphically define state machines and directly embed LabVIEW code into states, transitions and guards. After compilation, a statechart can be embedded into a VI and reacts to external messages by state transitions. Using statecharts, certain program logic can be implemented on a higher abstraction level, which enhances both implementation efficiency as well as understandability.

- *Unit Testing Framework:* Introduced with LabVIEW 2009, the Unit Testing Framework allows the developer to write unit tests for VIs using LabVIEW code. Unit tests provide the possibility to test programmatically whether certain software units are behaving as specified by their interface contracts. This is especially important to minimise the frequency of software bugs[23] introduced by code modifications. Unit tests work by feeding pre-defined test data vectors into the units to be tested and checking whether the produced output is as expected.

Subversion

In HelioScan, the forking problem (Section 2.1.1) is solved by splitting up the software into many components that can be modified independently. New functionality can be added by either extending an existing component accordingly or implementing it as a completely new component. Thus, an individual component is not subject to version branching, but maintains a linear version history.

In software development, a crucial productivity enhancement is achieved by introducing a *version control system (VCS)* [3]. Among others, a VCS brings the following major advancements:

- A developer has access to any version of a file that has been committed to the VCS repository in the past. Thus, he can easily revert changes that proved to be unsucessful. The same approach helps the developer to track down the version a certain software bug first appeared and the modification that introduced the bug in the first place.

- The same version of software can be accessed from different computers and by different developers or users. Here, the VCS acts as a means of synchronising different computers.

- Each revision has a unique identifier. It is time-stamped and optimally also supplied with a comment by the developer responsible for committing it to the repository.

---

[23]A software bug refers to a programming error that hinders a computer program from working as intended. See `http://americanhistory.si.edu/collections/object.cfm?key=35&objkey=30` for how in earlier times of computer programming the word *bug* had to be taken even more literally.

For HelioScan, I decided to use the very common *Subversion* as a VCS [59]. Both server[24] and client[25] software can be downloaded and used for free.

---

[24]http://subversion.tigris.org
[25]http://tortoisesvn.tigris.org

2.2   Results

2.2.1   Software architecture

Object-oriented implementation of components

The core building bricks of HelioScan are so-called *components*. By definition, a component is a piece of software that can be replaced by another piece that shares the same interface through which it interacts with the rest of the software. I decided to implement these components in an object-oriented fashion, i.e. as LabVIEW classes, in order to make use of the advantages of OOP (Section B.2). In the case of HelioScan, components of a certain kind share a common parent class and thus a common interface of methods through which they can be accessed and manipulated from superordinate program code. In the following, I will refer to the kind of a component as *component type*.

As a common rule, whenever I identified a functional or physical entity that could occur in different forms depending on the physical hardware of microscopes or functional requirements of the user, I specified these peculiarities as different child classes of a common abstract base class defining the common interface and thus the common component type.

Since even classes of different component types share some common functionality, the latter has been factored out into the common base class `GenericComponent`, from which all other component classes are derived (Figure 2.8 on page 55). This class provides both common abstract methods that only exist for interface definition and methods that provide actual functionality (Table 2.1 on page 51). Thus, all of these methods are available for any HelioScan component class, but not all of them will necessarily provide actual functionality.

Table 2.1: Some important methods of `GenericComponent`.

Method	Abstract?	Purpose
`cmp.construct`	no	calls `cmp.read_config_file` if a configuration name is specified
`cmp.configure`	yes	to be overridden to implement a configuration dialog
`cmp.initialise`	yes	to be overridden to initialise resources
`cmp.terminate`	yes	to be overridden to release resources
`cmp.read_config_file`	no	reads the configuration file
`cmp.write_config_file`	no	writes the configuration file

Component life cycle

All HelioScan components have the same basic life cycle (Figure 2.7 on page 52). Initially, its `construct` and `initialise` methods are executed[26] (Table 2.1 on page 51). Then, the component is ready for use until the `terminate` method is executed. It is important to note that all three methods have to be overridden mandatorily if the component harbours subcomponents. In these cases, the corresponding method of each subcomponent instance has to be executed in addition to performing any other operations. In addition, the corresponding parent's method has to be executed in order to execute any superordinate `construct/initialise/terminate` method in the inheritance hierarchy (which at least includes that of `GenericComponent`, see Table 2.1 on page 51).

Configuration files

Values that rarely change should be placed into configuration files. In contrast to hardcoding these values in the source code, this allows the user to customise them according to his goals and thus strongly increases flexibility. Furthermore, it allows different users to use the same program with different configuration values. Configuration files should comply with the following requirements:

- A HelioScan application assembles at run-time from individual components, the combination of which is usually different from case to case. Therefore, it makes sense to keep these components as independent as possible. Configuration files should not unnecessarily bind together different components.

- Different instances of the same component should be able to load different configurations.

- The configuration files should be easy to interpret for both humans and software.

I decided for the following solution: Each component type has its own configuration files. As a result, components are not bound together by a single, global configuration file. Component instances load configuration files with a name set at run-time. Therefore, different instances can load different configurations. Configuration values are encoded in the

---

[26]One might argue that the two methods could be merged into one. Historically, there initially was just a single method for initialisation. However, cases were encountered where a separation of the two steps was desirable. Thus, I decided to split them up into the two separate methods `construct` and `initialise`.
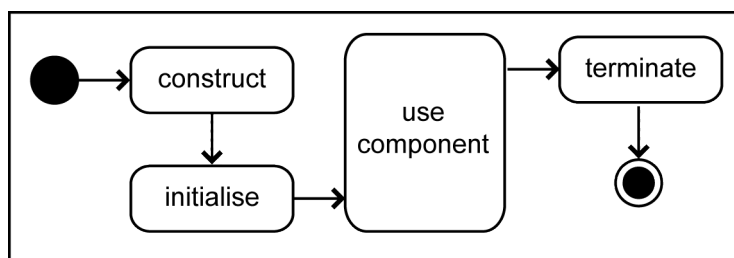
Figure 2.7: HelioScan component life cycle. In the `construct` activity, if specified, the configuration file is read. In the `initialise` activity, hardware or software resources are initialised, which are released in the `terminate` activity.

files using Extensible Mark-up Language (XML), which can be quickly parsed and generated programmatically[27]. It is also human-readable as the following example demonstrates:

```
<config_data>
  <device_name>img0</device_name>
  <camera_type>gray scale</camera_type>
  <connection_type>CameraLink</connection_type>
</config_data>
```

Top-level components (TLCs)

I distinguish between top-level components (TLCs) and subcomponents (SCs). Only TLCs can be directly accessed by the HelioScan main application (i.e. the main VI), whereas SCs exist merely as attributes of a superordinate component. Both TLCs and SCs can host their own SCs. TLCs share the following common features:

- *TLC queue:* TLCs are sent to the main application via the TLC queue either by the main application itself (when manually selected by the user) or by other TLCs (usually by the ImagingMode TLC, as specified in its configuration file; Figure 2.9 on page 56).

- *State machine:* TLC classes define a `run` method that is being executed continuously during nearly the whole life-cycle of a TLC object (or, more precisely, as soon as the TLC has been received by the main application). These `run` methods have their own GUIs, which are loaded into subpanels of the main application's GUI at run-time and are thus permanently available to the user. A `run` method executes its own state machine, which reacts to a defined set of messages from outside (in the following referred to as *triggers*) [78]. These triggers can either be issued due to user interaction or software-internal state transitions. The state machines of individual TLCs execute in parallel while communicating with each other mostly in an asynchronous manner. Thus, they exploit multi-threading technology and the multi-core CPU architecture of contemporary PCs.

- *Mutex:* In a running HelioScan application, there is always only a single most up-to-date instance available of a given TLC component type. In order to avoid race conditions[28] in the strongly multi-threaded HelioScan application, each TLC provides a mutex[29]. If a TLC's data (which includes any of its SCs) is to be modified, the modifying part of the software has to obtain the newest instance and lock the TLC. After modification, it has to release the TLC such that it becomes available again for modification to other parts of the software.

---

[27]HelioScan uses easyXML as a XML parser and generator. EasyXML is a commercial third-party add-on to LabVIEW: `http://jki.net/easyxml`

[28]A *race condition* refers to a situation where two processes try to access the same resource at the same time.

[29]Mutex stands for a *mutual exclusion* mechanism where only one process can access a resource at a time.

- *Command queue:* TLCs can send and receive command objects according to the command design pattern [100]. Command classes inherit from the abstract SC class `GenericCommand` and override its `execute` method.

- *Data queue:* TLCs can register as observers of other TLCs according to the observer design pattern [100]. If the observee has a data package ready, observers receive a copy of the data packets via the data queue.

These common features are defined in the class `GenericTopLevelComponent`, which is the common base class of all TLC classes (Figure 2.8 on page 55). Since SCs usually do *not* have these features, they also do not inherit from `GenericTopLevelComponent`, but rather from `GenericComponent` directly.

TLC component types

The component types of TLCs are defined by the corresponding generic component classes (Figure 2.8 on page 55) (as is also the case for SCs). The fact that each TLC inherits the functionality listed above from `GenericTopLevelComponent`, opens a wealth of possibilities for how actual implementations of TLCs can interact with each other. The types of interactions are as follows:

- In principle, each TLC can (like the main application) determine the instances used for other TLC component types (by dispatching them via the TLC queue). Before doing so, it can transfer values to these TLCs via so-called Adapter classes. Adapter classes are based on the mediator pattern [100] and allow the transfer of data between the two classes using more specialised accessor methods not present at the level of generic TLCs.

- Each TLC can send triggers to other TLCs. We distinguish between *common* triggers that are compatible with all TLC component types and TLC-specific triggers that can be sent only to a specific TLC component type.

- Each TLC can execute public methods of other TLCs. For methods that modify the callee, the mutex functions checkout/checkin have to be used to temporarily lock the callee and avoid race conditions.

- Each TLC can send pre-populated Command class instances to any other TLC. Depending on the level of abstraction, at which the Command object will act on the target TLC, more or less specialised Command classes have to be implemented. More specifically, if the Command acts on the target TLC only by executing methods defined at the generic level of the component type, it can act on any class of that component type. However, if the Command is designed to carry out very specific manipulations of a particular target TLC, it cannot be executed by another TLC of the same component type.
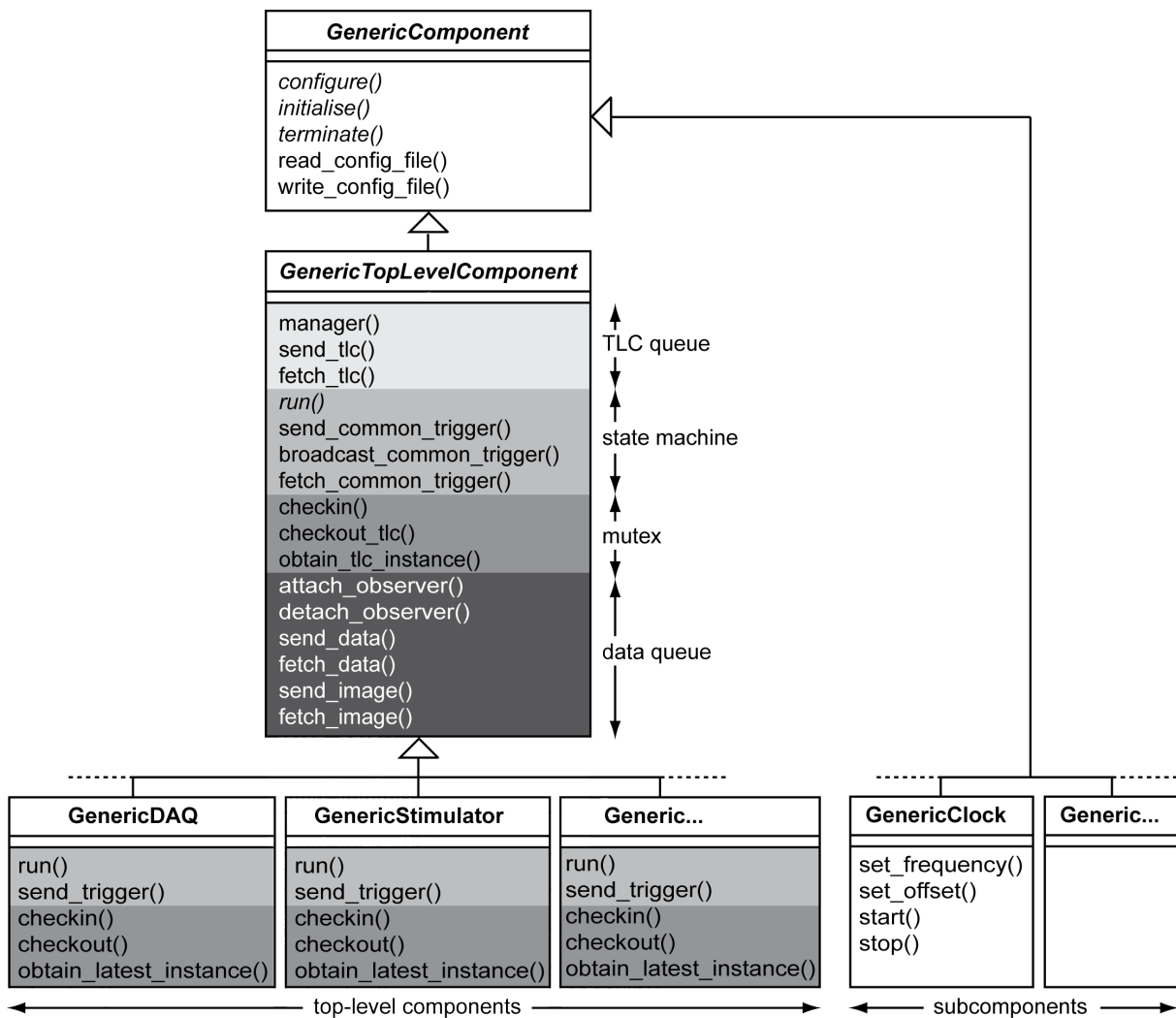
Figure 2.8: Hierarchy of HelioScan component classes. `GenericComponent` is the common parent from which all other components are derived. In contrast to SCs, top-level components (TLCs) have `Generic-TopLevelComponent` as a common intermediate base class. For each component class, some selected interface methods are displayed (coded with different shades of grey in the case of TLCs: methods related to the TLC queue; methods related to the state machine; mutex-related methods; methods related to the raw data and raw image queues). Abstract methods are shown in italic font, methods with implemented functionality in normal font.

- Each TLC can register as an observer of any other TLC component type and thus receive copies of the data produced by the observee. This allows to build arbitrary and even branched data processing pipelines (Figure 2.11 on page 58).

In the following, I will present the individual TLC component types. In addition to the purpose of each component type, I will also describe typical interactions between them. Although, on an abstract level, a huge number of different interactions between TLC component types are possible as outlined above, it makes sense to name here only
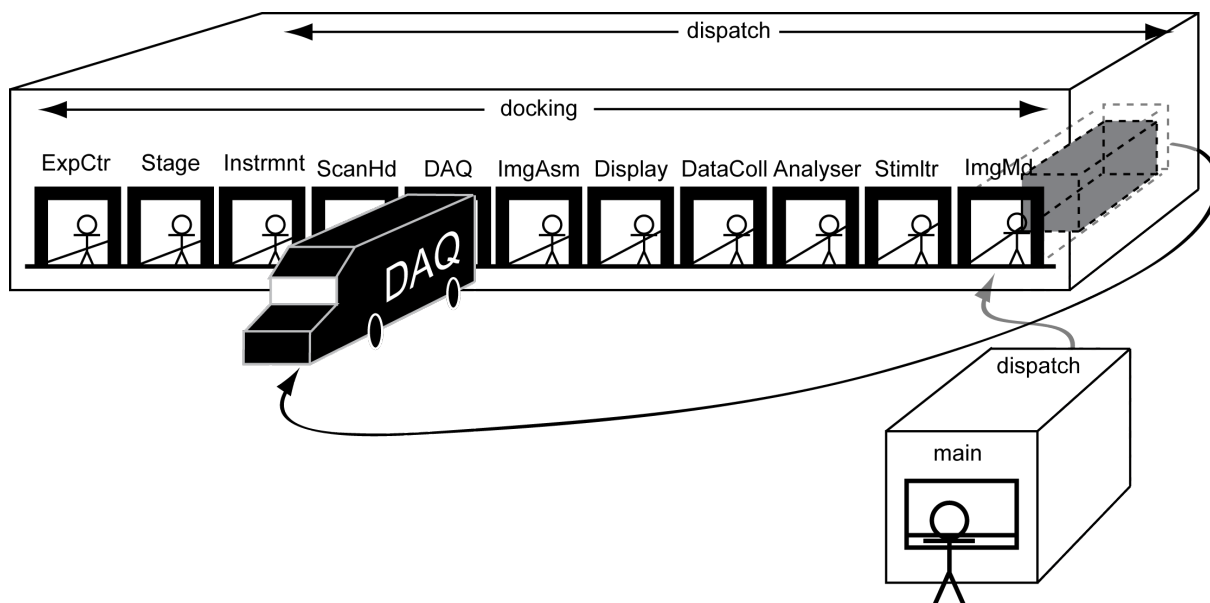
Figure 2.9: Dispatching top-level components (TLCs) via the TLC queue. In this metaphoric representation, the facility buildings stand for the main program. The slots in the larger building symbolise the place holders (one for each TLC component type), where TLCs can be housed. The TLC queues are represented by lorries transporting incoming TLCs to corresponding gates on the docking side of the building. The managers receiving the TLC instances are represented by little figures unloading the lorries and transporting the contained machine (i.e. the actual TLC instance) into the corresponding slots, where it becomes active. The machines can produce new machines that are packaged into lorries on the dispatch side of the building and shipped to the gates on the docking side. This stands for TLCs specifying other TLCs by sending them to the main program. Not only existing machines can create and dispatch TLC machines, but also the facility (i.e. main application) itself can. Here, the customer figure standing in front of the customer desk building stands for a user of a HelioScan application selecting a specific TLC to be loaded.

those interactions that are very common for the already implemented component classes. It should be kept in mind that HelioScan provides a flexible framework while the actual architecture can be flexibly determined by the component developer.

ImagingMode   The central TLC is the ImagingMode, which specifies the mode of imaging; for example, frame-scan laser scanning or IOS imaging. The ImagingMode class to be instanced is usually selected based on user input on the main application's GUI and sent to the class' `manager` by the main application itself (another common sender of the ImagingMode is the ExperimentController, see below). Via its GUI, the ImagingMode can accept user input further defining the represented mode of image acquisition (e.g. the scan rate, the number of frames to acquire). Due to its defining nature, it usually sends other, dependent TLCs via the corresponding TLC queues (Figure 2.10 on page 57). Those TLC types are marked with a star (*) in this list.

ScanHead* The ScanHead TLC controls the scanners that move the focal point of a laser through the sample. Thus, it is only important for laser-scanning-based modes of
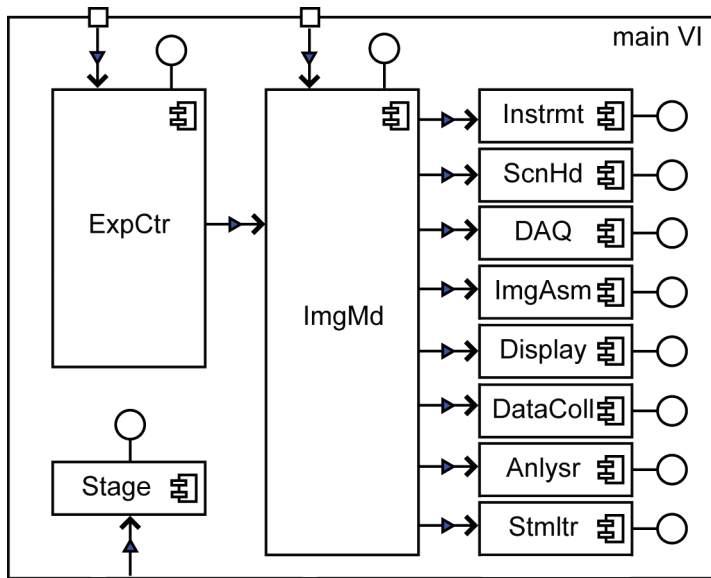
Figure 2.10: ImagingMode defining other TLCs. In this UML component diagram, arrows indicate the flow of component objects through the TLC queues, lollipops indicate trigger reception interfaces, and the little squares on the main VI box indicate ports through which the user can determine which component class (here: which ExperimentController and which ImagingMode class, respectively) is to be loaded. While the Stage component is determined by the main VI directly (based on the main configuration file), it is the ImagingMode, which usually defines all remaining TLCs. In multi-sweep mode, the ExperimentController can take over the role of the user by selecting the Imaging-Mode automatically.

imaging. The ScanHead receives from the ImagingMode a pre-configured Trajectory object that defines the path of the laser focal point. While the basic shape of this path is determined already when the ScanHead receives the Trajectory, modification of some trajectory properties such as scaling factor, rotation angle or laser intensity can still be possible during scanning. However, details depend on the actual ScanHead and Trajectory classes that are used.

DAQ* The DAQ TLC is responsible for continuous data acquisition, such as reading from an analog-to-digital converter (ADC) that digitises PMT signals. Thus, the DAQ component acts as a *source* of data and typically stands at the beginning of a data processing pipeline. Other TLCs that want to make use of this data can register as observers in order to receive a copy of the data (Figure 2.11 on page 58). The DAQ can read in data and pass it on to its observers either as a stream of samples from an arbitrary number of channels, or as complete images in the case of camera-based devices.

ImageAssembler* When present, the ImageAssembler TLC usually registers as an observer at the DAQ and assembles the raw pixel stream into complete images. Alternatively, when the DAQ component encapsulates a device that produces images instead of a pixel stream, an ImageAssembler can still be involved in order to perform post-processing of raw images.

DataCollection* The DataCollection TLC stores image data to hard disk for later retrieval. In addition, via its GUI, it can provide the functionality that the user can access image data already acquired. The image data is usually obtained from the ImageAssembler, at which the DataCollection has registered as a observer (Figure 2.11a on page 58).
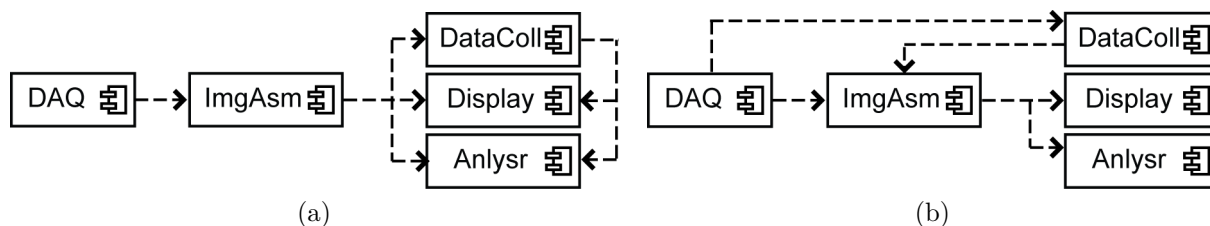
Figure 2.11: Data processing pipelines realised using the observer concept. **(a)** During data acquisition, the DAQ component reads in data and passes it on (symbolised by dashed arrows) to the ImageAssembler, which has registered as an observer at the DAQ component. Images produced by the ImageAssembler are in turn handed over to the DataCollection, Display and Analyser, which have registered as observers at the ImageAssembler. Independent of data acquisition, the DataCollection can also send stored images to Display and Analyser upon user interaction if the latter two have additionally registered as observers at the DataCollection. **(b)** If data acquisition is too fast and not all data can be processed by the ImageAssembler in real-time, this alternative connection pattern can be a solution. The DataCollection has registered as a DAQ observer and is thus directly receiving a copy of original raw data that it can stream to disk in a raw data format. The ImageAssembler—also registered as a DAQ observer and now only responsible for producing images for on-line display—can skip some of the data received if the input queue size is reaching a threshold. Independent of data acquisition, the DataCollection can play back past raw data to the ImageAssembler upon user input, as the latter has additionally registered as a observer at the DataCollection.

If very fast saving is of importance, one can also think of a architecture in which a Data-Collection component registers directly as a DAQ observer and streams raw image data directly to disk (Figure 2.11b on page 58).

Display[*]   The Display TLC is responsible for displaying images to the user. Thus acting as a image sink, it registers at any source of images, typically at the ImageAssembler and the DataCollection. Since the image data received are copies, it can carry out arbitrary image manipulation prior to display without affecting the original data.

Analyser[*]   The Analyser TLC can perform on- or off-line analysis on image data received from components at which it has registered as an observer (Figure 2.11a on page 58).

Stimulator[*]   The Stimulator TLC encapsulates and controls any kind of device capable of generating stimuli delivered to the specimen.

Stage   The Stage component is responsible for controlling and reading out any motorized microscope stage. Since the stage is usually a permanent part of a given setup and does not depend on the mode of imaging, it is defined by the main application itself, rather than by any of the TLCs.

Instrument[*]   The Instrument TLC can control and hold information about any further parts of the microscope, such as detectors, beam splitters, filters, lasers etc.

ExperimentController   The last type of TLC, which is only occasionally involved, is the ExperimentController. HelioScan can operate in three different run modes:

- *Free run:* In this run mode, image acquisition runs continuously, usually without storing data. This mode can be used to locate the right position within the sample and to adjust or test parameter settings.

- *Single sweep:* Here, a specified number of scans is performed or images acquired (corresponding to a single sweep). Acquired data is usually stored to disk.

- *Multi-sweep:* In this mode, sweep control is handed over to a user-selected ExperimentController. The ExperimentController can execute several sweep acquisitions in a sequential fashion.

Possible multi-sweep scenarios are, for example, when an ExperimentController starts sweeps at the edge of a transistor-transistor logic (TTL) trigger or in specific time intervals. It is even possible that the ExperimentController itself specifies the ImagingMode to be used, thus allowing the implementation of automation scripts in which the Experiment-Controller performs whole sequences of image acquisitions with different ImagingModes, configurations or GUI settings (Section 2.2.6).

2.2.2   The main VI

The HelioScan *main VI* provides the platform on which HelioScan TLCs are instanced at run-time and on which their GUIs (i.e. their front panels) are loaded into sub-panels that can be accessed by the user (Figure 2.12 on page 60). In principle, different HelioScan main programs can be implemented, according to the needs of the users. Currently, only one main VI exists. Although it serves its purpose well, it should not keep future developers from creating other main VIs. In the following, I will briefly describe the current implementation. Its GUI mainly contains the following elements:

- a sub-panel for each TLC component type, into which the GUIs of the respective TLCs are loaded at run-time;

- buttons to start image acquisition or saving of already acquired data;

- drop-down menus to select the currently mounted microscope objective, the imaging-Mode and the experimentController to load, as well as the run mode to use;

- a multi-line text field providing a notebook on which HelioScan writes basic parameters for each image acquisition during saving, and on which the user can take additional notes.

The main VI first initialises its own front panel (i.e. populates the drop-down menus mentioned above) and loads the Stage component. The data determining the details for this initialisation task is contained in a main configuration file that lists the ImagingModes,

(a)   (b)
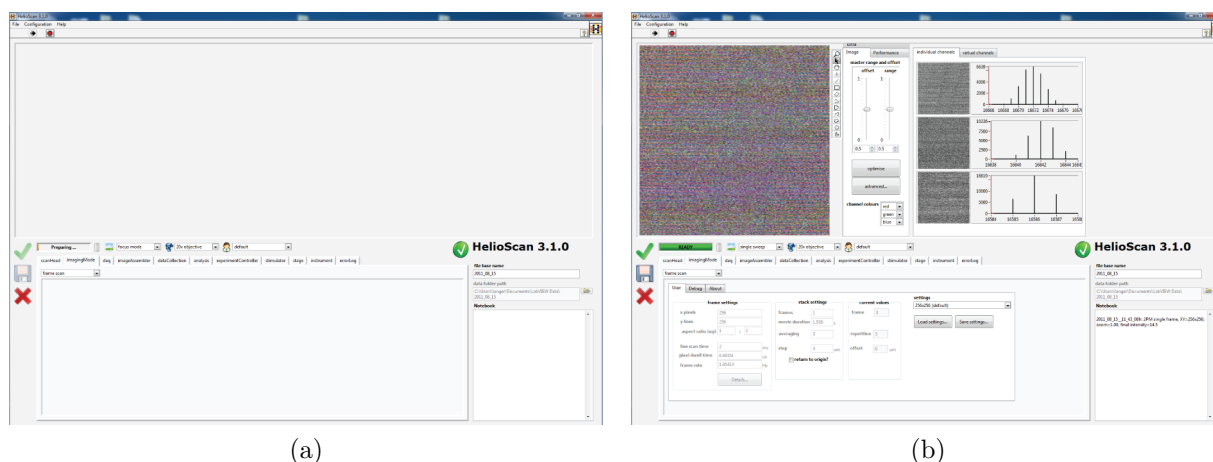
Figure 2.12: GUIs of the HelioScan main VI. **(a)** Before loading, all sub-panels are empty. **(b)** After loading, the sub-panels are populated with the GUIs of the individual TLCs.

ExperimentControllers and microscope objectives to be made available to the user, as well as the Stage component to be loaded. After initialisation, the main VI is responsible for GUI event handling. The first events to be handled are triggered by the main VI; the main VI automatically sets the selected drop-down menus to their default values specified in the main configuration file. As a result, the main VI loads the selected ImagingMode, ExperimentController and Objective components and sends them to their `manager` method, which in turn executes their `run` method (the main VI directly executes the `manager` method of each TLC component type as a subVI). Usually, it is the ImagingMode that, in turn, loads all the remaining TLCs and sends them to the corresponding `manager` methods where their `run` method will be executed (Figure 2.10 on page 57). It is the `run` method of each TLC that eventually loads the respective component GUI into the corresponding sub-panel of the main VI.

2.2.3   Extensibility

Rather than being a monolithic piece of software, HelioScan provides a framework for implementing software controlling custom-built microscopes. Many application requirements can already be covered by assembling a running HelioScan application from the available components by means of suitable configuration alone. If a required functionality cannot be obtained by configuration, new components can be developed in a straight-forward fashion, thus assuring that HelioScan can easily be extended to support new technological developments and future applications. In most cases, only minimal time is required to do so compared to modifying another, already existing software package or developing completely new microscopy control software from scratch. Productivity is enhanced due to the following points.

Best practices   Due to the highly structured framework approach, the developer of new functionality is well guided during the design and implementation phase. Already existing components serving as examples, as well as a collection of best practices, further facilitate a fast and clean implementation of new components.

Component generator   A generator program has been implemented, which automatically creates the basic structure of a new component. The user can specify the base class from which the component should be derived, whether configuration files or settings files will be used, and whether the component will contain SCs or a state machine. Using VI server technology and VI scripting, the generator accordingly creates the LabVIEW project file with a new component class, adapts the inheritance of the class accordingly, creates type definitions and method VIs and already fills them with content as far as possible. Since this automates steps that otherwise would have to be carried out manually, this not only saves time, but also makes the procedure easier for inexperienced developers.

Scaffolding   HelioScan is extensively modularised in horizontal direction in terms of its subdivision into many components, which means that only a limited piece of software has to be newly developed to add functionality. In addition, HelioScan is also vertically modularized: whenever functionality was thought to be useful for more than one component, it was factored out into separate methods and moved up to a more generic level in the class hierarchy. When it applied to both SCs and TLCs, it was placed into the `Generic-Component` class, the common base class of all components; when it applied only to TLCs, it was placed into `GenericTopLevelComponent`. If it applied only to components of a specific component type, it was placed into the defining base class of that type (e.g. `GenericDAQ` if the method was of potential use to all DAQ component classes). In addition, when I thought that certain functionality would be used only in a fraction, but not all current or future classes of a certain component type, I introduced intermediate classes, which harbour this common functionality and provide it to derived classes. I termed these classes *scaffold classes* because they provide scaffold functionality (e.g. a run method including a state machine), which does not have to be re-implemented in the inheriting child classes. This means that if a new component class has to be developed, in most cases it can make use of a lot of functionality inherited from the different levels of parent classes, thereby drastically minimizing the time the developer needs to implement the component.

Building bricks   A couple of common classes and libraries have been implemented that can be re-used wherever needed in HelioScan, for example to represent images, image stacks, 3D vectors/boxes, or dynamic XML trees. So-called *XControls* allow the LabVIEW developer to implement new user interface controls of arbitrarily complex structure and underlying logic. Basically, an XControl is a VI with both front panel and block diagram, which can be embedded on the *front panel* of actual VIs (as opposed to subVIs, which are used as modules on another VI's *block diagram*). Only recently, we started to use XControls as part of HelioScan components; however, the productivity increase was immense. For

example, we implemented the XControl `XImage`, which provides the functionality to load and display an image stack, draw, save and load various kinds of ROIs and display the Open Microscopy Environment (OME) header of the image stack file. An instance of `XImage` can simply be drag-and-dropped onto the front panel of the VI that will make use of it. Prior to having this new building brick available, the underlying functionality had to be replicated for and tediously integrated into each new VI that required the display of image stacks on its GUI.

2.2.4   Collaborative efforts

Due to the fact that a HelioScan application assembles at run-time from component classes based on user-defined configuration files, developers can work independently on their own component classes without interfering with each other. Each component is organized as an independent LabVIEW project in its own folder. Since components should be as self-contained as possible, the developer also can test most of their functionality independent from the main application.

It is the responsibility of the individual developer to ensure that his components are in line with adequate programming style and are working properly, both on their own, and in interaction with other components as part of a HelioScan application. When a new component is finished and working properly, it can be added to the central version control system (VCS) repository. Snapshots of the development branch are made available as software updates to the users on a regular basis. The fact that individual developers can work on their own component projects and that components are checked into the VCS repository under central coordination avoids version branching and ensures that only one central development branch unfolds over time.

At the time of writing this thesis, six developers were working in parallel on implementing special imaging modes or other features (Table 2.2 on page 62).

Table 2.2: HelioScan components currently being developed by different developers.

Functionality currently being implemented	Developer(s)
AOD-based random-access scan mode	Marcel van 't Hoff
fiber-scanner mode	Roland Krüppel
photo-stimulation mode	Marcel van 't Hoff
trajectory-optimisation for galvanometric mirrors	Adrian Negrean
frame-scan using a resonant scanner	Andreas Keller, Dominik Langer
3D spiral scan mode for galvanometric mirrors	Chetan Nagaraja, Dominik Langer

2.2.5 File format

Requirements

For storing imaging data, a file format with the following features is desired:

- *Metadata storage:* It should be able to contain metadata about the image acquisition, which includes both the configuration and settings values characterising the Helio-Scan application at the time of image acquisition, as well as experimental parameters. Optimally, metadata should be stored in a human-readable format.

- *Flexibility:* The file format should be flexible with regard to bit-depth, resolution, number of frames and number of channels.

- *Compatibility:* It should be possible to easily import the files into standard image processing software used in the microscopy community.

OME-TIFF format

The HelioScan component responsible for file storage is the DataCollection. In principle, the developer is free to implement a DataCollection in order to save files in any format he wants. A format or standard complying with the requirements listed in the previous paragraph is the OME-TIFF file format developed by the OME consortium[30] [272, 112]. It stores image data in multi-page Tagged Image File Format (TIFF) files and metadata in XML according to a well-defined and extensible schema[31] as part of the TIFF file header.

Each HelioScan component class can override the method `GenericComponent:provide_OME_data`. By doing so, it can add specific data to any location in the XML tree of OME-XML. Since the overriding methods are required to call the method of the base class, data can be added at any level in the component inheritance hierarchy. `GenericComponent:provide_OME_data`, which is eventually called, automatically converts configuration and settings data (if present) to XML and adds it as StructuredAnnotations to the OME-XML:

```
<?xml version="1.0" encoding='UTF-8'?>
  <OME xmlns="http://www.openmicroscopy.org/Schemas/OME/2009-09"
          xmlns:xsi="http://www.w3.org/2001/XMLSchema-instance"
          xsi:schemaLocation="http://www.openmicroscopy.org/Schemas/OME/2009-09/ome.xsd">
    [...official OME part...]
    <StructuredAnnotations>
      <XmlStringAnnotation>
        <HelioScan>
          <DAQ name="DAQ_MG090622Camera">
            <config_data>
              <device_name>img0</device_name>
              <camera_type>gray scale</camera_type>
```

---

[30]http://www.openmicroscopy.org
[31]http://www.ome-xml.org

```
            <connection_type>CameraLink</connection_type>
          </config_data>
        </DAQ>
        [... other \acp{TLC}...]
      </HelioScan>
    <XmlStringAnnotation>
  </StructuredAnnotations>
</OME>
```

Thus, all configuration and settings parameters provided by the individual components are stored in the OME-XML metadata and can be accessed by other programs via the corresponding XPath expression[32].

2.2.6   Automation of image acquisition sequences

For experiments in which long-lasting, but well-defined measurement protocols have to be carried out, it is desirable to automate these protocols. There are two approaches to achieve this: either with the already mentioned ExperimentController (Section 2.2.1) or with ActiveX scripting. These two approaches are presented in the following sections.

ExperimentController

In multi-sweep run mode, HelioScan hands over acquisition control to the currently loaded ExperimentController. Thus, it is possible to implement an ExperimentController that steers HelioScan in a fully automated fashion according to any thinkable protocol. An example is `ExperimentControllerDL090130Interval`, which performs a defined number of sweeps in a specified time interval. A sweep is defined by an object of a class derived from `GenericSweep`. For example, an instance of `SweepDL090926Automation` can be arbitrarily configured to perform a sequence of image acquisitions. Each of these image acquisitions is defined by the ImagingMode to be used, as well as the configuration and settings files to be loaded for this ImagingMode. In the simplest case, when the Sweep object is of the type `GenericSweep`, `ExperimentControllerDL090130Interval` just repeats an image acquisition of the currently selected ImagingMode with its already defined configuration and GUI settings every n seconds. In a more complex case involving `SweepDL090926Automation`, a sweep could consist of several image acquisitions involving different ImagingModes with different configurations and settings. The sweep protocol could in turn be automatically repeated every five minutes, for example.

---

[32]XPath is a query language to address specific elements in an XML document. In the example given above, the camera device name can be accessed by the xpath expression `OME/StructuredAnnotations/XmlStringAnnotation/Helioscan/DAQ/config_data/device_name`. For details, see http://www.w3.org/TR/xpath/

Interfacing to script languages

Script languages are easy to learn and script programs can be executed instantly without having to be compiled. As a consequence, they are ideally suited for automating often-used or extensive work sequences of other computer programs. The MPScope microscopy software package provides the possibility of automating image acquisition procedures using a script language via the Component Object Model (COM)/ActiveX interface [217, 216].

LabVIEW can act as an ActiveX server, thereby exporting its VIs and base types for access from other programs running on the same PC. It is possible to access HelioScan VIs (including component methods) from script languages (e.g. Matlab, Python, Ruby) using ActiveX and control image acquisition parameters and sequences from such scripts. To simplify this process, it makes sense to supply each HelioScan component with a wrapper class written in the script language. When writing an automation script, the user would not have to deal with low-level ActiveX functions, but can rather just instance the wrapper classes of the components he wants to manipulate, and call their methods.

As a proof of principle, I started implementing a wrapper class hierarchy in the Ruby language[33]. In this attempt, I succeeded in controlling image acquisition with a Ruby script. The following example performs a frame scan with 200x200 pixels resolution in free-run mode for a duration of five seconds.

```
require "./Helioscan.rb"
require "./ImagingModeDL090130Frame.rb"

helio = HelioScan.new    # get the HelioScan application instance
imagingMode = helio.imaging_mode    # obtain the ImagingMode wrapper

imagingMode.x_resolution = 200
imagingMode.y_resolution = 200
imagingMode.frame_rate = 3    # in Hz
imagingMode.update    # transfer the parameters to HelioScan

helio.start    # start image acquisition (we are in free-run mode by default)
sleep 5    # wait for 5 sec.
helio.stop    # stop image acquisition
```

However, an unsolved problem was that HelioScan responded to the Ruby commands only after a delay of a few seconds. This is problematic because neuroscience experiments require response times in the sub-second range. The problem of delay has to be solved before ActiveX automation of HelioScan can be used in practice.

2.2.7 Video camera mode

Background

Non-scanning microscopes usually acquire images using a camera. Even laser-scanning microscopes often use a camera to align the specimen and coarsely navigate to the site of

---

[33]http://www.ruby-lang.org

interest. For *in vivo* two-photon microscopy, the camera is especially important to acquire images of the brain surface blood vessels because they provide navigational landmarks. In two-photon-targeted patching, for example, the camera is used to guide the patch-pipette to the location where it is intended to enter the tissue [168]. From the software-engineering perspective, HelioScan as a general-purpose microscopy software framework provides the environment and base functionality to integrate camera-based image acquisition. From the user's perspective, support of a video camera mode is practical because it allows switching quickly between different modes of image acquisition from within the same environment, saving to a common file format and using the same metadata and documentation standard.

Hardware architecture

HelioScan accesses a camera via image acquisition interface for LabVIEW (IMAQ), which is part of LabVIEW's Vision Development Module. Any camera for which an IMAQ driver is available can be easily used.

Software architecture

Camera-based imaging modes in HelioScan differ from the laser-scanning-based modes discussed below; instead of a continuous pixel stream, complete image frames are read in from the hardware. As a consequence, the DAQ component (`DAQ_MG090622Camera`) hands sends an array of Image objects (index: channel) to all registered DAQ observers for each acquired frame. One could argue that the ImageAssembler component is thus not needed for camera-based imaging modes and that DataCollection, Display and Analyser components could register directly as DAQ observers. However, in the configuration presented here, we keep the ImageAssembler involved (Figure 2.13 on page 67). Specifically, we use the component `ImageAssemblerMG090623Binning`, which performs spatial and temporal binning on the raw image frames. This means that `DAQ_MG090622Camera` can acquire frames at maximum resolution and full speed, while `ImageAssemblerMG090623Binning` down-samples resolution and frame rate to the values desired by the user. Due to the temporal averaging during the binning processes, noise levels can be decreased (Figure 2.14 on page 67).

2.2.8   Intrinsic optical signal (IOS) imaging

Physiological background

The body surface is somatotopically represented in the somatosensory cortex. In humans, each half of the body surface is represented as a humonculus (lat. for "little man") on the somatosensory cortex of the contralateral hemisphere [155]. Similar somatosensory representations are found in rodents, where the whiskers—which serve as an important sensory organ in these species—are represented in the so-called barrel cortex [226][227]. This somatotopical representation allows researchers to study cell-activity population dynamics inside functional columns [210] into which sensory information can be fed in a controlled
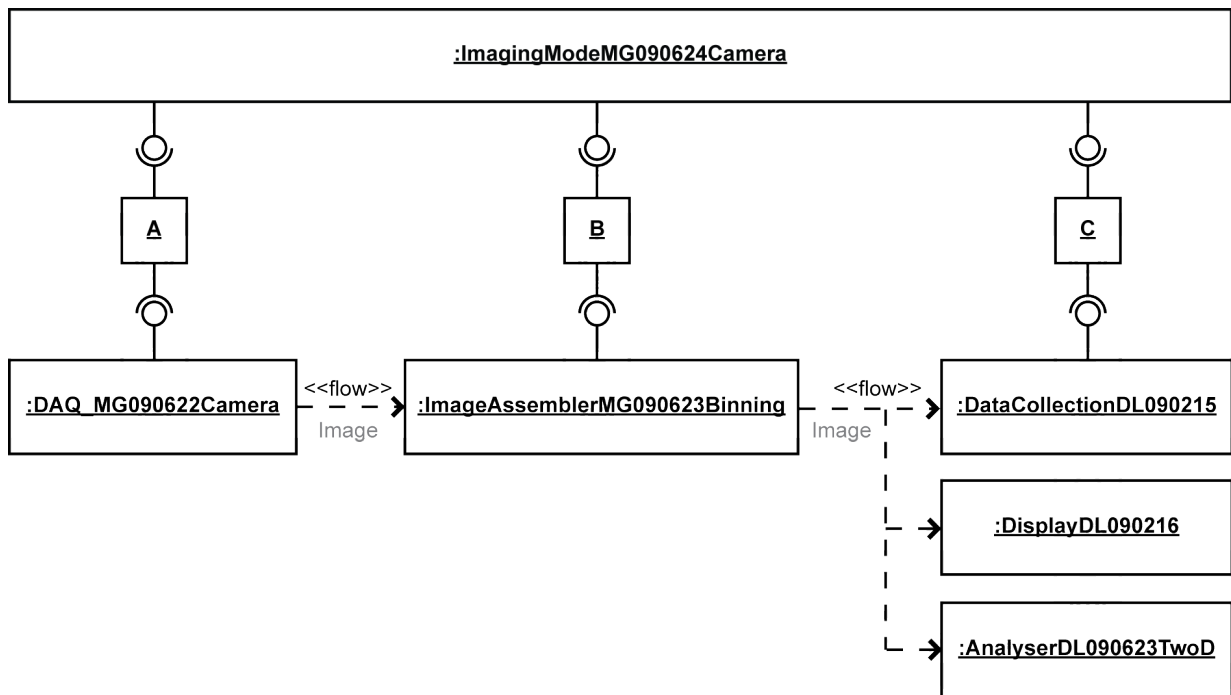
Figure 2.13: UML object diagram describing the interaction of core TLCs in video camera mode. The DAQ component hands over Image objects (one per channel and frame) to the ImageAssembler component that has registered as a DAQ observer. The DataCollection, Display and Analyser components have registered as ImageAssembler observers and thus receive individual copies of the Image object arrays spatially and temporally binned by the ImageAssembler component. The user enters acquisition parameters on the GUI of the ImagingMode. These values are handed over to the DAQ, ImageAssembler and DataCollection components by specific adapter components (A, B and C). Abbreviations: A, `AdapterDL091214Imaging-ModeToDAQ`; B, `AdapterMG090625ImagingModeToImageAssembler`; C, `AdapterMG090709ImagingModeTo-DataCollection`
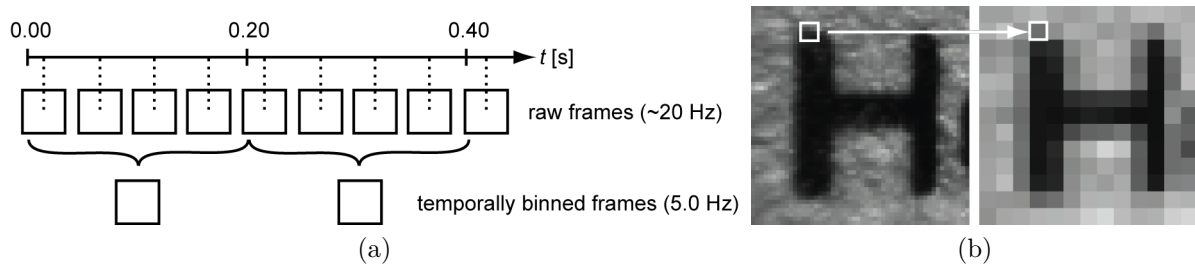
Figure 2.14: Noise-reduction by `ImageAssemblerMG090623Binning`. **(a)** Temporal binning: the frame rate is down-sampled to a lower, specified frame rate by averaging all frames within a period. **(b)** Spatial binning: the resolution of a frame is down-sampled to a lower, specified resolution by averaging pixels that converge onto a new pixel.

fashion by stimulating the corresponding sensory organ (e.g. a specific whisker) [220]. In order to target both the injection of fluorescent dyes and subsequent two-photon imaging to the cortical representation of a specific sensory system, a method is required that allows

one to localise such a representation with minimal invasion, high spatial resolution and within a reasonable time.

Imaging of the IOS is such a method. It can be employed through either a previously thinned skull (in young mice even through the intact skull) or after having performed a craniotomy, and it does not rely on dye application. Using IOS, the cortical representation of a sensory part of body surface can be localised within approximately ten minutes [26, 118, 97]. For example, the centre of a barrel column can be determined with a precision of roughly 100 μm.

The IOS refers to changes in light reflectance caused by local neural activity. Underlying these signals are activity-dependent changes in the optical properties (absorbance and scattering) of neural tissue. The mechanism with the strongest effect is based on the blood oxygenation level, which is shifted towards deoxy-hemoglobin during increased neural activity. Different absorption properties of oxy- and deoxy-hemoglobin lead to an intensity change of the reflected light. Reduced blood-oxygenation triggers an increase in local blood flow by vasodilation of capillaries, which in turn also affects light absorption [118, 97]. Other components of the intrinsic signal, although weaker, are attributed to modified light scattering due to changes in the ionic concentrations of extracellular fluid at higher AP firing rates [54].

Hardware architecture

The intrinsic optical signal is a very weak signal; during increased neural activity, the back-reflected light changes in the range of 1‰. For this reason, a camera with high bit depth per pixel is required. We decided on using the 3960DCL camera from Toshiba Teli Corporation, which provides a resolution of 12 bit per pixel (i.e. 4096 grey levels per pixel) and can be accessed from LabVIEW via a camera link card from NI.

We first built a stand-alone set-up exclusively designed for IOS imaging (Figure 2.15 on page 69). It consists of a Nikon microscope pinion to which we attached a custom-built holder carrying a macroscope built from two camera objectives facing each other's front lens. On the top side, the Teli camera was attached, while at the bottom of the assembly a ring with both green and red LEDs was mounted. A stable and adjustable power supply was built to power the LEDs, with the possibility to switch between green and red illumination [129].

Then, we decided to integrate an IOS imaging system into our two-photon microscopes. For this purpose, an LED ring was designed and built that can be attached to standard microscope objectives (Figure 2.16 on page 69) [129]. The same optical path as for the video camera mode was used to acquire images (Figure 2.16a on page 69).

Software architecture

Prior to the development of HelioScan, I implemented a stand-alone IOS imaging software using LabVIEW. In retrospect, it suffers from the already described problems (Section 2.1.1): i) bad coding style and no documentation, ii) therefore low extensibility and adapt-
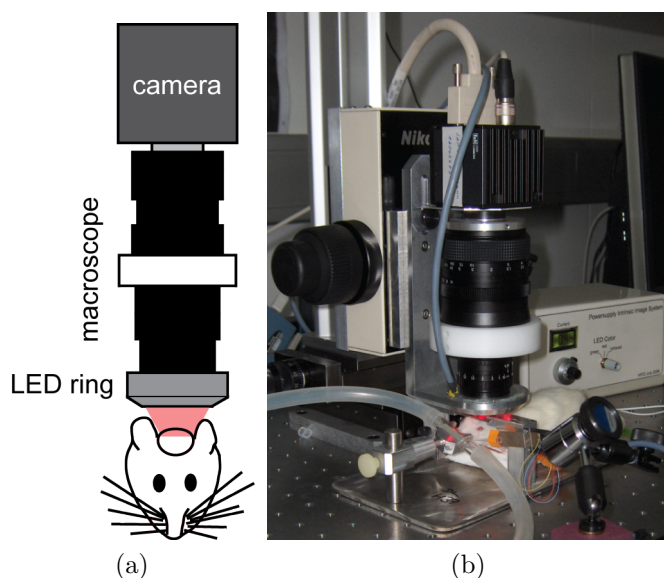
Figure 2.15: Stand-alone IOS imaging set-up. **(a)** Assembly of camera, macroscope and LED ring. **(b)** The complete imaging system with a rat (bottom middle), a piezo stimulator (bottom right) and the power-supply for the LED ring (right).
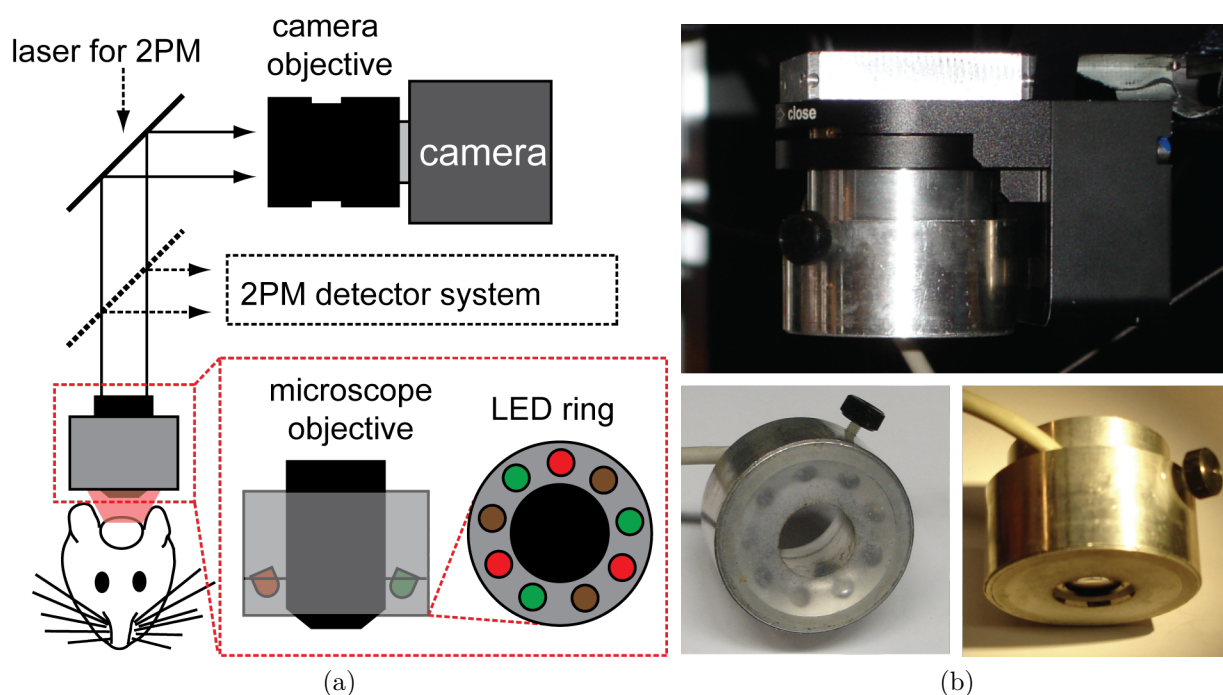
Figure 2.16: IOS imaging system integrated into a two-photon microscope. **(a)** For IOS imaging, the dichroic mirror used to guide the fluorescence light into the detector system during two-photon microscopy has to be removed whereas the mirror guiding the IOS image into the camera is blocking the laser beam path. The LED ring is mounted directly onto the microscope objective. **(b)** The LED ring attached to the microscope (upper picture), and alone (lower left) and mounted to a 4x objective (lower right).

ability, and iii) forking in order to support different hardware or functional requirements. Nevertheless, the software is currently still in nearly daily use by several researchers at our

laboratory due to its simple use and robustness, as well as for historical reasons.

Given the general architecture of HelioScan, I decided to integrate the functionality required for IOS imaging. Most top-level components already existed because they had been implemented for other imaging modes; only a new DataCollection and a new ImagingMode component had to be implemented: `DataCollectionMG091001IntrinsicImaging`. This DataCollection receives images that have previously been spatially and temporally binned by `ImageAssemblerMG090623Binning` (Figure 2.17 on page 70).
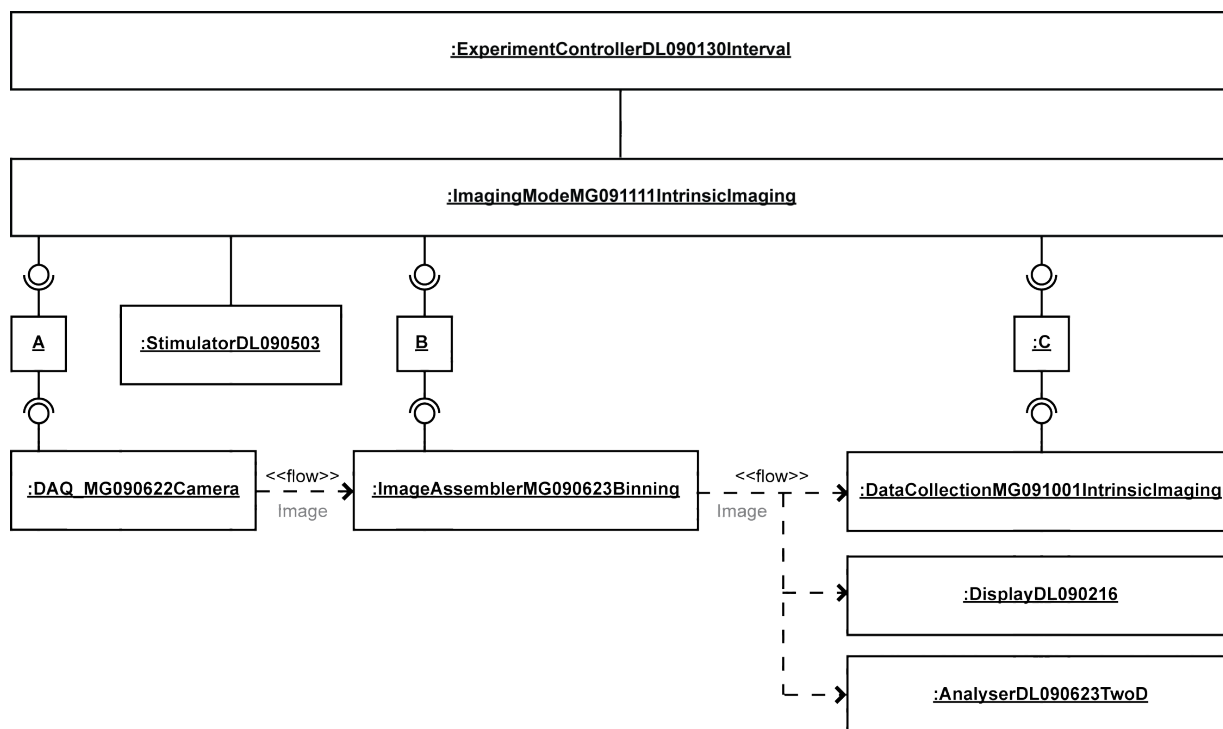
Figure 2.17: UML object diagram of the HelioScan top-level components during IOS imaging. Abbreviations: A, `AdapterDL091214ImagingModeToDAQ`; B, `AdapterMG090625ImagingModeToImageAssembler`; C, `AdapterMG090709ImagingModeToDataCollection`

Measurement protocol and results

An individual measurement (sweep) consists of the three image acquisition phases A, B and C, each with the same duration (Figure 2.18 on page 71). Only phase C is acquired with simultaneous sensory stimulation of the animal. For each time-point relative to the start of a phase, an image with the relative difference between B and C, and C and B, respectively, is calculated. Since both phase A and B are without sensory stimulation, the relative difference of A and B correspond to a control measurement, while the relative difference of B and C carries the actual IOS. The IOS is very weak; in order to achieve an acceptable signal-to-noise ratio, signal averaging is important. Therefore, measurements are usually repeated several times (using an appropriate ExperimentController component)
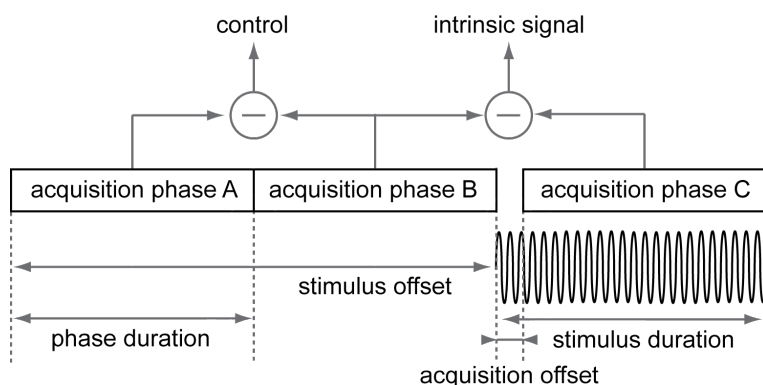
Figure 2.18: Single sweep for IOS imaging. Sweeps are repeated during an experiment in order to collect enough data for signal averaging.

and averaged (Figure 2.18 on page 71). For example, in order to localise the representations of individual whiskers in the mouse barrel cortex, I converged on the following protocol. Individual phases of a sweep had a duration of 5 s, while 15 of such sweeps were performed in a 35 s interval.
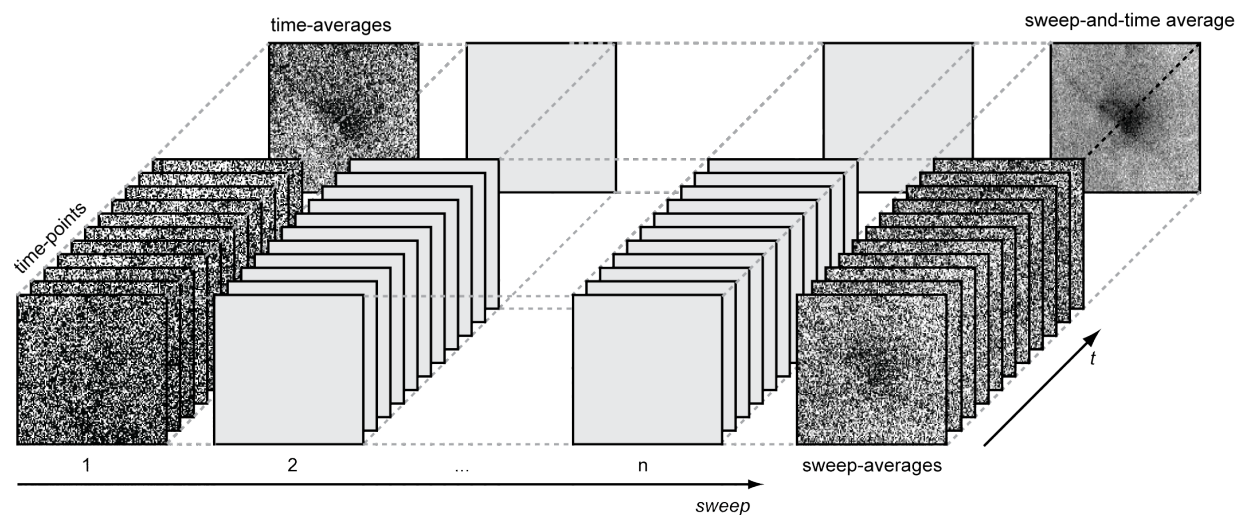
Figure 2.19: Different kinds of signal averaging that can be performed after an experiment of IOS imaging. Acquired images can be averaged independently for either a single measurement (sweep) yielding an average over the time-course of the IOS. These average images can in turn be averaged over several sweeps, leading to a better signal-to-noise ratio. If one is interested in the time-course of the signal, one can also average over several sweeps for each single time point.
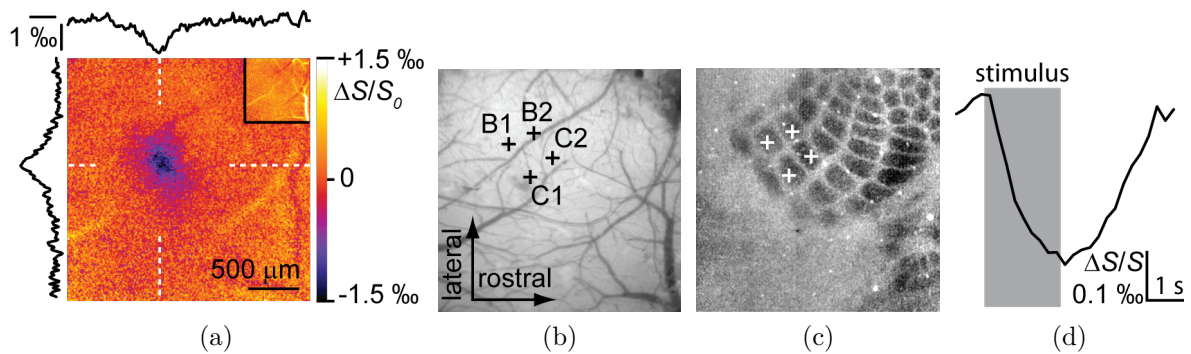
Figure 2.20: IOS imaging in the mouse barrel cortex. **(a)** Static IOS signal of a C1 whisker. **(b)** Same experiment as in (b), showing the position of four cortical whisker representations determined with IOS imaging. **(c)** The positions shown in (b) overlaid on a COX staining of the cortical tissue. The results obtained with the two methods are in very good accord. **(d)** Time-course of the IOS obtained in a separated experiment. Here, the stimulus was applied for only two seconds (indicated in grey).

2.2.9   Frame scan mode with galvanometric mirrors

Background   In normal frame scan mode, the specimen is sampled by the laser focal point line-wise in a horizontal plane. If, in addition to the x/y scan mirrors, a fast z-focusing device is used, the imaging plane can also be tilted (so-called arbitrary plane imaging [105]), thereby allowing the user to image oblique or vertical structures in the specimen. With a motorised stage or a z-focusing device, it is also possible to acquire image stacks by repeatedly moving the laser focal point in constant steps along the z-axis between frames.

Hardware architecture   PMT signals were digitised by a custom-built ADC and integrated during the duration of a pixel using an FPGA module from NI controlled by a LabVIEW VI (see Materials and Methods, Section A.1.3, for details). Pixel data was continuously transferred to the host personal computer (PC), where all channels were read out simultaneously and processed by HelioScan. The FPGA module also created a clock signal driving the generation of command signals controlling the galvanometric mirrors, a piezo-based z-scan device and the pockels cell for laser beam intensity adjustment.

Software architecture   The scanner command signals were calculated in the Trajectory component `TrajectoryDL090201Frame_Scan` based on parameters specified by the user via the GUI of the ImagingMode component `ImagingModeDL090130Frame`. They are then written to a digital-to-analog converter (DAC) card from NI by the ScanHead component `ScanHeadDL090202`. This ScanHead component allows the modification the trajectory coordinates in real-time to provide functionality such as zooming, rotation and tilting.

Results   This imaging mode was used to acquire all of the two-photon calcium imaging data as well as the anatomical image stacks presented in Chapter 3, such that no further

time-resolved and 3D stack data is presented here. Rather, the reader is referred to Figure 2.21 on page 73, which shows four different angle combinations for arbitrary plane imaging including both acquired three-channel fluorescence images and the underlying command signals used to drive the x, y and z scanners.

(a) $\phi = 0°, \theta = 0°$ (b) $\phi = 45°, \theta = 0°$ (c) $\phi = 45°, \theta = 30°$ (d) $\phi = 45°, \theta = 90°$
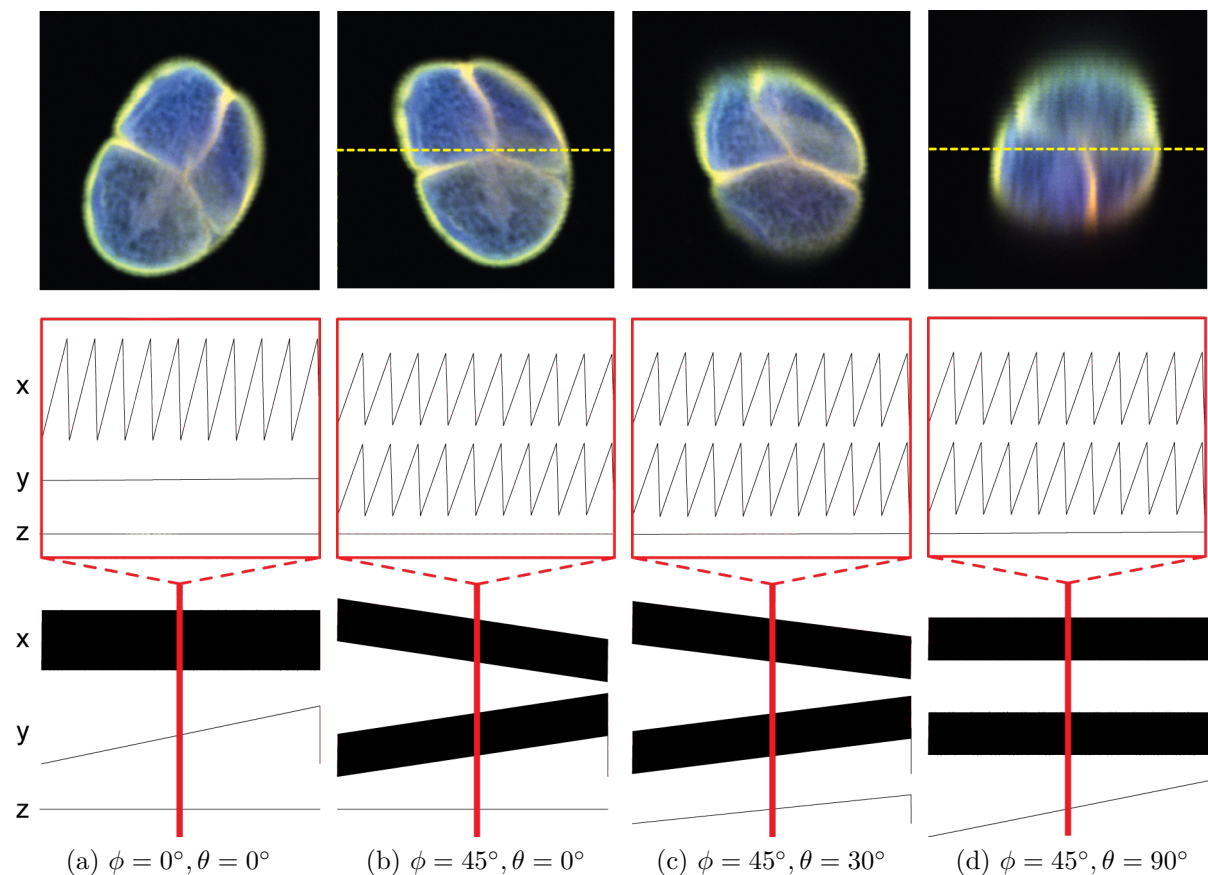
Figure 2.21: Galvanometric scan mirrors: arbitrary plane imaging of a fluorescently stained pollen grain. Command signals used for controlling the x, y and z scanners over a whole frame (512 lines) are shown in the bottom row. Insets (middle row) show a magnified version of the command signals for ten lines. **(a)** Horizontal frame scan. **(b)** Horizontal frame scan, rotated 45° around the z axis. **(c)** The imaging plane tilted by 30° around the relative x axis shown as dashed line in (b). **(d)** The imaging plane vertically oriented. The dashed line indicates the position of the horizontal imaging plane in (a).

2.3 Discussion

2.3.1 Summary

In this chapter, I presented HelioScan as a software framework for microscopy control applications. The framework solves some major problems observed with previous custom microscopy software used in the academic environment. In particular, it copes with hardware and functional diversity by assembling at run-time from individual software components. The high combinatorial flexibility is complemented by easy extensibility; due to a highly structured approach, new software components can be rather quickly implemented. In combination with the well-documented framework classes, the structured approach facilitates understandability of existing and newly implemented source code. High modularity further allows multiple developers to work in parallel on extending HelioScan functionality. I demonstrated the applicability of this approach by implementing different imaging modes based on different image acquisition modalities. At peak times, up to four developers were independently working on individual components in parallel, proving that a collaborative effort is possible without version branching.

2.3.2 Technical issues

LabVIEW instabilities

The LabVIEW IDE itself is a highly complex piece of software. Especially new releases of the LabVIEW core or of add-on modules can still contain serious software bugs. In the HelioScan project, some of the most recent LabVIEW technology was used—often as soon as it was released by NI—due to the advantages promised and expected. Particularly the combination of such new technologies revealed underlying software bugs. Most likely, such combinations had not been tested extensively enough by NI before release of the respective LabVIEW versions. Software bugs in a given LabVIEW version could usually be overcome by patches eventually provided by NI or by subsequent releases of LabVIEW. Nevertheless, in total, several months of full-time work were lost for debugging[34], communicating with NI engineers and finding work-arounds[35]. Examples of the problems that were encountered are:

- In the first version of the LabVIEW statechart module, state editing was extremely slow when HelioScan component classes were used in the state code[36]. Later, LabVIEW even crashed when closing states containing HelioScan classes after editing[37].

---

[34]For many bugs it was initially not clear whether a problem occurring was due to a flaw in HelioScan or in the underlying LabVIEW itself.

[35]Usually by a trial-and-error approach or simply re-programming the affected part of the source code.

[36]http://tiny.cc/statechartEditingSlow

[37]http://tiny.cc/statechartCrashes

- During the first months of the HelioScan project, all component classes were part of the same LabVIEW project. As the project grew larger, it became more and more unstable. Crashes of the LabVIEW IDE occurred frequently during programming. This was the original reason to create an individual LabVIEW project for every HelioScan component. This not only rendered LabVIEW behaviour more stable, but also allowed multiple programmers to work independently on different components (Section 2.2.4).

- Certain run-time errors occurred that could *not* be attributed to flaws in the HelioScan source code and that could only by solved by re-implementing part of the source code[38] or explicit mass compiling, respectively[39].

- LabVIEW crashed either when loading or editing certain files or when HelioScan was executed[40].

- With earlier versions of the LabVIEW FPGA module, dynamic FPGA VI references led to strange behaviour in conjunction with FPGA VI containing strict type definitions[41]. In addition, FPGA VI references lost their type definition binding when HelioScan was installed on other setup PCs[42].

- Seriously reduced performance of image acquisition with HelioScan was observed under certain conditions, without obvious explanation[43].

In conclusion, one has to be aware that when introducing new LabVIEW technology into HelioScan, problems may arise. They may even show up with a delay or be detectable only when using particular HelioScan component combinations or on specific PC models. In the future, it might make sense to wait for the second release of a new LabVIEW version or add-on before making use of it because it usually already includes some bug fixes. An additional possibility would be to upgrade LabVIEW on a separate Subversion branch and merge with the trunk when all emerged problems have been solved.

Hardware-related problems

Various hardware-related problems were encountered. In most cases, they were related to upgrading driver software, installing HelioScan on a new PC model or re-inserting PXI modules that had be temporarily removed from the PXI chassis. Examples of such problems encountered include:

---

[38]http://tiny.cc/DAQmxInvokeNode

[39]http://tiny.cc/dynamicDispathBug

[40]http://tiny.cc/LVCrash1
http://tiny.cc/LVCrash2

[41]http://tiny.cc/FPGARefBroken

[42]http://tiny.cc/FPGATypeDefLost

[43]http://tiny.cc/LVSystemSubpanelSlow

- Certain NI hardware permanently stopped working properly, but was still functioning when tested on another setup PC[44].

- NI hardware stopped working temporarily until the system was rebooted[45].

- A previously properly working NI device permanently stopped working on all tested PCs[46].

- A newly delivered NI device did not work on one PC, but it did properly work on another PC[47].

- The NI hardware administration tool *Measurement & Automation Explorer (MAX)* repeatedly corrupted its own database after start-up[48].

All these problems could finally be resolved by either re-installing NI software, upgrading drivers, installing bug-fixing patches released by NI, updating the BIOS of the setup PC or sending affected devices back to NI for repair. However, as with the LabVIEW instabilities mentioned above, weeks of work had to be invested in total to track down the actual sources of the problems and find appropriate solutions. When the setup affected could not be used to perform biological experiments while the problem was being solved, a further loss in productivity resulted. In cases where the setup was shared by several investigators—which was usually the case—multiple research projects could be blocked. I therefore suggest to always create a backup image of the system disk before installing new NI hardware or software (especially device drivers).

Upgrading the HelioScan release

A few problems occurred when users updated from an older HelioScan release to a newer one. Here, they are discussed together with suggested solution approaches.

New software bugs Developers can unwillingly introduce new software bugs when modifying source code with the intent to improve or extend HelioScan[49]. These bugs may range from simply broken VIs to complex hardware-dependent timing problems emerging only for certain component combinations under certain specific conditions. A HelioScan distribution consists of many different components, a particular HelioScan application can

---

[44]`http://tiny.cc/DAQcardNotSelectable`
`http://tiny.cc/FPGAFifoError`
`http://tiny.cc/DAQmxCardNotRecognised`

[45]`http://tiny.cc/FPGADiagramReset`

[46]`http://tiny.cc/DAQmxCardBroken`

[47]`http://tiny.cc/FlexRIOBIOS`

[48]`http://tiny.cc/MAXCorrupted`

[49]This was especially the case with design changes performed from time to time at the framework level in order to improve simplicity, performance or flexibility. The consequences of such changes often sent ripples through the whole HelioScan class hierarchy. All potentially affected components had to be manually checked and adapted if necessary.

assemble from even more potential combinations of such components and a user can interact with it in countless different ways. As a consequence, it is virtually impossible to manually test every possible scenario before creating a new release. In order to minimise the occurrence of the first two type of bugs mentioned, I recommend to use the LabVIEW Unit Test Framework (see Section 2.1.3) in the future [89, 259]. Unit tests could be executed before each commit or even in regular time intervals on a dedicated test server. They would identify VIs that are broken or otherwise not correctly operating. Regarding software bugs that only emerge in a running HelioScan application, a shorter and tighter feedback cycle between users and developers is required. Users should be taught to properly use the existing issue tracking system by reporting bugs immediately and with a precise description of the circumstances under which they occurred.

Installing a new LabVIEW version For some release upgrades, a newer LabVIEW version must be installed (indicated by an increase of the left-most part of the release number, see Figure 2.22 on page 78). In the past, the procedure of installing newer versions of LabVIEW modules or NI device drivers in some cases caused problems with other LabVIEW programmes or installed hardware. As in the previous paragraph (Section 2.3.2) I recommend to always create a system disk backup image before upgrading NI software. Alternatively, a new hard disk with a fresh Windows installation (quickly created by copying a previously prepared disk image) is used to install the new LabVIEW environment. When the new HelioScan release as well as all peripheral devices and other installed programs are working properly, the new hard disk can be permanently used. In the case of unresolved problems, the original hard disk can still be temporarily connected in order to use the microscope for biological measurements.

Incompatibility of configuration or settings files Many HelioScan components require configuration or settings files to work properly (Section 2.2.1). When advancing the functionality of components, developers sometimes decide to change the configuration files. Currently, existing configuration files of affected components[50] have to be either deleted and re-created from scratch or manually modified when up-grading or down-grading an installed HelioScan version. However, this procedure is not only cumbersome, but also error-prone. For example, developers might forget to properly communicate the change to the user, the user might simply oversee the information or be confused by the description of the steps to be undertaken. As a solution, I recommend the maintenance of migration files for each component that requires configuration or settings files. These migration files would keep track of all structure modifications that took place for the corresponding configuration/settings files between different HelioScan revisions (i.e. on a finer-grained level than releases) in a machine-readable fashion. Components would contain a `migrate` method that reads in the migration file and automatically performs all necessary modifications to existing configuration or settings files. The user would only get involved if the

---

[50]These components are usually mentioned in the blog entry accompanying a new HelioScan release, see `http://www.helioscan.org`.

Figure 2.22: HelioScan version updates. The subversion trunk tracks the continuous further development of HelioScan including all components. At specific versions, the core development team decides to create a public release, which basically corresponds to a snapshot of the trunk at a specific moment (i.e. it corresponds to a specific revision of the trunk). Each release obtains a release number consisting of three parts. A change of the first part indicates that an upgrade of the LabVIEW version is required, whereas a change of the second part indicates that the structure of configuration or settings files has changed.
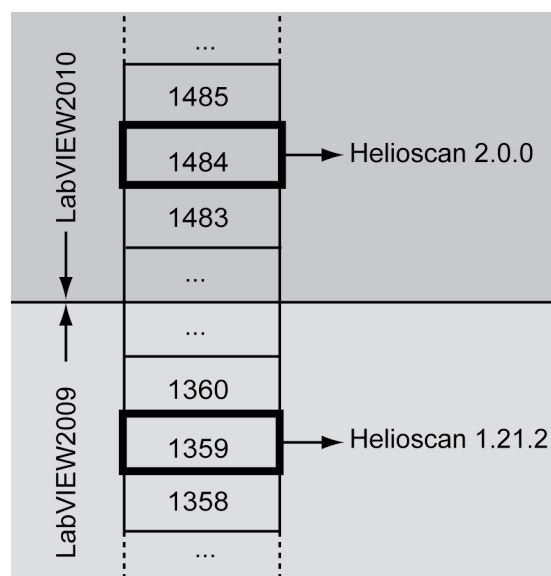
`migrate` method determines that missing information has to be filled in.

Further development

Further development of HelioScan as a collaborative effort faces the following problems.

Complexity   Due to the fact that flexibility always has been the most important design goal, HelioScan features a rather high complexity that can be daunting to people used to monolithic software or not familiar with OOP.

A new developer can familiarise himself with the HelioScan principles either in a *top-down* or *bottom-up* approach. My recommendation is to start bottom-up by implementing a simple new subcomponent (optimally without using the HelioScan component generator mentioned in Section 2.2.3). To do so, no knowledge about interacting TLCs is required and the developer can familiarise himself with the basic features of a HelioScan component step by step. In a next phase, the new developer can start to understand a HelioScan application in a top-down approach. He has to familiarise himself on an abstract level with the purpose of the individual TLCs component types and their way of interacting. After that, he can start to dive down into the specific class hierarchy of the component type he is interested in. In general, it is important to take note of the fact that the HelioScan framework structure may be complex, but that there *is* structure and it follows a very limited number of rules. Once a developer has understood these rules, the framework structure will work in his favour.

Documentation   At the time of writing this thesis, a complete documentation of all existing HelioScan component classes was still missing. Such a documentation both for the perspective of the developer and for that of the user will have to be created during the coming months.

- For developers, the documentation of a component class should describe its purpose, specify the base class from which it inherits, list the triggers it responds to including the corresponding reaction (in the case of TLCs), as well as briefly describe the most important methods (if this information is not already available in the base class). Interface-defining component classes should precisely outline their interface contract.

- For users, information about how the component can be configured and used should be given.

Just like the components themselves, the documentation should be locally managed (i.e. *not* as a central file that holds all the documentation for the whole HelioScan). A possibility would be to maintain an individual PDF file per class that is stored in the corresponding component project folder and is maintained by the responsible developer. However, I would recommend that documentation should be provided online, optimally via the already existing wiki[51]. In that case, each component would have its own wiki page that could be maintained by more than one person (but with the component lead developer as a responsible). The wiki page would allow comments and discussions by both developers and user (e.g. questions and answers, problems encountered etc.). It would also allow the integration of hyperlinks pointing to the wiki pages of other components or the explanation of procedures by means of embedded webcast videos.

Man power   Having enough qualified and committed man power is clearly a key criterion determining whether HelioScan will prosper or disintegrate. For HelioScan to stay a project that is continuously perpetuated rather than splitting up into several poorly maintained programs (see Section 2.1.1), it is of tremendous importance that it does not depend on a single person, but rather that a team of several experienced developers familiar with the HelioScan framework form a core team. This core team would be responsible for further development at the framework level, the coordination of bug fixing, testing, creation of releases and documentation. HelioScan core team members should be enthusiastic about the HelioScan project (i.e. not only see it as a means but also as an end), dedicate a major fraction of their work-time on it, possess an engineering mentality and quality awareness, and have strong skills in structured programming and significant theoretical knowledge in software engineering.

Usability

In the introduction of this chapter, usability was mentioned as one of the key requirements for HelioScan (Section 2.1.1). Here I want to discuss two usability-related issues of HelioScan that can still be improved.

Configuration   HelioScan is not a ready-made software that can be started right after downloading. Rather, a combination of components has to be configured to assemble an ap-

---

[51]http://www.helioscan.org

plication suiting the user's needs. This configuration process can be difficult for newcomers as it includes many individual steps. Specifically, the process has to occur bottom-up: all subcomponents of a superordinate component have to be configured before the latter can be configured itself. A configuration wizard simplifies this process significantly, especially for the inexperienced user. However, all of the configuration data still has to be entered manually even though a significant part of it is the same in most applications. In order to further simplify this process, it would make sense to provide template configuration files—either individually for each component or as complete collections covering several components and targeting a specific application. The configuration wizard would still be executed, but many of the configuration data would already be filled in and the user just has to verify and complete it.

Speed   Speed has a major impact on the usability of a data acquisition software. If the sampling rates required for a measurement cannot be handled by the software, effectiveness is affected. If the software reacts slowly to user inputs or needs a lot of time for central operations like start-up, saving or loading files, user satisfaction is affected. Even on the contemporary computer hardware used to run HelioScan, such speed problems still exist. The architecture of HelioScan has been designed with the major goal of combinatorial flexibility and easy extensibility. Some of the design choices made with these goals in mind cause a significant overhead that decreases speed. However, it can be expected that despite of this trade-off, speed optimisations are still possible without significantly decreasing flexibility and extensibility. Especially when it comes to the speed of processing acquired data, gains are expected from identifying and tackling the major bottlenecks[52]. Further approaches to deal with speed problems are discussed in the outlook section below (Section 2.3.3).

2.3.3   Outlook

Using the new FlexRIO system

Due to the architecture of HelioScan based on the different TLCs running in parallel, a HelioScan application can make use of the multi-core architecture of current CPUs. In addition, for applications employing an FPGA module, some computation can be outsourced from the setup PC. An overflow of the FPGA-to-PC transfer buffer has been encountered with the PXI FPGA module we used (PXI-7813R), especially when acquiring at high sampling rates. I think that in the future this problem can be overcome by using one of the new FlexRIO systems from NI[53]. In a FlexRIO pilot system we implemented recently, the FPGA module harbours 512 MB of random-access memory (RAM), which is enough to store several high-resolution images. Hence, it will be possible to perform the image assembly process

---

[52]The LabVIEW *VI Analyzer* is expected to be a powerful tool in the search for bottlenecks and the most time-consuming VIs.

[53]A FlexRIO system is a combination of a special FPGA module and an adapter module that can be flexibly chosen to perform on-board analogue or digital data acquisition.

directly *on the FPGA*. Due to the higher number of direct memory access (DMA) channels provided by PXI express (PXIe) systems, it is also not necessary anymore to perform multiplexing for multi-channel acquisition. Rather, up to 16 target-to-host FIFO buffers can transfer data simultaneously to the setup PC. In the case of limited computational power of a single FPGA module, the FlexRIO generation of FPGA modules allows peer-to-peer data streaming from one module to another[54]. A further advantage of the new FlexRIO FPGA modules is their external clock input, which could allow the digitising process to be clocked by the pulsed laser used in 2PM. This would ensure a constant number of laser pulses per pixel, thus eliminating a noise source present in the current system.

The FPGA module is well-suited for outsourcing simple computation close to I/O processes. More complex algorithms will still be performed on the setup PC itself. An additional aspect not to be neglected is that the key feature of HelioScan is its combinatorial flexibility. While the PC-hosted part of HelioScan dynamically assembles at run-time from individual components, an FPGA VI has to be compiled before run-time. As a consequence, for each distinct combination of functionalities that is required by a user, a corresponding FPGA VI would have to be programmed in advance. Combinatorial flexibility could be realised by combining several FPGA modules, each downloading at run-time a certain FPGA VI and acting in principle like a hardware-based TLC. However, this approach would be rather expensive at current FPGA prices[55].

Distributed computing and distributed experiments

Apart from the above-mentioned outsourcing of certain simple but highly repetitive computation to an FPGA module, a HelioScan application runs on a single computer. For several reasons one can argue that the HelioScan component architecture should be extended so it becomes possible to run a single HelioScan application instance in a distributed fashion on several computers simultaneously:

- Certain applications may bring about a computational load that cannot be handled by a single computer alone or is impractical to outsource to an FPGA. Examples include advanced on-line analysis or visualisation schemes. Currently, each TLC component type is present as only one instance in a HelioScan application. For future applications such as multi-area imaging, it might be necessary that certain TLC component types are present in several instances simultaneously (e.g. multiple ScanHead instances controlling different trajectories at the same time), which might in turn exceed the capabilities of a single computer.

- Scenarios would become possible where an experiment is performed by several researchers in a truly collaborative approach. While the space available close to the microscope may be limited and not allow more than one or two persons being present, an unlimited number of researchers could plug into the HelioScan application with

---

[54]http://tiny.cc/ptpStreaming

[55]Currently, an NI PXIe-7962R module is available for an off-the-shelf price of roughly 7000 CHF if academic or original equipment manufacturer (OEM) discount is not taken into account.

their own computers. Given enough network bandwidth, they would not even have to be physically present at the same institute. Given that *in vivo* 2PM is currently only performed in rich countries due to the expensive equipment required, this could in principle allow scientists lacking the money for an own 2PM setup to take part in collaborations.

- Users might want to connect to third-party software or to their own data processing routines written in programming languages other than LabVIEW. Also in this case, these other programs might run on a separate computer for performance reasons.

In the envisioned scenario, a computer can execute a HelioScan application implementing one or several data processing pipelines according to the observer principle outlined in Section 2.2.1, but with the novelty that data sources and sinks do not necessarily have to run on the same computer (compare to [263]). This would for example allow to perform high-speed data acquisition (by a DAQ component instance) and streaming of raw-data to disk (by a dedicated DataCollection instance) on one computer, while images are assembled (by an ImageAssembler instance), displayed (by a Display instance) and stored (by an instance of a different DataCollection component) on a second computer. While one person is performing the experiment on-site using these two PCs, another researcher located in another country and dedicated to on-line analysis sits in front of a third PC on which HelioScan is running with a DataCollection, a Display and several different Analyser instances that have registered as remote observers (clients) at the host ImageAssembler instance running on the setup PC.

Workflow improvements

In addition to realising these on-line data processing pipelines, the off-line approach based on copying and processing image files should also be advanced to allow a smoother workflow, better reproducibility of the performed data processing steps and easier interaction between collaborators. For this purpose, a DataCollection component could be implemented that interfaces directly to an microscopy image database, such as the OMERO platform [206] developed by the Open Microscopy Environment (OME) consortium[56]. Along this line, it would also make sense to extend the OME-XML by a StructuredAnnotations schema dedicated to *in vivo* brain imaging in order to store metadata describing the experiment parameters and subsequent off-line analysis steps.

2.3.4   Conclusion

During the next couple of months, the primary goal should be to tackle the problems discussed in Section 2.3.2 with a special focus on usability. Furthermore, I recommend the active promotion of HelioScan in the *in vivo* 2PM community in order to increase the level of awareness of its existence and strengths.

---

[56]http://www.openmicroscopy.org

In addition, basic HelioScan features should be advanced as suggested in this outlook section. Even if a first distributed experiment is performed merely as a proof of principle, it could allow new levels of collaboration that so far have only been known to very few scientific disciplines such as astronomy or particle physics [58]—but not neuroscience.

2.4   Contributions

Camera-based imaging mode   I designed all required HelioScan components. Implementation was performed together with Maurice Göldi.

IOS imaging mode   I designed the architecture for the stand-alone IOS imaging set-up together with Helge Johannssen, Fritjof Helmchen and Stefan Giger. All electronics were designed and built by Hansjörg Kasper, whereas mechanical components were built by Stefan Giger. The LED ring for the second generation of the IOS imaging system was designed by Hansjörg Kasper, who built it with Stefan Giger. The original stand-alone IOS imaging software I programmed with minor contributions from Werner Göbel. I designed all required HelioScan components, whereas implementation was performed together with Maurice Göldi. I modified a stimulation and image acquisition protocol kindly provided by Carl Petersen.

Component generator   The HelioScan component generator was implemented together with Markus Ruchty.

3 Post hoc immunohistochemistry

The brain is a tissue. It is a complicated, intricately woven tissue, like nothing else we know of in the universe, but it is composed of cells, as any tissue is. They are, to be sure, highly specialized cells, but they function according to the laws that govern any other cells. Their electrical and chemical signals can be detected, recorded and interpreted and their chemicals can be identified; the connections that constitute the brain's woven feltwork can be mapped. In short, the brain can be studied, just as the kidney can.

David H. Hubel

3.1 Introduction

Cortical information processing relies on the intricate balance of excitation and inhibition in neocortical networks [126], with inhibition playing a crucial role not only for the control of excitatory signal flow but also for synchronisation of neural activity and the generation of rhythmic oscillations [5, 298]. Inhibition in the neocortex is provided by GABAergic interneurons, which constitute around 10 to 20 % of cortical cells and exhibit a remarkable diversity in terms of their morphological characteristics (in particular axonal targeting patterns), electrophysiological properties and molecular composition [192, 261, 35, 79, 94]. Based on these features, many subtypes of GABAergic interneurons have been defined; however, no consensus on a full catalogue of distinct classes has been reached [13, 94]. In addition, little information is available on the *in vivo* activation patterns of particular subtypes, especially during specific behaviours. This lack of information is due to the fact that GABAergic interneurons are sparsely distributed within cortical microcircuits, which makes it difficult to identify and target these cells *in vivo*.

Direct studies of behaviour-related membrane potential dynamics in specific GABAergic subtypes have become possible only recently with the availability of mice expressing fluorescent proteins in genetically-defined neuronal subtypes [221, 198, 275] and with the employment of whole-cell or cell-attached recordings guided to target cells using two-photon laser-scanning microscopy (2PM) [168]. These studies highlighted the functional diversity of the GABAergic population [109, 61, 185]. In addition to electrophysiological recordings, *in vivo* two-photon calcium imaging enables activity measurements in neocortical populations (reviewed in [131, 115, 296]). To distinguish excitatory and inhibitory interneurons, a small number of studies have applied bulk-loading of synthetic calcium indicators to transgenic mice in which all GABAergic neurons express a fluorescent protein [275], revealing for example differences in orientation tuning in visual cortex [260, 162]. Further discrimination of GABAergic subtypes is desirable, and, in principle, can be achieved with two

methods. First, *in vivo* calcium imaging can be performed in mice expressing a fluorescent protein in a particular subset of GABAergic neurons. This promising approach has been taken up only very recently [244, 317]. Second, various subtypes of GABAergic neurons may be discriminated post mortem by means of IHC. For that purpose, cells previously imaged *in vivo* have to be identified in fixed brain slices treated with antibodies against specific chemical markers. Recently, the feasibility of such post hoc IHC for discriminating GABAergic subtypes has been demonstrated in a few studies [296, 220, 162]. However, this approach is just emerging and experimental procedures are not yet satisfactorily established. Therefore, advancing the combination of *in vivo* calcium imaging and post hoc IHC is an important direction for further dissection of neocortical population activity into its different cellular components.

Here, I present post hoc IHC as a valuable method to identify GABAergic subtypes in cortical networks, from which calcium indicator measurements have been performed previously in the living animal. I evaluate the method in terms of post hoc cell identification yield, different antibody stains against calcium-binding proteins and its applicability to tissue labelled with either synthetic or genetically-encoded calcium indicators. I demonstrate spontaneous calcium transients in interneurons of identified subtype. Combining *in vivo* calcium imaging with post hoc IHC opens numerous opportunities for investigating specific activity patterns within local neural circuits.

3.2 Results

3.2.1 Discrimination of excitatory neurons, GABAergic cells and astrocytes *in vivo*

Triple-labelling *in vivo*

To broadly discriminate between excitatory and GABAergic neurons, I first employed *in vivo* two-photon imaging in GAD67-GFP transgenic mice [275], in which GABAergic interneurons express enhanced green fluorescent protein (here simply referred to as GFP). Astrocytes were counterstained by brief application of SR101 to the cortical surface [219]. In addition, cells were unspecifically loaded with the calcium indicator OGB-1 by MCBL (Section 1.4.2; [266]). Using a single excitation wavelength (850 nm), SR101-labelled astrocytes were readily identified in the red detection channel, while both OGB-1 and GFP were visible in the blue and the green channel with the optical settings chosen (see Figure A.4a on page 176 for details about the detector system and Figure 3.1a on page 87 for details about channel bleed-through). Despite this cross-talk, GFP-positive cells could be unambiguously
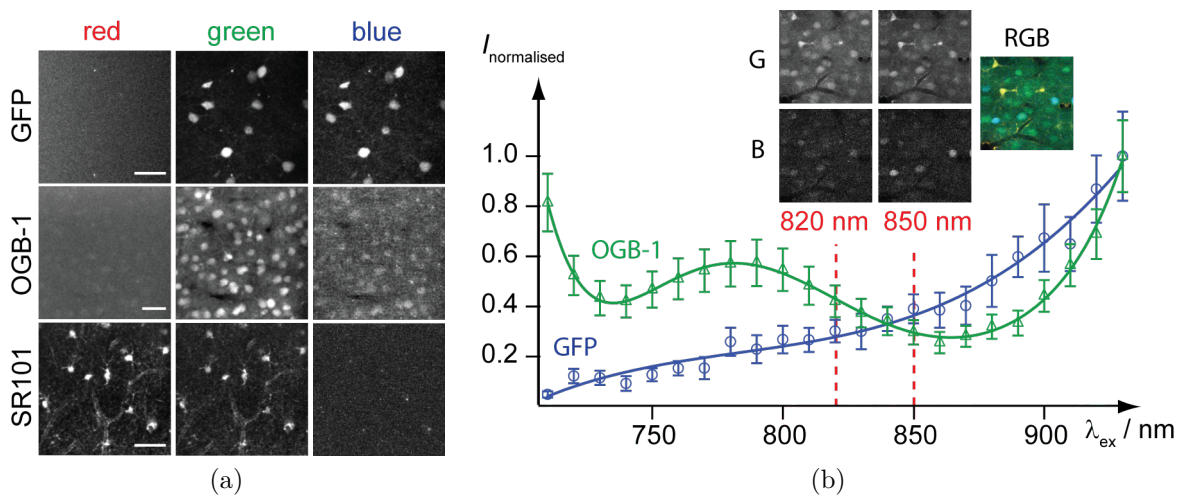
Figure 3.1: Emission and excitation of *in vivo* triple-labelling fluorophores. **(a)**. Separate imaging of the three *in vivo* fluorophores (GFP, OGB-1 and SR101) in three independent experiments with excitation at 850 nm (detector scheme A$_1$ in Figure A.4 on page 176). From [175]. Scale bars: 50 µm. GFP-positive cells (top row) in GAD67-GFP mice were identified by their strong contribution to the blue channel (450-500 nm) but they are also visible in the green channel (500-590 nm). The OGB-1 signal (middle) is strongest in the green channel but also partially bleeds through in the blue channel. SR101-stained astrocytes (bottom) are detected in the green and red channel but are the only cells visible in the red channel (590-650 nm). **(b)** Two-photon excitation spectra of GFP and OGB-1. The measured emission values were compensated for changes in output laser power. Note that due to wavelength-dependent transmission efficiency of the lenses in the microscope, this might not necessarily correspond to constant excitation power at the sample.

identified in triple-labelled populations based on the ratio of fluorescence in the blue and green channel (Figure 3.2b on page 88). In a control experiment, I counted GFP-positive

(a)   (b)
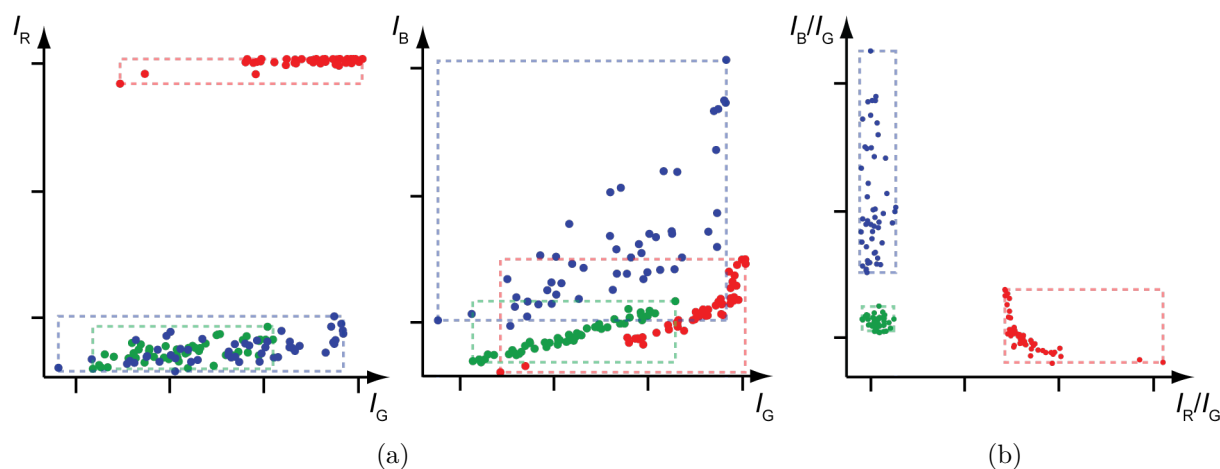
Figure 3.2: Discrimination of GABAergic and non-GABAergic cells *in vivo*. **(a)** These two diagrams show 150 cells (50 astrocytes in red, 50 non-GABAergic neurons and 50 GABAergic neurons). Left: red channel intensity plotted versus green channel intensity; right: blue channel intensity versus green channel intensity. Note that the flat distribution of astrocytes in the left diagram is due to saturation of the red channel's ADC. **(b)** This diagram shows the same cells as in (a), but now with the channel intensity ratio blue:green plotted versus the channel intensity ratio red:green. Here, each cell group forms a distinct cluster, which is either horizontally or vertically clearly separate from the other two clusters.

cells before and after MCBL of OGB-1 and found that $100\,\%$ of GFP-positive cells (63 of 63 cells) could be identified. Thus, this triple-labelling approach enabled discrimination of astrocytes, GABAergic cells and excitatory neurons *in vivo* (Figure 3.3a on page 89).

In vivo two-photon calcium imaging

In all three cell types, spontaneous calcium transients could be observed (Figure 3.3b on page 89). Astrocytes showed slow fluctuations of the OGB-1 fluorescence traces consistent with previous reports [137, 297, 219]. In identified excitatory neurons, individual and compound calcium transients were evident with sharp onsets, $10\,\%$ to $50\,\%$ $\Delta F/F_0$ amplitude and slow exponential decays over a few hundred milliseconds (Figure 3.3b on page 89), which is consistent with action potential-evoked calcium transients [163, 101, 266, 313, 162]. In contrast, spontaneous calcium transients in GABAergic interneurons were more variable. Some cells displayed individual, sharp calcium transients similar to excitatory neurons while others showed rather slow fluctuations of the OGB-1 fluorescence signal (Figure 3.3b on page 89). These differences in calcium transient shape might reflect differences in electrophysiological and calcium buffering properties between subtypes of GABAergic interneurons [87]. The discrimination of these subtypes and their functional signals *in vivo* will be essential for understanding local microcircuit dynamics. Therefore, I set out to devise a method to further dissect cell types within neuronal populations characterised by *in vivo* two-photon calcium imaging.

(a) $\lambda_{ex} = 850$ nm (GFP/OGB-1/SR101) (b) $\lambda_{ex} = 850$ nm
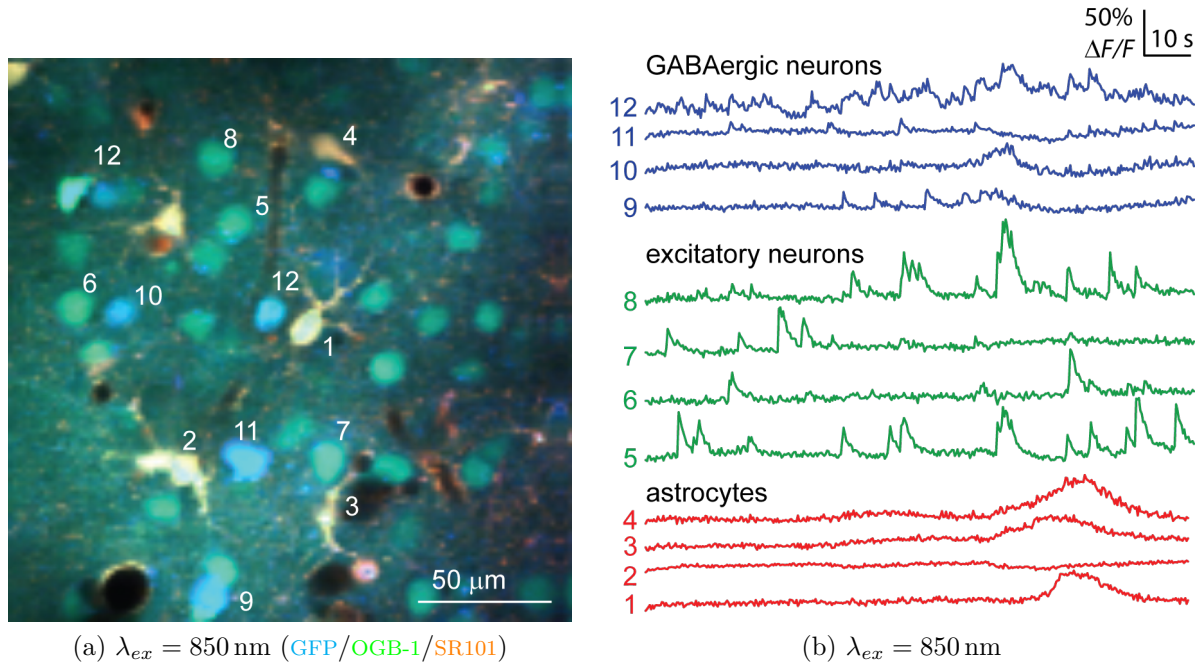
Figure 3.3: Triple-stain enabling calcium imaging of identified GABAergic neurons *in vivo* (from [175]). **(a)** Overlay of simultaneously acquired two-photon images in all three spectral channels in an experiment in which OGB-1 and SR101 labelling were applied to the neocortex of a GAD67-GFP mouse. Astrocytes (yellow), excitatory neurons (green) and GABAergic neurons (blue) can be readily discriminated with this *in vivo* triple stain. **(b)** Spontaneous calcium transients for all three distinguishable cell types for the example cells numbered in (a).

3.2.2 Identification of cells previously imaged *in vivo*: in coronal sections

My goal was to establish subtype discrimination within the GABAergic population by IHC against neurochemical markers. For this purpose, the brain has to be perfusion-fixed and cut into slices. In principle, coronal, parasagittal, transverse or surface-tangential slices may be used (see Section 3.3). I decided to start by exploring coronal[1] sections.

Finding the relevant slices

In a first step, I aimed at identifying those coronal brain slices that contained a particular cortical volume previously imaged *in vivo* (Figure 3.4 on page 90). For this purpose, I used GAD67-GFP mice without extra labelling. In addition to an overview camera image of the brain surface vasculature, a high-resolution two-photon reference image stack was acquired *in vivo*, which defined the volume of interest (Figure 3.4a on page 90). After perfusion fixation of the brain, a large-field-of-view surface map of the whole craniotomy

---

[1]In the context of this thesis, the term *coronal* is used according to the homologous sections of the human brain, i.e. perpendicular to the rostrocaudal axis.

(a) *in vivo*   (b) fixed tissue
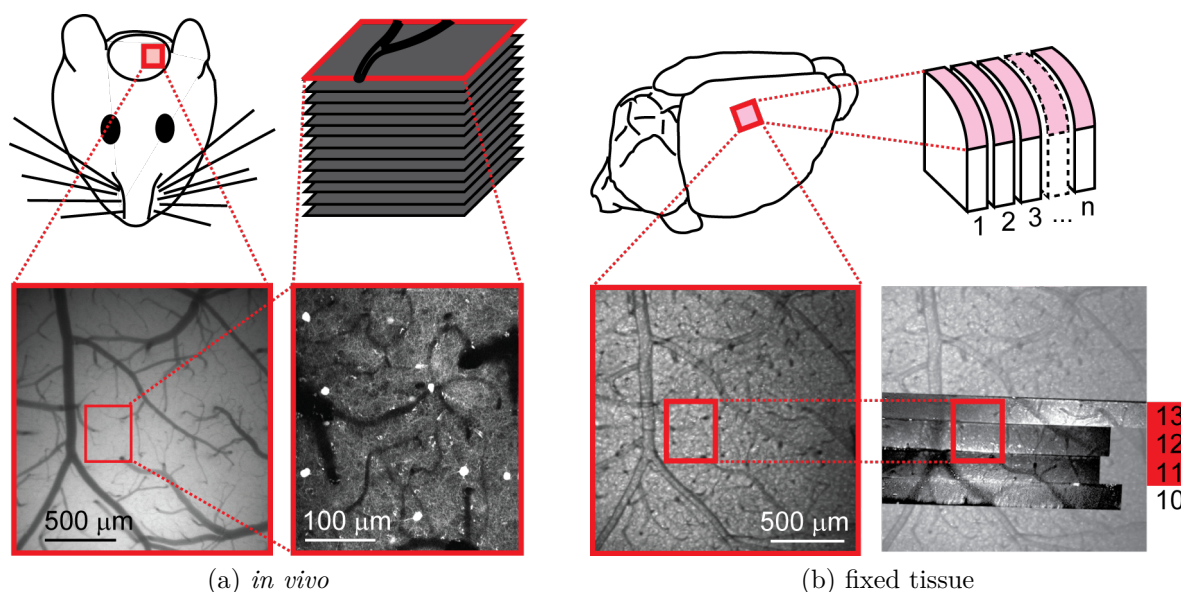
Figure 3.4: Preparation of fixed coronal brain slices and registration to the volume of interest (from [175]). **(a)** Left: *in vivo* large-field-of-view camera image of the blood vessel pattern at the cortical surface within a craniotomy in a GAD67-GFP mouse. Right: high-resolution reference stack acquired *in vivo* with the two-photon microscope from the region indicated by the red box on the camera image, revealing the sub-population of GFP-expressing cells. **(b)** Left: large-field-of-view two-photon image of the cortical surface originally below the craniotomy, captured after perfusion fixation. This additional reference map of the surface blood vessels complements the camera reference map acquired *in vivo*. Right: After coronal sectioning of the fixed brain, two-photon image stripes acquired from the pial surfaces of slices were registered to, and overlaid on, the two-photon blood-vessel reference map. In this example, slices 11 to 13 were identified as being the relevant ones because they cover the volume contained in the *in vivo* two-photon reference image stack shown in 3.4a (marked by a red box)

area was obtained with the two-photon microscope, with larger blood vessels still clearly visible (Figure 3.4b on page 90). A tissue block containing the craniotomy area was then cut into coronal slices of 140 μm to 200 μm thickness using a cryostat. The resulting slices were individually mounted between two cover slips and positioned vertically under the two-photon microscope to image their segment of pial brain surface (Figure A.6 on page 178). By matching the surface blood vessel pattern of each slice against the large-field-of-view surface map, I was able to identify the slices that contained the volume of interest (Figure 3.4b on page 90). Only these slices (typically two to three) were selected for further processing.

Relocating the same cells

In the next step, I used GAD67-GFP mice to re-identify in fixed coronal sections those cells that were previously imaged *in vivo*. Slices selected according to the procedure described in the previous paragraph were mounted horizontally and high-resolution two-photon image stacks were acquired in coronal view (XZ-view). Fields-of-view corresponded to the *in vivo* reference image stack. I employed tissue clearing with a sucrose gradient [285], which

allowed me to acquire image stacks throughout the entire slice thickness (up to 200 μm) without a significant loss in imaging quality. In contrast to tissue clearing with Murray's clear [73], sucrose clearing preserved cell-specific localization of GFP fluorescence.

(a) *in vivo* (b) brain slices (c)

(d) *in vivo* (e) brain slices (f)
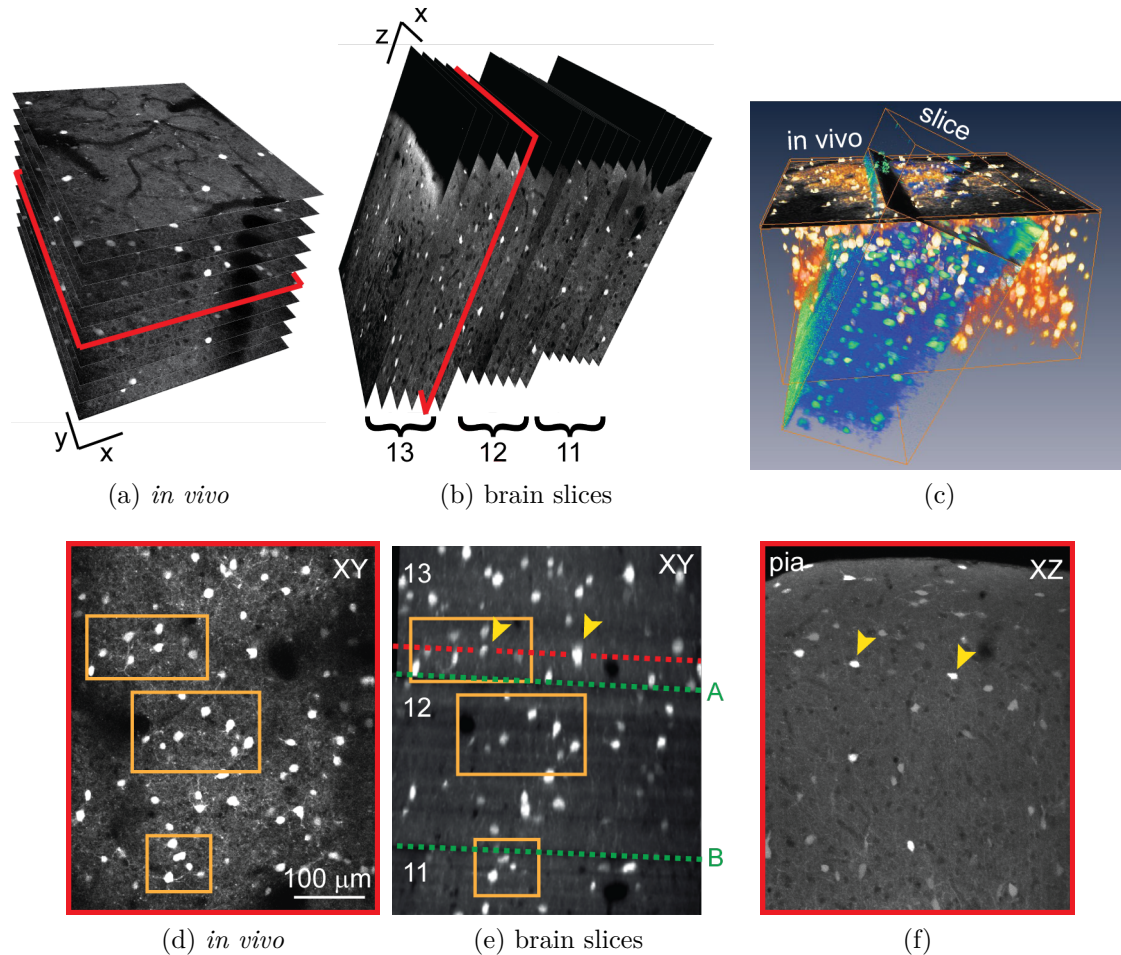
Figure 3.5: Identifying the same GABAergic neurons in images acquired *in vivo* and from coronal brain slices (adapted from [175]). **(a)** High resolution reference image stack acquired *in vivo* from a GAD67-GFP mouse. **(b)** Image stacks acquired from coronal slices covering the volume of interest (the same slices as in Figure 3.5b on page 91). **(c)** Three-dimensional composite view of the *in vivo* stack and a single slice stack following rotation fitting and alignment. **(d)** Example XY-view from the marked frame in the *in vivo* reference stack in (a). **(e)** XY-view reconstructed from several adjacent slices showing the same area as in (d). Slice borders are indicated by green dashed lines. Matching the same GFP-expressing neurons in the *in vivo* reference stack and in the brain slices is possible; orange boxes highlight example constellations of cells that are easily recognised in both images. The dashed red line corresponds to the frame shown in (f) (arrow heads indicating corresponding cells). **(c)** Example coronal XZ-view from the marked frame of slice 13 stack in (b).

For slice cutting, the sectioning plane was oriented as perpendicularly as possible to the pial brain surface. Nevertheless, the *in vivo* reference image stack and the 90°-rotated image stacks acquired from the corresponding coronal slices were usually slightly tilted

with respect to each other (Figure 3.5c on page 91). Therefore, the image stacks from each coronal slice were fitted to the *in vivo* two-photon reference stack by applying linear transformations (rotating, scaling and translating). Surface and descending blood vessels served as key landmarks. In spite of slight non-linear tissue distortions, cells imaged *in vivo* could readily be identified in the image stacks from brain slices following this alignment procedure. For comparing cellular staining patterns, it was beneficial to view both stacks (obtained *in vivo* and in fixed slices) in either XY- or XZ-view. Local neighbourhood relations between cells in 3D space (e.g. characteristic groups of cells, proximity to prominent blood vasculature features) facilitated the identification of the exact same cells in the two data sets (Figures 3.5d and 3.5e on page 91).

I quantified the fraction of GFP-positive cells that could be re-identified in brain slices in this manner. The overall percentage of manually matched cells depended on the time invested. Matching rates of around 80 % could be readily achieved with about 20 h of work (one person) for a cortical volume of about 300 µm to 400 µm side length containing approximately one thousand GFP-expressing GABAergic neurons (647, 826, 1056 and 1039 cells, respectively; on average about one cell per minute). With more time invested (around 50 h), cells in more difficult regions could also be matched. The achieved matching rates increased to between 95 % and 100 % for similarly sized volumes. Essentially, all GFP-positive cells could be identified in the middle of the brain slices, while at the cut surface a few cells were either lost or could not be unambiguously identified (Figure 3.6a on page 93). However, even close to the cut surface, high matching rates (>95 %) were reached (Figure 3.6b on page 93). This analysis demonstrates that large cell populations imaged *in vivo* can be re-identified almost completely in coronal slices following brain fixation.

3.2.3 Identification of cells previously imaged *in vivo*: in tangential sections

Finding the relevant slices

Tangential sectioning is a sensible alternative to coronal sectioning (see Section 3.3.2 for a discussion of advantages and disadvantages). In the following paragraphs, I describe a procedure that facilitates the matching between *in vivo* and fixed tangential slices at the volume and cell level. The key objective is to obtain sections that are as parallel as possible to the *in vivo* imaging plane. In a recently published study, this is achieved by sectioning the whole mouse head including skull after aligning it based on the head plate to which it is still glued. Only once the head plate is oriented perfectly parallel to the cryostat blade the former is removed and sectioning started [162].

The procedure described here similarly makes use of the head plate as an alignment guide. The frozen head was sawed parallel to the plate. Then, the upper half of the head was glued to a cryostat sample socket (Figure A.5b on page 178). The head plate was removed, and the head embedded and sectioned parallel to the original orientation of the head plate. Like this, the obtained sections were very well aligned to the frames of the *in vivo* reference image stack.
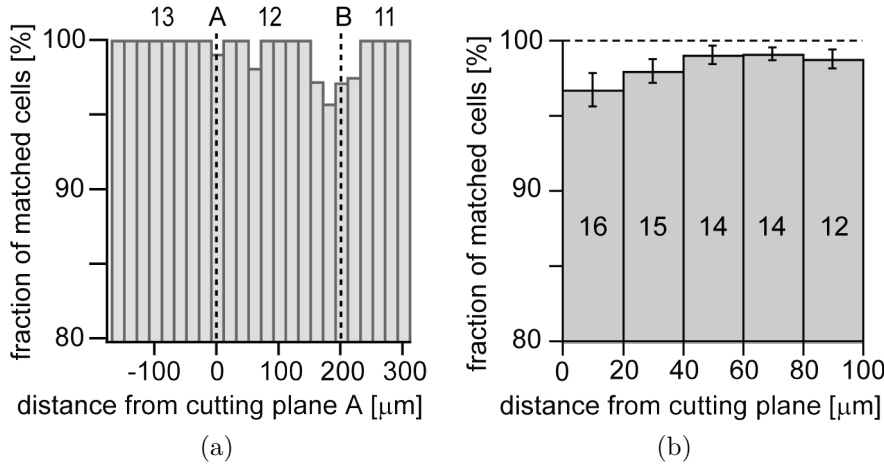
Figure 3.6: Cell matching efficiency for coronal brain slices (from [175]). **(a)** Fraction of matched GFP-positive cells analysed in 20 µm-bins for the single example volume shown in Figure 3.5e on page 91. Slice borders are indicated as dotted lines. **(b)** Pooled analysis of the average fraction of matched cells as a function of distance from the closest cutting plane. The number of slices considered is specified for each bin (slices from 4 mice; error bars indicate SEM)).

(a)

(b)

After sectioning, the slices of interest have to be selected using a similar approach as that for coronal sections (compare Section 3.2.3). The overall procedure is as follows:

1. *In vivo*: a high-resolution camera image of the brain surface providing a map of the surface blood vessels is acquired.

2. After perfusion fixation but before sectioning, a high-resolution, low magnification (4x objective) surface reference map of the brain surface inside the craniotomy is acquired using the two-photon microscope. This second surface reference map complements the *in vivo* camera image because it emphasises the locations where surface blood vessels vertically descend (visible as dark spots; Figure 3.7b on page 94).

3. The head is tangentially sectioned as described in the paragraph above.

4. Using the same settings as in step 2, an overview image of the horizontally aligned top-most section is acquired. Using surface blood vessels as clues, it is then registered to the merged surface reference map acquired in steps 1 and 2 (Figure 3.7c on page 94).

5. If the slice already contains part of the volume-of-interest, an image stack of this region is acquired with the 20x objective. This gives information about up to which depth the volume-of-interest is already covered. Furthermore, it facilitates fast fine-alignment of the slice when re-imaging after immunostaining, thus minimising fluorophore bleaching.

6. Steps 4 and 5 are repeated until the whole volume-of-interest is completely covered and assigned to individual slices. Since slices get bigger with increasing depth of the sectioning plane, after a certain depth they might not fit anymore into a single

(a) *in vivo*   (b) post mortem

(c) slice 1   (d) slice 2   (e) slice 3
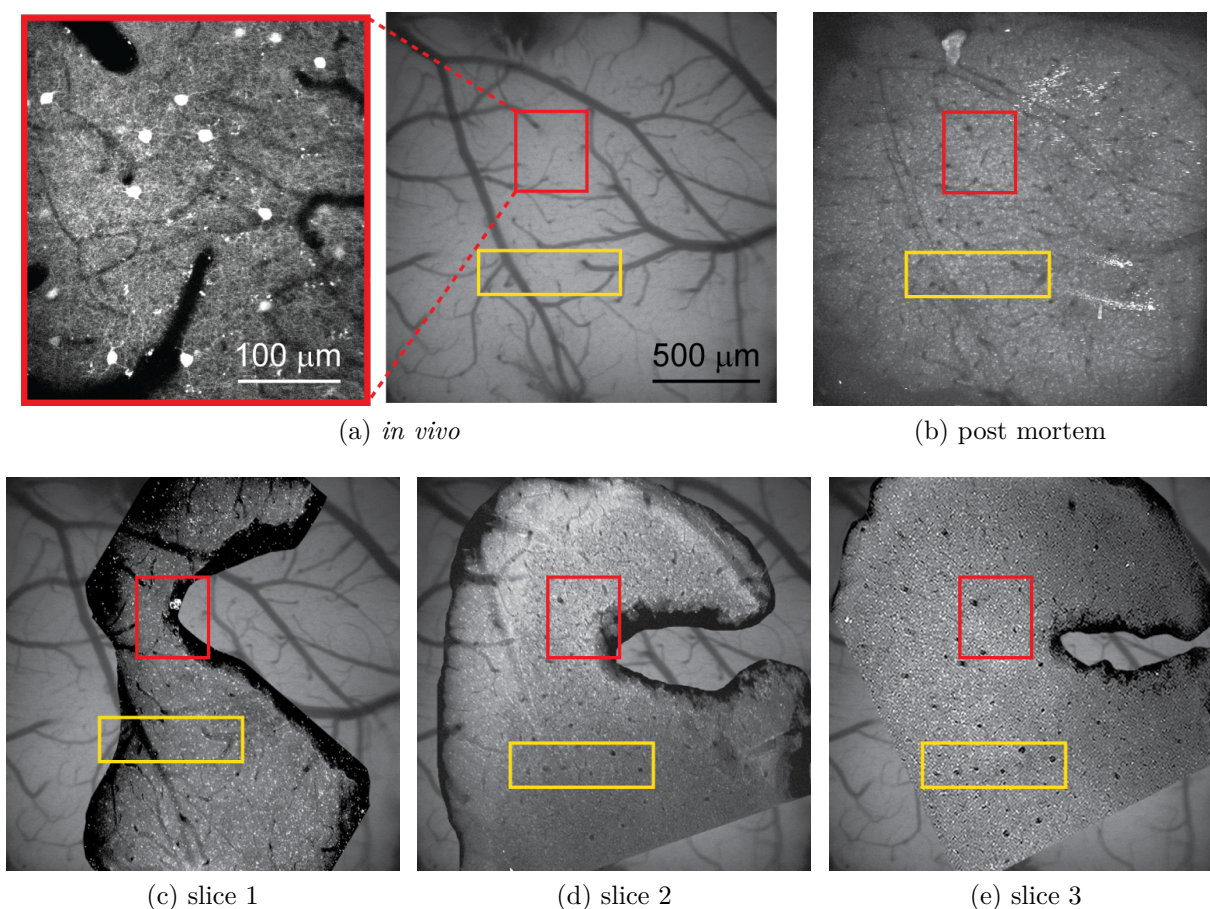
Figure 3.7: Registering and selecting tangential slices ($100\,\mu$m thick in this experiment). **(a)** Left: Topmost frame of reference map of volume-of-interest acquired *in vivo*. Right: *In vivo* camera reference image acquired from craniotomy. **(b)** Two-photon surface reference map acquired after perfusion fixation. This image emphasises descending blood vessels as dark spots and thus complements the *in vivo* reference map obtained with the camera. **(c)**-**(e)** First three tangential slices registered to the blood vessel pattern in the camera image and to each other. While the first two slices contain surface blood vessels that can be registered to those in the camera image, the third slice has to be registered using characteristic cross-section patterns of vertically descending blood vessels (marked by yellow boxes). Note that in the experiment shown, the brain surface got damaged during or after perfusion fixation (see crevice on the right side of the slices). Thus, it is highly important to protect the brain surface during the whole procedure until sectioning is performed.

low-magnification image stack due to a restricted field of view. Landmarks such as blood vessel cross-sections or characteristics of the slice border may then be used to guide stack acquisition to the most promising region. While for the first slice, surface blood vessels are most helpful as landmarks for registration, subsequent sections rely on both surface blood vessel fragments contained in the stripe of brain surface surrounding each slice and on the cross-sections of vertically descending blood vessels. At a certain depth, the surface contained in the slice border is not contained in

the craniotomy anymore and registration has to rely entirely on blood vessel cross-sections (Figure 3.7e on page 94).

Relocating the same cells

Stacks acquired in step 5 of the procedure outlined in the previous paragraph (or, accordingly, at the same place and orientation *after* IHC has been performed) can be readily used for assigning cells to the *in vivo* reference image stack. In a pilot experiment performed, the two image stacks were already intrinsically very well aligned such that no further rotation-fitting was required (Figure 3.8 on page 95).

3.2.4 Subtype discrimination of GABAergic neurons by triple immunostaining

After the successful identification of individual GABAergic neurons in fixed brain slices, I next aimed to discriminate subtypes by IHC. First, I decided on a suitable set of antibodies. In general, antibody combinations can be flexibly chosen as long as antibodies do not cross-react, permit independent signal acquisition and the resulting staining sufficiently penetrates the tissue. Here, I chose three classical interneuron markers that are commonly used to define multiple subtypes, namely the calcium-binding proteins PV, CR and CB [160, 192, 79]. Primary antibodies were taken from different host species and appropriate fluorescence labels for secondary antibodies were selected to enable multi-colour IHC (Table A.2 on page 180; Figure A.7 on page 180).

A critical issue is how well antibodies penetrate into slices because the diffusion of high-molecular antibodies is hindered by the extracellular matrix. To test antibody penetration, I analysed the depth-dependence of the antibody stain and found an exponential decline of intensity with distance from the slice border (space constant 25 μm in the case of the anti-PV stain; Figure 3.9a on page 96). I chose 140 μm thick slices, which enabled sufficient staining of cell bodies in the slice center (Figure 3.9b on page 96; Figure 3.10 on page 96)

(a) *in vivo*   (b) post mortem
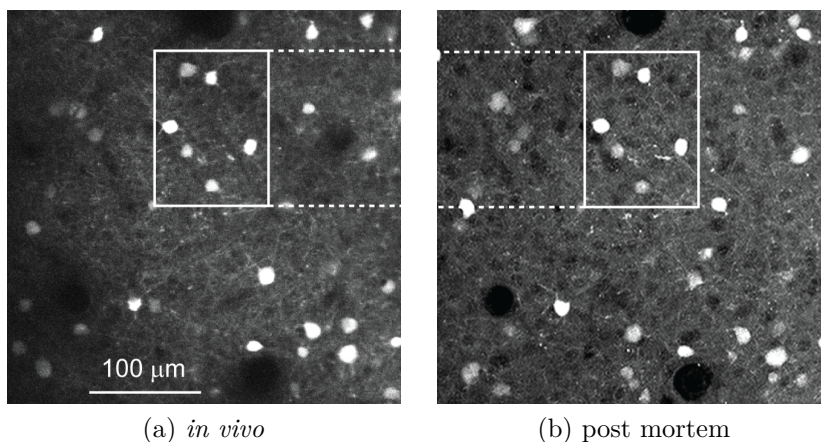
Figure 3.8: Identifying the same GABAergic neurons in images acquired *in vivo* and from tangential brain slices. **(a)** Part of the *in vivo* image stack shown in Figure 3.7a on page 94. **(b)** Corresponding area in slice 3 shown in Figure 3.7d on page 94. Note that *no* rotation-fitting has been performed on the acquired image stack. A characteristic cell constellation is marked with a white box.
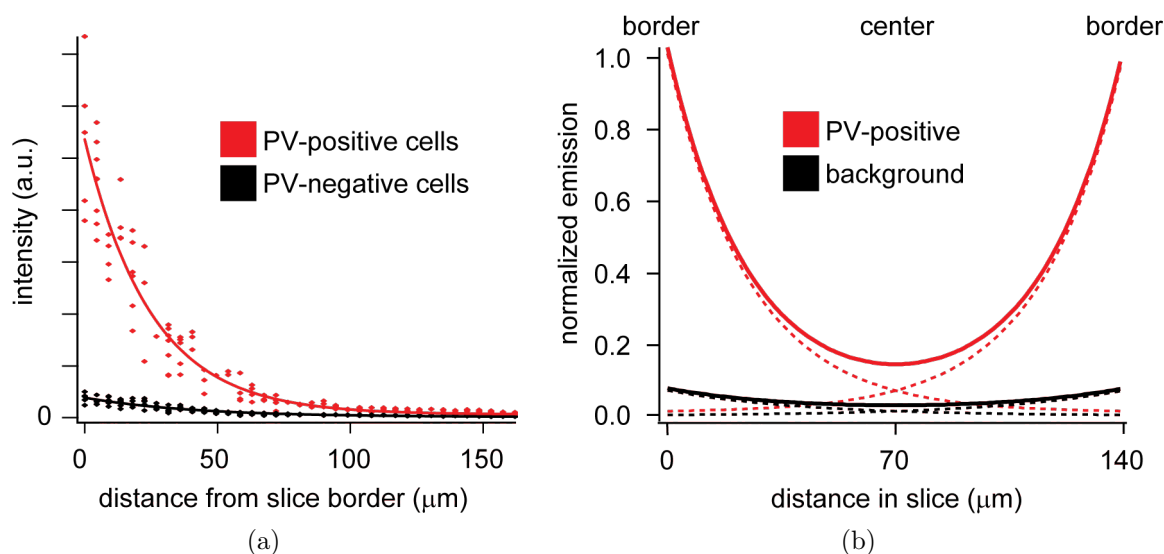
Figure 3.9: Antibody penetration into coronal brain slices (from [175]). **(a)** Intensity of anti-Parvalbumin (PV) staining decreases exponentially with distance from cut surface but positive and negative cells can still be distinguished at depths up to 100 μm. **(b)** Predicted penetration profile for 140 μm thick slices with antibodies penetrating from both sides (solid lines: effective stain; dashed lines: contribution from each side). Anti-PV-staining is clearly above background staining in the slice center.

while providing enough blood vessel surface pattern for convenient slice selection.
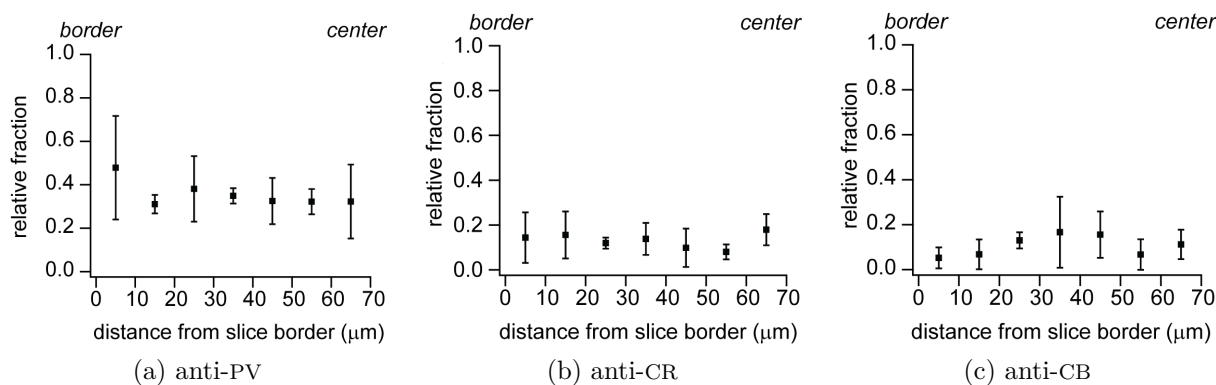
Figure 3.10: Labelling efficiency for coronal slices (from [175]): abundance of cells identified as PV-, CR- and CB-positive, respectively, as a function of distance from the slice surface for 140 μm thick slices (relative to GFP-positive cells in L2/3 of GAD67-GFP cortical slices; mean ± SD; $n = 4$ slices). No significant depth-dependence was observed ($P > 0.3$; one-way ANOVA), proving that antibody penetration is sufficient for this slice thickness. **(a)** anti-PV stain. **(b)** anti-CR stain. **(c)** anti-CB stain.

Following antibody staining, I acquired stacks of two-photon images from horizontally mounted coronal slices using 3-channel fluorescence detection. The red anti-PV stain marked a subset of GFP-positive cells, all of which were clearly visualised using 850 nm excitation wavelength. Switching the excitation wavelength to 720 nm, the green anti-CR

and blue anti-CB stain could be well discriminated because negligible GFP fluorescence was excited at this wavelength (Figure 3.11 on page 98). With this approach, I was able to distinguish cells that were negative for all three markers and those that contained one or several markers (Figure 3.12 on page 98).

In principle, the sequence of *in vivo* imaging, slice cutting, slice selection, immunostaining and cell matching can be applied to large volumes, limited only by the *in vivo* penetration depth of the two-photon microscope. In my experiments, I was able to cover volumes as large as the supragranular part of a whole barrel column, covering L1 through L2/3 with nearly one thousand GABAergic interneurons (874 and 842, respectively; Figure 3.13a on page 99). For two such data sets I analysed the depth-dependent distribution of different interneuron subtypes (Figure 3.13b on page 99). GABAergic cells in L1 nearly exclusively were negative for all three markers. PV-positive cells were more abundant with increasing depth, approaching around 45 % of the GFP-positive cells at 250 μm depth. CR-positive cells were sparsely found in L1 but constituted about 10 % to 20 % throughout L2. CB-positive cells started to appear at 50 μm to 100 μm depth and accounted for 7 % to 14 % of all GABAergic cells down to 250 μm, roughly half of this fraction in co-localization with PV. Overall, this depth-dependent marker distribution in superficial cortical layers is in accordance with previous studies [113, 114, 275].

3.2.5 Combination of *in vivo* calcium imaging with post hoc immunostaining

Next, I applied post hoc IHC to interneurons for which spontaneous calcium transients had been previously measured *in vivo*, similar to those shown in Figure 3.3 on page 89. The additional *in vivo* stains of SR101 (red) and OGB-1 (green) did not interfere with post hoc antibody staining. SR101 was washed out in fixed slices while OGB-1 remained as a diffuse background of a much lower intensity than the green anti-CR stain (Figure 3.14c on page 100). Thus, it was possible to assign the CaBP expression pattern to spontaneous calcium traces (Figure 3.14d on page 100) by identifying the same set of GABAergic cells in fixed slices following triple-staining IHC. The calcium transients recorded in GABAergic neurons varied in their temporal characteristics, confirming the results of previous measurements (Figure 3.3b on page 89). PV-positive interneurons typically showed relatively slow and low-amplitude fluctuations of the calcium signal. CR-positive cells displayed fewer and sharper calcium transients while triple-negative interneurons tended to exhibit larger-amplitude and superimposed calcium transients. However, attempts to reveal significant differences among the spontaneous calcium transients (e.g. with respect to frequency, amplitude or shape of transients) that would correspond to the post hoc classification obtained by IHC remained inconclusive. Nonetheless, my experiments demonstrate that it is possible to relate functional signals measured in local populations under *in vivo* conditions to the neuronal subtypes as identified by post hoc IHC.

Figure 3.11: Superficial cortical layers in a coronal slice stained for PV, CR and CB (from [175]). Different stains can be excited at different wavelengths. **(a)** At 850 nm excitation, GFP-positive cells are clearly visible as blue cells while PV-positive neurons appear orange. **(b)** At 720 nm excitation, the three antibody stains for PV, CR and CB are visible in the red, green and blue channel, respectively.

(a) exc. 850 nm (GFP/PV)   (b) exc. 720 nm (PV/CR/CB)

(a) GFP+PV+CB-   (b) GFP+PV+CR-CB-   (c) GFP+PV+CB-   (d) GFP+PV+CB-   (e) GFP+PV+CR-CB-

Figure 3.12: Examples of GABAergic interneurons with different combinations of marker proteins (from [175]). Coronal views from fixed slices; upper left insets: *in vivo* images of the same, GFP-expressing cells. Scale bars: 20 μm. **(a)** PV-positive GABAergic cell with multipolar dendritic morphology, presumably a basket cell. **(b)** CR-positive cell with typical bipolar dendritic morphology [192]. **(c)** CB-positive cell. **(d)** Neuron positive for both PV and CB. **(e)** Triple-negative GABAergic cell.

3.2.6 Post hoc immunostaining of cortical neurons expressing a genetically encoded calcium indicator

Recently, improved genetically-encoded calcium indicators have emerged as powerful tools that enable repeated, chronic functional measurements from local neuronal populations [184, 7, 189]. Therefore, in a collaboration with colleagues experienced in this type calcium imaging, I examined whether my approach can also be applied to cortical populations expressing the genetically-encoded calcium indicator YC3.60 [212]. We processed the brains of three wildtype mice, in which neuron-specific YC3.60 expression had been induced by local injection of an adeno-associated viral construct [184] (Figure 3.15a on page 101). Cell identification in fixed brain slices was possible like in GAD67-GFP mice, although matching had to mainly rely on prominent blood vessel curvatures and bifurcations in the densely YC3.60-labeled populations (Figures 3.15a and 3.15c on page 101).

In another experiment, we successfully applied double-labeling IHC to YC3.60-expressing

(a) PV/CR/CB/unmatched (b)
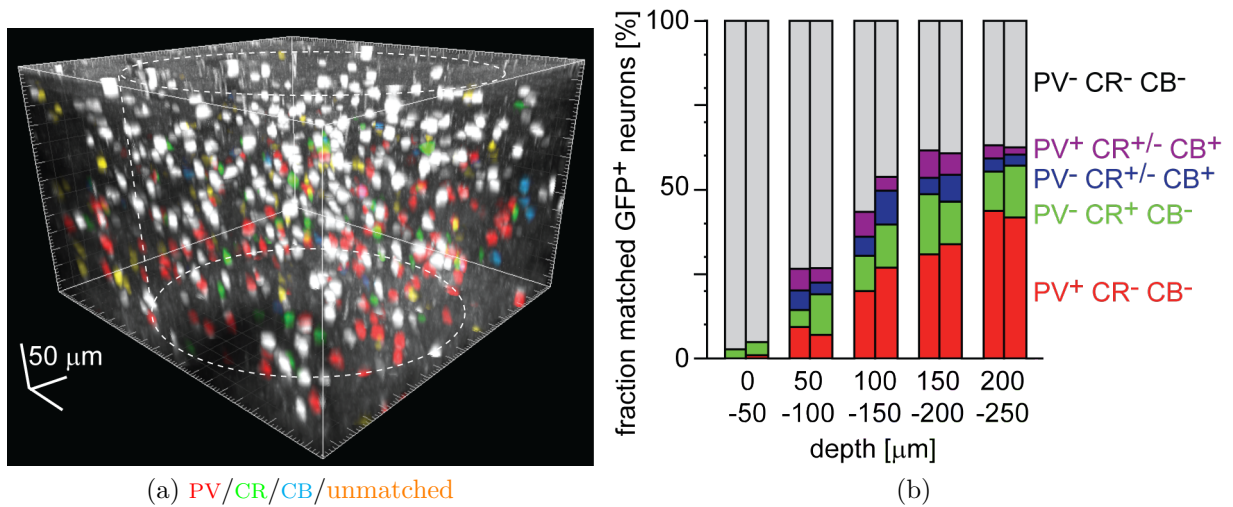
Figure 3.13: Depth-dependent distribution of GABAergic cell subtypes identified by triple-immunostaining against CaBPs. **(a)** Three-dimensional view of an image stack of a large population of GABAergic neurons (874 cells) acquired in vivo with colour-coded overlay of the classification determined by post hoc immunostaining: PV$^+$ (red), CR$^+$ (green), CB$^+$ (blue), PV$^+$/CB$^+$ (pink), GFP$^+$ only (grey), GFP$^+$ but not matched (yellow). The estimated extent of the C2 barrel column located by intrinsic optical imaging is indicated with dashed lines. **(b)** Layer-dependence of the abundance of GABAergic interneurons expressing different protein marker combinations. The percentage fraction of a specific marker combination from all GFP-positive neurons is shown in 50 μm bins for two volumes from two different animals (left: centered to C2 barrel; right: centered to D2 barrel). CR$^{+/-}$ indicates that the presence or absence of CR can not be specified with certainty due to bleed-through from the blue channel under our conditions.

cell populations, identifying both PV-positive and CR-positive subsets of interneurons (Figure 3.15d on page 101). For dual-immunostaining, we chose a slightly different set of antibodies that was more compatible with the YC3.60 fluorescence spectrum (Table A.2 on page 180).

In conclusion, interneuron subtype discrimination with post hoc IHC is possible in local cortical circuits densely labelled with genetically-encoded functional markers.

(a) $\lambda_{ex} = 850\,\text{nm}$
GFP/OGB-1/SR101

(b) $\lambda_{ex} = 850\,\text{nm}$
GFP/PV

(c) $\lambda_{ex} = 720\,\text{nm}$
PV/CR/CB

(d)

(e)
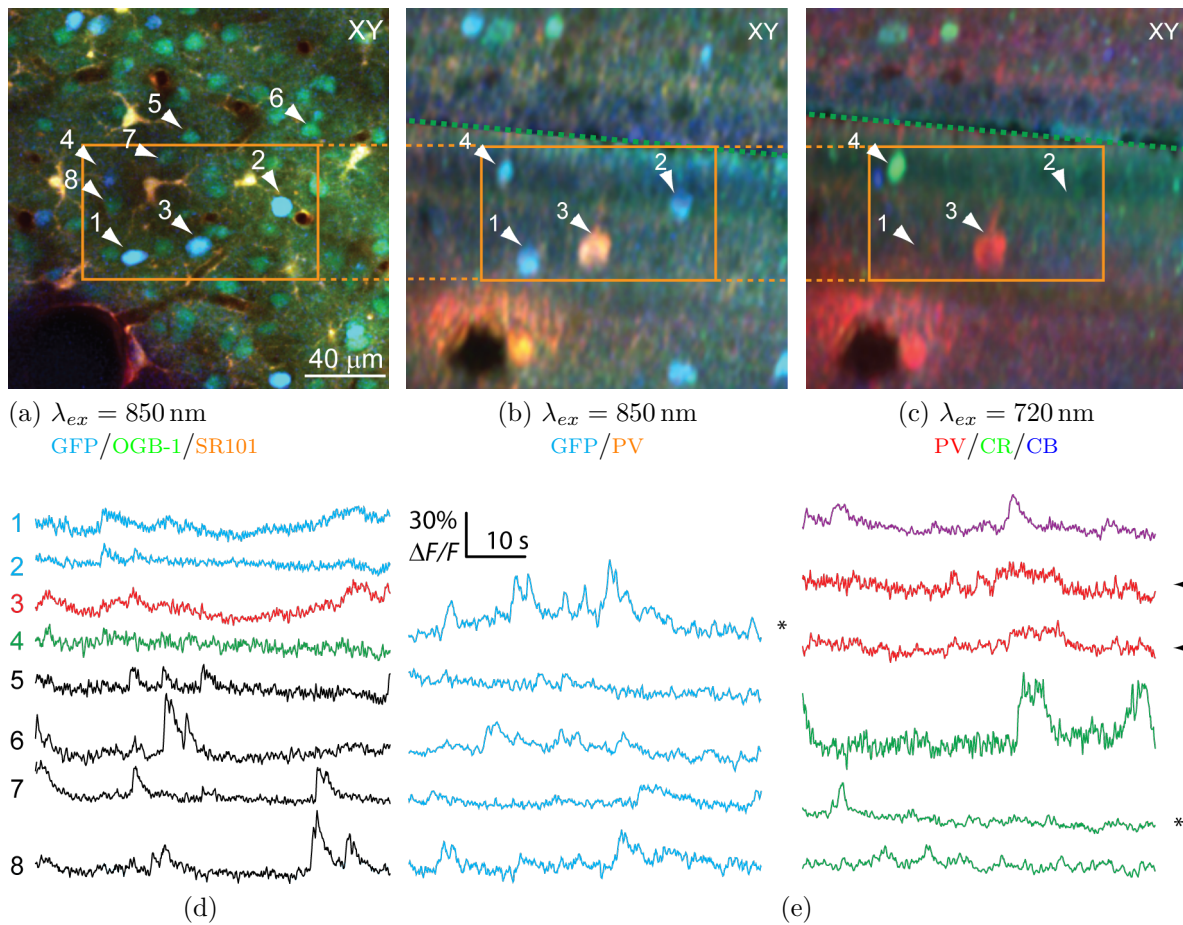
Figure 3.14: Post hoc classification of *in vivo* calcium traces from GABAergic interneurons according to the expression profiles of CaBPs (from [175]). **(a)** Field of view in barrel cortex of a GAD67-GFP mouse (150 µm depth below the pia), in which two-photon calcium imaging was performed *in vivo*. **(b)** The same area reconstructed from immunostained coronal slices by means of rotation fitting; excitation at 850 nm. A slice border is indicated as a green dotted line. Matching of GABAergic neurons 1-4 with the *in vivo* image in 3.14a is indicated. **(c)** Same as in 3.14b, but with excitation at 720 nm. **(d)** Spontaneous calcium transients recorded in the example cells marked with arrows in 3.14a (1-4: GABAergic neurons; 5-8: excitatory neurons). Trace colours indicate the cell type classification as revealed in 3.14a - 3.14c: GFP$^+$PV$^-$CR$^-$CB$^-$, GFP$^+$PV$^+$CR$^-$CB$^-$, GFP$^+$PV$^-$CR$^+$CB$^-$, GFP$^+$PV$^+$CR$^{+/-}$CB$^+$, GFP$^-$SR101$^-$. **(e)** Examples of spontaneous calcium transients from identified GABAergic neurons with different types of marker combinations; observed in two animals. All traces are recorded at different time-points except for those marked by arrows and stars.

3.3   Discussion

In this chapter, I presented how *in vivo* two-photon calcium imaging can be combined with post hoc triple-immunostaining to discriminate functional signals in GABAergic neuronal subtypes. I re-identified cells in fixed brain slices by matching corresponding neuronal populations in relatively large volumes. Antibody staining against calcium-binding proteins

(a) *in vivo*   (b) fixed (YC3.60/PV)   (c) fixed (YC3.60/PV)   (d) fixed (YC3.60/PV/CR)
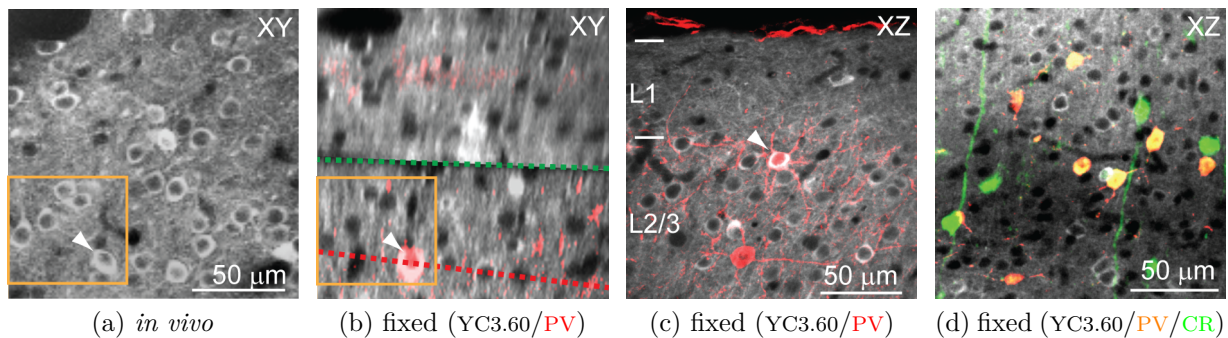
Figure 3.15: Post hoc single-stain IHC and cell matching in cortical tissue expressing YC3.60 (from [175]). **(a)** *In vivo* two-photon image of a L2/3 neuronal population expressing YC3.60 following viral injection. A particular cell constellation is highlighted by a orange box. **(b)** The same cell population in two adjacent fixed slices, rotation-fitted to the *in vivo* XY-view. The anti-PV immunostain is overlaid in red. The green dashed line indicates the slice border. **(b)** Coronal side-view at the level of the dashed red line in (b). The PV-positive cell marked by the arrow head is the same cell marked in the cell constellation in (a) and (b). **(d)** Anti-PV/anti-CR double-immunostaining of YC3.60-expressing cells in neocortex. In this coronal side-view the bipolar morphology of CR-positive interneurons is evident.

permitted me to start comparing calcium transients in specific GABAergic subtypes. The method can be combined with both synthetic and genetically-encoded calcium indicators. Therefore, it is particularly well-suited for cell discrimination following chronic *in vivo* imaging. Post hoc IHC opens novel and flexible possibilities to decompose *in vivo* network activity patterns into circuit sub-components and thereby advance our understanding of signal flow through neuronal microcircuits.

3.3.1 Genetic markers versus post hoc immunostaining

Two main approaches currently exist to distinguish different cell types, according to differential gene expression, in two-photon calcium imaging studies.

Genetic approaches

First, advanced transgenic methods enable the expression of fluorescent proteins in specific cell types *in vivo* (reviewed in [203, 20]). For example, transgenic rodent lines have been produced that express a fluorescent protein in either nearly all GABAergic neurons [275, 289] or a subset thereof [221, 47, 186, 198]. Moreover, driver lines with cell-type-specific expression of the site-specific recombinase Cre can be used to express an arbitrary fluorescent protein either through cross-breeding with a reporter line [187] or through local injection of customised viral shuttles [172]. Another promising approach to label specific interneuron subtypes is genetic fate mapping by conditional activation of Cre recombinase expression at different time points during development [37]. While two-photon calcium imaging in the GAD67-GFP mouse has already been performed in several studies [175, 260, 162, 304], the combination with Cre lines driving fluorophore expression in subclasses of GABAergic

neurons is just emerging [244, 317]. A major advantage of transgenic approaches is that specific cells can be identified and targeted during the *in vivo* imaging experiment. In particular, imaging of the local population activity may be combined with targeted electrophysiological recordings [109, 61]. However, the production of transgenic mouse lines is still time-intensive [187] and the possibilities to combine multiple fluorescent labels and indicators are limited.

Post hoc immunostaining

The second, IHC-based approach detects cell-specific marker proteins post hoc in fixed tissue, as shown in this thesis and in a few recent studies for GABAergic neurons [162, 296, 220]. This method is not limited to GABAergic neurons or the three CaBP used in this thesis. First, it can be applied to any mouse line expressing a fluorescent protein in a cell-type-specific manner in order to further dissect the labelled cell population. Second, as I have demonstrated by applying the method to YC3.60-expressing cortical tissue, it also masters situations where no sparse candidate cells are present, but rather all cells are more or less equally fluorescent. Thus, the method could even be applied to other species, for which transgenic lines with cell-type specific labelling are not available [156, 130, 51]. Third, in principle, the set of primary antibodies used can be freely chosen as long as the penetration depth and sensitivity is compatible with the chosen thickness of sections. Key advantages of post hoc IHC are its high flexibility, combinatorial application of multiple fluorophores and that both the target antigen and the fluorescence labels can be exchanged quickly. However, a disadvantage of the IHC-based approach is that staining is available only post mortem. Unless other readily accessible features such as typical cell morphology can be correlated to the presence of a marker protein or peptide, the respective cells of interest cannot be identified and targeted *in vivo*. Nevertheless, since the two approaches (genetic vs. immunostaining) are complementary, they can also be combined to first achieve *in vivo* targeting of one cell type, followed by a more complete post hoc IHC discrimination of subtypes (this is essentially what I did with the GAD67-GFP mice).

3.3.2   Technical aspects

Coronal versus tangential sectioning

Fixed tissue can be sectioned in different orientations. While I originally chose coronal sectioning, tangential sectioning is a reasonable alternative as demonstrated in Section 3.2.3 and [162]. The two sectioning orientations have different advantages when compared to each other. First, with the coronal sectioning approach, a high-resolution side-view of the cell morphology is readily available. Especially for cells with dendritic and axonal arborisations extending over several cortical layers, morphology reconstruction is easier in coronal sections because it does not have to follow neural processes over several tangential sections. In addition, coronal sectioning is also compatible with the recent achievement of performing *in vitro* electrophysiology on acute slices obtained from cortex on which

calcium imaging has been previously performed *in vivo* [167]. For acute slices, coronal or parasagittal sectioning is mandatory because tangential sectioning would largely destroy layer-spanning neurons. Second, with coronal sectioning, the thickness of all slices can be precisely controlled as opposed to tangential sectioning, where the thickness of the first slice is usually not well defined. In contrast, tangential sections can be cut arbitrarily thin, while the coronal sectioning approach requires a certain slice thickness to enable slice identification based on the pial surface blood vessel patterns. For antigens of low abundance, sections as thin as possible are usually required. In addition, with tangential sectioning it is easier to ensure that the orientation of slicing closely matches the *in vivo* imaging plane [162]. We can conclude that the two approaches complement each other, so that in future studies one can choose whichever method better fits the experimental requirements.

Approaches to facilitate matching

For coronal sections, optimal rotation fitting of the fixed-tissue image stack to the *in vivo* reference stack greatly simplifies matching cells. This is especially the case for YC3.60-infected cortical volumes, where characteristic 3D constellations of sparse landmarks are missing. While I obtained good results by empirically determining angles for rotation by a trial-and-error approach, automated rotation fitting could be used in the future. Based on a set of at least three matched landmarks, rotation angles can either be determined by iterative optimisation algorithms [34] or directly calculated [167, 141, 11]. In addition, matching could be assisted by algorithms suggesting the expected position of a cell in the fixed tissue image stack based on its position in the *in vivo* reference image stack and the coordinate system transformation defined by the already matched landmarks. Such algorithms could even be extended to suggest the most likely match of available candidate cells based on local energy minimisation. Furthermore, image segmentation algorithms could be employed for automated detection of soma positions [178].

Decreased matching efficiency at slice borders

Despite the high matching rates achieved for coronal sectioning, I observed a slight decrease towards slice borders (Fig. 4e). Two reasons may account for this observation. First, cells cut in half may be more difficult to identify. Second, the local neighbourhood, which helps the identification a particular cell, is only partly available at slice borders. Both of these underlying problems could be circumvented by rotation-fitting the *in vivo* reference image stack to the image stack acquired from the stained slices and comparing both in coronal XZ-view. Especially in combination with a matching-assistance algorithm as suggested above, this approach could further improve the matching rate at slice borders.

Channel bleed-through

With my choice of fluorophores for tagging the secondary antibodies and the detection system used, I still experienced some channel bleed-through. The green channel was sub-

stantially contaminated by the blue fluorophore (aminomethylcoumarin acetate (AMCA)) and slightly also by the red fluorophore (DyLigth594). Both the choice of fluorophores and of filters in the detector system could be further optimised to minimise this bleed-through. For example, the emission spectrum of DyLight405 is slightly blue-shifted compared to AMCA and would thus contaminate the green channel less. Furthermore, the band-pass filter I used in the green channel (BG 39) has a rather broad spectral window. A filter with a narrower window (e.g. a 535/50 bandpass filter) would lead to a purer signal. Alternatively, modern, commercially available confocal microscopes provide sophisticated fluorescence excitation and detection schemes. With these, the contributions of the individual fluorophores can be separated much better than with the custom-built two-photon microscope used to achieve the results presented here. Therefore, we can expect simultaneous immunostaining and discrimination of four markers instead of three without significant channel bleed-through to be possible.

3.3.3 Calcium imaging of GABAergic subtypes

Besides the expression pattern of marker proteins and neuropeptides as revealed by IHC or single-cell RT-PCR [281], the electrophysiological properties of GABAergic neurons, specifically their AP firing characteristics, are key criteria for classification. Despite controversy in the field, some correlations between the presence of certain markers and the firing pattern of a GABAergic neuron have been found [124, 192, 44, 45]. AP-evoked calcium transients in the soma presumably differ between subtypes of GABAergic neurons because they depend on AP shape, abundance of voltage-dependent calcium channels, as well as the presence of CaBPs [52, 87]. In particular, PV is expressed in fast-spiking GABAergic neurons that can fire at high frequencies [196, 159]. These neurons exhibit short APs that elicit elementary somatic calcium transients with an amplitude about ten-fold smaller compared to pyramidal neurons [162]. Therefore, one might expect that in PV-positive neurons, single-AP-evoked calcium transients will be hard to detect [95]. Rather, fluctuations in AP frequency should be reflected in a modulation of the fluorescence signal. My results are at least qualitatively consistent with this expectation. However, similar calcium transients might result from the summation of a few large-amplitude or many small-amplitude calcium transients, respectively. My failure to observe clear correlations between the presence of GABAergic subtype markers and characteristic features of the corresponding calcium signals thus indicates that it may not be straightforward to classify neurons solely based on their calcium transients. This, in turn, further emphasises the value of post hoc IHC.

Further marker combinations for post hoc immunostaining

Further steps are necessary to understand the relationship between observed calcium transients and underlying firing patterns throughout an entire local population with all different neuronal types identified. First, a better characterisation of elementary somatic calcium transients, evoked by single APs, is necessary for the various subtypes of GABAergic interneurons. These data would be best obtained from *in vivo* measurements, and they

should take into account AP characteristics and calcium-buffering properties. Second, advances in high-speed *in vivo* calcium imaging [116, 49] may help to reveal small but characteristic differences in calcium transient shapes. Third, other neurochemical marker combinations might be better suited for coarse subtype discrimination. For example, PV, SOM and VIP have recently been shown to label three non-overlapping subpopulations of the GABAergic cells [312, 162]. Moreover, the combination of PV, SOM and the ionotropic serotonin receptor 5HT3a has been identified to label 100 % of the neocortical GABAergic neurons while distinguishing three major cell groups of different developmental origin [243].

The goal of characterizing the cell-type-specific relationships between calcium indicator fluorescence changes and underlying APs would be to enable the reconstruction of neural spike trains from fluorescence recordings also in the diverse GABAergic neuron population. Only this will provide a full picture of the temporal sequence of suprathreshold activation of the various components of a local cortical circuit under *in vivo* conditions.

3.3.4 Future prospects

In recent years, *in vivo* two-photon calcium imaging of neocortical populations has advanced significantly along several lines. First, new scanning methods have been developed that permit measurements from larger populations in three dimensions and/or at a higher cell sampling rate [106, 116, 49]. Application of post hoc IHC methods to populations monitored with these specialised techniques should help to obtain a comprehensive picture not only of the distribution of neuronal tuning properties within local networks but also of network dynamics occurring on a short timescale. Second, two-photon imaging is now increasingly applied to behaving animals under either head-restrained or freely behaving conditions [74, 76, 7, 220, 250]. This type of experiment opens entirely new directions for examining the neural correlates of certain behaviours or—vice versa—the behavioural relevance of activity in particular cell types. Post hoc IHC can be expected to have a large impact for this research field because it allows the assignment of behaviour-specific activity patterns to particular GABAergic subtypes and thus should help expand on recent findings of differential interneuron activation in an electrophysiological study [109]. Finally, genetically-encoded calcium indicators now enable repeated imaging of the same cells over extended periods of time, sometimes over months [189, 278, 7]. At the end of such longitudinal experiments, post hoc IHC would offer the unique opportunity to gain additional information about particularly interesting sub-ensembles of neurons—identified during the course of an experiment—especially if these constitute only a small fraction of the population.

In conclusion, we can expect post hoc IHC to become a valuable method for assigning specific cell types to functional neuronal signals and thereby contributing to new insights into the fine-scale functional organisation of cortical microcircuits.

3.4   Contributions

The *in vivo* triple-stain two-photon imaging using GAD67-GFP mice was developed based on an idea by Fritjof Helmchen. Mara Modest helped with establishing the first IHC staining protocols. Steven Broadley and Sarah Hintermayer contributed to the implementation of an iterative rotation-fit optimisation algorithm (not presented in this thesis). Flavio Cueni contributed significantly to cell matching in experiments with GAD67-GFP mice. Kristina Schulz collaborated on applying the method based on coronal slices to YC3.60-expressing mice. Dubravka Göckeritz carried out many of the immunostainings and prepared custom-made solutions. The pilot experiment for tissue-reconstruction from tangential slices was carried out together with Lazar Sumanovski. The underlying idea of tangential sawing of the head was provided by Fritjof Helmchen.

4 General discussion

How can a three-pound mass of jelly that you can hold in your palm imagine angels, contemplate the meaning of infinity, and even question its own place in the cosmos? Especially awe inspiring is the fact that any single brain, including yours, is made up of atoms that were forged in the hearts of countless, far-flung stars billions of years ago. These particles drifted for eons and light-years until gravity and change brought them together here, now. These atoms now form a conglomerate—your brain—that can not only ponder the very stars that gave it birth but can also think about its own ability to think and wonder about its own ability to wonder. With the arrival of humans, it has been said, the universe has suddenly become conscious of itself. This, truly, is the greatest mystery of all.

Vilayanur S. Ramachandran [233]

Here, I will provide a general discussion of the topics and results presented in the previous two chapters. Since the latter also feature their own, more specialised discussions, I will remain on a more general level. I will start with a short summary of the two key achievements presented in this thesis. In the subsequent section, I will look at some organisational aspects of research in the field; from a local perspective on laboratories engaged in two-photon calcium imaging, I will zoom out to more general aspects of data management in neuroscience in general[1]. I then continue with a discussion of the biological aspects of my work and end with some final conclusions.

---

[1]The reader may not have expected to read about such *meta*-aspects in this thesis. However, considering that my personal interest is mainly in methodology (as is also reflected in the topics presented in the previous two chapters) and that I have been concerned with the aspects presented in the following sections during most of the past few years, it may be less surprising.

4.1   Summary, motivation and conclusion

In this thesis, I mainly presented two new tools for functional *in vivo* 2PM imaging. These tools were the following:

A new microscopy control software written in LabVIEW

The new software HelioScan was introduced. It serves the dual role of i) a *software framework* facilitating the structured development of new microscope control applications and ii) a toolbox of components from which the individual user can assemble various applications in a highly flexible manner.

   The motivation to start this project grew from discontent with previously existing scan software that was intrinsically limited in its extensibility and adaptability to meet certain requirements intrinsic to my biological project[2].

   In conclusion, HelioScan allows microscopists to cope with many different hardware and functional requirements in an effective fashion; thus, it reduces the total costs compared to other existing systems or new developments. The toolbox of available components is currently used in ten different laboratories and is being further extended with the goal to establish a well-known system supporting various available imaging modalities out of the same box. Due to the intrinsic support for multi-developer scenarios, a collaborative effort of several programmers working on different components could be established, which I would like to be further extended in the future.

A new method for cell type discrimination in *in vivo* two-photon calcium imaging

As a second achievement, I presented a method based on post hoc IHC that allows the discrimination between different cell types in a cell population on which two-photon calcium imaging has been previously performed *in vivo*. In brief, two different approaches employing coronal and tangential sectioning, respectively, were introduced and quantified.

   The development of this method was motivated by the well-established diversity among GABAergic neurons in the neocortex and the assumption that this diversity underlies different functional roles. These different roles may be deciphered by means of *in vivo* two-photon calcium imaging only if methods exist that allow the discrimination of GABAergic from non-GABAergic cells in the first place and enable further discrimination of subtypes among them. Both possibilities were not yet established at the time I started my thesis work.

   Although a few similar attempts have been published by other research groups in the meantime [162, 244, 260, 304], all approaches feature advantages and drawbacks, sug-

---

[2]Specifically, I needed i) three-channel image acquisition to enable simultaneous imaging of GFP, OGB-1 and SR101 in the preparation presented in Chapter 3, ii) flexible control of a whisker stimulation device and iii) a bit-depth higher than 8 bit per pixel and channel in order to accommodate the large intensity difference between GFP-positive and -negative cells in the functional channel.

gesting a complementary use of the different available methods in the future. Cell type discrimination employing the presented techniques is expected to be a key tool in future *in vivo* two-photon calcium studies aiming at understanding the functional role of different subcomponents of neuronal networks in the living animal.

4.2   Organisational aspects

Obviously, every organisation and endeavour has aspects that can still be further optimised—scientific research is not an exception. In the following sections, I will look at various organisational aspects of the scientific endeavour of understanding the brain, in particular by means of imaging-based approaches. For different categories of aspects, I will try to present the facts, the consequences and suggest possible approaches that might have a positive impact on the factual situation. I want to stress that the points raised here are based on my personal observations and thoughts. The reader may disagree on certain aspects and the feasibility of certain suggestions may be debatable. Nevertheless, I think it is worthwhile to discuss them.

4.2.1   Human and non-human resources

The situation

Due to the expensive components required, 2PM setups in many laboratories are used by two or more researchers. If the researchers sharing a setup do not work on the same scientific project, they essentially compete for a common resource, i.e. setup time. If no common projects are pursued, no synergies exist; while one researcher is using the microscope, it is blocked for other users, and they are not able to benefit from any progress achieved at the microscope during that time. Due to the usually long (up to twelve or more hours) and only imprecisely predictable duration of acute *in vivo* experiments, setup sharing on a single workday can become impractical.

The consequences

During certain phases, this situation can create a bottleneck for the progress of individual projects, whereas at other times, the setup may remained unused for days. In addition to arguments about setup time, conflicts may arise due to different ways of using the microscope. Sources of conflict can be:

- extensive physical re-configuration of the setup space due to different experimental requirements of different researchers;

- technological developments requiring frequent software or hardware modifications that impair the availability of the setup for biological experiments (see Section 2.3.2).

In summary, this situation creates costs in the form of i) increased stress levels of involved parties, ii) slower progress in the individual projects due to bottlenecks, iii) an expensive microscope setup not always used at full capacity and iv) overhead created because the setup has to be re-configured when handed over between users.

Suggested solution

I recommend that researchers sharing a microscope setup should work as a team on a common project. As a result, they would have common goals and benefit from each other in a symbiotic fashion. If one person is using the microscope, this would not represent a cost to the other team members, but rather a profit. One could argue that conflicts could arise in such a scenario due to the prevalent system of how credits are attributed in life sciences [23]; for Ph.D. students and junior postdocs, the key currency is first authorships that need to be collected in order to build and raise one's own academic reputation. For senior postdocs and group leaders, it is the last authorship that serves a similar role. This system can provide a significant obstacle for such team-based scenarios. I thus further recommend that a team using the same microscope setup is hierarchically structured (Figure 4.1 on page 111). A senior postdoctoral researcher could supervise one or two Ph.D. students, which in turn might supervise students working on their master or bachelor thesis. As
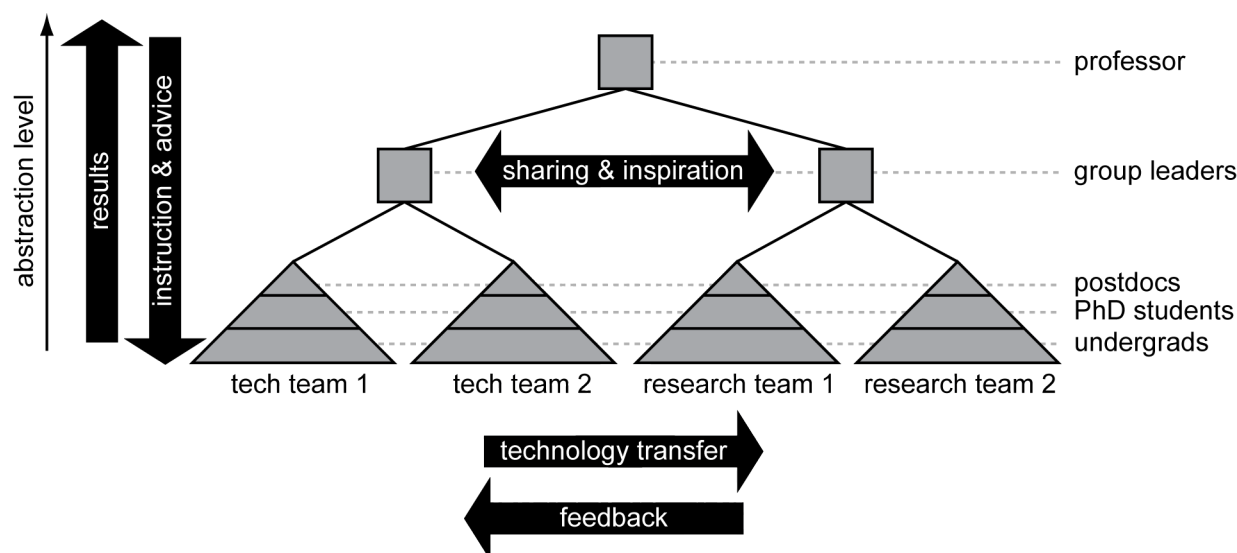
Figure 4.1: Hierarchical model of team-organisation for optimised use of resources.

a consequence, results obtained at one level would ascend through the hierarchy with each superior level being able to profit accordingly and earn the appropriate credits. For example, a master student could optimise a method that is in turn used by a Ph.D. student to gain data that are eventually analysed and put into context by the postdoc.

In this approach, it might also make sense to separate technology development and biological research completely. Technology development would be performed by dedicated teams on dedicated setups, and so would biological research. In this way, the above-mentioned problems could be avoided. New technology would then percolate into the biological divisions only once it is properly tested and members of the technology teams could dedicate time to install the technology properly on the biology setups and assist during the first experiments. In the other direction, feedback from the biology teams would need to be properly and constructively channelled back to the technology teams by

appropriate technical and organisational means. The advantages of such a model are the following:

- *Scalability:* The structure is fully scalable in vertical and horizontal direction. The principal investigator can steer the orientation of the whole laboratory (i.e. more or less technology-oriented) by choosing the number of the teams accordingly.

- *Robustness:* This system is rather resilient in the instance of the temporary or permanent loss of an individual person. Due to the modular architecture, know-how is distributed throughout the individual teams and thus not tightly attached to a single person. Also, if a superordinate person is not available, feedback can be obtained from colleagues of the same level, and instructions from the next superordinate level. In the case of a loss, a specific replacement can be recruited.

- *Fault tolerance:* According to a rule of thumb, a single person in an academic research environment should not directly supervise or manage more than six subordinates (the so-called *span of control* [119]). In the model presented here, a new layer can be easily introduced if this number is exceeded somewhere in the hierarchy. The smaller the span of control, the tighter the interaction among people in the corresponding branch, both on the same level and on the levels immediately above and below. This tight interaction ensures frequent feedback and the availability of dedicated people when help is needed, and it prevents errors or mistakes from occurring.

- *Efficiency:* The structure is highly efficient because each person has more time for supervision and thus bigger impact. Information can more easily be propagated to all of those concerned because only a small number of people has to be informed. They, in turn, will take care of informing their subordinates or superordinates, respectively (depending on whether the information has to flow down or up the hierarchy; the so-called *chain of command*). Standards and other rules imposed by superordinates can be more easily enforced, because only the direct subordinates have to be briefed and made responsible for supervising their direct subordinates accordingly.

- *Training:* Leading and supervising experience can be systematically achieved at nearly all hierarchy levels.

4.2.2   Performing *in vivo* experiments

The situation

Acute experiments involving *in vivo* MCBL of a calcium sensitive dye last several hours. Preparation of the craniotomy followed by dye application may take between 2.5 and 4 hours, depending on the experience of the experimenter. If IOS imaging is applied in order to localise the position of a well-accessible, functionally-defined cortical region, at least another hour has to be added. In sum, up to 5 hours may be needed until the actual measurements can start. The whole procedure, especially the micro-surgical parts, require

the highest level of concentration from the experimenter. During the entire experiment, many variables have to be monitored or controlled for, including:

- *physiological parameters* such as anaesthesia level, breathing, supply of liquid and nutrients;

- *preparation parameters*, such as the quality of the craniotomy, including optical clarity and mechanical stability, or adjustment and positioning of stimulation devices;

- quality of *the microscope's optical system*, such as a well-adjusted beam path, shielding from external light sources, mechanical stability including a well-balanced optical table, isolation from vibrational sources (e.g. the air-conditioning system, the laser chiller or clapping doors);

- quality of *the electronical part of the data acquisition system*; this mainly implies the base-line noise level, which can be affected by the path of cables, by the exact position of key elements such as the ADC box, by ground loops or various radio frequency (RF) sources (e.g. neighbouring setups or centrifuges used in the same building).

The consequences

Overlooking a single critical parameter (e.g. a maladjusted set point of the temperature controller used to maintain the body temperature of the animal) may lead to a failed experiment, which, in consequence, has to be terminated after hours of work already invested. Furthermore, the high concentration required for the surgery, dye injection and associated procedures consume a lot of energy.

Suggested solutions

Checklists for critical points   In order to avoid a situation in which certain important details are overlooked in the heat of the moment, I recommend that checklists are routinely used at certain key steps of an experiment. Such key steps and corresponding check list items could be:

- Immediately *before an experiment* session is started (i.e. before the animal is put under anaesthesia): Are the microscope and all required data acquisition and stimulation devices properly wired and working? Are all tools and consumables ready and well-arranged?

- Immediately *before the surgery* begins (i.e. when the animal is already under anaesthesia and mounted under the surgery stereoscope): Is the body temperature well adjusted? Is the anaesthesia level well maintained?

- Immediately *after the animal has been transferred* to the setup: Is the body temperature well adjusted? Is the anaesthesia level well maintained?

- Immediately *after the experiment* is finished: Are all acquired data saved properly? Are all devices shut down? Are all valves closed? Are all personal devices put away, public devices and work places cleaned and consumables refilled?[3]

In the organisational structure suggested in Section 4.2.1, it would be the responsibility of the superordinate person to ensure that all subordinates make proper use of such checklists. If the use of checklists is not enforced, in particular the last point on the list above will not be taken care of. As I experienced, already a single co-worker not playing according to the rules can render rules useless.

Team-based experiments   In addition, I recommend acute *in vivo* experiments to be performed in a team of at least two persons, which would be in perfect accord with the organisational model suggested in Section 4.2.1. This would provide several advantages:

- *Divided work:* This not only allows recovery phases but also parallel work. For example, one person could perform the craniotomy on the animal, while the other is already checking, optimising and preparing the microscope. He would take over once the animal is ready for the next step (e.g. IOS imaging or dye injection). Once dye injection is finished, the first person—in the meantime recovered—can again take over for the first rounds of data acquisition.

- *Higher success rate:* During the process, the researcher who is temporarily not the main responsible for the animal can provide a second pair of eyes and make sure that all parameters remain in the target range. In emergency situations, he would be available and provide assistance. During the phase of data acquisition, the two experimenters would complement each other; one of them could be responsible for data acquisition, whereas the other would still monitor the vital parameters, but can also already engage in preliminary ad-hoc analysis of acquired data and thus serve as a navigator guiding the team through a successful experiment.

- *Lower stress level:* As I frequently observed, *in vivo* experiments can be rather stressful. Under certain conditions, a small problem can easily escalate in a chain reaction at the end of which the experiment has to be terminated. Not only due to the above advantages, but also due to mutual emotional support in a team working towards a common goal, stress can be strongly reduced, eventually resulting in better results.

Distributed experiments as suggested in Section 2.3.3 could at least partially serve a similar purpose. I see them as an additional benefit, rather than a full replacement for a team working physically together on an acute *in vivo* experiment.

---

[3]Points on the checklist for this last point do not only serve the experimenter, but can prevent a lot of hassle with co-workers.

These two suggestions, check lists and teams of two, are well established in some other professional fields where the highest concentration is required over durations of several hours (e.g. for pilots of commercial aircraft—although in that case, of course, the costs of a failed "experiment" are much higher).

It has to be mentioned that chronic preparations based on GECIs alleviate some of the problems described above. The lengthy procedure of performing a craniotomy, IOS imaging and dye application has to be performed only once in the beginning. As long as the preparation stays in good quality, an individual experimental session can be prepared much more easily; the animal merely needs to be anaesthetised and mounted on the setup.

4.2.3 Analysis workflow

The situation

A two-photon calcium imaging session usually produces multiple raw data files, each of which can in principle be described by a set of metadata, including i) *biological parameters* (e.g. animal species, age and sex), ii) *preparative parameters* (e.g. surgical parameters and applied dyes), iii) *measurement parameters* (e.g. scan type and sampling rate) and iv) *environmental parameters* (e.g. stimulus parameters). Mostly, only part of the potentially applicable metadata is actually stored, and only a fraction of stored data is stored in a machine-readable form. For example, some data might be written into a physical or electronic notebook, whereas HelioScan—if configured accordingly—stores all available measurement parameters in the OME-XML format, which is fully machine-readable.

Raw data files are subsequently processed in a series of steps, each of which results in one or more intermediate files. For example, based on the raw data files, ROIs may be defined manually or by a segmentation algorithm. Using these ROIs, individual fluorescence intensity time series can be extracted. These, in turn, may be subject to filtering before being fed into a spike inference algorithm that creates a time series of putative AP events. The AP event data of different cells or different trials may be compared to each other using appropriate algorithms. Individual steps in this procedure might be carried out by different programs or even by different people.

Each intermediate file generated in this process can be annotated with a set of metadata describing the software and/or algorithm including parameters that were used to produce them. Again, as for the raw data files, only part of these details are usually stored and even a smaller fraction is stored in machine-readable format. Finally, some of these files are archived—sometimes in a not very systematic fashion—on some storage media. The amount of archived data may grow up to several hundred gigabytes for individual researchers and dozens of terabytes for a whole research group. Only rarely, the procedure from raw data files, over intermediate files, to condensed result files is fully standardised or even automated within a research group.

The consequences

Several consequences result from the situation described above:

- Incomplete metadata and a lack of standards for procedures impair *reproducibility* of result data.

- A lack of standards for procedures combined with less-than-possible automation results in suboptimal *efficiency.*

- A non-standardised way of storing metadata decreases *compatibility* between different software and researchers.

- A non-standardised way of archiving data makes it more difficult to *relocate data* after some time has passed[4] and also decreases the efficiency with which researchers can *exchange data.* In addition, the storage capacities are only used suboptimally because unnecessary data files are often not deleted.

Suggested solutions

Common standards   First, it is important to establish standards for common analysis procedures. These standards would be valid for a whole research group, or a subbranch thereof (Figure 4.1 on page 111), depending on the requirements disposed by individual subbranches or research teams. In order to maximise the compatibility between subbranches, the scope of application for standards should be as wide as possible, as long as different requirements are not violated.

In any case, the standards need to be documented online, optimally on a wiki. This ensures that newcomers can familiarise themselves with the standards quickly, and it facilitates data exchange between researchers employing different standards. Modifications on a standard need to be tracked in a revision history because otherwise reproducibility of data analysed in the past is impaired. Wiki systems often automatically store old versions of a wiki page for later access. Nevertheless, I recommend the use of an appropriate nomenclature (which should also be standardised for the whole research group) to individually name revisions of a standard. A possible naming convention could be:

```
std_<category>_<description>_<date (YYMMDD)>_<initials of editor>
```

where each fragment in brackets[5] is written in camel case[6]; for example:

```
std_analysis_dFFExtractionFrameScan_110324A_DL
```

---

[4]This is an especially serious problem for supervisors who want to review data of employees that have left their group.

[5]In general, dates in naming conventions should be in a format where year comes before month and month comes before day. Furthermore, month and day should be in a two-digit format also for the one-digit numbers between zero and nine. These two rules allow alphabetic sorting to imply chronological sorting.

[6]*Camel case* refers to a convention where individual words are concatenated without spaces and each word instead starts with a capital letter (e.g. *camelCase*).

A flexible metadata format   Furthermore, an extendible, flexible and maximally complete metadata standard should be introduced and used. A chain of analysis steps results in various intermediate and result files. Each of these files requires all the parameters that describe its creation in addition to the already existing metadata.

Crucial for this purpose is a machine-readable format in order to enable analysis programs to automatically extract the parameters they need (see the paragraph about automated analysis pipelines below). The human- and machine-readable format of the OME-XML standard can serve as a starting point because it already covers basic microscopy details, and can be flexibly extended via so-called *structured annotations* [112][7]. Here, the dynamically developing requirements of imaging-based neuroscience have to be captured and periodically updated. With regard to special requirements, individual subbranches in the organisational structure suggested in Section 4.2.1 can define their own structured annotations that would be valid for all subordinate members working in the respective subbranch.

Importantly, as many as possible of the data elements need to be automatically filled in for a given data file in order to disburden the experimenter. This requires user-, project- and setup-based configuration files that contain all the information that does not change on a daily basis. Information that is common to a whole experimental session, but cannot be deduced from configuration files, needs to be automatically queried from the user at start-up. Similarly, information that is specific for a given image acquisition and cannot be automatically deduced needs to be queried from the user each time before or after acquisition start. Such *mandatory* queries are key in this approach because otherwise the user tends to forget or skip entering of information.

File storage   As a third suggestion, I recommend the standardisation of the way raw data, intermediate and result files are stored. If files are not directly stored in a database [206], this recommendation concerns the storage location as defined by the *directory path* and *file name* structure.

Interfaces   The realisation of the above three suggestions would allow well-defined interfaces via which an authorised group member could access any step of an analysis sequence in order to display or further process the data (Figure 4.2 on page 118). Using a unique identifier, he knows *where* to find a certain processing stage of specific data, he can understand in detail how it was created and he has all information available to feed the data into further analysis steps.

Automated analysis pipelines   In addition, common standards in combination with an extensive metadata format could go hand in hand with fully or partially automated analysis pipelines. Essentially, such pipelines could both *implement* or *define* an analysis standard, and their individual steps would *use* and *extend* the information items contained

---

[7]Another flexible, but not microscopy-centred format would be the *Dataset Publishing Language* developed by Google (`http://code.google.com/intl/de-DE/apis/publicdata/`).

Figure 4.2: Workflow using well-defined data interfaces. Invididual analysis steps can be carried out by different researchers, different analysis programmes or on different computers.
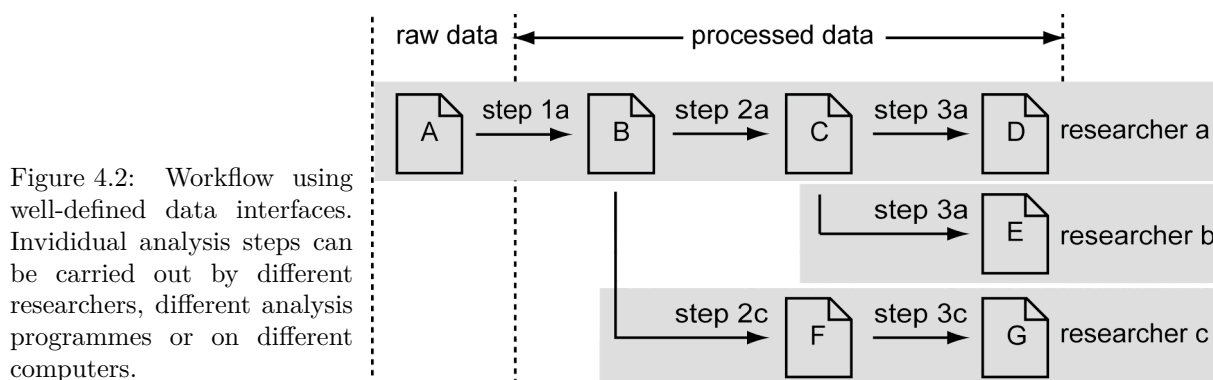
in the metadata. Optimally, such pipelines are not hardcoded, but flexibly assembled from modules representing the individual steps of the pipeline. Due to the well-defined interfaces mentioned in the previous paragraph, these modules could even be implemented in different programming languages and run on different machines[8].

4.2.4 Data organisation and sharing

The situation

The current standard in life sciences is that data are published in a very condensed fashion in research articles. In these articles the results are presented mostly in the form of figures and natural language, which are both not easily machine-readable. As mentioned in Section 4.2.3, raw data and intermediate files are only sparsely accessible. Unlike in other domains, such as molecular biology, data sharing is still uncommon in neuroscience, but it is expected to become more and more important in the future [12].

Data generated in neuroscience research are highly complex and extremely heterogeneous: they are obtained with various different methods, and they concern many different aspects (e.g. anatomy, biochemistry, physiology) of structures with sizes of different orders of magnitude. As a result, many different types do exist and further ones can be expected in the future. These different kinds of data are acquired in different brain regions, in animals of different species, ages, sexes, from different environments, with different genetic background or under different pathological conditions [173].

The consequences

In research articles, only full-text searches are possible[9], whereas complex semantical queries are not supported. Regarding full-text search, the imprecise use of language as well

---

[8]*Kepler* allows the implementation of such data processing pipelines: `http://www.kepler-project.org`.

[9]Using *PubMed*, the full-text search is essentially limited to title and abstract. *Web of Science* additionally provides the possibility of a limited relational search using citations as links between documents. *Google Scholar* allows a full-text search of the whole document body.

as different synonyms used by different authors just further increases the search space. For example, scientists often use the words *interneuron, GABAergic neuron* and *inhibitory neuron* (or combinations thereof) as synonyms, despite of the fact that these terms do strongly, but not completely, overlap (see Section 1.1.2). With a growing number of web-accessible neuroscience resources (Figure 4.3 on page 119), it will become more and more difficult to find a specific resource and judge the relevance of search results. In basic research, publications (apart from reviews) mainly publish newly acquired data. Given the above-mentioned amount and diversity of data already generated, it can be expected that future studies will more and more focus on multi-scale integration of already existing data by means of re- and meta-analysis or comparisons between datasets obtained with different methods, in different domains or from different sources (e.g. different species). However, such studies crucially depend on the availability of datasets, common or at least convertible data formats, appropriate metadata and semantic linkage between data items [103]. In addition to the obstacle that most scientific data is not available in a machine-readable format, but rather only as text and figures in research articles, data repositories providing experimental results in machine-readable format mostly do not link to each other.

Suggested solutions

A standardised common language The most important requirement to solve the above-mentioned problems is a common, highly precise and formalised language that allows scientists to describe life science data and knowledge in a fully machine-compatible fashion. Such systems are already being developed, for example as part of the *Open Biomedical Ontologies (OBO)* initiative [258], but some life science domains other than neuroscience have a big head start (especially molecular biology acted as trailblazer in the field). Fortunately, various initiatives have been launched during the last few years to respond to this situation [158, 194]. An important example is the *Neuroscience Information Framework* [103], which provides mechanisms that enable flexible interoperation [32, 191, 122] between different data sources as well as integrated querying of different data sources [190].
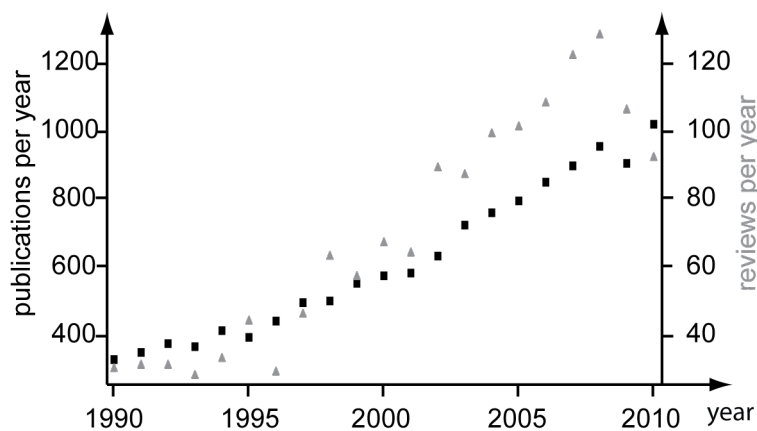
Figure 4.3: Increase of the publication rate over time: the number of publications per year containing the keyword *GABAergic* is plotted for every year (source: PubMed). Black squares: total number of publications per year; grey triangles: reviews per year. Over the time span of twenty years, the publication rate has roughly tripled. Note that a plot of the total number of papers *already published* plotted against time would be roughly exponential for the time span shown.

Ontology-based inference systems integrating multiple databases   Key components of many of the above-mentioned initiatives are *ontologies*[10], which allow individual data or metadata items to be semantically linked on different levels of abstraction. The basic value added is that ontologies enable inference and complex semantic queries integrating data from different databases. For example, a team around Kei-Hoi Cheung used commonly available frameworks and tools to interface different databases in a combined fashion based on ontologies built semi-automatically on top of their database schemas:

- The query "return all neurons that use GABA as a neurotransmitter and that have receptors for Glutamate located on their dendrites" accessed the repositories *NeuroDB* and *ModelDB* [246]; whereas

- "Find all receptors contained in the apical dendrite compartment of all types of pyramidal neurons in the neocortex, which have been measured for an ionic sodium current having a voltage threshold of at least $35\,\mathrm{mV}$" queried *NeuronDB* and *CoCoDat* in an integrated fashion [173].

In conclusion, I see the future of data publication in publicly accessible relational databases that support various data formats. Quantitative data should be stored in a quantitative format (i.e. not as pictures of diagrams), directly as data series that can be translated to diagrams *on-the-fly* [158][11]. Various pre-processing stages of data could be made available—optimally up to the original raw data. Using a standardised metadata format as suggested in Section 4.2.3, the whole data processing chain could be reproduced accordingly. In addition, data would be annotated according to a suitable ontology as suggested above. As a result, complex queries would allow researchers to find freely-definable data sets in a *semantic* rather than keyword-based search.

---

[10]An *ontology* formally specifies the relationship between terms and operationally defined structural concepts represented by them.

[11]The *Google public data explorer* (`http://www.google.com/publicdata/home`) goes into exactly that direction.

4.3 Biological aspects

4.3.1 The interneuron diversity problem

A community perspective

GABAergic interneurons in the neocortex of a single individual animal display a huge diversity in all phenotypical aspects (Section 1.2). Within the individuum, diversity is a function of space (i.e. the location in the cortex) and time (i.e. changes during the ontological development of an animal). When we look at the body of scientific data currently available on the topic, we are immediately confronted with two problems, which mutually entrain each other.

First, we face an additional level of diversity on top of that already present within a single brain. Due to different methods and model systems used, the data from different studies can often hardly be compared to each other. It is fair to assume that a common goal of interneuron researchers is to bring structure into an already highly multidimensional feature space in order to derive concepts that allow them to understand the underlying mechanisms and governing principles. Unfortunately, as a result of their heterogeneous approaches, they actually introduce additional dimensions into the feature space, and consequently increase the problem complexity. The situation is made even more difficult by the fact that until recently, no common terminology or classification scheme existed that could have been used to name and describe the features or types of interneurons studied in a standardised way [316]. As a result, the conclusions drawn in reviews based on different individual studies sometimes seem far-fetched given the fact that the underlying data represent only a few points scattered over different dimensions in the above-mentioned multi-dimensional feature space.

With the Petilla convention, a number of researchers specialised in the field have agreed on a systematic collection of descriptive criteria for GABAergic interneurons [13]. Although it was explicitly stated that a committee will update the scheme as needed, no such activity could be observed on the homepage of the initiative at the time of writing this thesis. This could be due to the fact that only three years have passed since the convention—maybe not enough time for the aspect of ontogenetic origin of interneurons to maturate to a state where an appropriate extension of the Petilla scheme is justified. Recent successes in classification based on genetic fate mapping suggest that such an extension will make sense in the future (see [37, 36] and the yet unpublished work by Z. Josh Huang at Coldspring Harbor Laboratory[12]). Also, the Petilla convention can be criticised because it lacks specifications on how to provide quantitative data and it is not available in a machine-readable format (i.e. as XML schema). Both are required to interface with appropriate databases and algorithms in the future (see Section 4.2.4).

Second, mainly as result of the point above, there is a frightening lack of principles that would allow us to integrate the various observations made about GABAergic interneurons.

---

[12]`http://huanglab.cshl.edu/research.html`

As a result, reviews on interneuron diversity often are frustrating listings of observations without a big picture [79, 192]; the situation is reminiscent of the narration of a child walking through a flowering meadow and describing the countless properties of different flowers and insects it encounters, unable to put its observations into the context that a trained taxonomist operating within the framework of evolutionary biology could provide. In consequence, we are currently at point where we are mainly confronted with a lot of factual knowledge, rather than conceptual.

Many of the functional properties of the brain are emergent properties, i.e. they result from the interaction of individual constituents and thus are intrinsically rooted in a certain level of complexity. We can conclude that a situation consisting of a lot of atomised data (as described above) clearly limits the scientific community's understanding of how the brain works. A significant further obstacle stems from the fact that our intellectual capabilities are clearly limited when it comes to dealing with highly complex network-based processes such as those underlying the human brain[13]. Network-based processes are fundamentally different from other natural phenomena in that some features cannot be described in a simplified fashion because they are rooted in their very own complexity. Certain crucial roles that GABAergic neurons play as part of a neural network may correspond to exactly such non-simplifiable processes. Statements such as "GABAergic interneurons are involved in shaping response properties of their postsynaptic targets" may be true and experimentally testable, but they provide a qualitatively different simplification of reality than a formulation such as "rhythmic contractions of the heart muscle pump blood into the aorta". The latter can be immediately related to various personal experiences we already acquired during childhood; for example, when squeezing mud through the gaps between our fingers. However, there is no everyday experience that we can relate to properties that emerge only at a certain complexity level in a network of interacting components. This principle is demonstrated nearly on a daily basis by turbulences at the stock or currency exchange market, when established experts repeatedly fail to make reliable predictions.

Maybe our brain is too limited to understand its own functioning and we might be condemned to remain at a level of understanding that is limited to collecting phenomenological descriptions of individual neural units and causal relationships at a simple level of complexity or high level of abstraction, respectively. Maybe our attempts to divide the brain into a hierarchy of modules down to the level of single molecules—and understand each level of abstraction completely in all detail of the involved complexity—will never explain all of the brain's features. Although evolution may have capitalised on the use of modules (Section 1.1.4) to create more and more complex brains, it is also well-known that evolution exploits what is already available[14] [41]. In the case of the brain, these are not only potential constituent modules, but also the whole entirety of the physical neural network. As a consequence, it is well possible that certain features and processes cannot be explained using module-based concepts because they emerge from the neural network

---

[13]This is not very surprising given that human evolution occurred to a large extent in an environment where other capabilities were much more important for selective fitness [309].

[14]The reader may forgive me for using vocabulary associated with goal-directed behaviour when talking about the goal- and soul-less process of evolution.

(that might include so far largely neglected components such as the astroglial network [297, 143, 137]) as a whole.

Be that as it may, I regard it as absolutely necessary that we can start feeling—metaphorically speaking—the mud squeezing through our fingers in neuroscience. In more concrete terms, we need an integrative approach that allows us to interact with combined datasets in a highly efficient fashion. These can be sophisticated simulations at the network level, in which neural activities can be both observed and perturbed in real-time. Optimally, such simulations are part of an embodied system in which environmental interaction is taken into account (Section 4.3.3). Such systems would allow researchers to probe how different network connectivities, node and connection properties, as well as body morphologies, affect emerging activity patterns [253, 197, 170, 254, 255]. However, such attempts require—in addition the concepts underlying the network models—a well-populated basis of real-world data in order to initialise the network parameters with sensible values. In another approach, ontology-based inference systems integrating qualitative and quantitative neuroscience data available in different databases can be directly probed. Importantly, both of these approaches profit from a data space that is as highly populated as possible. As already discussed in Section 4.2.3, data acquired about components of the brain need to be precisely and extensively annotated such that each data item can be assigned as precisely as possible to a specific place in the multidimensional data space that captures all variability in the metadata in appropriate dimensions. It becomes immediately clear that if annotation has to be as extensive and population of the data space as dense as possible, one might consider restricting unnecessary variability in the metadata. This could be achieved by, for example, focusing research efforts on research animals of a highly homogeneous genetic background (e.g. by focusing on mice with a specific age, sex and genetic background). Evidently, such restrictions can only be followed in coordinated efforts, e.g. by dedicated consortia. Another way to gain large amounts of data is using high-throughput screening, which in the *in vivo* implementation is not equally feasible for all research animal species [200, 176, 82].

How to proceed

Acute preparations   In Chapter 3, I presented a method for post hoc cell type discrimination for two-photon calcium imaging. Specifically, I intended to use this method to find differences in the properties of spontaneous calcium transient observed in different types of GABAergic cells. The calcium imaging measurements presented in that chapter have been acquired in acute, anaesthetised preparations. With my approach, different types GABAergic cells characterised by specific combinations of CaBP cannot be optically discriminated *in vivo*. As a consequence of this fact and intrinsic variability that is *not* related to different marker expression, many different cells have to be sampled, optimally with several trials, in order to find correlations—if they exist.

However, acute preparations suffer from several drawbacks. First, an acute preparation allows for only a rather limited number fluorescence time series to be recorded and has a high overhead. Assuming an experiment with a preparation time of 5 h and a recording

time 5 h, we are faced with a clearly limited number of GABAergic neurons that can be recorded from if we take into account that we want to record for around two minutes per sweep and acquire several sweeps per spot. Given the high diversity of interneurons and the fact that we will be able to record only from a comparably small number of GABAergic cells, we might be unable to conclude from the results whether certain variability is due to interspecies variability or due to differences intrinsic to different cell types.

In addition to the comparably small overhead due to the micro-surgical preparation and dye injection that is associated with each measurement session, we will have to perform the whole rather laborious post hoc immunostaining for each experiment that yielded high quality recordings. The work that has to be invested for the whole procedure per animal is significant: several days of full-time work.

An additional concern is that during the duration of an acute experiment, the anaesthesia level or other vital parameters are not entirely constant, which could result in further variability. Therefore, the use of an artificial respiration device, continuously applied anaesthetics (either as gas anaesthesia or automated gradual injection) and sophisticated monitoring of vital parameters would be desired. Furthermore, water immersion objectives act as heat sinks that can lower the brain temperature below the craniotomy significantly below the natural body temperature. Suboptimal temperatures, in turn, may affect the neural properties being investigated, and intracranial temperature gradients may induce variability in the cells from which data are recorded. I did not observe obvious differences in the spontaneous activity when perfusing the craniotomy with normal rat ringer (NRR) of 37 °C in a pilot experiment (data not shown in this thesis). Nevertheless, the use of an objective heating jacket or superfusion with pre-heated NRR in future experiments may be considered.

In order to capture as many GABAergic cells as possible in one experiment, the approach to follow is to acquire a reference stack of the MCBL-affected volume at the beginning of the measurement phase and to define all cells from which calcium imaging will be performed (either random sampling or selection based on parameters that can already be assessed in this *in vivo* reference stack). Visual navigation through the three-dimensional neocortical tissue can be non-trivial and lead to loss of precious time. Two possibilities are suggested for the as quick as possible navigation to the sites of interest:

- Using a motorised stage controlled by a HelioScan Stage component that allows multiple sites of interest to be stored, to which it can automatically navigate to.

- Perform the experiment in a team of two: one person is responsible for controlling the stage and signal acquisition while his partner is concerned with determining the sites of interest and guides his partner accordingly.

Chronic preparations   In order to decrease the overhead associated with data acquisition, I recommend the use of preparations expressing a GECI below a chronically implanted window. Such preparations allow repeated data acquisition from the same animal over durations of weeks and months (depending on how stable the window quality is), thus enabling the researcher to acquire hundreds of time series from dozens of cells.

The GECI should be expressed in a transgenic mouse in which all, or a subset of, GABAergic cells are fluorescently labelled. Such double-expression of fluorescent proteins are possible by either cross-breeding two different transgenic lines or by viral expression of a GECI in the cortex of a transgenic line. A problem can arise if a spectral overlap of the two fluorophores exists. For example, when YC3.60 is expressed in GAD67-GFP mice, it fluoresces so brightly that the GFP labelling of interneurons cannot be discriminated anymore. This will require to either acquire an *in vivo* reference stack of the GFP expression pattern at the site of viral injection *before* YC3.60 expression has started, or, alternatively, the use of a spectrally better compatible fluorophore combination. For example, red fluorescent protein could be expressed in a transgenic Cre driver line in which Cre is only present in GABAergic cells or a subset thereof.

As suggested above for acute preparations, the essential procedure would be to acquire as many calcium traces as possible from cells pre-defined in a reference image stack. The use of a chronic preparation allows—due to a reduced overhead per data item—shorter imaging sessions (in the anaesthetised case), implying less perturbation of vital parameters. Alternatively, it facilitates recordings to be taken from the awake animal. I highly recommend the latter because it avoids artifacts related to pharmacological effects of the anaesthesia and allows the researcher to record data under quasi-natural conditions.

4.3.2 Understanding neuronal networks

Activity

Frame-scan-based data-acquisition features a relatively low number of cells per recording and is rather limited in the achievable sampling rates. In the recordings I presented in Chapter 3, the number of GABAergic cells was usually between two and five per field of view, not all of which were necessarily optimally in focus. As explained in Section 1.4.4, cells that are not optically sectioned in the equatorial plane have a worse SNR and suffer from increased neuropil contamination when compared to cells that are optimally focused [104].

During the last few years, various advancements in 2PM imaging technology have been made and also partially integrated into the HelioScan framework. 3D scanning allows one to simultaneously sample from three-dimensional volumes rather than a single two-dimensional plane [106, 105, 117, 256, 49]. This not only allow the researcher to record from a larger number of cells at the same time, but can also partially alleviate the out-of-focus problem [106]. Using multi-focal approaches, future attempts may also allow neuroscientists to record from several spatially segregated areas simultaneously [256].

This strive for possibilities to acquire calcium signals from larger cell populations simultaneously is complemented by developments that aim at increasing the sampling frequency. The common denominator of these attempts is to minimise the time that the laser focal point spends on non-relevant areas [180]. I was able to contribute to an especially promising approach that is based on AODs for laser deflection [116] and allowed sampling rates of up to several hundred Hertz for multiple cells. With such high temporal resolution,

neural events can be observed that are invisible in regular frame-scan-based calcium imaging [163]. This is especially promising for the investigation of GABAergic neurons, where shorter spiking events and higher spontaneous firing rates, compared to pyramidal neurons, can be expected in at least some subtypes [109][15]. With increases in the sampling rate, probabilistic inference of neural connectivity based on neural activity may eventually become possible [253, 202].

Connectivity

In an initial idea, we intended to electrophysiologically control the spiking activity of selected GABAergic neurons by means of two-photon targeted patching [168], while performing 3D calcium imaging of the surrounding neural cell population [106] (Figure 4.4 on page 126). Such experiments would allow neurophysiologists to shine light on the functional role of specific GABAergic neurons *in vivo*. For example, this would be particularly interesting for Chandelier cells, given the recent evidence on their potentially excitatory action *in vitro* ([307, 273], reviewed in [308]) and the possibility to limit the number of candidate cells significantly by new genetic labelling techniques [307]. In addition, such an approach could also give first hints on the underlying connectivity by means of activity-based inference [202].

The recent advent of optogenetical tools might allow for a more efficient probing of individual neurons than with tedious two-photon targeted patching. By means of virus-mediated [172, 314] or transgenic expression of light-gated ion channels or pumps [92, 166] it might soon become possible to stimulate or suppress neuronal activity on the single-cell level using two-photon excitation [318, 237, 204]. Alternatively, a principal cell could be recorded from by targeted patching while neighbouring GABAergic cells are sequentially optogenetically perturbed. Similar to a very recent study by Raphael Yuste using two-photon uncaging in slices [93], connectivity could be inferred from the responses recorded in the principal cell.

---

[15]Unfortunately, the calcium signal intensity per AP is especially small in fast-spiking interneurons [162], currently excluding the reconstruction of single APs.
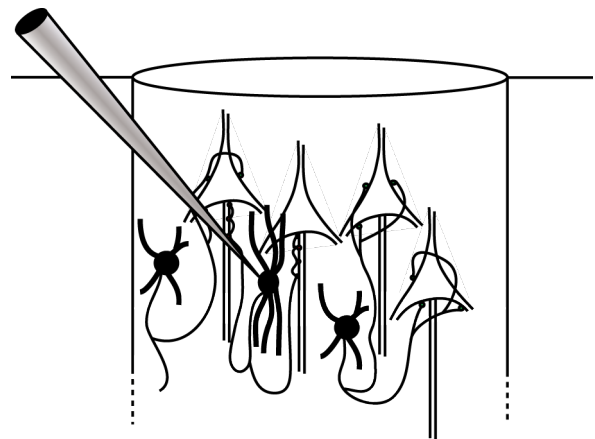

Figure 4.4: Targeted control of an identified GABAergic neuron by means of two-photon-targeted patching. With a specific cell under electrophysiological control, the effect of driving or suppressing its spiking activity could be observed in the surrounding cell population using 3D two-photon calcium imaging.

If two-photon-targeted patching is employed to gain control of a specific GABAergic neuron, further information about its connectivity can be gained by filling it with biocytin for later reconstruction of its morphology. A modified rabius virus serving as monosynaptic retrograde tracers can label cells from which a given GABAergic neuron receives input, thus further elucidating the local connectivity [302, 295, 53, 193].

Newest achievements have combined *in vivo* two-photon calcium imaging with either post mortem serial section electron microscopy to elucidate the detail anatomical connection pattern in a small volume around the cells previously imaged *in vivo* [25], or with *in vitro* electrophysiology of coronal sections to probe the functional connectivity [139, 167]. Although these new techniques have been demonstrated on acute preparations in these pilot studies, the same argument as above, to combine such techniques with chronic preparations, applies here, due to the highly labour-intensive procedures involved in both cases.

As I have briefly explained in Section 1.2.3, the function of individual neurons with the neuronal network strongly depends on how they are interconnected with the rest of the network. Knowledge about the underlying connectivity is required to causally explain activity that is observed in experiments, as well as to predict it. Understanding these causal relationships, in turn, is crucial to clarify the principles determining neuron function.

4.3.3 Taking the body into account

In artificial intelligence, a paradigm shift was provoked when the concept of embodiment was introduced, i.e. the concept that any intelligent system is mandatorily rooted in a physical body [230, 228]. In fact, the original idea that computers alone can become intelligent one day—provided enough computational power and proper algorithms—was completely abandoned in embodied artificial intelligence. An important principle in embodiment artificial intelligence research is the *principle of sensory-motor coordination*, which states that an intelligent agent actively structures the information perceived about the environment in order to facilitate learning; i.e. perception and action are tightly coupled [230, 229].

Biological organisms to which we attribute intelligence possess a physical manifestation (that we may call body) by definition, so they are always embodied. Nevertheless, many neuroscientific studies—although trying to understand the biological processes and components that underlie intelligent behaviour—focus on the brain while completely neglecting the role of the body. Also in the typical *in vivo* calcium imaging studies that have been carried out in the last decade, the bodies harbouring the brains under investigation were either completely ignored [163, 137] or merely used to feed sensory input into the system to emulate passive sensing [248, 317, 162]. Only recently, two-photon calcium imaging studies began to use awake, head-restrained mice that are able to make at least minimal active use of their sensory organs in order to interact with their environment [220, 7]. Studies using virtual realities in which animals can navigate, although being physically head-fixed, allow them to engage in even more extended sensory-motor coordination [75]. The ultimate discipline of *in vivo* two-photon calcium imaging is that of freely behaving animals [250]. So far it has only been achieved in a few pilot experiments, but they have had the

clear goal to study natural interaction of the subject with its environment under controlled conditions.

An alternative approach that neuroscientists and roboticists have followed together is the use of bio-inspired robots in order to test hypotheses about the mechanisms governing complete agents. For example, Gerald Edelman and colleagues used a series of "brain-based devices" to test neural models in a real-world environment [169, 83]. While such devices were solving a specific task, neural activity of structures such as hippocampus or cerebellum could be probed or even manipulated at arbitrary resolution [253, 197, 170, 254, 255]. In the future, *in vivo* two-photon calcium imaging and brain-based devices may become allies. In one approach, brain-based devices may be used to test hypotheses formulated based on *in vivo* imaging data or vice versa. Furthermore, experiments can be envisaged, in which neural activity measured *in vivo* is copied in real-time onto the cellular counterparts of brain-based devices. Or, the other way around, the neural activity observed in a brain-based device may be entrained in cells optogenetically controlled in a living animal. Such experiments would blur the boundaries between the two systems (i.e. between the animal and the brain-based device), and in some sense correspond to a cyborg with two bodies.

While the focus of Edelman and coworkers was mainly on how neural activity in their brain-based devices related to the their behaviour, another team led by Rolf Pfeifer at University of Zurich tested the effect of different body geometries on behavioural performance using both real robots and simulations [91]. In the future, this concept could also inspire *in vivo* two-photon calcium imaging experiments; sensory input could be fed into an awake, but head-restrained mouse, in a way that various different sensor morphologies are emulated. For example, while a mouse is navigating in a virtual environment, different whisker arrangements and movements could be simulated while the mouse interacts with virtual objects (Figure 4.5 on page 129). The virtual sensory input generated would be translated in real-time to corresponding input patterns applied to the mouse's whisker pads using an appropriate multi-whisker stimulation device [149]. With this setup, the impact of different whisker morphologies on neural activity could be investigated in a single experiment. Using similar approaches, other central principles of the embodiment paradigm, such as the redundancy principle[16] or the value principle[17] could be experimentally tested in a biological system [230].

---

[16]The *redundancy principle* states that an intelligent system requires multiple sensory channels with a potential information overlap. This information overlap serves as substrate for associative learning.

[17]The *value principle* states that an agent has to be equipped with a value system, which funnels unsupervised learning by means of self-organisation.
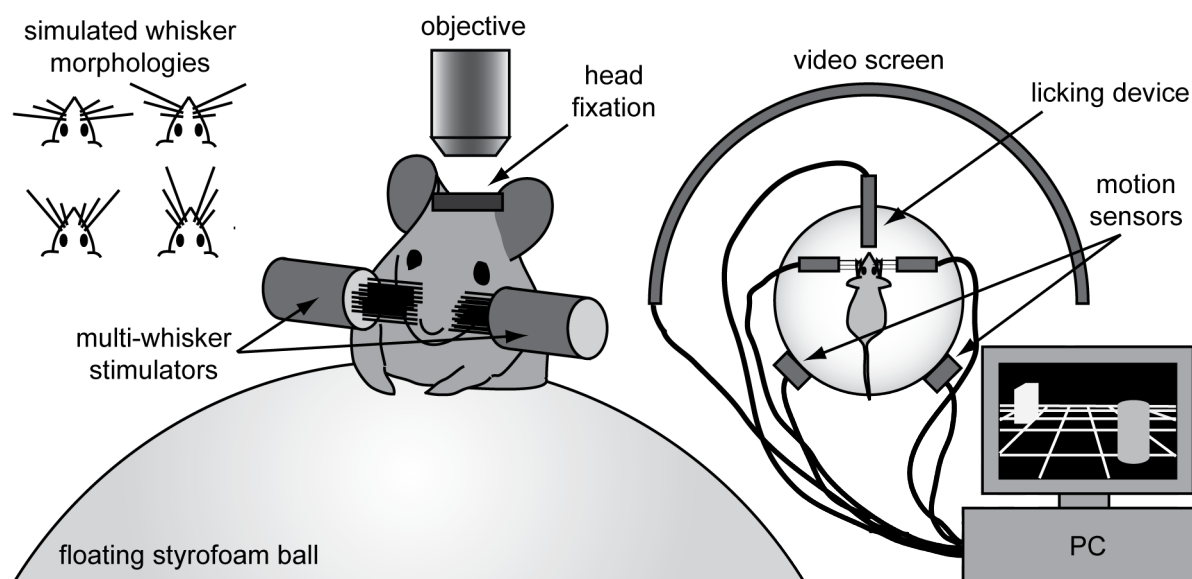
Figure 4.5: Simulating different sensor morphologies for navigation in a virtual environment. The head-fixed mouse is walking on a free-floating styrofoam ball while being presented with the visual scene of a virtual landscape on a video screen. The motion of the ball is captured by sensors and results in rotation or translation of the first-person perspective of the mouse in the virtual environment. If the whiskers belonging to the simulated body in the virtual environment come in contact with virtual objects of that environment, the real (but trimmed) whiskers of the mouse are stimulated accordingly by a multi-whisker stimulation device. Different whisker morphologies or movement can be simulated (see upper left for examples). Reinforcement learning of the mouse can be provoked by providing an appropriate reward (such as water in the case of a water-deprived animal) for certain behaviour by means of a controllable licking device. Left: front view; right: top view.

4.4 Final conclusion

In summary, I believe that we are currently not far from a *tipping point* of *in vivo* two-photon calcium imaging. Due to the recent availability of sufficiently sensitive GECIs and suitable viral transfection tools, we can now create chronic preparations that are stable over weeks and months. The relative overhead to create such preparations, relative to the amount of data that can be gained, is much smaller than for acute preparations based on MCBL of membrane-permeable calcium indicators. As a consequence, intricate preliminary and post-processing procedures become worthwhile. Thus, I expect not only quantity but also quality of obtainable data to strongly increase during the next few years. Combined experiments will soon become possible; while awake animals engage in a specific task, the activity of large cell populations in their brain can be observed in real-time, and large-scale cell type characterisation and connectivity analysis are performed *post mortem*. I expect methods for IHC-based cell type characterisation, as presented in this thesis, to become a routine procedure in future chronic experiments, thereby flexibly extending limited *in vivo* cell type discrimination capabilities based on transgenic labels.

On the microscopy side, the developments of the last few years paved the way towards

high-speed interrogation of large cell populations in three-dimensional volumes. With HelioScan, I introduced a software package that allows laboratories employing *in vivo* 2PM imaging to capitalise, with minimal effort, on achievements in the fast-paced field of new scanning technologies. Researchers can make use of software components that have already been developed by other people, and, if required, they can implement extensions and customisations in a structured fashion. Currently, HelioScan is still strongly dependent on the efforts of a few lead developers. In order for HelioScan to maturate into a self-sustaining initiative, it will be crucial to significantly expand both the user and the developer base during the next months and years.

Apart from highly promising developments on the methodological side, I detect a large backlog in the field when it comes to efficiently making use of the resulting data, which is being generated at an increasing rate. Thus, I recommend efforts aiming at efficient analysis, annotation and integration of both raw and post-processed data into interoperable databases that enable the scientific community to access them in a quantitative and semantically meaningful way for the purpose of re- and meta-analysis.

List of abbrevations

λ_{ex}	excitation wavelength
2PM	two-photon laser-scanning microscopy
3D	three-dimensional
ADC	analog-to-digital converter
ADT	abstract data type
AIP	average-intensity projection
AIS	axon initial segment
AM	acethoxymethyl ester
AMCA	aminomethylcoumarin acetate
ANOVA	analysis of variance
AOD	acousto-optic deflector
AP	action potential
BAPTA	1,2-bis(o-aminophenoxy)ethane-N,N,N',N'-tetraacetic acid
BNC	Bayonet Neill-Concelman
BP	band-pass filter
BIOS	basic input/output system
CaBP	calcium-binding protein
CB	Calbindin
CCD	charge-coupled device
CCK	Cholecystokinin
CFP	cyan fluorescent protein
CNS	central nervous system
COM	Component Object Model

COX	cytochrome-oxidase C
CPU	central processing unit
CR	Calretinin
DAB	3,3'-diaminobenzidine
DAC	digital-to-analog converter
DAPI	4',6-diamidino-2-phenylindole
DC	dichroic mirror
DMA	direct memory access
DNA	deoxyribonucleic acid
DL488	DyLight 488
DL594	DyLight 594
DL649	DyLight 649
DMSO	dimethyl sulfoxide
dNTP	deoxyribonucleotide
EDTA	ethylenediaminetetraacetic acid
FIFO	first-in-first-out
FISH	fluorescence *in situ* hybridisation
FPGA	field-programmable gate array
FRET	fluorescence resonance energy tranfer
GABA	γ-amino butyric acid
GAD67	γ-amino butyric acid dehydrogenase 67
GAD67-GFP	knock-in mouse line expressing GFP at the GAD67 locus
GECI	genetically encoded calcium indicator
GFP	green fluorescent protein
GUI	graphical user interface
HEPES	2-(4-(2-hydroxyethyl)-1-piperazinyl)-ethansulfonic acid

IDE	integrated development environment
IHC	immunohistochemistry
IMAQ	image acquisition interface for LabVIEW
I/O	input/output
ICA	independent component analysis
IOS	intrinsic optical signal
IPSP	inhibitory postsynaptic potential
IR	infrared
L1	cortical layer I
L2	cortical layer II
L2/3	cortical layer II/III
L4	cortical layer IV
LED	light-emitting diode
LP	long-pass filter
LVOOP	LabVIEW object-oriented programming
LSM	laser-scanning microscopy
MAX	Measurement & Automation Explorer
MCBL	multi-cell bolus loading
mRNA	messenger RNA
NA	numerical aperture
NDS	normal donkey serum
NI	National Instruments
NIF	Neuroscience Information Framework
NRR	normal rat ringer
NPY	Neuropeptide Y
OBO	Open Biomedical Ontologies

OEM   original equipment manufacturer

OGB-1   Oregon Green 488 BAPTA-1

OME   Open Microscopy Environment

OOP   object-oriented programming

PBS   phosphate-buffered saline

PC   personal computer

PCI   Peripheral Component Interconnect

PCR   polymerase chain reaction

PFA   paraformaldehyde

PV   Parvalbumin

PXI   PCI eXtensions for Instrumentation

PXIe   PXI express

PMT   photo-multiplier tube

PSF   point-spread function

rAAV   recombinant adeno-associated virus

RAM   random-access memory

RF   radio frequency

RNA   ribonucleic acid

ROI   region-of-interest

RRX   Rhodamine Red-X

RT-PCR   reverse transcription PCR

SC   subcomponent

SD   standard deviation

SDS   sodium dodecyl sulfate

SEM   standard error of the mean

SMB   SubMiniature version B

SNR	signal-to-noise ratio
SOM	Somatostatin
SP	short-pass filter
SR101	sulforhodamine 101
TBE	TRIS-borat-EDTA
TIFF	Tagged Image File Format
TLC	top-level component
TPA	two-photon absorption
TRIS	tris(hydroxymethyl)-aminomethan
TTL	transistor-transistor logic
UML	Unified Modeling Language
UV	ultraviolett
VI	Virtual Instrument
VIP	Vasointestinal Peptide
VCS	version control system
VPL	visual programming language
XML	Extensible Mark-up Language
YC3.60	Yellow Cameleon 3.60
YFP	yellow fluorescent protein

Bibliography

[1] L. F. Abbott and S. B. Nelson. Synaptic plasticity: taming the beast. *Nat Neurosci*, 3 Suppl:1178–1183, 2000.

[2] M.D. Abramoff, P.J. Magelhaes, and S.J. Ram. Image processing with ImageJ. *Biophotonics International*, 11(7):36–42, 2004.

[3] B. Aiello and L. Sachs. *Configuration management best practices: practical methods that work in the real world.* Addison-Wesley, Upper Saddle River, NJ, 2011.

[4] B. Alberts, A. Johnson, J. Lewis, M. Raff, K. Roberts, and P. Walter. *Molecular Biology of the Cell.* Garland Science, New York, NY, 4th edition, 2002.

[5] H. J. Alitto and Y. Dan. Function of inhibition in visual cortical processing. *Curr Opin Neurobiol*, 20(3):340–346, 2010.

[6] W.B. Amos, J.G. White, and M. Fordham. Use of confocal imaging in the study of biological structures. *Appl. Opt.*, 26(16):3239–3243, 1987.

[7] M. L. Andermann, A. M. Kerlin, and R. C. Reid. Chronic cellular imaging of mouse visual cortex during operant behavior and passive viewing. *Front Cell Neurosci*, 4:3, 2010.

[8] P. J. Andres-Barquin. Santiago Ramón y Cajal and the Spanish school of neurology. *Lancet Neurol*, 1(7):445–452, 2002.

[9] M.A. Arbib, P. Érdi, and J. Szentágothai. *Neural Organization.* The MIT Press, Cambridge, MA, 1998.

[10] D.J. Armstrong. The quarks of object-oriented development. *Communications of the ACM*, 49(2):123–128, 2006.

[11] K.S. Arun, T.S. Huang, and S.D. Blostein. Least-squares fitting of two 3-D point sets. *IEEE Transactions on Pattern Analysis and Machine Intelligence*, 9(5):698–700, 1987.

[12] G. A. Ascoli. Mobilizing the base of neuroscience data: the case of neuronal morphologies. *Nat Rev Neurosci*, 7(4):318–324, 2006.

[13] G. A. Ascoli, L. Alonso-Nanclares, S. A. Anderson, G. Barrionuevo, R. Benavides-Piccione, A. Burkhalter, G. Buzsaki, B. Cauli, J. Defelipe, A. Fairen, D. Feldmeyer, G. Fishell, Y. Fregnac, T. F. Freund, D. Gardner, E. P. Gardner, J. H. Goldberg,

M. Helmstaedter, S. Hestrin, F. Karube, Z. F. Kisvarday, B. Lambolez, D. A. Lewis, O. Marin, H. Markram, A. Munoz, A. Packer, C. C. Petersen, K. S. Rockland, J. Rossier, B. Rudy, P. Somogyi, J. F. Staiger, G. Tamas, A. M. Thomson, M. Toledo-Rodriguez, Y. Wang, D. C. West, and R. Yuste. Petilla terminology: nomenclature of features of GABAergic interneurons of the cerebral cortex. *Nat Rev Neurosci*, 9(7):557–568, 2008.

[14] C. C. Ashley. Aequorin-monitored calcium transients in single maia muscle fibres. *J Physiol*, 203(1):32P–33P, 1969.

[15] P.W. Atkins. *Physical Chemistry*. Oxford University Press, Oxford, United Kingdom, 5th edition, 1994.

[16] K. G. Baimbridge, M. R. Celio, and J. H. Rogers. Calcium-binding proteins in the nervous system. *Trends Neurosci*, 15(8):303–308, 1992.

[17] P. F. Baker, A. L. Hodgkin, and E. B. Ridgway. Depolarization and calcium entry in squid giant axons. *J Physiol*, 218(3):709–755, 1971.

[18] E. Baroth and C. Hartsough. Visual programming in the real world. In *Visual Object-Oriented Programming: Concepts and Environments*, pages 21–42. Prentice Hall, Upper Saddle River, NJ, 1995.

[19] K. J. Bender and L. O. Trussell. Axon initial segment Ca^{2+} channels influence action potential generation and timing. *Neuron*, 61(2):259–271, 2009.

[20] A. Bernard, S. A. Sorensen, and E. S. Lein. Shifting the paradigm: new approaches for characterizing and classifying neurons. *Curr Opin Neurobiol*, 19(5):530–536, 2009.

[21] F. Bestvater, E. Spiess, G. Stobrawa, M. Hacker, T. Feurer, T. Porwol, U. Berchner-Pfannschmidt, C. Wotzlaw, and H. Acker. Two-photon fluorescence absorption and emission spectra of dyes relevant for cell imaging. *J Microsc*, 208(Pt 2):108–115, 2002.

[22] J. Bewersdorf, R. Pick, and S. W. Hell. Multifocal multiphoton microscopy. *Opt Lett*, 23(9):655–657, 1998.

[23] M. Biagioli. Rights or rewards? Changing frameworks of scientific authorship. In M. Biagioli and P. Galison, editors, *Scientific authorship: credit and intellectual property in science*, pages 253–280. Routledge, New York, NY, 2003.

[24] P.A. Blume. *The LabVIEW Book*. Prentice Hall, Upper Saddle River, NJ, 2007.

[25] D. D. Bock, W. C. Lee, A. M. Kerlin, M. L. Andermann, G. Hood, A. W. Wetzel, S. Yurgenson, E. R. Soucy, H. S. Kim, and R. C. Reid. Network anatomy and in vivo physiology of visual cortical neurons. *Nature*, 471(7337):177–182, 2011.

[26] T. Bonhoeffer and M. Hübener. A practical guide: Intrinsic optical imaging of functional map development in mammalian visual cortex. In *Imaging in Neuroscience and Development: a Laboratory Manual*, pages 233–238. Cold Spring Harbor Laboratory Press, Woodbury NY, 2005.

[27] E. J. Botcherby, R. Juskaitis, M. J. Booth, and T. Wilson. An optical technique for remote focusing in microscopy. *Opt Comm*, 281:880–887, 2008.

[28] K. Brodmann. *Vergleichende Lokalisationslehre der Grosshirnrinde*. Barth, Leipzig, Germany, 1909.

[29] J. E. Brown, L. B. Cohen, P. De Weer, L. H. Pinto, W. N. Ross, and B. M. Salzberg. Rapid changes in intracellular free calcium concentration. detection by metallochromic indicator dyes in squid giant axon. *Biophys J*, 15(11):1155–1160, 1975.

[30] C. Brum, L. McKane, and G. Karp. *Biology: Exploring Life (Volume 5: Diversity and Classification)*. John Wiley & Sons, New York, NY, 2nd edition, 1994.

[31] J. Bu, V. Sathyendra, N. Nagykery, and C. Geula. Age-related changes in calbindin$_{D28k}$, calretinin, and parvalbumin-immunoreactive neurons in the human cerebral cortex. *Exp Neurol*, 182(1):220–231, 2003.

[32] W. J. Bug, G. A. Ascoli, J. S. Grethe, A. Gupta, C. Fennema-Notestine, A. R. Laird, S. D. Larson, D. Rubin, G. M. Shepherd, J. A. Turner, and M. E. Martone. The NIFSTD and BIRNLex vocabularies: building comprehensive ontologies for neuroscience. *Neuroinformatics*, 6(3):175–194, 2008.

[33] D. V. Buonomano and W. Maass. State-dependent computations: spatiotemporal processing in cortical networks. *Nat Rev Neurosci*, 10(2):113–125, 2009.

[34] E.K. Burke and G. Kendall. *Search Methodologies: Introductory Tutorials in Optimization and Decision Support Techniques*. Springer, New York, 2005.

[35] A. Burkhalter. Many specialists for suppressing cortical excitation. *Front Neurosci*, 2(2):155–167, 2008.

[36] S. J. Butt, M. Fuccillo, S. Nery, S. Noctor, A. Kriegstein, J. G. Corbin, and G. Fishell. The temporal and spatial origins of cortical interneurons predict their physiological subtype. *Neuron*, 48(4):591–604, 2005.

[37] S. J. Butt, V. H. Sousa, M. V. Fuccillo, J. Hjerling-Leffler, G. Miyoshi, S. Kimura, and G. Fishell. The requirement of Nkx2-1 in the temporal specification of cortical interneuron subtypes. *Neuron*, 59(5):722–732, 2008.

[38] D. P. Buxhoeveden and M. F. Casanova. The minicolumn and evolution of the brain. *Brain Behav Evol*, 60(3):125–151, 2002.

[39] D. P. Buxhoeveden and M. F. Casanova. The minicolumn hypothesis in neuroscience. *Brain*, 125(Pt 5):935–951, 2002.

[40] G. Buzsaki. Feed-forward inhibition in the hippocampal formation. *Prog Neurobiol*, 22(2):131–153, 1984.

[41] N.A. Campbell. *Biology*. Benjamin Cummings Publishing Company, San Francisco, CA, 1996.

[42] L. Cancedda, H. Fiumelli, K. Chen, and M. M. Poo. Excitatory GABA action is essential for morphological maturation of cortical neurons in vivo. *J Neurosci*, 27(19):5224–5235, 2007.

[43] E. Carbone, F. Conti, and R. Fioravanti. Fluorescence polarization studies of squid giant axons stained with N-methylanilinonaphthalenesulfonates. *Biophys Struct Mech*, 1(3):221–237, 1975.

[44] B. Cauli, E. Audinat, B. Lambolez, M. C. Angulo, N. Ropert, K. Tsuzuki, S. Hestrin, and J. Rossier. Molecular and physiological diversity of cortical nonpyramidal cells. *J Neurosci*, 17(10):3894–3906, 1997.

[45] B. Cauli, J. T. Porter, K. Tsuzuki, B. Lambolez, J. Rossier, B. Quenet, and E. Audinat. Classification of fusiform neocortical interneurons based on unsupervised clustering. *Proc Natl Acad Sci U S A*, 97(11):6144–6149, 2000.

[46] M. R. Celio and C. W. Heizmann. Calcium-binding protein parvalbumin as a neuronal marker. *Nature*, 293(5830):300–302, 1981.

[47] B. Chattopadhyaya, G. Di Cristo, H. Higashiyama, G. W. Knott, S. J. Kuhlman, E. Welker, and Z. J. Huang. Experience and activity-dependent maturation of perisomatic GABAergic innervation in primary visual cortex during a postnatal critical period. *J Neurosci*, 24(43):9598–9611, 2004.

[48] X. Chen, U. Leischner, N. L. Rochefort, I. Nelken, and A. Konnerth. Functional mapping of single spines in cortical neurons in vivo. *Nature*, 475(7357):501–505, 2011.

[49] A. Cheng, J. T. Goncalves, P. Golshani, K. Arisaka, and C. Portera-Cailliau. Simultaneous two-photon calcium imaging at different depths with spatiotemporal multiplexing. *Nat Methods*, 8(2):139–142, 2011.

[50] K.R. Chi. Imaging and detection: focusing on software. *Nat Methods*, 5(7):651–653, 2008.

[51] Y. H. Ch'ng and R. C. Reid. Cellular imaging of visual cortex reveals the spatial and functional organization of spontaneous activity. *Front Integr Neurosci*, 4, 2010.

[52] K. H. Cho, J. H. Jang, H. J. Jang, M. J. Kim, S. H. Yoon, T. Fukuda, F. Tennigkeit, W. Singer, and D. J. Rhie. Subtype-specific dendritic Ca^{2+} dynamics of inhibitory interneurons in the rat visual cortex. *J Neurophysiol*, 104(2):840–853, 2010.

[53] J. Choi, J. A. Young, and E. M. Callaway. Selective viral vector transduction of ErbB4 expressing cortical interneurons in vivo with a viral receptor-ligand bridge protein. *Proc Natl Acad Sci U S A*, 107(38):16703–16708, 2010.

[54] L. B. Cohen. Changes in neuron structure during action potential propagation and synaptic transmission. *Physiol Rev*, 53(2):373–418, 1973.

[55] L. B. Cohen, B. Hille, and R. D. Keynes. Changes in axon birefringence during the action potential. *J Physiol*, 211(2):495–515, 1970.

[56] L. B. Cohen, B. Hille, R. D. Keynes, D. Landowne, and E. Rojas. Analysis of the potential-dependent changes in optical retardation in the squid giant axon. *J Physiol*, 218(1):205–237, 1971.

[57] A. Colin, M. Faideau, N. Dufour, G. Auregan, R. Hassig, T. Andrieu, E. Brouillet, P. Hantraye, G. Bonvento, and N. Deglon. Engineered lentiviral vector targeting astrocytes in vivo. *Glia*, 57(6):667–679, 2009.

[58] The ATLAS Collaboration. Search for a heavy particle decaying into an electron and a muon with the ATLAS detector in $\sqrt{s} = 7$ TeV *pp* collisions at the LHC. *Phys Rev Lett*, 106(25), 2011.

[59] B. Collins-Sussman, B.W. Fitzpatrick, and C.M. Pilato. *Version Control with Subversion*. O'Reilly Media, Sebastopol, CA, 2nd edition, 2008.

[60] J. Conway and S. Watts. *A Software Engineering Approach to LabVIEW*. Prentice Hall, Upper Saddle River, NJ, 2003.

[61] S. Crochet, J. F. Poulet, Y. Kremer, and C. C. Petersen. Synaptic mechanisms underlying sparse coding of active touch. *Neuron*, 69(6):1160–1175, 2011.

[62] N. M. da Costa and K. A. Martin. Whose cortical column would that be? *Front Neuroanat*, 4:16, 2010.

[63] O. Dahl and K. Nygaard. Class and subclass declarations. In J.N. Buxton, editor, *Simulation Programming Languages*, pages 158–174, Amsterdam, the Netherlands, 1967.

[64] J. A. De Carlos and J. Borrell. A historical reflection of the contributions of Cajal and Golgi to the foundations of neuroscience. *Brain Res Rev*, 55(1):8–16, 2007.

[65] F. de Castro, L. Lopez-Mascaraque, and J. A. De Carlos. Cajal: lessons on brain development. *Brain Res Rev*, 55(2):481–489, 2007.

[66] G. I. de Jong, P. A. Naber, E. A. Van der Zee, L. T. Thompson, J. F. Disterhoft, and P. G. Luiten. Age-related loss of calcium binding proteins in rabbit hippocampus. *Neurobiol Aging*, 17(3):459–465, 1996.

[67] J. DeFelipe. Neocortical neuronal diversity: chemical heterogeneity revealed by colocalization studies of classic neurotransmitters, neuropeptides, calcium-binding proteins, and cell surface molecules. *Cereb Cortex*, 3(4):273–289, 1993.

[68] J. DeFelipe. From the connectome to the synaptome: an epic love story. *Science*, 330(6008):1198–1201, 2010.

[69] W. Denk, J. H. Strickler, and W. W. Webb. Two-photon laser scanning fluorescence microscopy. *Science*, 248(4951):73–76, 1990.

[70] W. Denk and K. Svoboda. Photon upmanship: why multiphoton imaging is more than a gimmick. *Neuron*, 18(3):351–357, 1997.

[71] J. Diez-Garcia, S. Matsushita, H. Mutoh, J. Nakai, M. Ohkura, J. Yokoyama, D. Dimitrov, and T. Knöpfel. Activation of cerebellar parallel fibers monitored in transgenic mice expressing a fluorescent Ca^{2+} indicator protein. *Eur J Neurosci*, 22(3):627–635, 2005.

[72] T. Dingermann. *Gentechnik - Biotechnik*. Wissenschaftliche Verlagsgesellschaft mbH, Stuttgart, 1999.

[73] H. U. Dodt, U. Leischner, A. Schierloh, N. Jahrling, C. P. Mauch, K. Deininger, J. M. Deussing, M. Eder, W. Zieglgansberger, and K. Becker. Ultramicroscopy: three-dimensional visualization of neuronal networks in the whole mouse brain. *Nat Methods*, 4(4):331–336, 2007.

[74] D. A. Dombeck, M. S. Graziano, and D. W. Tank. Functional clustering of neurons in motor cortex determined by cellular resolution imaging in awake behaving mice. *J Neurosci*, 29(44):13751–13760, 2009.

[75] D. A. Dombeck, C. D. Harvey, L. Tian, L. L. Looger, and D. W. Tank. Functional imaging of hippocampal place cells at cellular resolution during virtual navigation. *Nat Neurosci*, 13(11):1433–1440, 2010.

[76] D. A. Dombeck, A. N. Khabbaz, F. Collman, T. L. Adelman, and D. W. Tank. Imaging large-scale neural activity with cellular resolution in awake, mobile mice. *Neuron*, 56(1):43–57, 2007.

[77] R. J. Douglas and K. A. Martin. Mapping the matrix: the ways of neocortex. *Neuron*, 56(2):226–238, 2007.

[78] B.P. Douglass. *Doing Hard Time - Developing Real-Time Systems with UML, Objects, Frameworks, and Patterns*. Addison Wesley Longman, Inc., Reading, MA, 1999.

[79] R. Druga. Neocortical inhibitory system. *Folia Biol (Praha)*, 55(6):201–217, 2009.

[80] H. Du, R.A. Fuh, A. Corkan, and J.S. Lindsey. PhotochemCAD: A computer-aided design and research tool in photochemistry. *Photochem Photobiol*, 68(2):141–142, 1998.

[81] G. Duemani Reddy, K. Kelleher, R. Fink, and P. Saggau. Three-dimensional random access multiphoton microscopy for functional imaging of neuronal activity. *Nat Neurosci*, 11(6):713–720, 2008.

[82] J. Dunlop, M. Bowlby, R. Peri, D. Vasilyev, and R. Arias. High-throughput electrophysiology: an emerging paradigm for ion-channel screening and physiology. *Nat Rev Drug Discov*, 7(4):358–368, 2008.

[83] G. M. Edelman. Learning in and from brain-based devices. *Science*, 318(5853):1103–1105, 2007.

[84] A. Edelstein, N. Amodaj, K. Hoover, R. Vale, and N. Stuurman. Computer control of microscopes using μManager. *Curr Protoc Mol Biol*, Chapter 14:Unit 14.20, 2010.

[85] Editorial. Software by any name. *Nat Methods*, 6(8):547–548, 2009.

[86] C. J. Engelbrecht, R. S. Johnston, E. J. Seibel, and F. Helmchen. Ultra-compact fiber-optic two-photon microscope for functional fluorescence imaging in vivo. *Opt Express*, 16(8):5556–5564, 2008.

[87] A. Evstratova, S. Chamberland, and L. Topolnik. Cell type-specific and activity-dependent dynamics of action potential-evoked Ca^{2+} signals in dendrites of hippocampal inhibitory interneurons. *J Physiol*, 589(Pt 8):1957–1977, 2011.

[88] D. W. Eyles, J. J. McGrath, and G. P. Reynolds. Neuronal calcium-binding proteins and schizophrenia. *Schizophr Res*, 57(1):27–34, 2002.

[89] D. Farley. *Continuous Delivery: Reliable Software Releases Through Build, Test, and Deployment Automation.* Addison-Wesley Longman, Boston, MA, 2010.

[90] R. Fdez Galan, S. Sachse, C. G. Galizia, and A. V. Herz. Odor-driven attractor dynamics in the antennal lobe allow for simple and rapid olfactory pattern classification. *Neural Comput*, 16(5):999–1012, 2004.

[91] M. Fend, S. Bovet, and R. Pfeifer. On the influence of morphology of tactile sensors for behavior and control. *Artificial Intelligence*, 8(54):686–695, 2006.

[92] L. Fenno, O. Yizhar, and K. Deisseroth. The development and application of optogenetics. *Annu Rev Neurosci*, 34:389–412, 2011.

[93] E. Fino and R. Yuste. Dense inhibitory connectivity in neocortex. *Neuron*, 69(6):1188–1203, 2011.

[94] G. Fishell and B. Rudy. Mechanisms of inhibition within the telencephalon: "where the wild things are". *Annu Rev Neurosci*, 34:535–567, 2011.

[95] R. Franconville, G. Revet, G. Astorga, B. Schwaller, and I. Llano. Somatic calcium level reports integrated spiking activity of cerebellar interneurons in vitro and in vivo. *J Neurophysiol*, 2011.

[96] T. F. Freund and I. Katona. Perisomatic inhibition. *Neuron*, 56(1):33–42, 2007.

[97] R. D. Frostig, E. E. Lieke, D. Y. Ts'o, and A. Grinvald. Cortical functional architecture and local coupling between neuronal activity and the microcirculation revealed by in vivo high-resolution optical imaging of intrinsic signals. *Proc Natl Acad Sci U S A*, 87(16):6082–6086, 1990.

[98] H. Frowein. Titan-Saphir Laser. *Optik & Photonik*, 2(1):48–53, 2007.

[99] T. Förster. Zwischenmolekulare Energiewanderung und Fluoreszenz. *Ann. Phys.*, 437(1-2):55–75, 1948.

[100] E. Gamma, R. Helm, R. Johnson, and J.M. Vlissides. *Design Patterns. Elements of Reusable Object-Oriented Software.* Addison-Wesley Longman, Amsterdam, the Netherlands, 1994.

[101] O. Garaschuk, R. I. Milos, C. Grienberger, N. Marandi, H. Adelsberger, and A. Konnerth. Optical monitoring of brain function in vivo: from neurons to networks. *Pflugers Arch*, 453(3):385–396, 2006.

[102] O. Garaschuk, R. I. Milos, and A. Konnerth. Targeted bulk-loading of fluorescent indicators for two-photon brain imaging in vivo. *Nat Protoc*, 1(1):380–386, 2006.

[103] D. Gardner, H. Akil, G. A. Ascoli, D. M. Bowden, W. Bug, D. E. Donohue, D. H. Goldberg, B. Grafstein, J. S. Grethe, A. Gupta, M. Halavi, D. N. Kennedy, L. Marenco, M. E. Martone, P. L. Miller, H. M. Muller, A. Robert, G. M. Shepherd, P. W. Sternberg, D. C. Van Essen, and R. W. Williams. The Neuroscience Information Framework: a data and knowledge environment for neuroscience. *Neuroinformatics*, 6(3):149–160, 2008.

[104] W. Göbel and F. Helmchen. In vivo calcium imaging of neural network function. *Physiology*, 22:358–365, 2007.

[105] W. Göbel and F. Helmchen. New angles on neuronal dendrites in vivo. *J Neurophysiol*, 98(6):3770–3779, 2007.

[106] W. Göbel, B. M. Kampa, and F. Helmchen. Imaging cellular network dynamics in three dimensions using fast 3D laser scanning. *Nat Methods*, 4(1):73–79, 2007.

[107] J. Gehrmann, Y. Matsumoto, and G. W. Kreutzberg. Microglia: intrinsic immuneffector cell of the brain. *Brain Res Brain Res Rev*, 20(3):269–287, 1995.

[108] D. M. Gelman and O. Marin. Generation of interneuron diversity in the mouse cerebral cortex. *Eur J Neurosci*, 31(12):2136–2141, 2010.

[109] L. J. Gentet, M. Avermann, F. Matyas, J. F. Staiger, and C. C. Petersen. Membrane potential dynamics of GABAergic neurons in the barrel cortex of behaving mice. *Neuron*, 65(3):422–435, 2010.

[110] A. J. Giessel and B. L. Sabatini. M1 muscarinic receptors boost synaptic potentials and calcium influx in dendritic spines by inhibiting postsynaptic SK channels. *Neuron*, 68(5):936–947, 2010.

[111] M. Goeppert-Mayer. Über Elementarakte mit zwei Quantensprüngen. *Ann Phys*, 401(3):273–295, 1931.

[112] I. G. Goldberg, C. Allan, J. M. Burel, D. Creager, A. Falconi, H. Hochheiser, J. Johnston, J. Mellen, P. K. Sorger, and J. R. Swedlow. The Open Microscopy Environment (OME) data model and XML file: open tools for informatics and quantitative analysis in biological imaging. *Genome Biol*, 6(5):R47, 2005.

[113] Y. Gonchar and A. Burkhalter. Three distinct families of GABAergic neurons in rat visual cortex. *Cereb Cortex*, 7(4):347–358, 1997.

[114] Y. Gonchar, Q. Wang, and A. Burkhalter. Multiple distinct subtypes of GABAergic neurons in mouse visual cortex identified by triple immunostaining. *Front Neuroanat*, 1:3, 2007.

[115] B. F. Grewe and F. Helmchen. Optical probing of neuronal ensemble activity. *Curr Opin Neurobiol*, 19(5):520–529, 2009.

[116] B. F. Grewe, D. Langer, H. Kasper, B. M. Kampa, and F. Helmchen. High-speed in vivo calcium imaging reveals neuronal network activity with near-millisecond precision. *Nat Methods*, 7(5):399–405, 2010.

[117] B. F. Grewe, F. F. Voigt, M. van 't Hoff, and F. Helmchen. Fast two-layer two-photon imaging of neuronal cell populations using an electrically tunable lens. *Biomed Opt Express*, 2(7):2035–2046, 2011.

[118] A. Grinvald, D. Sharon, H. Slovin, and I. Vanzetta. Intrinsic signal imaging in the neocortex: Implications for hemodynamic-based function imaging. In R. Yuste and A. Konnerth, editors, *Imaging in Neuroscience and Development: a Laboratory Manual*. Cold Spring Harbor Laboratory Press, Woodbury NY, 2005.

[119] L. Gulick. *Notes on the Theory of Organization*. Papers on the Science of Administration. Institute of Public Administration., New York, NY, 1936.

[120] A. T. Gulledge and G. J. Stuart. Excitatory actions of GABA in the cortex. *Neuron*, 37(2):299–309, 2003.

[121] H.-P. Gumm and M. Sommer. *Einführung in die Informatik*. R. Oldenbourg Verlag, München, Germany, 1998.

[122] A. Gupta, W. Bug, L. Marenco, X. Qian, C. Condit, A. Rangarajan, H. M. Muller, P. L. Miller, B. Sanders, J. S. Grethe, V. Astakhov, G. Shepherd, P. W. Sternberg, and M. E. Martone. Federated access to heterogeneous information resources in the Neuroscience Information Framework (NIF). *Neuroinformatics*, 6(3):205–217, 2008.

[123] A. Gupta, Y. Wang, and H. Markram. Organizing principles for a diversity of GABAergic interneurons and synapses in the neocortex. *Science*, 287(5451):273–278, 2000.

[124] H. Gutch, D. Battaglia, A. Karagiannis, T. Gallopin, and B. Cauli. Fuzzy classification and inference of interneuronal types. *FENS Abstr*, 5:027.23, 2010.

[125] B. Haider and D. A. McCormick. Rapid neocortical dynamics: cellular and network mechanisms. *Neuron*, 62(2):171–189, 2009.

[126] B. Haider and D. A. McCormick. Rapid neocortical dynamics: cellular and network mechanisms. *Neuron*, 62(2):171–189, 2009.

[127] F. Haiss, R. Jolivet, M. T. Wyss, J. Reichold, N. B. Braham, F. Scheffold, M. P. Krafft, and B. Weber. Improved in vivo two-photon imaging after blood replacement by perfluorocarbon. *J Physiol*, 587(Pt 13):3153–3158, 2009.

[128] K. D. Harris. Neural signatures of cell assembly organization. *Nat Rev Neurosci*, 6(5):399–407, 2005.

[129] T. C. Harrison, A. Sigler, and T. H. Murphy. Simple and cost-effective hardware and software for functional brain mapping using intrinsic optical signal imaging. *J Neurosci Methods*, 182(2):211–218, 2009.

[130] B. Heider, J. L. Nathanson, E. Y. Isacoff, E. M. Callaway, and R. M. Siegel. Two-photon imaging of calcium in virally transfected striate cortical neurons of behaving monkey. *PLoS One*, 5(11):e13829, 2010.

[131] F. Helmchen and W. Denk. Deep tissue two-photon microscopy. *Nat Methods*, 2(12):932–940, 2005.

[132] F. Helmchen, K. Imoto, and B. Sakmann. Ca^{2+} buffering and action potential-evoked Ca^{2+} signaling in dendrites of pyramidal neurons. *Biophys J*, 70(2):1069–1081, 1996.

[133] F. Helmchen and A. Konnerth. *Imaging in Neuroscience: A Laboratory Manual*. Cold Spring Harbor Laboratory Press, Cold Spring Harbour, NY, 2011.

[134] F. Helmchen, K. Svoboda, W. Denk, and D. W. Tank. In vivo dendritic calcium dynamics in deep-layer cortical pyramidal neurons. *Nat Neurosci*, 2(11):989–996, 1999.

[135] Hesiod. To Helios. In H.G. Evelyn-White, editor, *Hesiod: The Homeric Hymns and Homerica.* Harvard University Press, Harvard, MA, 1914.

[136] S. Higo, N. Udaka, and N. Tamamaki. Long-range GABAergic projection neurons in the cat neocortex. *J Comp Neurol*, 503(3):421–431, 2007.

[137] H. Hirase, L. Qian, P. Bartho, and G. Buzsaki. Calcium dynamics of cortical astrocytic networks in vivo. *PLoS biology*, 2(4):E96, 2004.

[138] P. R. Hof, II Glezer, F. Conde, R. A. Flagg, M. B. Rubin, E. A. Nimchinsky, and D. M. Vogt Weisenhorn. Cellular distribution of the calcium-binding proteins parvalbumin, calbindin, and calretinin in the neocortex of mammals: phylogenetic and developmental patterns. *J Chem Neuroanat*, 16(2):77–116, 1999.

[139] S. B. Hofer, H. Ko, B. Pichler, J. Vogelstein, H. Ros, H. Zeng, E. Lein, N. A. Lesica, and T. D. Mrsic-Flogel. Differential connectivity and response dynamics of excitatory and inhibitory neurons in visual cortex. *Nat Neurosci*, 14(8):1045–1052, 2011.

[140] R. Hooke. *Micrographia: or some physiological descriptions of minute bodies made by magnifying glasses with observations and Inquiries thereupon.* Royal Society, London, United Kingdom, 1665.

[141] B.K.P Horn. Closed-form solution of absolute orientation using unit quaternions. *Journal of the Optical Society of America*, 4(4):629–642, 1987.

[142] J. C. Horton and D. L. Adams. The cortical column: a structure without a function. *Philos Trans R Soc Lond B Biol Sci*, 360(1456):837–862, 2005.

[143] V. Houades, A. Koulakoff, P. Ezan, I. Seif, and C. Giaume. Gap junction-mediated astrocytic networks in the mouse barrel cortex. *J Neurosci*, 28(20):5207–5217, 2008.

[144] A. Howard, G. Tamas, and I. Soltesz. Lighting the chandelier: new vistas for axo-axonic cells. *Trends Neurosci*, 28(6):310–316, 2005.

[145] D. H. Hubel and T. N. Wiesel. Shape and arrangement of columns in cat's striate cortex. *J Physiol*, 165:559–568, 1963.

[146] Invitrogen. Fluorescence SpectraViewer. 2011.

[147] ISO. ISO 9241 - Ergonomics of human system interaction, 2011.

[148] V. Iyer, T. M. Hoogland, and P. Saggau. Fast functional imaging of single neurons using random-access multiphoton (RAMP) microscopy. *J Neurophysiol*, 95(1):535–545, 2006.

[149] V. Jacob, L. Estebanez, J. Le Cam, J. Y. Tiercelin, P. Parra, G. Paresys, and D. E. Shulz. The matrix: a new tool for probing the whisker-to-barrel system with natural stimuli. *J Neurosci Methods*, 189(1):65–74, 2010.

[150] Y. Jiao, C. Zhang, Y. Yanagawa, and Q. Q. Sun. Major effects of sensory experiences on the neocortical inhibitory circuits. *J Neurosci*, 26(34):8691–8701, 2006.

[151] W.M. Johnston, J.R.P. Hanna, and R.J. Millar. Advances in dataflow programming languages. *ACM Computing Surveys*, 36(1):1–34, 2004.

[152] P. Jonas and G. Buzsaki. Neural inhibition. *Scholarpedia*, 2(9):3286, 2007.

[153] B. Judkewitz, M. Rizzi, K. Kitamura, and M. Hausser. Targeted single-cell electroporation of mammalian neurons in vivo. *Nat Protoc*, 4(6):862–869, 2009.

[154] W. Kaiser and C.G.B. Garrett. Two-photon excitation in $CaF_2:Eu^{2+}$. *Phys Rev Lett*, 7(6):229–231, 1961.

[155] E.R. Kandel, J.H. Schwartz, and T. Jessell. *Principles of Neural Science*. McGraw-Hill Professional, 4th edition, 2000.

[156] P. Kara and J. D. Boyd. A micro-architecture for binocular disparity and ocular dominance in visual cortex. *Nature*, 458(7238):627–631, 2009.

[157] F. Karube, Y. Kubota, and Y. Kawaguchi. Axon branching and synaptic bouton phenotypes in GABAergic nonpyramidal cell subtypes. *J Neurosci*, 24(12):2853–2865, 2004.

[158] P. S. Katz, R. Calin-Jageman, A. Dhawan, C. Frederick, S. Guo, R. Dissanayaka, N. Hiremath, W. Ma, X. Shen, H. C. Wang, H. Yang, S. Prasad, R. Sunderraman, and Y. Zhu. NeuronBank: A tool for cataloging neuronal circuitry. *Front Syst Neurosci*, 4:9, 2010.

[159] Y. Kawaguchi and Y. Kubota. Correlation of physiological subgroupings of nonpyramidal cells with parvalbumin- and calbindin$_{D28k}$-immunoreactive neurons in layer V of rat frontal cortex. *J Neurophysiol*, 70(1):387–396, 1993.

[160] Y. Kawaguchi and Y. Kubota. GABAergic cell subtypes and their synaptic connections in rat frontal cortex. *Cereb Cortex*, 7(6):476–486, 1997.

[161] R.M. Keller. *Computer Science: Abstraction to Implementation*. Harvey Mudd College, Claremont, CA, 2001.

[162] A. M. Kerlin, M. L. Andermann, V. K. Berezovskii, and R. C. Reid. Broadly tuned response properties of diverse inhibitory neuron subtypes in mouse visual cortex. *Neuron*, 67(5):858–871, 2010.

[163] J. N. Kerr, D. Greenberg, and F. Helmchen. Imaging input and output of neocortical networks in vivo. *Proc Natl Acad Sci U S A*, 102(39):14063–14068, 2005.

[164] S. Kügler, E. Kilic, and M. Bahr. Human synapsin 1 gene promoter confers highly neuron-specific long-term transgene expression from an adenoviral vector in the adult rat brain depending on the transduced area. *Gene Ther*, 10(4):337–347, 2003.

[165] K. Kitamura, B. Judkewitz, M. Kano, W. Denk, and M. Häusser. Targeted patch-clamp recordings and single-cell electroporation of unlabeled neurons in vivo. *Nat Methods*, 5(1):61–67, 2008.

[166] T. Knöpfel, M. Z. Lin, A. Levskaya, L. Tian, J. Y. Lin, and E. S. Boyden. Toward the second generation of optogenetic tools. *J Neurosci*, 30(45):14998–15004, 2010.

[167] H. Ko, S. B. Hofer, B. Pichler, K. A. Buchanan, P. J. Sjostrom, and T. D. Mrsic-Flogel. Functional specificity of local synaptic connections in neocortical networks. *Nature*, 2011.

[168] S. Komai, W. Denk, P. Osten, M. Brecht, and T. W. Margrie. Two-photon targeted patching (TPTP) in vivo. *Nat Protoc*, 1(2):647–652, 2006.

[169] J. L. Krichmar and G. M. Edelman. Brain-based devices for the study of nervous systems and the development of intelligent machines. *Artif Life*, 11(1-2):63–77, 2005.

[170] J. L. Krichmar, A. K. Seth, D. A. Nitz, J. G. Fleischer, and G. M. Edelman. Spatial navigation and causal analysis in a brain-based device modeling cortical-hippocampal interactions. *Neuroinformatics*, 3(3):197–221, 2005.

[171] L. S. Krimer, A. V. Zaitsev, G. Czanner, S. Kroner, G. Gonzalez-Burgos, N. V. Povysheva, S. Iyengar, G. Barrionuevo, and D. A. Lewis. Cluster analysis-based physiological classification and morphological properties of inhibitory neurons in layers 2-3 of monkey dorsolateral prefrontal cortex. *J Neurophysiol*, 94(5):3009–3022, 2005.

[172] S. J. Kuhlman and Z. J. Huang. High-resolution labeling and functional manipulation of specific neuron types in mouse brain by Cre-activated viral gene expression. *PLoS One*, 3(4):e2005, 2008.

[173] H. Y. Lam, L. Marenco, G. M. Shepherd, P. L. Miller, and K. H. Cheung. Using Web Ontology Language to integrate heterogeneous databases in the neurosciences. *AMIA Annu Symp Proc*, pages 464–468, 2006.

[174] P. W. Land and D. J. Simons. Cytochrome oxidase staining in the rat SmI barrel cortex. *J Comp Neurol*, 238(2):225–235, 1985.

[175] D. Langer and F. Helmchen. Post hoc immunostaining of gabaergic neuronal subtypes following in vivo two-photon calcium imaging in mouse neocortex. *Pflugers Arch*, 463(2):339–354, 2011.

[176] E. S. Lein, M. J. Hawrylycz, N. Ao, M. Ayres, A. Bensinger, A. Bernard, A. F. Boe, M. S. Boguski, K. S. Brockway, E. J. Byrnes, L. Chen, T. M. Chen, M. C. Chin, J. Chong, B. E. Crook, A. Czaplinska, C. N. Dang, S. Datta, N. R. Dee, A. L. Desaki, T. Desta, E. Diep, T. A. Dolbeare, M. J. Donelan, H. W. Dong, J. G. Dougherty, B. J. Duncan, A. J. Ebbert, G. Eichele, L. K. Estin, C. Faber, B. A. Facer, R. Fields, S. R. Fischer, T. P. Fliss, C. Frensley, S. N. Gates, K. J. Glattfelder, K. R. Halverson, M. R. Hart, J. G. Hohmann, M. P. Howell, D. P. Jeung, R. A. Johnson, P. T. Karr, R. Kawal, J. M. Kidney, R. H. Knapik, C. L. Kuan, J. H. Lake, A. R. Laramee, K. D. Larsen, C. Lau, T. A. Lemon, A. J. Liang, Y. Liu, L. T. Luong, J. Michaels, J. J. Morgan, R. J. Morgan, M. T. Mortrud, N. F. Mosqueda, L. L. Ng, R. Ng, G. J. Orta, C. C. Overly, T. H. Pak, S. E. Parry, S. D. Pathak, O. C. Pearson, R. B. Puchalski, Z. L. Riley, H. R. Rockett, S. A. Rowland, J. J. Royall, M. J. Ruiz, N. R. Sarno, K. Schaffnit, N. V. Shapovalova, T. Sivisay, C. R. Slaughterbeck, S. C. Smith, K. A. Smith, B. I. Smith, A. J. Sodt, N. N. Stewart, K. R. Stumpf, S. M. Sunkin, M. Sutram, A. Tam, C. D. Teemer, C. Thaller, C. L. Thompson, L. R. Varnam, A. Visel, R. M. Whitlock, P. E. Wohnoutka, C. K. Wolkey, V. Y. Wong, M. Wood, et al. Genome-wide atlas of gene expression in the adult mouse brain. *Nature*, 445(7124):168–176, 2007.

[177] L. Leybaert, A. de Meyer, C. Mabilde, and M. J. Sanderson. A simple and practical method to acquire geometrically correct images with resonant scanning-based line scanning in a custom-built video-rate laser scanning microscope. *J Microsc*, 219(Pt 3):133–140, 2005.

[178] G. Li, T. Liu, J. Nie, L. Guo, J. Chen, J. Zhu, W. Xia, A. Mara, S. Holley, and S. T. Wong. Segmentation of touching cell nuclei using gradient flow tracking. *J Microsc*, 231(Pt 1):47–58, 2008.

[179] G. Li, T. Liu, A. Tarokh, J. Nie, L. Guo, A. Mara, S. Holley, and S. T. Wong. 3D cell nuclei segmentation based on gradient flow tracking. *BMC Cell Biol*, 8:40, 2007.

[180] K. P. Lillis, A. Eng, J. A. White, and J. Mertz. Two-photon imaging of spatially extended neuronal network dynamics with high temporal resolution. *J Neurosci Methods*, 172(2):178–184, 2008.

[181] B.H. Liskov and J.M. Wing. A behavioral notion of subtyping. *ACM Transactions on Programming Languages and Systems*, 16(4):1811–1184, 1994.

[182] P.G. Liudkovskaia, V.B. Emel'aniov, and B.K. Lemazhikhin. Study of the optic properties of the giant axon of the squid during rest and at various stages of excitation. *Tsitologiia*, 7(4):520–530, 1965.

[183] R. Lorente de No. The cerebral cortex of the mouse (a first contribution — the "acoustic" cortex). *Somatosens Mot Res*, 9(1):3–36, 1992.

[184] H. Lütcke, M. Murayama, T. Hahn, D. J. Margolis, S. Astori, S. M. Zum Alten Borgloh, W. Göbel, Y. Yang, W. Tang, S. Kügler, R. Sprengel, T. Nagai, A. Miyawaki, M. E. Larkum, F. Helmchen, and M. T. Hasan. Optical recording of neuronal activity with a genetically-encoded calcium indicator in anesthetized and freely moving mice. *Front Neural Circuits*, 4:9, 2010.

[185] W. P. Ma, B. H. Liu, Y. T. Li, Z. J. Huang, L. I. Zhang, and H. W. Tao. Visual representations by cortical somatostatin inhibitory neurons–selective but with weak and delayed responses. *J Neurosci*, 30(43):14371–14379, 2010.

[186] Y. Ma, H. Hu, A. S. Berrebi, P. H. Mathers, and A. Agmon. Distinct subtypes of somatostatin-containing neocortical interneurons revealed in transgenic mice. *J Neurosci*, 26(19):5069–5082, 2006.

[187] L. Madisen, T. A. Zwingman, S. M. Sunkin, S. W. Oh, H. A. Zariwala, H. Gu, L. L. Ng, R. D. Palmiter, M. J. Hawrylycz, A. R. Jones, E. S. Lein, and H. Zeng. A robust and high-throughput Cre reporting and characterization system for the whole mouse brain. *Nat Neurosci*, 13(1):133–140, 2010.

[188] M. Mank and O. Griesbeck. Genetically encoded calcium indicators. *Chem Rev*, 108(5):1550–1564, 2008.

[189] M. Mank, A. F. Santos, S. Direnberger, T. D. Mrsic-Flogel, S. B. Hofer, V. Stein, T. Hendel, D. F. Reiff, C. Levelt, A. Borst, T. Bonhoeffer, M. Hübener, and O. Griesbeck. A genetically encoded calcium indicator for chronic in vivo two-photon imaging. *Nat Methods*, 5(9):805–811, 2008.

[190] L. Marenco, Y. Li, M. E. Martone, P. W. Sternberg, G. M. Shepherd, and P. L. Miller. Issues in the design of a pilot concept-based query interface for the neuroinformatics information framework. *Neuroinformatics*, 6(3):229–239, 2008.

[191] L. Marenco, R. Wang, G. M. Shepherd, and P. L. Miller. The NIF DISCO Framework: facilitating automated integration of neuroscience content on the web. *Neuroinformatics*, 8(2):101–112, 2010.

[192] H. Markram, M. Toledo-Rodriguez, Y. Wang, A. Gupta, G. Silberberg, and C. Wu. Interneurons of the neocortical inhibitory system. *Nat Rev Neurosci*, 5(10):793–807, 2004.

[193] J. H. Marshel, T. Mori, K. J. Nielsen, and E. M. Callaway. Targeting single neuronal networks for gene expression and cell labeling in vivo. *Neuron*, 67(4):562–574, 2010.

[194] M. E. Martone, A. Gupta, and M. H. Ellisman. E-neuroscience: challenges and triumphs in integrating distributed data from molecules to brains. *Nat Neurosci*, 7(5):467–472, 2004.

[195] S. McConnell. *Code Complete.* Microsoft Press (O'Reilly Media), Sebastopol, CA, 2nd edition, 2004.

[196] D. A. McCormick, B. W. Connors, J. W. Lighthall, and D. A. Prince. Comparative electrophysiology of pyramidal and sparsely spiny stellate neurons of the neocortex. *J Neurophysiol*, 54(4):782–806, 1985.

[197] J. L. McKinstry, A. K. Seth, G. M. Edelman, and J. L. Krichmar. Embodied models of delayed neural responses: spatiotemporal categorization and predictive motor control in brain based devices. *Neural Netw*, 21(4):553–561, 2008.

[198] A. H. Meyer, I. Katona, M. Blatow, A. Rozov, and H. Monyer. In vivo labeling of parvalbumin-positive interneurons and analysis of electrical coupling in identified neurons. *J Neurosci*, 22(16):7055–7064, 2002.

[199] R. Miles. Perspectives: neurobiology. Diversity in inhibition. *Science*, 287(5451):244–246, 2000.

[200] G. Miller. Massively parallel brain imaging. *Science*, 326(5951):390, 2009.

[201] M. Minsky. Microscopy apparatus. *US Patent 3013467*, 1961.

[202] Y. Mishchencko, J.T. Vogelstein, and L. Paninski. A Bayesian approach for inferring neuronal connectivity from calcium fluorescent imaging data. *Ann Appl Stat*, 5(2B):1229–1261, 2011.

[203] G. Miyoshi and G. Fishell. Directing neuron-specific transgene expression in the mouse CNS. *Curr Opin Neurobiol*, 16(5):577–584, 2006.

[204] S. K. Mohanty, R. K. Reinscheid, X. Liu, N. Okamura, T. B. Krasieva, and M. W. Berns. In-depth activation of channelrhodopsin 2-sensitized excitable cells with high spatial resolution using two-photon excitation with a near-infrared laser microbeam. *Biophys J*, 95(8):3916–3926, 2008.

[205] Z. Molnar and A. F. Cheung. Towards the classification of subpopulations of layer V pyramidal projection neurons. *Neurosci Res*, 55(2):105–115, 2006.

[206] J. Moore, C. Allan, J. M. Burel, B. Loranger, D. MacDonald, J. Monk, and J. R. Swedlow. Open tools for storage and management of quantitative image data. *Methods Cell Biol*, 85:555–570, 2008.

[207] P.F. Moulton. Spectroscopic and laser characteristics of Ti:Al$_2$O$_3$. *J Opt Soc Am B*, 3(1):125–133, 1986.

[208] V. Mountcastle. The evolution of ideas concerning the function of the neocortex. *Cereb Cortex*, 5(4):289–295, 1995.

[209] V. B. Mountcastle. Modality and topographic properties of single neurons of cat's somatic sensory cortex. *J Neurophysiol*, 20(4):408–434, 1957.

[210] V. B. Mountcastle. The columnar organization of the neocortex. *Brain*, 120 (Pt 4):701–722, 1997.

[211] E. A. Mukamel, A. Nimmerjahn, and M. J. Schnitzer. Automated analysis of cellular signals from large-scale calcium imaging data. *Neuron*, 63(6):747–760, 2009.

[212] T. Nagai, S. Yamada, T. Tominaga, M. Ichikawa, and A. Miyawaki. Expanded dynamic range of fluorescent indicators for Ca^{2+} by circularly permuted yellow fluorescent proteins. *Proc Natl Acad Sci U S A*, 101(29):10554–10559, 2004.

[213] S. Nagayama, S. Zeng, W. Xiong, M. L. Fletcher, A. V. Masurkar, D. J. Davis, V. A. Pieribone, and W. R. Chen. In vivo simultaneous tracing and Ca^{2+} imaging of local neuronal circuits. *Neuron*, 53(6):789–803, 2007.

[214] T. Nevian and F. Helmchen. Calcium indicator loading of neurons using single-cell electroporation. *Pflugers Arch*, 454(4):675–688, 2007.

[215] Q. T. Nguyen, N. Callamaras, C. Hsieh, and I. Parker. Construction of a two-photon microscope for video-rate Ca^{2+} imaging. *Cell Calcium*, 30(6):383–393, 2001.

[216] Q.-T. Nguyen, J. Driscoll, E. M. Dolnick, and D. Kleinfeld. MPScope 2.0: A computer system for two-photon laser scanning microscopy with concurrent plasma-mediated ablation and electrophysiology. In R. Frostig, editor, *In Vivo Optical Imaging of Brain Function*, pages 117–142. CRC Press, Boca Raton, FL, 2nd edition, 2009.

[217] Q. T. Nguyen, P. S. Tsai, and D. Kleinfeld. MPScope: a versatile software suite for multiphoton microscopy. *J Neurosci Methods*, 156(1-2):351–359, 2006.

[218] A. Nimmerjahn, F. Kirchhoff, and F. Helmchen. Resting microglial cells are highly dynamic surveillants of brain parenchyma in vivo. *Science*, 308(5726):1314–1318, 2005.

[219] A. Nimmerjahn, F. Kirchhoff, J. N. Kerr, and F. Helmchen. Sulforhodamine 101 as a specific marker of astroglia in the neocortex in vivo. *Nat Methods*, 1(1):31–37, 2004.

[220] D. H. O'Connor, S. P. Peron, D. Huber, and K. Svoboda. Neural activity in barrel cortex underlying vibrissa-based object localization in mice. *Neuron*, 67(6):1048–1061, 2010.

[221] A. A. Oliva, M. Jiang, T. Lam, K. L. Smith, and J. W. Swann. Novel hippocampal interneuronal subtypes identified using transgenic mice that express green fluorescent protein in GABAergic interneurons. *J Neurosci*, 20(9):3354–3368, 2000.

[222] L. Ouda, R. Druga, and J. Syka. Changes in parvalbumin immunoreactivity with aging in the central auditory system of the rat. *Exp Gerontol*, 43(8):782–789, 2008.

[223] D.L. Parnas. On the criteria to be used in decomposing systems into modules. *Communications of the ACM*, 15(12):1053–1058, 1972.

[224] P. Parra, A. I. Gulyas, and R. Miles. How many subtypes of inhibitory cells in the hippocampus? *Neuron*, 20(5):983–993, 1998.

[225] J.B. Pawley. *Handbook of Biological Confocal Microscopy*. Springer Science+Business Media, LLC, New York, NY, 2006.

[226] C. C. Petersen. The barrel cortex–integrating molecular, cellular and systems physiology. *Pflugers Arch*, 447(2):126–134, 2003.

[227] C. C. H. Petersen. The functional organization of the barrel cortex. *Neuron*, 56(2):339–355, 2007.

[228] R. Pfeifer and J. Bongard. *How the body shapes the way we think - a new view of intelligence.* The MIT Press, Cambrdige, MA, 2006.

[229] R. Pfeifer, M. Lungarella, and F. Iida. Self-organization, embodiment, and biologically inspired robotics. *Science*, 318(5853):1088–1093, 2007.

[230] R. Pfeifer and C. Scheier. *Understanding Intelligence.* The MIT Press, Cambridge, MA, 1999.

[231] T. A. Pologruto, B. L. Sabatini, and K. Svoboda. Scanimage: flexible software for operating laser scanning microscopes. *Biomed Eng Online*, 2:13, 2003.

[232] D. L. Qiu, W. Akemann, C. P. Chu, R. Araki, and T. Knöpfel. Targeted optical probing of neuronal circuit dynamics using fluorescent protein sensors. *Neurosignals*, 16(4):289–299, 2008.

[233] V.S. Ramachandran. *The Tell-Tale Brain: A Neuroscientist's Quest for What Makes Us Human.* W.W. Norton & Company, New York, NY, 2010.

[234] S. Ramón y Cajal. La rétine des vertébrés. *La cellule*, 9:121–255, 1892.

[235] S. Ramón y Cajal. *Neuron Theory or Reticular Theory? Objective Evidence of the Anatomical Unity of Nerve Cells.* Consejo Superior de Investigaciones Científicas Instituto Ramón y Cajal, Madrid, [1908] 1954.

[236] G. P. Reynolds, Z. J. Zhang, and C. L. Beasley. Neurochemical correlates of cortical GABAergic deficits in schizophrenia: selective losses of calcium binding protein immunoreactivity. *Brain Res Bull*, 55(5):579–584, 2001.

[237] J. P. Rickgauer and D. W. Tank. Two-photon excitation of channelrhodopsin-2 at saturation. *Proc Natl Acad Sci U S A*, 106(35):15025–15030, 2009.

[238] D. Riehle. *Framework Design: A Role Modeling Approach*. Phd thesis, 1999.

[239] T. J. Rink, R. Y. Tsien, and A. E. Warner. Free calcium in Xenopus embryos measured with ion-selective microelectrodes. *Nature*, 283(5748):658–660, 1980.

[240] K. S. Rockland and N. Ichinohe. Some thoughts on cortical minicolumns. *Exp Brain Res*, 158(3):265–277, 2004.

[241] W. N. Ross, B. M. Salzberg, L. B. Cohen, A. Grinvald, H. V. Davila, A. S. Waggoner, and C. H. Wang. Changes in absorption, fluorescence, dichroism, and birefringence in stained giant axons: : optical measurement of membrane potential. *J Membr Biol*, 33(1-2):141–183, 1977.

[242] M. Rudin. *Molecular Imaging: Basic Principles and Applications in Biomedical Research*. Imperial College Press, London, United Kingdom, 2005.

[243] B. Rudy, G. Fishell, S. Lee, and J. Hjerling-Leffler. Three groups of interneurons account for nearly 100% of neocortical GABAergic neurons. *Dev Neurobiol*, 71(1):45–61, 2011.

[244] C. A. Runyan, J. Schummers, A. Van Wart, S. J. Kuhlman, N. R. Wilson, Z. J. Huang, and M. Sur. Response features of parvalbumin-expressing interneurons suggest precise roles for subtypes of inhibition in visual cortex. *Neuron*, 67(5):847–857, 2010.

[245] P. Saggau, A. Bullen, and S. S. Patel. Acousto-optic random-access laser scanning microscopy: fundamentals and applications to optical recording of neuronal activity. *Cell Mol Biol*, 44(5):827–846, 1998.

[246] M. Samwald, H. Chen, A. Ruttenberg, E. Lim, L. Marenco, P. Miller, G. Shepherd, and K. H. Cheung. Semantic SenseLab: Implementing the vision of the semantic web in neuroscience. *Artif Intell Med*, 48(1):21–28, 2010.

[247] M. J. Sanderson and I. Parker. Video-rate confocal microscopy. *Methods Enzymol*, 360:447–481, 2003.

[248] T. R. Sato, N. W. Gray, Z. F. Mainen, and K. Svoboda. The functional microarchitecture of the mouse barrel cortex. *PLoS Biol*, 5(7):e189, 2007.

[249] J. Sawinski and W. Denk. Miniature random-access fiber scanner for in vivo multi-photon imaging. *J Appl Phys*, 102:034701, 2007.

[250] J. Sawinski, D. J. Wallace, D. S. Greenberg, S. Grossmann, W. Denk, and J. N. Kerr. Visually evoked activity in cortical cells imaged in freely moving animals. *Proc Natl Acad Sci U S A*, 106(46):19557–19562, 2009.

[251] S. Schiffer. Visuelle Programmierung - Potential und Grenzen. In H.C. Mayr, editor, *Beherrschung von Informationssystemen, Tagungsband der Informatik '96*, pages 267–286. Oldenbourg, Wien, 1996.

[252] D. Schubert, R. Kotter, and J. F. Staiger. Mapping functional connectivity in barrel-related columns reveals layer- and cell type-specific microcircuits. *Brain Struct Funct*, 212(2):107–119, 2007.

[253] A. K. Seth. Causal networks in simulated neural systems. *Cogn Neurodyn*, 2(1):49–64, 2008.

[254] A. K. Seth, J. L. McKinstry, G. M. Edelman, and J. L. Krichmar. Visual binding through reentrant connectivity and dynamic synchronization in a brain-based device. *Cereb Cortex*, 14(11):1185–1199, 2004.

[255] A. K. Seth, O. Sporns, and J. L. Krichmar. Neurorobotic models in neuroscience and neuroinformatics. *Neuroinformatics*, 3(3):167–170, 2005.

[256] K. E. Sheetz, E. E. Hoover, R. Carriles, D. Kleinfeld, and J. A. Squier. Advancing multifocal nonlinear microscopy: development and application of a novel multibeam Yb:KGd$(WO_4)_2$ oscillator. *Opt Express*, 16(22):17574–17584, 2008.

[257] I. P. Shmelev and G. M. Frank. The optical properties of a giant axon in polarized light. *Dokl Akad Nauk SSSR*, 166(6):1451–1453, 1966.

[258] B. Smith, M. Ashburner, C. Rosse, J. Bard, W. Bug, W. Ceusters, L. J. Goldberg, K. Eilbeck, A. Ireland, C. J. Mungall, N. Leontis, P. Rocca-Serra, A. Ruttenberg, S. A. Sansone, R. H. Scheuermann, N. Shah, P. L. Whetzel, and S. Lewis. The OBO Foundry: coordinated evolution of ontologies to support biomedical data integration. *Nat Biotechnol*, 25(11):1251–1255, 2007.

[259] IEEE Computer Society. IEEE standard for software unit testing (ANSI/IEEE Std 1008-1987), 1986.

[260] K. Sohya, K. Kameyama, Y. Yanagawa, K. Obata, and T. Tsumoto. GABAergic neurons are less selective to stimulus orientation than excitatory neurons in layer II/III of visual cortex, as revealed by in vivo functional Ca^{2+} imaging in transgenic mice. *J Neurosci*, 27(8):2145–2149, 2007.

[261] I. Soltesz. *Diversity in the Neuronal Machine - Order and Variability in Interneuronal Microcircuits.* Oxford University Press, Inc., New York, NY, 2005.

[262] P. Somogyi, T. F. Freund, and A. Cowey. The axo-axonic interneuron in the cerebral cortex of the rat, cat and monkey. *Neuroscience*, 7(11):2577–2607, 1982.

[263] D. Spahni and S. Clavadetscher. USC - Universal Sensor Center. Verknüpfen, Steuern und Nutzen verteilter RF-Komponenten. *NIDays 2011*, 2011.

[264] C. F. Stevens. Neuronal diversity: too many cell types for comfort? *Curr Biol*, 8(20):R708–R7010, 1998.

[265] W. Stevens, G. Myers, and L. Constantine. Structered design. *IBM Systems Journal*, 13(2):115–139, 1974.

[266] C. Stosiek, O. Garaschuk, K. Holthoff, and A. Konnerth. In vivo two-photon calcium imaging of neuronal networks. *Proc Natl Acad Sci U S A*, 100(12):7319–7324, 2003.

[267] A. Streitwieser, C.H. Heathcock, and E.M. Kosower. *Introduction to Organic Chemistry.* Macmillan Publishing Co., New York, NY, 1992.

[268] N. Stuurman, N. Amodaj, and R.D. Vale. μmanager: Open source software for light microscope imaging. *Microscopy Today*, 15(3):42–43, 2007.

[269] K. Sugino, C. M. Hempel, M. N. Miller, A. M. Hattox, P. Shapiro, C. Wu, Z. J. Huang, and S. B. Nelson. Molecular taxonomy of major neuronal classes in the adult mouse forebrain. *Nat Neurosci*, 9(1):99–107, 2006.

[270] K. Svoboda, W. Denk, D. Kleinfeld, and D. W. Tank. In vivo dendritic calcium dynamics in neocortical pyramidal neurons. *Nature*, 385(6612):161–165, 1997.

[271] H. A. Swadlow. Fast-spike interneurons and feedforward inhibition in awake sensory neocortex. *Cereb Cortex*, 13(1):25–32, 2003.

[272] J. R. Swedlow, I. Goldberg, E. Brauner, and P. K. Sorger. Informatics and quantitative analysis in biological imaging. *Science*, 300(5616):100–102, 2003.

[273] J. Szabadics, C. Varga, G. Molnar, S. Olah, P. Barzo, and G. Tamas. Excitatory effect of GABAergic axo-axonic cells in cortical microcircuits. *Science*, 311(5758):233–235, 2006.

[274] N. Tamamaki and R. Tomioka. Long-range GABAergic connections distributed throughout the neocortex and their possible function. *Front Neurosci*, 4:202, 2010.

[275] N. Tamamaki, Y. Yanagawa, R. Tomioka, J. Miyazaki, K. Obata, and T. Kaneko. Green fluorescent protein expression and colocalization with calretinin, parvalbumin, and somatostatin in the GAD67-GFP knock-in mouse. *J Comp Neurol*, 467(1):60–79, 2003.

[276] P. Theer, M. T. Hasan, and W. Denk. Two-photon imaging to a depth of $1000\,\mu m$ in living brains by use of a Ti:Al$_2$O$_3$ regenerative amplifier. *Opt Lett*, 28(12):1022–1024, 2003.

[277] P. Thévenaz, U.E. Ruttimann, and M. Unser. A pyramid approach to subpixel registration based on intensity. *IEEE Transactions on Image Processing*, 7(1):27–41, 1998.

[278] L. Tian, S. A. Hires, T. Mao, D. Huber, M. E. Chiappe, S. H. Chalasani, L. Petreanu, J. Akerboom, S. A. McKinney, E. R. Schreiter, C. I. Bargmann, V. Jayaraman, K. Svoboda, and L. L. Looger. Imaging neural activity in worms, flies and mice with improved GCaMP calcium indicators. *Nat Methods*, 6(12):875–881, 2009.

[279] P.A. Tipler. *Physics for Scientists and Engineers*. Worth Publishers, Inc., New York, NY, 1991.

[280] M. Toledo-Rodriguez, B. Blumenfeld, C. Wu, J. Luo, B. Attali, P. Goodman, and H. Markram. Correlation maps allow neuronal electrical properties to be predicted from single-cell gene expression profiles in rat neocortex. *Cereb Cortex*, 14(12):1310–1327, 2004.

[281] M. Toledo-Rodriguez, P. Goodman, M. Illic, C. Wu, and H. Markram. Neuropeptide and calcium-binding protein gene expression profiles predict neuronal anatomical type in the juvenile rat. *J Physiol*, 567(Pt 2):401–413, 2005.

[282] M. Toledo-Rodriguez and H. Markram. Single-cell RT-PCR, a technique to decipher the electrical, anatomical, and genetic determinants of neuronal diversity. *Methods Mol Biol*, 403:123–139, 2007.

[283] R. Tomioka, K. Okamoto, T. Furuta, F. Fujiyama, T. Iwasato, Y. Yanagawa, K. Obata, T. Kaneko, and N. Tamamaki. Demonstration of long-range GABAergic connections distributed throughout the mouse neocortex. *Eur J Neurosci*, 21(6):1587–1600, 2005.

[284] G. E. Truett, P. Heeger, R. L. Mynatt, A. A. Truett, J. A. Walker, and M. L. Warman. Preparation of PCR-quality mouse genomic DNA with hot sodium hydroxide and TRIS (HotSHOT). *Biotechniques*, 29(1):52–54, 2000.

[285] P. S. Tsai, B. Friedman, A. I. Ifarraguerri, B. D. Thompson, V. Lev-Ram, C. B. Schaffer, Q. Xiong, R. Y. Tsien, J. A. Squier, and D. Kleinfeld. All-optical histology using ultrashort laser pulses. *Neuron*, 39(1):27–41, 2003.

[286] P. S. Tsai, B. Migliori, K. Campbell, T. Kim, Z. Kam, A. Groisman, and D. Kleinfeld. Spherical aberration correction in nonlinear microscopy and optical ablation using a transparent deformable membrane. *Appl. Phys. Lett.*, 91:191102, 2007.

[287] R. Tsien. Spectra of various fluorescent proteins. *http://www.tsienlab.ucsd.edu*, 2011.

[288] R. Y. Tsien. A non-disruptive technique for loading calcium buffers and indicators into cells. *Nature*, 290(5806):527–528, 1981.

[289] M. Uematsu, Y. Hirai, F. Karube, S. Ebihara, M. Kato, K. Abe, K. Obata, S. Yoshida, M. Hirabayashi, Y. Yanagawa, and Y. Kawaguchi. Quantitative chemical composition of cortical GABAergic neurons revealed in transgenic venus-expressing rats. *Cereb Cortex*, 18(2):315–330, 2008.

[290] A Verkhratsky and A. Butt. *Glial Neurobiology.* John Wiley & Sons, Hoboken, NJ, 1st edition, 2007.

[291] J. T. Vogelstein, A. M. Packer, T. A. Machado, T. Sippy, B. Babadi, R. Yuste, and L. Paninski. Fast nonnegative deconvolution for spike train inference from population calcium imaging. *J Neurophysiol*, 104(6):3691–3704, 2010.

[292] J. T. Vogelstein, B. O. Watson, A. M. Packer, R. Yuste, B. Jedynak, and L. Paninski. Spike inference from calcium imaging using sequential Monte Carlo methods. *Biophys J*, 97(2):636–655, 2009.

[293] C. von Economo and G.N. Koskinas. *Die Cytoarchitektonik der Hirnrinde des erwachsenen Menschen.* Springer, Berlin, Germany, 1925.

[294] A. von Muralt. The optical spike. *Philos Trans R Soc Lond B Biol Sci*, 270(908):411–423, 1975.

[295] N. R. Wall, I. R. Wickersham, A. Cetin, M. De La Parra, and E. M. Callaway. Monosynaptic circuit tracing in vivo through Cre-dependent targeting and complementation of modified rabies virus. *Proc Natl Acad Sci U S A*, 107(50):21848–21853, 2010.

[296] D. J. Wallace and J. N. Kerr. Chasing the cell assembly. *Curr Opin Neurobiol*, 20(3):296–305, 2010.

[297] X. Wang, N. Lou, Q. Xu, G. F. Tian, W. G. Peng, X. Han, J. Kang, T. Takano, and M. Nedergaard. Astrocytic Ca^{2+} signaling evoked by sensory stimulation in vivo. *Nat Neurosci*, 9(6):816–823, 2006.

[298] X. J. Wang. Neurophysiological and computational principles of cortical rhythms in cognition. *Physiol Rev*, 90(3):1195–1268, 2010.

[299] Y. Wang, A. Gupta, M. Toledo-Rodriguez, C. Z. Wu, and H. Markram. Anatomical, physiological, molecular and circuit properties of nest basket cells in the developing somatosensory cortex. *Cereb Cortex*, 12(4):395–410, 2002.

[300] Y. Wang, H. Markram, P. H. Goodman, T. K. Berger, J. Ma, and P. S. Goldman-Rakic. Heterogeneity in the pyramidal network of the medial prefrontal cortex. *Nat Neurosci*, 9(4):534–542, 2006.

[301] A. Watakabe. Comparative molecular neuroanatomy of mammalian neocortex: what can gene expression tell us about areas and layers? *Dev Growth Differ*, 51(3):343–354, 2009.

[302] A. P. Weible, L. Schwarcz, I. R. Wickersham, L. Deblander, H. Wu, E. M. Callaway, H. S. Seung, and C. G. Kentros. Transgenic targeting of recombinant rabies virus reveals monosynaptic connectivity of specific neurons. *J Neurosci*, 30(49):16509–16513, 2010.

[303] K.N. Whitley and A.F. Blackwell. Visual programming in the wild: A survey of LabVIEW programmers. *J Visual Lang Comput*, 12:435–472, 2001.

[304] J. M. Wilson, D. A. Dombeck, M. Diaz-Rios, R. M. Harris-Warrick, and R. M. Brownstone. Two-photon calcium imaging of network activity in XFP-expressing neurons in the mouse. *J Neurophysiol*, 97(4):3118–3125, 2007.

[305] C. P. Wonders and S. A. Anderson. The origin and specification of cortical interneurons. *Nat Rev Neurosci*, 7(9):687–696, 2006.

[306] M. Wong-Riley. Changes in the visual system of monocularly sutured or enucleated cats demonstrable with cytochrome oxidase histochemistry. *Brain Res*, 171(1):11–28, 1979.

[307] A. Woodruff, Q. Xu, S. A. Anderson, and R. Yuste. Depolarizing effect of neocortical chandelier neurons. *Front Neural Circuits*, 3:15, 2009.

[308] A. R. Woodruff, S. A. Anderson, and R. Yuste. The enigmatic function of chandelier cells. *Front Neurosci*, 4:201, 2010.

[309] R. Wright. *The Moral Animal*. Vintage Books, New York, NY, 1994.

[310] C. Xu, W. Zipfel, J. B. Shear, R. M. Williams, and W. W. Webb. Multiphoton fluorescence excitation: new spectral windows for biological nonlinear microscopy. *Proc Natl Acad Sci U S A*, 93(20):10763–10768, 1996.

[311] Q. Xu, I. Cobos, E. De La Cruz, J. L. Rubenstein, and S. A. Anderson. Origins of cortical interneuron subtypes. *J Neurosci*, 24(11):2612–2622, 2004.

[312] X. Xu, K. D. Roby, and E. M. Callaway. Immunochemical characterization of inhibitory mouse cortical neurons: three chemically distinct classes of inhibitory cells. *J Comp Neurol*, 518(3):389–404, 2010.

[313] E. Yaksi and R. W. Friedrich. Reconstruction of firing rate changes across neuronal populations by temporally deconvolved Ca^{2+} imaging. *Nat Methods*, 3(5):377–383, 2006.

[314] O. Yizhar, L. E. Fenno, M. Prigge, F. Schneider, T. J. Davidson, D. J. O'Shea, V. S. Sohal, I. Goshen, J. Finkelstein, J. T. Paz, K. Stehfest, R. Fudim, C. Ramakrishnan, J. R. Huguenard, P. Hegemann, and K. Deisseroth. Neocortical excitation/inhibition balance in information processing and social dysfunction. *Nature*, 2011.

[315] A. Yoshida, Y. Yamaguchi, K. Nonomura, K. Kawakami, Y. Takahashi, and M. Miura. Simultaneous expression of different transgenes in neurons and glia by combining in utero electroporation with the Tol2 transposon-mediated gene transfer system. *Genes Cells*, 15(5):501–512, 2010.

[316] R. Yuste. Origin and classification of neocortical interneurons. *Neuron*, 48(4):524–527, 2005.

[317] H. A. Zariwala, L. Madisen, K. F. Ahrens, A. Bernard, E. S. Lein, A. R. Jones, and H. Zeng. Visual tuning properties of genetically identified layer 2/3 neuronal types in the primary visual cortex of cre-transgenic mice. *Front Syst Neurosci*, 4:162, 2011.

[318] P. Zhu, Y. Narita, S. T. Bundschuh, O. Fajardo, Y. P. Scharer, B. Chattopadhyaya, E. A. Bouldoires, A. E. Stepien, K. Deisseroth, S. Arber, R. Sprengel, F. M. Rijli, and R. W. Friedrich. Optogenetic dissection of neuronal circuits in zebrafish using viral gene transfer and the Tet system. *Front Neural Circuits*, 3:21, 2009.

Acknowledgements

I want to cordially express my thanks to the following people who contributed to my thesis or supported me physically, mentally or emotionally during my time at the Brain Research Institute:

- My thesis supervisor Fritjof Helmchen for the opportunity to carry out my thesis work in such an interdisciplinary and stimulating environment, and for his encouragement and openness to inputs and new ideas.

- My thesis committee members, Kevan Martin and Jean-Marc Fritschy, for all of their contributions in their honourable function.

- The electronics and mechanics crew, including Hansjörg Kasper, Stefan Giger and Martin Wieckhorst, for their technical contributions, assistance, inspiring inputs and discussions.

- The IT crew, with Roland Schöb, Patrick Scheuble and Pietro Morciano, for providing an excellent uptime of the server infrastructure as well as for their technical support and expertise.

- All of the others that I had the pleasure to work with; in particular: Marcel van 't Hoff, Marcel Göldi, Chetan Nagaraja, Andreas Keller, Samuel Häusler, Steven Broadley, Sarah Hintermayer, Bruno Weber, Benjamin Grewe, Markus Ruchty, Werner Göbel, Christoph Engelbrecht, Roland Krüppel and Florent Haiss for their contributions or input on software development; Helge Johannssen for building a two-photon microscope together with me; Tina Schulz and David Margolis for collaborating on immunostaining experiments; Dubravka Göckeritz, Abigail Manalastas, Mara Modest, Lazar Sumanovski, Franziska Christ, Beat Stierli, Carl Petersen and Oliver Weinmann for their help, contribution and advice with various laboratory procedures; Flavio Cueni for assistance with data analysis; Björn Kampa, Henry Lütcke and Morgane Roth for their technical and scientific advice; as well as Markus Ruchty, Marcel van't Hoff and Hansjörg Kasper for comments on parts of this thesis.

- All of those people outside of the institute who nevertheless played crucial roles; in particular: Bernie and Raphi for valuable brief escapes now and then; Susanne, Alina and Sarah for cheering me on during this endeavour; my parents for their emotional support and for always being there; and Amélia and Cali for their great day-and-night encouragement during the last phase of this thesis.

Appendix

A   Materials and Methods

A.1   Microscopy

A.1.1   Two-photon microscope setup

Fluorescence signals were detected with PMTs (R6357SELECT; Hamamatsu Photonics, Hamamatsu City, Japan), the gain of which was controlled by custom-built power supplies based on a module from Hamamatsu (C4900-01). PMT signals were pre-amplified with transimpedance amplifiers (150 kΩ, 1 MHz; XPG-ADC-PREAMP from Sigmann Elektronik GmbH, Hüffenhardt, Germany) and fed into a multichannel ADC (details in Section A.1.3).

A.1.2   Setup PC

A PC (Dalco AG, Wilen, Switzerland) with the following features was used: an Intel® Core i7 960 central processing unit (CPU) (3.20 GHz) processor, an ASRock X58 Deluxe3 mainboard, 6 GB DDR3-SDRAM (1333 MHz) and a NVIDIA Quadro NVS 295 graphics card. The Windows 7 Enterprise 32 bit operating system (Microsoft, Redmond, WA) was installed with the following additional software: LabVIEW 2010 SP1, including Statechart Module, FPGA module, Xilinx FPGA Tools, Vision Development Module and device drivers (all from National Instruments (NI), Ennetbaden, Switzerland), VI Package Manager Community Edition with easyXML (both from JKI, Walnut Creek, CA) and TortoiseSVN.

A.1.3   Data acquisition for laser-scanning modes

First generation Hifo ADC box   The setup PC was interfaced to an NI PXI-1036 chassis harbouring the following modules: two NI PXI-6229 cards (four 16 bit analogue output channels per card, with 833 kS/s per channel) controlling galvanometric scan mirrors, z-focusing device, pockels cell and a whisker stimulation device; an NI PXI-6122 for fast acquisition of analogue position-feedback signals from galvanometric scan mirrors and z-focusing device; and an NI PXI-7813R FPGA module (featuring a Virtex-II 3M chip) interfacing to the Hifo ADC box. NI BNC-2110 connector boxes were used to connect periphery devices to the analogue I/O cards listed above.

The Hifo ADC (custom-built by CSEM, Neuchâtel, Switzerland) features four analogue input channels based on the LTC2247 ADC chip (14 bit, 40 MS/s; from Linear Technology, Milpitas, CA). The FPGA code was created and interfaced using LabVIEW. Briefly, a 40 MHz TTL clock signal was generated by the FPGA module and delivered to the ADC box. The digitised channel values from the ADC were read in, decoded and integrated by

167

simple summation for each pixel (as unsigned 32 bit integer values).

$$I_{pixel} = \sum_{i=1}^{N_{cycles}} I_{ADC,i} \tag{A.1}$$

The number of integration cycles per pixel, $N_{cycles} \in \mathbb{N}$, is given by:

$$N_{cycles} = \lfloor \frac{f_{sampling}}{f_{pixel}} + 0.5 \rfloor = \lfloor \frac{40\,\text{MHz}}{f_{pixel}} + 0.5 \rfloor = \lfloor (40\,\text{MHz})t_{pixel} + 0.5 \rfloor \tag{A.2}$$

Due to the small block RAM size of the PXI-7813R card (see above), FPGA-to-host first-in-first-out (FIFO) buffers were strictly limited in size. In addition, the used FPGA module allows only three of these DMA-based transfer buffers. To transfer the four channels of the ADC to the host PC, multiplexing[1] over two FIFO buffers was employed. In order to increase the FIFO size, pixel values were converted from 32 bit to 16 bit integer values involving a bit-shift operation prior to DMA transfer. The number of bits to shift was calculated as follows:

$$b_{max} = \lceil \frac{\ln(N_{cycles})}{\ln(2)} \rceil + b_{adc} \tag{A.3}$$

where $b_{adc} = 14$ (the ADC bit depth).

Second generation Hifo ADC The same interfacing hardware and integration algorithm as described in the previous paragraph was used for the second generation Hifo ADC (the latter also custom-built by CSEM). This device featured four analogue input channels (based on the LTC2247 ADC chips, see above) and a seven-channel ADC (12 bit resolution; based on the AD5328 chip from Analog Devices GmbH, Munich, Germany) controllable by the FPGA via a serial interface.

NI FlexRIO system The setup PC interfaced to an NI PXIe-1079 chassis harbouring an NI PXI-6229 card for scan signal generation and a NI PXIe-7962R FlexRIO FPGA module (with Virtex-5 SX50T chip and 512 MB on-board DDR2-SDRAM) connected to an NI 5751 FlexRIO adapter module (16 analogue input channels, 14 bit resolution, sampled at 50 MS/s) for signal acquisition. An NI SMB-2147 and an NI SMB-2148 accessory[2] were used to connect the FlexRIO adapter module to pre-amplified PMT signal inputs and shutter controller, respectively. Since PXI express (PXIe)-based systems allow up to 16 DMA-channels for FPGA-to-host data transfer, multiplexing of channels was not required. Conversion to 16 bit integer values by a bit-shift operation, was still performed prior to DMA transfer (according to equation A.3 on page 168, but with $b_{adc} = 16$).

---

[1]Multiplexing refers to combining several data streams in order to transmit them over a single communication channel.

[2]These devices provide SubMiniature version B (SMB) connectors.

A.1.4 Laser scanning using galvanometric scan mirrors

A custom-built two-photon microscope controlled by the HelioScan software package (see Chapter 2) and powered by a Ti:Sapphire laser system tunable between 710 nm to 1090 nm (MaiTai Broadband, Spectra-Physics, Santa Clara, CA) was used. Beam-size was adjusted with a telescope and laser intensity modulated with a Pockels cell (model 350/80, with controller model 302RM; Conoptics, Danbury, CT) was used. Two galvanometric mirrors (model 6210; Cambridge Technology, Lexington, MA) were used for x/y scanning and a piezoelectric focusing device (P-725.4CD PIFOC; Physik Instrumente, Karlsruhe, Germany) for stack acquisition.

Generation of scan signals

A template scan pattern p_{template} is calculated (see below for details), where each pixel i is described by a vector $\vec{p}_{\text{template}, i}$ in µm-space (consisting of an x, y and z component):

$$\vec{p}_{\text{template}, i} = \begin{pmatrix} x \\ y \\ z \\ 1\,\mu\text{m} \end{pmatrix} \tag{A.4}$$

This pattern can be modified by affine transformations in the following sequence:

1. *Scaling* of the scan pattern by the inverse of the zoom factor f_{zoom}:

$$\vec{p}_i = \frac{1}{f_{\text{zoom}}} \vec{p}_{\text{template}, i} \tag{A.5}$$

2. *Rotation* of the scan pattern around the vertical z axis by an angle ϕ [105]:

$$\vec{p}_i = \mathbf{R_z}\vec{p}_{\text{template}, i} = \begin{pmatrix} 1 & 0 & 0 & 0 \\ 0 & \cos\theta & -\sin\theta & 0 \\ 0 & \sin\theta & \cos\theta & 0 \\ 0 & 0 & 0 & 1 \end{pmatrix} \vec{p}_{\text{template}, i} \tag{A.6}$$

3. *Tilting* by an angle θ around the new x axis obtained by the previous rotation step [105]:

$$\vec{p}_i = \mathbf{R_x}\vec{p}_{\text{template}, i} = \begin{pmatrix} \cos\phi & -\sin\phi & 0 & 0 \\ \sin\phi & \cos\phi & 0 & 0 \\ 0 & 0 & 1 & 0 \\ 0 & 0 & 0 & 1 \end{pmatrix} \vec{p}_{\text{template}, i} \tag{A.7}$$

4. *Translation* by an offset vector $\vec{v}_{\text{offset}}$:

$$\vec{p}_i = \vec{p}_{\text{template}, i} + \vec{v}_{offset} = \mathbf{T}\vec{p}_{\text{template}, i} = \begin{pmatrix} 1 & 0 & 0 & v_x \\ 0 & 1 & 0 & v_y \\ 0 & 0 & 1 & v_z \\ 0 & 0 & 0 & 1 \end{pmatrix} \vec{p}_{\text{template}, i} \tag{A.8}$$

All four operations can be combined using the following transformation matrix $\mathbf{A}$:

$$\mathbf{A} = \frac{1}{f_{zoom}}\mathbf{R_z}\mathbf{R_x}\mathbf{T} = \frac{1}{f_{zoom}}\begin{pmatrix} \cos\phi & -\sin\phi\cos\theta & \sin\phi\sin\theta & v_x \\ sin\phi & \cos\phi\cos\theta & -\cos\phi\sin\theta & v_y \\ 0 & \sin\theta & \cos\theta & v_z \\ 0 & 0 & 0 & 1 \end{pmatrix} \quad (A.9)$$

For each user- or software-induced change of the modifying values f_{zoom}, ϕ, θ and $\vec{v}_{offset}$, the actual scan pattern is re-calculated based on the original template scan pattern by multiplying each pixel of the template pattern $p_{template}$ with the transformation matrix $\mathbf{A}$.

Frame scan   The template scan pattern for the frame scan was created with $z = const. = 0$ (i.e. as a horizontal plane through the point of origin). For the x-component, a biphasic ramp pattern was repeated once for every line: a linear fly-forward phase was followed by a linear fly-back phase (Figure A.1 on page 170). The y-component was kept constant during a line and increased step-wise at the end of each line, thus resulting in a stair-like pattern. During the fly-back phase of the last line, the y-component was linearly reset to its initial value.

A.1.5   Intrinsic optical signal IOS imaging

Image acquisition was performed with a 12 bit grey scale charge-coupled device (CCD) camera (Teli CS3960DCL; Thoshiba Teli Corporation, Tokyo, Japan) and a 4x objective (UPlanFL N, 4x/0.13; Olympus, Tokyo, Japan). A blood vessel reference map was acquired under green light illumination (peak wavelength 525 nm, L5-G61N-GT LED; Sloan LED, Delft, The Netherlands). Subsequent IOS imaging was performed under red light illumination (peak wavelength 660 nm, L-7113SRD LED; Kingbright Electronic, Taipai, Taiwan) using the HelioScan software package (see Section 2.2.8).

Figure A.1: Template frame scan trajectory for galvanometric mirrors (x and y components). The x resolution (in pixels) is specified by the user. The number of pixels for the scan cut-off and the fly-back phase are determined based on the x resolution and the cut-off and fly-back fraction, respectively (which are read from a configuration file). The maximum and the minimum value for each component is determined by the maximum deflection of the respective scanners and the aspect ratio specified by the user.
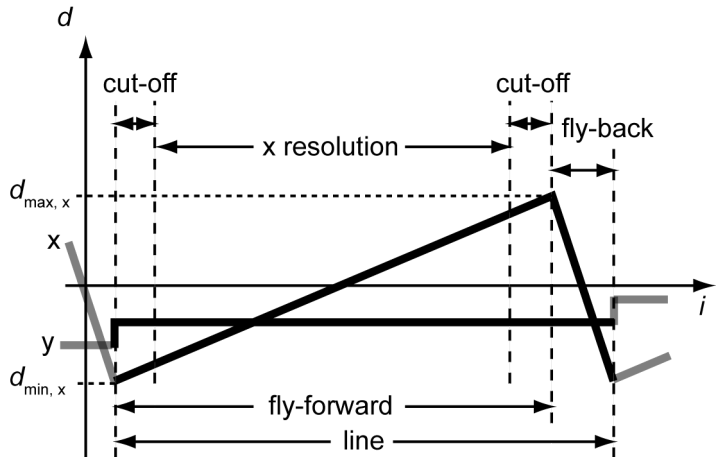
A.2 *In vivo* procedures

A.2.1 Mice breeding

C57/BL6 wild-type mice

For breeding, two female and one male animal were housed in plastic cages (Eurostandard type III, 425 x 266 x 155 mm; Tecniplast S.p.A., Buguggiate, Italy) featuring a constant supply of water and food pellets. A day/night light cycle with a period of 24 h (12 h light / 12 h dark) was maintained. Litters were kept in the respective breeding cage until P21 (maximally up to P28 when body size was smaller than normal) and then transferred to new cages with female and male animals separated. The breeding animals were replaced when littering frequency became sparser than normal.

GAD67-GFP (Δneo) mice

The genotype of original founder animals was confirmed by polymerase chain reaction (PCR) (see protocol below). For breeding, male GAD67-GFP (Δneo)-positive animals (heterozygous, C57BL/6 background) were paired with female C57BL/6 wild-type mice according to the procedure described for wild-type animals above. GAD67-GFP-positive pups were selected based on transcranial fluorescence at P2-3.

PCR genotyping PCR was carried out using the primers listed in Table A.1 on page 172 (Microsynth AG, Balgach, Switzerland). Samples were obtained from tail tip biopsies (length 2 mm to 3 mm). Briefly, the procedure was as follows. First, DNA was prepared according to the HotSHOT protocol [284] by incubating the biopsies in sodium hydroxide solution (25 mM NaOH, 0.2 mM ethylenediaminetetraacetic acid (EDTA) disodium salt; 300 µL per tail tip) for 30 min at 95 °C. Then, samples were gently shaken and neutralised (with 300 µL of 300 40 mM TRIS-HCl). PCR reaction mixtures were prepared as follows: 2 µL deoxyribonucleotides (dNTPs) (5 mM diluted aliquots; Sigma, Buchs, Switzerland), 0.1 µL of each primer (from 100 µM aliquots in purified water), 0.3 µL DNA polymerase (JumpStart Taq; Sigma, Buchs, Switzerland), 5 µL buffer (part of the polymerase kit), 40 µL purified water, 2 µL DNA sample (previously diluted 1:10 in purified water). PCR was performed on a thermocycler (Mastercycler Gradient; Eppendorf, Hamburg, Deutschland) using the following program:

1. 96 °C for 1 min
2. 96 °C for 30 s
3. 58 °C for 30 s
4. 70 °C for 1 min
5. Steps 2 to 4 were repeated 40 times in total.
6. 68 °C for 5 min
7. 4 °C until further processing

Table A.1: PCR primers for genotyping of GAD67-GFP (Δneo) mice.

Primer	Sequence
TR1b	5'-GGC ACA GCT CTC CCT TCT GTT TGC-3'
TRGFP-8	5'-CTG CTT GTC GGC CAT GAT ATA GAC-3'
TR3	5'-GCT CTC CTT TCG CGT TCC GAC AG-3'

PCR products were separated using agarose gel electrophoresis. Gels were prepared with 1.5% agarose (Sigma, Buchs, Switzerland) in TRIS-borat-EDTA (TBE) buffer (89.2 mM TRIS base, 89.0 mM boric acid, 4.0 mL per litre of 0.5 M EDTA pH 8.0) using ethidium bromide (0.16 mg L^{-1}; Sigma, Buchs, Switzerland) as a DNA marker. Each PCR product sample was mixed with 5 uL loading buffer (2% w/w glycerol, 10 mM EDTA disodium salt with pH 8, 0.1% (w/w) sodium dodecyl sulfate (SDS), 0.005% (w/w) bromophenol blue). Gels were run at 120 V (Model 200/2.0 Power Supply; Inotech AG, Wohlen, Switzerland).

An animal was considered positive for GAD67-GFP if two bands were visible in the respective lane at approximately 250 bp and 500 bp. It was considered negative if only the band near 250 bp was present (Figure A.2 on page 173).

A.2.2 Animal preparation

Anaesthesia

Anaesthesia of mice (2 to 3 months old) [275] was induced with 5 % isoflurane in air, followed by urethane (0.8 mg g^{-1} and 1.4 mg g^{-1} body weight, respectively, for wild-type and GAD67-GFP mice) injected i.p. as 20 % aqueous solution. Body temperature was maintained at 37 °C using a feedback-based system with rectal probe (DC Temperature Control System; FHC Inc., Bowdoin, ME). During surgery, the level of anaesthesia was monitored based on whisker movement and foot-pinch reflex. If required, urethane anaesthesia was temporarily supplemented with isoflurane.

Craniotomy

After removal of the skin covering the caudal part of the head, a head plate was glued tangentially to the skull at the expected location of the left barrel cortex using cyanoacrylate superglue (Pattex Gel; Henkel & Cie AG, Pratteln, Switzerland) and dental cement (Paladur; Heraeus, Hanau, Germany). A craniotomy was then made (centered 3.5 mm lateral, 1 mm post bregma) under a stereo microscope (Leica Zoom MZ6; Leica Microsystems GmbH, Wetzlar, Germany) using a dental drill (EXL-M40 with LHP12 handpiece from Osada Electric Co., Tokyo, Japan; used in combination with H71 drill inserts from Säntis Dental, Wald, Switzerland). Also, the dura was removed and the exposed was brain superfused with NRR solution (145 mM NaCl, 5.4 mM KCl, 10 mM HEPES, 1.0 mM MgCl$_2$, 1.8 mM CaCl$_2$; pH 7.2 adjusted with NaOH). To dampen heartbeat- and breathing-induced motion artefacts, the cranial window was covered with a layer of agarose (0.5 mm to 1 mm
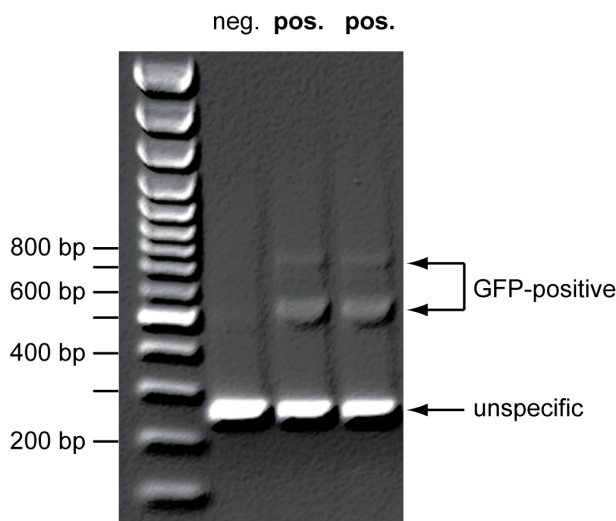
Figure A.2: Results for PCR-based genotyping of GAD67-GFP (Δneo) mice. 100 bp DNA ladder is shown on the left side of the gel. Three sample lanes: negative, positive, positive genotypes, respectively.

thick; type III-A from Sigma; 1.5 % in NRR) and an immobilised cover slip.

Fluorescence labelling in acute experiments

Selective astrocyte staining was achieved by exposing the brain to 50 µM SR101 (Sigma-Aldrich, Buchs, Switzerland) during 5 min to 10 min [219]. For functional calcium measurements, L2/3 cell populations were labelled with the green fluorescent calcium indicator OGB-1 by MCBL [266, 102, 101]. Briefly, 50 µg of the acetoxymethyl AM ester of OGB-1 (OGB-1 AM; Invitrogen, Basel, Switzerland) was dissolved in 5 µL of a solution of 20% Pluronic F-127 in dimethyl sulfoxide (DMSO) (both from Sigma-Aldrich, Buchs, Switzerland) and diluted in Ca^{2+}-free NRR to a final concentration of 1 mM. 1 µL of 2.0 mM Alexa Fluor 594 hydrazide solution (sodium salt; Invitrogen) was added to facilitate the visualisation of the dye solution under the two-photon microscope during injection. Dye solution was pressure-injected with a patch pipette (300 mbar during 1 min to 2 min) into a barrel column previously identified by IOS imaging (Section A.2.3).

Virus-mediated expression of YC3.60

Recombinant adeno-associated virus (rAAV) harbouring YC3.60 under control of the human synapsin promoter was produced and purified according to the procedure described in [184] (virus titer in transducing units: $3 \times 10^8 \, l^{-1}$. The virus solution was diluted 1:1 with a solution of 20 % mannitol in phosphate-buffered saline (PBS); 0.1 M, pH 7.3) and delivered into cortical tissue (volume 200 nL to 300 nL; depth about 250 µm) through a glass pipette (tip size 8 µm to 12 µm) by stereotactic injection [184] through a craniotomy. After virus injection, the craniotomy was covered with a glass window and sealed with UV-hardening, tissue-compatible glue. Animals were imaged 3.5 to 9 months after infection.

A.2.3   Intrinsic optic signal (IOS) imaging

Space-resolved imaging

Space-resolved IOS imaging was employed to identify the position of the cortical representation of specific whiskers in the mouse barrel cortex. Briefly, baseline images were acquired during 5 s without stimulation. During the following 5.5 s, a single whisker was tapped (50 Hz rectangular motion along whisker axis using a pipette tip mounted on a loudspeaker) and images were acquired during 5 s after an initial delay of 0.5 s. Images from periods without and with stimulation were separately averaged and subtracted. The procedure was repeated at intervals of 20 s until a clear intrinsic signal was obtained.

A.2.4   *In vivo* two-photon microscopy

Microscope

A two-photon microscopy setup as described in Section A.1.1 was used. Signal acquisition was performed with a Hifo ADC of the first generation (Section A.1.3). Fluorescence light from the up to three fluorophores (Figure A.3 on page 175) was captured with a custom-built three-channel detector system with two dichroic mirrors (DC-Blue and DC-Red; Linos, Göttingen, Germany) (Figure A.4a on page 176). Appropriate band-pass filters were selected for each channel. Blue channel: D480/60 M (AHF Analysentechnik, Tübingen, Germany); green channel: BG39 glass (3 mm thick; Schott AG, Mainz, Germany); red channel: HQ 610/75 M-2P (AHF Analysentechnik).

Image acquisition

High-resolution overview image stacks were acquired using a 20x objective (XLUMPlanFI 20x/0.95; Olympus, Tokyo, Japan) at 850 nm excitation wavelength (configuration A_1 in Figure A.4 on page 176). Calcium imaging was performed using a 40x objective (LUMPlan-FI/IR 40x/0.80W; Olympus), usually 820 nm to reduce contribution of GFP fluorescence to the green channel (configuration A_2 in Figure A.4 on page 176). When measuring calcium transients in GFP-positive neurons, the signal-to-noise ratio in the functional (i.e. green) channel could be improved by using 820 nm excitation wavelength, which minimized GFP fluorescence contribution in the green channel (configuration A_2 in Figure A.4 on page 176).

A.2.5   Data analysis

Two-photon calcium imaging time series acquired from the functional channel were registered using the ImageJ plug-in TurboReg [277] and then processed as follows. First, the mean background value $F_{background}$ was determined inside a blood vessel and subtracted from the individual frames.

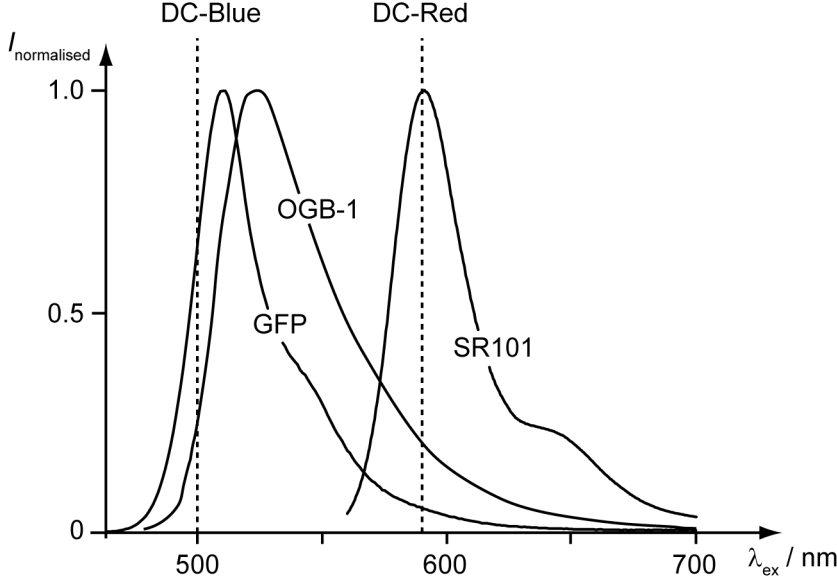$$F(x,y) = F(x,y) - F_{background} \tag{A.10}$$

Figure A.3: Emission spectra of *in vivo* triple stain fluorophores. Cut-off wavelengths of dichroic mirrors used in the microscope detector system are shown as dotted lines. Abbreviations: green fluorescent protein (GFP), Oregon Green 488 BAPTA-1 (OGB-1), sulforhodamine 101 (SR101). Data sources: [80, 146, 287]

Then, a base-line image F_0 was defined as the average of the first 20 frames.

$$F_0(x,y) = \frac{1}{n} \sum_{i=1}^{n=20} F_i(x,y) \tag{A.11}$$

Finally, relative percentage fluorescence changes ($\Delta F/F_0$) were calculated pixel-wise by subtracting F_0 from the image time series and dividing the result by F_0:

$$\Delta F/F_0(x,y) = \frac{F(x,y) - F_0(x,y)}{F_0(x,y)} \tag{A.12}$$

Single-cell ROIs were drawn by hand in a way that their contours were within the visually perceived cell boundary (with at least one pixel distance to it in order to exclude surrounding neuropil). Calcium signals from cells of interest were extracted using ImageJ and further processed with Excel (Microsoft Corporation, Redmont, WA) and Igor Pro 5 (WaveMetrics Inc., Portland, OR).
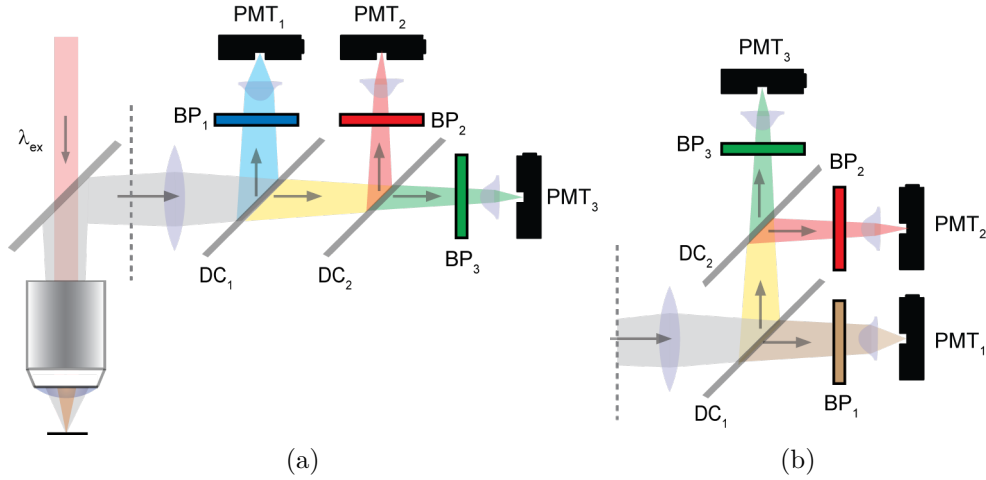
Dye combination	config.	λ_{ex}	DC$_1$	DC$_2$	BP$_1$	BP$_2$	BP$_3$
GFP/SR101/OGB-1, anat.	A$_1$	850	500LP	590SP	480/60	605/75	BG39
GFP/**SR101/OGB-1**, funct.	A$_2$	820	500LP	590SP	480/60	605/75	BG39
GFP/AMCA/DL488/**DL594**	A$_3$	850	500LP	590SP	480/60	605/75	BG39
GFP/**AMCA/DL488/DL594**	A$_4$	720	500LP	590SP	450/50	605/75	BG39
YC3.60/RRX/DL649	B	825	650LP	590SP	697/75	605/75	BG39

Figure A.4: Fluorescence excitation and detection beam paths used for two-photon imaging with different fluorophore combinations. Fluorophores in bold: visible; non-bold: invisible with the respective settings. Abbreviations: excitation wavelength (λ_{ex}); photo-multiplier tube (PMT); band-pass filter (BP); dichroic mirror (DC); short-pass filter (SP); long-pass filter (LP). Filter wavelengths are specified in nanometres. For BP filters, the centre wavelength and the width of the transmission range is given. **(a)** Configuration A. **(b)** Configuration B.

A.3   Post hoc histology procedures

A.3.1   Tissue preparation

Perfusion fixation

After *in vivo* experiments, mice were deeply anaesthetized by injection of ketamine (Narketan 10 from Vétoquinol AG, Ittigen, Switzerland; dose 0.1 mL, 50 mg mL^{-1}, i.p.). Following injection of heparin into the left heart ventricle (Heparin-Na 25 000 I.E./5 mL from B. Braun Medical AG, Emmenbrücke, Switzerland; dose 0.05 mL), animals were intracardially perfused with 10 mL to 20 mL of PBS (0.1 M, pH 7.3, 4 °C) at 12 mL min^{-1}, followed by 20 mL of paraformaldehyde (PFA) solution (4% in 0.1 M PBS, pH 7.3, 4 °C) at 12 mL min^{-1}. The cranial window was removed after perfusion with PBS but before perfusion with PFA solution. In experiments with YC3.60-expressing mice, animals were subsequently perfused with 5 mL of warm agarose solution (type III-A from Sigma; 1.5 % in 0.1 M PBS). This prevented small capillaries from collapsing, which later provided crucial landmarks for cell

matching.

Preparing coronal cryostat sectioning

For later coronal sectioning, the brain was removed from the skull and postfixed in 4% PFA at 4 °C overnight. Then the brain was rinsed 3 times with PBS (0.1 M, pH 7.3, room temperature). A tissue block containing the cortical volume below the craniotomy was excised and glued to a plastic petri dish with the pial brain surface horizontally oriented. With the tissue block submerged in PBS (0.1 M, pH 7.3), a large-field-of-view surface reference map (average-intensity projection (AIP) of an image stack with 20 µm z-steps) of the fixed tissue block was acquired under the two-photon microscope using a 4x objective (UPlanFL N 4x/0.13; Olympus, Tokyo, Japan) and 850 nm excitation wavelength (Figure A.4 on page 176, configuration A1). The tissue block was afterwards kept in 30 % sucrose at 4 °C until sedimented.

Preparing tangential cryostat sectioning

For brains later subject to tangential sectioning, the head was not removed from the head plate. Rather, instead of excising the brain from the skull, just the lower jaw and the tip of the snout was removed to enhance access of PFA solution during post-fixation without damaging the upper half of the head. After post-fixation and rinsing (see previous section), the aggregate of head and head plate was mounted on a head-plate holder and a surface reference map acquired under the two-photon microscope (using the settings described in the previous paragraph). The head was subsequently kept in 30 % sucrose at 4 °C for two days. Afterwards, the head was removed from the sucrose solution and frozen at −20 °C. Head plate holder and circular saw were cooled down to −80 °C to prevent premature thawing during the following sawing procedure. With the frozen head mounted to the cooled-down head-plate holder and the circular saw attached to a pillar drilling machine, the head was horizontally sawed to produce a cutting surface oriented parallel to the head plate (Figure A.5 on page 178). After sawing, the upper part of the head was immediately cooled down to −20 °C again to prevent thawing. Working at 4 °C, the head plate was then carefully removed from the skull.

A.3.2 Sectioning procedures

Coronal sectioning with cryostat

The tissue block was embedded in TissueTek O.C.T.™ Compound (Sakura Finetek, Alphen aan den Rijn, The Netherlands) and frozen at −20 °C before being cut into 140 to 200 µm thick coronal slices using a cryostat (both sample and blade temperature were kept at −16 °C to avoid tissue fragmentation during sectioning). Sections were mounted vertically between two cover slips (No. 1; Menzel-Gläser, Braunschweig, Germany) using two strips of cover slip as spacer. The pial brain surface segment of the slice was then imaged

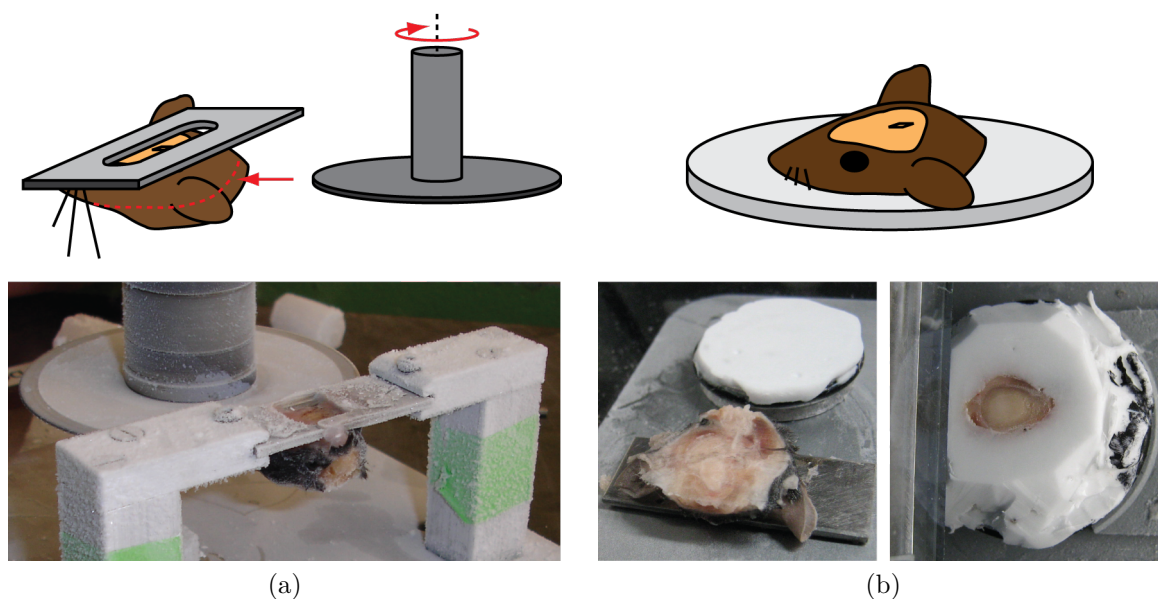(a)   (b)

Figure A.5: Preparation for tangential sectioning of a brain by sawing the frozen head parallel to the craniotomy surface. **(a)** The head still glued to the head plate used during the *in vivo* experiment. The head plate is mounted on a head plate holder. Using a vertically mounted circular saw, the frozen head can be sawed perfectly parallel to the head plate and the craniotomy surface). **(b)** After sawing and removal of the head plate, the upper half of head is glued to a cryostat mounting socket (lower right). In this arrangement, the craniotomy surface is oriented parallel to the socket and can easily be aligned with the cryostat blade to enable tangentional sectioning (lower left).

under the two-photon microscope (Figure A.4 on page 176, configuration A1) using the 4x objective mentioned above. In order to identify the slices covering the volume of interest, images of the pial slice surfaces were overlaid onto the surface map acquired before sectioning (and/or a camera image of the surface blood vessel pattern acquired *in vivo*) using Photoshop CS 3 (Adobe Systems, Mountain View, CA).

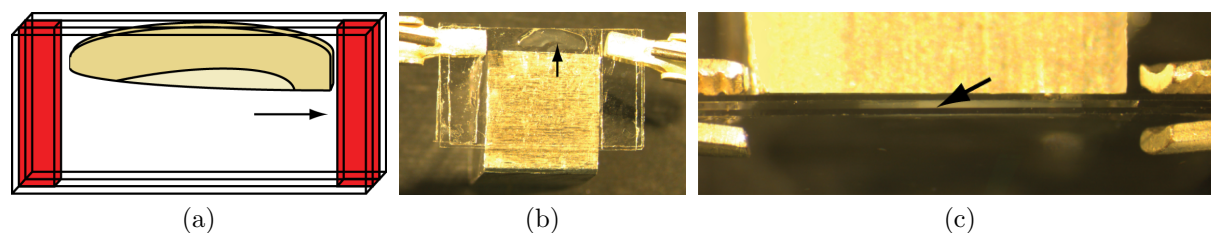(a)   (b)   (c)

Figure A.6: Vertical mounting for coronal slices allowing imaging of their pial surface. **(a)** Coronal slices were mounted between two cover-slips with two stripes of cover slip glass as spacers (medial side of slice indicated by arrow). **(b)** The glass assembly was held together by two clips and glued to a metal bearing (brain slice indicated by arrow). The mount was placed vertically under the two-photon microscope to image the pial surface segments. **(c)** Top view with pial slice surface visible as a pale stripe (indicated by an arrow).

Tangential sectioning with cryostat

A cryostat sample socket was prepared by freezing TissueTek O.C.T.™ Compound onto its surface and subsequently cutting a plane surface using the cryostat. The frozen head was then placed onto the prepared TissueTek surface with its cut surface and then completely embedded in the compound. The head was cut into tangential sections of 100 μm thickness (blade and sample temperature were both −16 °C). Sections were horizontally mounted in PBS (0.1 M) on microscopy slides. Slices of interest were selected by acquiring two-photon images (AIP of stacks acquired with 20 μm z-step size) and overlaying them on images acquired before sectioning (see previous paragraph for details).

Sectioning for cytochrome-oxidase C (COX) staining

After fixation, the brain was separated into two hemispheres. The hemisphere of interest was cut tangentionally to the barrel cortex region using a razor blade. The remaining part containing the cortex was glued to a vibratome sample socket using cyanoacrylate superglue (Pattex Gel, Henkel & Cie AG, Pratteln, Switzerland). On the vibratome (752M Vibroslice; Campden Instrumends Ltd., Loughborough, Leicester, UK), the cortex was submerged in 0.1 M PBS and sectioned tangentionally to the barrel cortex region (100 μm slice thickness). Sections were collected in 24-well plates with 0.1 M PBS.

A.3.3 Staining procedures

Immunohistochemistry (IHC)

Slices were blocked in carrier solution (10 % normal donkey serum (NDS) from Jackson ImmunoResearch, West Grove, PA; 2 % Triton X-100 from Sigma-Aldrich, Buchs, Switzerland; 0.04 % NaN_3 in 0.1 M PBS) overnight at room temperature on either a shaker (IKA-VIBRAX-VXR; IKA, Staufen, Germany) or a rotation incubator (CMV-ROM; Fröbel Labortechnik, Lindau, Germany). Slices were then incubated with primary antibodies (Table A.2 on page 180) in carrier solution for three days at room temperature on the shaker. Afterwards, they were briefly rinsed three times with 0.1 M PBS, washed three times with PBS for 30 min and subsequently incubated with secondary antibodies (Table A.2 on page 180; see Figure A.7 on page 180 for emission spectra) in carrier solution for 1 d at room temperature on the shaker or rotation incubator. After further rinsing and washing (three times each), slices were cleared in a sequence of sucrose solutions (15 %, 30 %, 45 % and 60 % of sucrose in 0.1 M PBS / 2 % Triton X-100) with periods of 4 h per sucrose concentration. A negative control with secondary antibody only was performed on brain slices from C57/BL6 mice (Figure A.8 on page 181).

Cytochrome-oxidase C (COX) staining

COX staining was used to confirm the position of barrel columns previously identified with IOS imaging. A protocol based on [174, 306] was used. Briefly, slices (see Section A.3.2
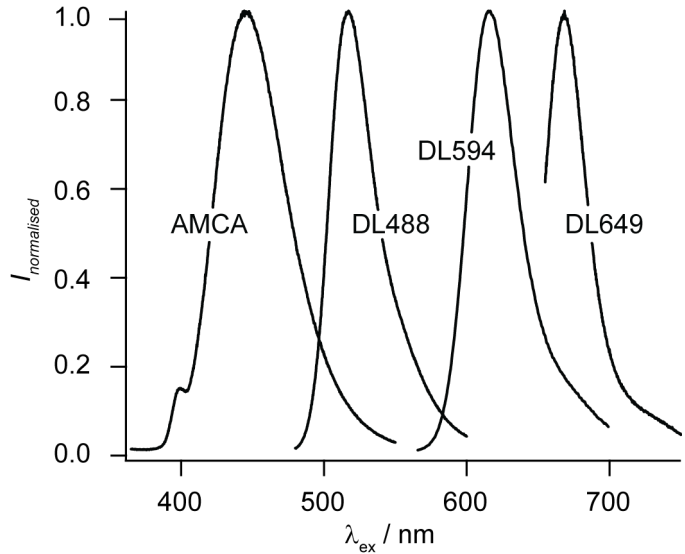
Figure A.7: Emission spectra of the fluorophores used as secondary antibody labels. Abbreviations: aminomethylcoumarin acetate (AMCA); DyLight 488 (DL488); DyLight 594 (DL594); DyLight 649 (DL649).

Table A.2: Primary and secondary antibodies used in this work. Abbreviations: green fluorescent protein (GFP); sulforhodamine 101 (SR101); Oregon Green 488 BAPTA-1 (OGB-1); Yellow Cameleon 3.60 (YC3.60); Parvalbumin (PV); Calretinin (CR); Calbindin (CB). Primary antibodies were purchased from Swant (Marly, Switzerland) and secondary antibodies from Jackson ImmunoResearch (Newmarket, Suffolk, UK).

In vivo stain	Marker	Primary antibody	Sec. antibody	Colour
GFP/SR101/OGB-1	PV	goat anti-Parvalbumin (Swant PVG-214), 1:2000	DyLight 594 donkey anti-goat (705-515-147), 1:200	red
GFP/SR101/OGB-1	CR	rabbit anti-Calretinin (Swant 7699/4), 1:2000	DyLight 488 donkey anti-rabbit (711-485-152), 1:200	green
GFP/SR101/OGB-1	CB	mouse anti-Calbindin (Swant #300), 1:2000	AMCA donkey anti-mouse (715-155-151), 1:50	blue
GFP/SR101/OGB-1	PV	mouse anti-Parvalbumin (Swant 235), 1:2000	RRX goat-anti mouse (115-295-003), 1:200	red
GFP/SR101/OGB-1	CR	mouse anti-Calbindin (#300), 1:2000	DyLight 649 donkey anti-rabbit (711-495-152), 1:200	IR

for preparation) were incubated for 2 h in a solution of 3,3'-diaminobenzidine (DAB), cytochrome C and sucrose (1.4 mM DAB tetrahydrochloride from Sigma, Buchs, Switzerland; 0.3 mg/mL bovine heart cytochrome c from Fluka, Buchs Switzerland; 117 mM sucrose) in 0.1 M PBS at 37 °C. After staining, slices were rinsed three times for 10 min with 0.1 M PBS. Images were acquired using a stereo microscope (Leica Zoom MZ6; Leica Microsystems GmbH, Wetzlar, Germany) with an inbuilt camera (Leica IC D; Microsystems GmbH). Photoshop CS3 (Adobe Systems, Mountain View, CA) with its interactive layer operations (transparency, rotation, translation) was used to create an overlay of all slices; and
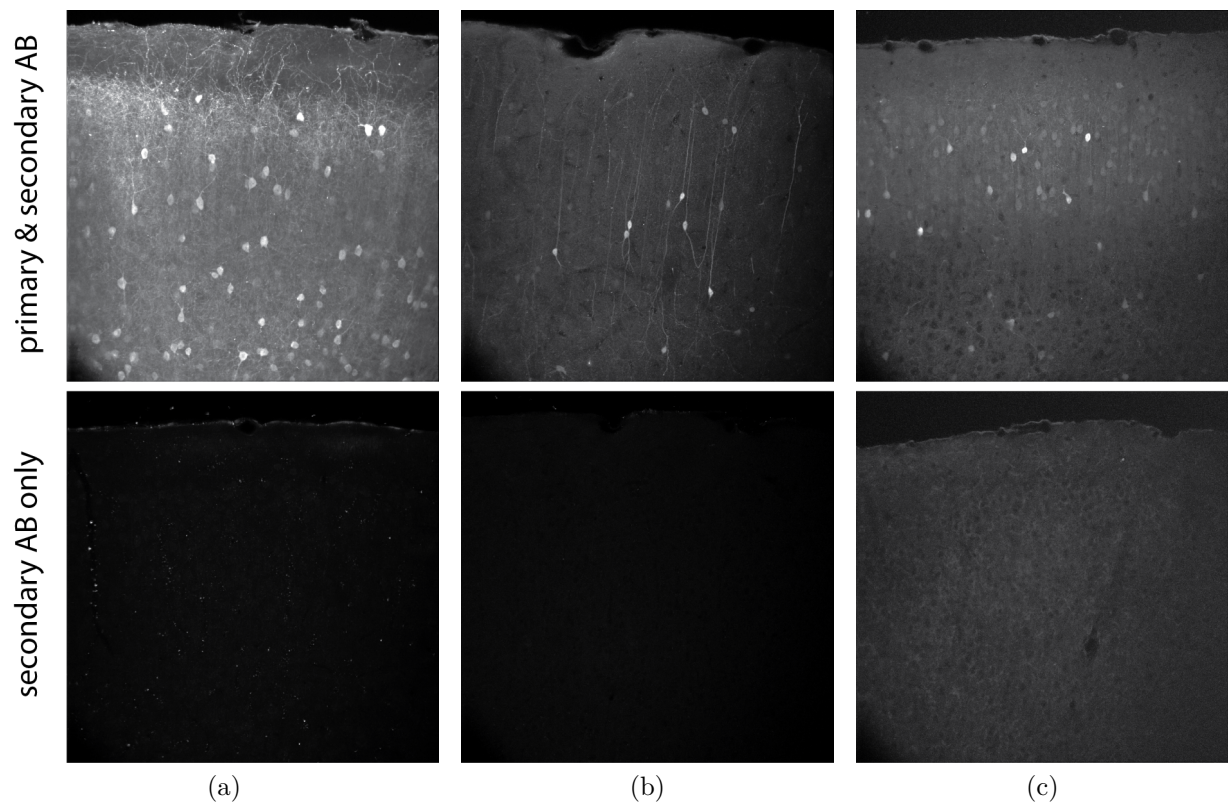
Figure A.8: Negative control of antibody stains. Top row: 140 µm-thick coronal slices from C57/BL6 mice incubated with primary and secondary antibody. Bottom row: negative control performed with brain slices incubated with secondary antibody only (same range and offset as for top row). **(a)** anti-PV: in the negative control, all cells bodies were slightly more fluorescent than the neuropil. However, when using the same range and offset as for the positive-control, this unspecific stain was not visible. **(b)** anti-CR: negative control did not contain any stained cell bodies. **(c)** anti-CB: negative control did not contain any stained cell bodies.

thus an overlay of the barrels and the surface blood vasculature.

A.3.4   Brain slice imaging and image stack alignment

Brain slices (on which IHC may have been performed) were mounted on microscopy slides in 45 % sucrose solution (see above) and protected with cover slips using strips of cover slips as spacers. For each slice, two image stacks (3 µm z-steps) of the region corresponding to the *in vivo* reference image stack were acquired using the two-photon microscope with a 20x objective (see above). At 850 nm excitation wavelength, triple-immunostained brain slices from GAD67-GFP mice were imaged with the same filter set as for *in vivo* imaging (configuration A_3 in Figure A.4 on page 176). For excitation at 720 nm, a different band-pass filter was used for the blue channel (EP 450/50; AHF Analysentechnik, Tübingen, Germany; configuration A_4 in Figure A.4 on page 176). For slices from YC3.60-expressing mice, yet another detector configuration (configuration B in Figure A.4 on page 176) with another dichroic mirror (Q 650 LP; AHF Analysentechnik) and an appropriate filter combination for the infrared channel (BrightLine HC 697/75 in series with a Semrock FF01-750/SP-25 infrared block filter, both from AHF Analysentechnik) was used.

Coronal sections

The exact locations for stack acquisition were identified using surface blood vessel cross-sections as landmarks. Image stacks were resliced using ImageJ [2] to obtain a 90° rotation. Further rotational fine-tuning was carried out using the TransformJ plug-in[3] for ImageJ. In detail, a series of rotations around the horizontal x and y axes were performed in a systematic trial-and-error approach until optimal rotation-fitting was achieved, including scaling and translation operations if required.

Tangential sections

For each slice, location and orientation for stack acquisition was identified based on the overlay image obtained during the slice selection step. A comparison of characteristic blood vessels contained in the the *in vivo* reference image stack with cross-sections present in the slices provided further hints. 3D Rotation-fitting was not necessary as the pre-orientation obtained by means of the sawing procedure was already of high quality.

A.3.5   Data analysis

Custom-written LabVIEW software was used for *in-vivo*-to-fixed-slices cell matching and cell annotation.

---

[3]Kindly provided by Erik Meijering, Rotterdam.

Analysis of matching efficiency

For bin-wise analysis of the fraction of matched cells, the distance of the cell from the cutting plane has to be calculated. In the *in vivo* reference image stack, the cutting plane was defined by selecting three points $A(a_x/a_y/a_z)$, $B(b_x/b_y/b_z)$ and $C(c_x/c_y/c_z)$ in the cutting plane (Figure A.9 on page 183).

From these points the parametric version of the plane equation was calculated:

$$\vec{p}_{plane} = \vec{p}_V + m\vec{a} + n\vec{b} \tag{A.13}$$

where

$$\vec{a} = \overrightarrow{AB} = \begin{pmatrix} d \\ e \\ f \end{pmatrix} = \begin{pmatrix} b_x - a_x \\ b_y - a_y \\ b_z - a_z \end{pmatrix} \qquad \vec{b} = \overrightarrow{AC} = \begin{pmatrix} g \\ h \\ i \end{pmatrix} = \begin{pmatrix} c_x - a_x \\ c_y - a_y \\ c_z - a_z \end{pmatrix} \tag{A.14}$$

As anchor point $V(v_x/v_y/v_z)$, the point that is on the plane normal vector pointing towards the origin of the coordinate system was chosen:

$$\vec{p}_V = \begin{pmatrix} v_x \\ v_y \\ v_z \end{pmatrix} = l_0 \vec{n}_{unit} \tag{A.15}$$

where

$$\vec{n}_{unit} = \begin{pmatrix} j \\ k \\ m \end{pmatrix} = \frac{\vec{n}}{|\vec{n}|} \quad \text{with} \quad \vec{n} = \vec{a} \times \vec{b} = \begin{pmatrix} ei - fh \\ fg - di \\ dh - eg \end{pmatrix} \tag{A.16}$$

From there we conclude the following equation system:

$$l_0 j = a_x + sd + tg \tag{A.17}$$
$$l_0 k = a_y + se + th \tag{A.18}$$
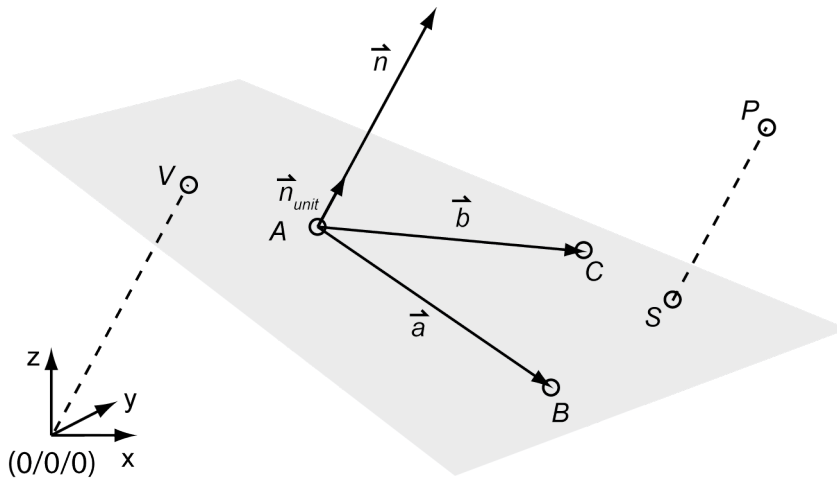$$l_0 m = a_z + sf + ti \tag{A.19}$$

Figure A.9: Deriving the equations for bin-wise matching statistics. A, B, C: reference points defining the cutting plane; V: origin of the normal vector that points towards the origin of the coordinate system; P: arbitrary point in space; S: origin of the normal vector pointing towards P.

This was solved for l using Maple V (Waterloo Maple Inc., Waterloo, Ontario, Canada):

$$l_0 = \frac{fa_y g - fha_x - a_y di + eia_x - ea_z g + hda_z}{jei - jfh + dmh - dik + gfk - gem} \tag{A.20}$$

The distance of the plane from the origin is then equal to l in the equation of the line going through the anchor point and the origin. The plane can be shifted back- and forth by varying the parameter l (this shifts the anchor point along the plane normal going through the origin):

$$l = l_0 + \Delta l \tag{A.21}$$

The distance of a point $P(p_x/p_y/p_z)$ from the plane can be calculated as follows. The equation of the line through P and orthogonal to the plane is:

$$\vec{p}_{line} = \vec{p}_P + l\vec{n}_{unit} \tag{A.22}$$

The point of intersection S of this line and the plane is thus:

$$\vec{p}_S = \vec{p}_P + l\vec{n}_{unit} = \vec{p}_a + s\vec{a} + t\vec{b} \tag{A.23}$$

We conclude the equation system

$$p_x - lj = v_x + sd + tg \tag{A.24}$$
$$p_y + lk = v_y + se + th \tag{A.25}$$
$$p_z + lm = v_z + sf + ti \tag{A.26}$$

which was solved with Maple V for the distance l:

$$l = -\frac{v_y di + ev_z g - hdv_z - eiv_x - p_y di + p_y gf - fv_y g - ep_z g + eip_x + hdp_z - hp_x f + fhv_1}{jei - jfh + dmh - dik + gfk - gem} \tag{A.27}$$

B   Software engineering concepts

B.1   Important aspects

Within the following four paragraphs, the problems mentioned in Section 2.1.1, with regards to the software, are taken into consideration.

Cohesion

Cohesion is a measure of how strongly the elements of a software module are related to each other. We aim for high cohesion, especially in terms of function [265, 60, 195]. Simply speaking, what belongs together goes together. In OOP (see Section B.2), strong cohesion means that the methods of a class revolve a around a common functionality and that a single method should have a very focused functionality (optimally represented in its name). High cohesion makes a module (a class, method, or function) easier to understand, easier to maintain and easier to reuse [60].

Coupling

Coupling refers to how strongly individual modules depend on each other. We aim for loose coupling as opposed to tight coupling between modules in order to keep their potential reusability high and to minimise the changes required in other modules when we decide to modify the implementation of a specific module [265, 60].

Information hiding

This concept refers to hiding complexity behind a simple interface. This is achieved by *encapsulating* the implementation of a functionality in a module and allowing access only through a well-defined interface [223, 60]. Information hiding provides the following advantages:

- In the design phase of a software life-cycle it allows the developers to focus on the abstract level of interfaces and their interactions instead of concrete implementations;

- It increases *maintainability* of a software application by minimising changes required to the interacting modules when the implementation (but not the interface) of a module is modified.

- It increases *understandability* of a code because an outsider can focus on what a module does (defined by its interface and the corresponding interface contract) rather than on the concrete implementation of the module.

Information hiding typically results in looser coupling due to the fact that modules only interact via their simple and thus limited interfaces.

Abstraction

Abstraction is an approach used to simplify problems by eliminating factors that are not relevant to the core concept. By layering several levels of abstraction, complexity of software systems can be managed more easily. In a top-down approach, a system is modelled using just a few interacting components, each of which is again composed of its components, down to the most basic level. In a bottom-up approach, we implement new components using already existing components of a lower abstraction level [161].

B.2   Object-oriented programming

Since its introduction in the 1960s, object-oriented programming (OOP) has become a standard paradigm in modern software development [10, 63]. In OOP, the programmer defines a special kind of data types, so-called *classes*[1], which can be instanced as so-called *objects*[2]. Classes differ from other kinds of data types in that they cannot only store data as so-called *member variables*[3], but also can contain functions, so-called *methods*, that can access or manipulate the class' data .

B.2.1   Key concepts

OOP is based on the following key concepts [10]:

- *Abstraction:* An abstract data type (ADT) is a combination of data and a definition of the operations that can be performed on this data. In OOP, ADTs are realised as classes. In less technical terms, abstraction refers to the fact that classes model reality using distinctions inherent to the problem.

- *Encapsulation:* The data of a class are hidden from the user and can only be accessed via interface methods.

- *Inheritance:* A class is used as the basis for another class. The *derived class*[4] inherits the functionality of the *base class*[5], and can provide additional methods or override methods of the base class.

---

[1]Reference [10] conceptualises a class as "a description of the organization and actions shared by one or more similar objects".

[2][10] refers to an object as "a individual, identifiable item, either real or abstract, which contains data about itself and descriptions of its manipulations of the data".

[3]Also referred to as *attributes*

[4]Also referred to as *child class*

[5]Also referred to as *parent class*

- *Polymorphism:* Code operating on a set of objects instanced from related classes does not necessarily have to distinguish between different types of child classes. Rather, objects of different child classes can be treated as if they belong to the common base class as long as the methods invoked are present in the base class[6]. With *late binding*[7], the decision which exact class is to be used can even be made by the software at run time.

- *Messaging:* Objects can communicate with each other by passing messages, thereby transmitting data or invoking methods.

B.2.2 Strengths

For our context, I would like to emphasize three main advantages of OOP that are a result of the above-mentioned concepts.

Structure

First, it facilitates writing software in a structured manner because it naturally enforces the software designer to split up the code into classes and their methods. Optimally, when designing the classes, the designer identifies discrete entities in the system he is going to represent in his software and implements them as classes in his software (abstraction). Properties of these entities are implemented as member variables of these classes, while operations these entities can perform, or that can be performed on them, are implemented as methods of the classes. This approach, called *object-oriented design*, does not only make designing the software architecture easier. It also helps outsiders or newcomers to the project to understand it because classes, member variables and methods can be immediately related to an entity of the physical system, in our case the microscope.

Reusability

The second advantage is reusability of code as a result of encapsulation. Encapsulation means that member variables can have – or even should have – private access scope (which is the default in LabVIEW), such that they cannot be directly accessed from outside the class. Instead, access is only possible via accessor methods (getter and setter methods). This provides a defined and steady interface through which the class' functionality can be accessed, while preventing other developers from making their code dependent on any assumptions about the class' interior that might change over time and render the dependent code unusable. Rather, the class' interior does not even have to be understood by somebody who wants to use it, as long as the methods it exposes are well documented.

---

[6]Liskov Substitution Principle: a subtype should behave the same as the base class; an object of a derived class can be substituted by an object of the base class [181].

[7]also referred to as *dynamic binding*

Adaptability

The third advantage, adaptability, is a result of inheritance and polymorphism. One can make use of an existing class by creating a derived class that uses some of the functionality of its parent, while customising other or providing completely new functionality. Due to the fact that the derived class inherits the public method interface through which its objects are accessed from outside, any software that had been built using the base class, will still function with the derived class.